LASER DIRECTED ENERGY DEPOSITION OF INCONEL 625 ALLOY FOR REPAIR & FEATURE ADDITION APPLICATIONS: AN EXPERIMENTAL AND NUMERICAL INVESTIGATION

Thesis

Submitted in partial fulfilment of the requirements for the degree of

DOCTOR OF PHILOSOPHY

By

JITENDER KUMAR CHAURASIA

DEPARTMENT OF MECHANICAL ENGINEERING
NATIONAL INSTITUTE OF TECHNOLOGY KARNATAKA,
SURATHKAL, MANGALORE – 575025

AUGUST – 2023

DECLARATION

I hereby declare that the Research Thesis entitled **"LASER DIRECTED ENERGY DEPOSITION OF INCONEL 625 ALLOY FOR REPAIR & FEATURE ADDITION APPLICATIONS: AN EXPERIMENTAL AND NUMERICAL INVESTIGATION"** which is being submitted to the National Institute of Technology Karnataka, Surathkal in partial fulfilment of the requirements for the award of the Degree of **Doctor of Philosophy** in **Department of Mechanical Engineering** is a *bonafide report of the research work carried out by me*. The material contained in this Research Thesis has not been submitted to any University or Institution for the award of any degree.

Registration number: **177003ME004**

Name of the Research Scholar: **JITENDER KUMAR CHAURASIA**

Signature of the Research Scholar: ______________________

Department of Mechanical Engineering

Place : NITK Surathkal

Date : 22/08/2023

CERTIFICATE

This is to certify that the Research Thesis entitled **"LASER DIRECTED ENERGY DEPOSITION OF INCONEL 625 ALLOY FOR REPAIR & FEATURE ADDITION APPLICATIONS: AN EXPERIMENTAL AND NUMERICAL INVESTIGATION"** submitted by **Mr. JITENDER KUMAR CHAURASIA (Register number: 177003ME004)** as the record of the research work carried out by him, is accepted as the Research Thesis submission in partial fulfilment of the requirements for the award of degree of **Doctor of Philosophy**.

Research Guide

Dr. Srikanth Bontha
Associate Professor,
Department of Mechanical Engineering
NITK, Surathkal

Chairman – DRPC
Date: 22.8.2023

ACKNOWLEDGMENTS

This thesis embodies the results of several studies carried out in the last couple of years which were not possible with the support of many people. Therefore, I would first like to take the opportunity to express my gratitude to all of them.

It has been a great honour for me to work under the supervision of **Dr. Srikanth Bontha**, Department of Mechanical Engineering, National Institute of Technology Karnataka (NITK). With a deep sense of gratitude, I express my sincere thanks to my supervisor for his valuable guidance throughout the course. His guidance and directions are invaluable and will be forever appreciated.

Next, I thank **Dr. C. P. Paul**, Raja Ramanna Centre for Advance Technology (RRCAT), Indore, for his immense guidance and for extending the infrastructure support available at RRCAT. Without the technical and experimental support provided by Dr. Paul and his team at RRCAT, the work presented here would not have been possible. I must say a special thanks to **Dr. A. N. Jinoop**, Post-Doctoral Fellow, Multi-Scale Additive Manufacturing Lab, University of Waterloo, Canada, for his encouragement and support during this work.

I would like to thank the members of the Research Progress Assessment Committee (RPAC), **Dr. N. Gnanasekaran**, Assistant Professor, Dept. of Mechanical Engineering, NITK and **Dr. Vadivuchezhian Kaliveeran**, Assistant Professor, Department of Water Resources & Ocean Engineering, NITK for enlightening me through the journey of doctoral work. I also wish to express my sincere thanks to **Prof. Ravikiran Kadoli**, Head, Department of Mechanical Engineering, and all former HOD's, faculty members, and technical and administrative staff of the Mechanical Engineering Department, NITK, for their kind help in providing the facilities as and when needed.

I sincerely thank the scholars from Additive Manufacturing Laboratory, NITK, Dr. Mallikarjuna B, Dr. Praveen Jeyachandran, Dr. Uzwalkiran Rokkala, Mr. Ravichandan, Mr. Amit Kumar Praharaj, Mr. Shambhu Kumar Manjhi and Mr. Raja TMS. I thank all

the master's students for being a part of my research and learning, Mr. Sai Krishna, Mr. Danish Asraf, Mr. Srinivaslu B., Mr. Mithun, Mr. Vishnu Swaroop and Mr. Shashank Anar, Mr. Malathesh and Mr. Saket Dixit.

I am thankful to the Director and administration of the NITK, for providing all the necessary infrastructure and funds to carry out the research activities. I also acknowledge the financial support from the Ministry of Education, the Government of India and NITK. I would also thank Central Research Facility at NITK for providing access to various characterization and testing facilities. Finally, I would like to thank my friends for their encouragement and support throughout my stay at NITK.

Above all, I am thankful to the almighty, my parents and family members for their blessings and support. At last, I thank my wife, **Mrs. Pooja Chaurasia** and my son **Advik Chaurasia** for supporting me in every possible way and being with me in the journey full of ups and downs.

(Jitender Kumar Chaurasia)

ABSTRACT

Engineering components after the prolonged hours of service in harsh environments often go through several defects such as wear, cracks and deformation. These defects alter the actual part geometry thereby affect its performance. In general, these parts are changed with new one during the overhauling process. However, replacing a part with new one is uneconomical specially if the part has high intrinsic value. For high value engineering parts, repairing the damages surfaces is more cost effective than replacing the entire part with new one. Welding has been the primary method for repair practices. However, this method has limitations, such as high heat affected zone and inability to repair complex shape cracks. With the advancement in metal Additive Manufacturing (AM), it is anticipated that this technology can be a game changer for repair industries.

To this end, the present thesis is focused to explore the repair capabilities of Laser Directed Energy Deposition (LDED) process which is a class of metal AM process where material is deposited by feeding the stock material (usually metal powder) through a nozzle into the melt pool formed on a substrate by a laser source. The work presented in this thesis starts with the fundamental understanding of LDED process to its applications in the sector of repair and feature addition for Inconel 625 (IN625). First, a laser surface melting study is presented where the focus is to understand how laser material interaction occurs. Effect of the process parameters, such as laser power and scan speed on the melt pool geometry and microstructure were studied. In addition, a Finite Volume Method based numerical model was established to understand the effect of considering fluid dynamics on the predicted melt pool geometry, cooling rates and thermal gradients. For the validation of numerical model, the results of cooling rates and thermal gradients were compared with the microstructure. Next, a single-track study was conducted to identify the process parameter window for sound deposition and to understand effect of process parameters on the deposited track height and width. A finite element based numerical model was established to predict the track height and width. Subsequentially, the optimized process parameters were chosen and a total of six thin walls were built to mimic feature addition applications on a IN625 substrate. Effect of process parameters on the thin wall build geometry, surface roughness, microstructure and mechanical properties were investigated. A FE based numerical model was established to understand the variation in melt pool geometry, cooling rates and thermal gradients with the change in process parameters and over the layers. Further, a study was carried out to understand the repair capabilities of LDED process, where the samples were extracted from a wrought plate of IN625 and were subjected to a fatigue load to mimic a component in service for repairing. Further, deposition was carried out on the surfaces (i.e., Top, Top & bottom, One side and Both sides) of these fatigued tensile sample. The samples were also solution-treated at 1200°C for 90 mins. Microstructure and mechanical properties were evaluated and then compared between the different deposition strategies and sample heat-treatment conditions. Tensile properties were compared for all the three sample conditions viz., wrought alloy, as repaired and solution treated. Results indicate sound deposition with minimal porosity in all the four deposition strategies using the LDED process. IN625 being a choice of material for high temperature applications, it is important to understand the thermal stability of the parts repaired using LDED process. To this end, the repaired samples were also tested for high temperature oxidation. Using the LDED process, an IN625 block was fabricated. The LDED IN625 samples were also subjected to solution treatment. In order to compare the performance of both LDED IN625 and solution treated LDED IN625, test coupons were also extracted from the wrought plate. Oxidation study was carried out for as-built, solution treated and wrought alloy at 800° and 1000°C for up to 100 hours in air.

In the conclusions of this thesis, LDED is found to be a promising technique to repair and add features on existing component with least porosity and high mechanical properties. However, the results of this study do indicate that the selection of an optimum process parameter can be useful to achieve consistent build quality during the thin wall deposition. Also, a suitable post-processing technique such as solution treatment is required for the achieving a homogenized microstructure, consistent mechanical properties and high thermal stability in the repair components.

TABLE OF CONTENTS

DECLARATION

CERTIFICATE

ACKNOWLEDGEMENTS

ABSTRACT .... **I**

TABLE OF CONTENTS .... **III**

LIST OF FIGURES .... **IX**

LIST OF TABLES .... **XIX**

ABBREVIATIONS .... **XXI**

NOMENCLATURE .... **XXIII**

CHAPTER 1 INTRODUCTION **1**

1.1 Background 1
1.2 Metal additive manufacturing 4
    1.2.1 Powder bed fusion processes 5
    1.2.2 Laser directed energy deposition process 7
1.3 LDED as repair technology 11
1.4 Computational modelling 12
    1.4.1 Steps involved in FEM 14
    1.4.2 Element birth and death technique 15
1.5 Nickel-based super alloys 17
    1.5.1 Inconel 625 alloy 18
1.6 Layout of thesis 20

CHAPTER 2 LITERATURE REVIEW **23**

2.1 Repair using conventional techniques 23
2.2 LDED process as a repair technology 25
2.3 Thin wall deposition using LDED 27
2.4 Deposition of IN625 using LDED 29
2.5 Oxidation behaviour of IN625 30

2.6 Conclusions from literature survey 31
2.7 Objectives 32
CHAPTER 3 EXPERIMENTAL METHODS 33
3.1 Experimental setups 33
    3.1.1 LDED setup 33
3.2 Furnace 34
3.3 Sample preparation 35
    3.3.1 Sectioning and mounting 35
    3.3.2 Grinding and polishing 36
    3.3.3 Etching 36
3.4 Characterization 37
    3.4.1 Optical microscopy 37
    3.4.2 Scanning electron microscopy and energy dispersive spectroscopy 37
    3.4.3 X-ray diffraction 38
    3.4.4 Tensile testing 39
    3.4.5 Microhardness 40
    3.4.6 3D scanning 41
CHAPTER 4 EFFECT OF FLUID FLOW ON MELT POOL GEOMETRY DURING LASER SURFACE MELTING OF IN625 43
4.1 Materials and methods 43
    4.1.1 Materials 43
    4.1.2 Experimental setup 44
4.2 Numerical modelling 46
    4.2.1 Assumptions 48
    4.2.2 Governing equations 49
    4.2.3 HCS model 49
    4.2.4 HCS-FD model 49
4.3 Boundary conditions 51
    4.3.1 Heat source model 51
4.4 Material properties 52
4.5 Results and discussion 53

4.5.1 Comparison of melt pool dimensions at different laser powers and scan speeds......54
4.5.2 Peak temperatures and velocity fields......59
4.5.3 Solidification characteristics......60
4.6 Conclusions......65
CHAPTER 5 SINGLE-TRACK DEPOSITION USING LDED PROCESS......67
5.1 Materials and methodology......67
5.1.1 Materials......67
5.1.2 Experimental setup......67
5.2 Numerical modelling description and approach......69
5.2.1 Assumptions......69
5.2.2 Governing equation......69
5.2.3 Boundary conditions......70
5.2.4 Material properties......72
5.2.5 Enthalpy approach......72
5.3 Results and discussion......76
5.3.1 Track Geometry: Experimental observations......76
5.3.2 Prediction of track geometry using enthalpy approach......79
5.4 Conclusions......82
CHAPTER 6 THIN WALL DEPOSITION OF IN625: EXPERIMENTAL AND NUMERICAL INVESTIGATION......83
6.1 Materials and methods......83
6.1.1 Material......83
6.1.2 Deposition of thin walls......84
6.1.3 Testing and characterization......86
6.2 Results and discussion......87
6.2.1 Geometrical analysis of thin walls......87
6.2.2 Density measurement......91
6.2.3 Surface quality analysis......93
6.2.4 Microstructural analysis......94
6.2.5 Tensile properties & fractography......96

6.2.6 Microhardness....100
6.3 Numerical modeling thin walls....101
6.3.1 Description of the numerical model....102
6.3.2 Results & discussion....104
6.4 Conclusions....112
CHAPTER 7 LASER DIRECTED ENERGY DEPOSITION AS A REPAIR TECHNOLOGY FOR SERVICED INCONEL 625 PARTS....115
7.1 Materials and methods....115
7.1.1 Materials....115
7.1.2 Experimental setup....116
7.1.3 Material characterization....119
7.2 Results and discussion....120
7.2.1 Macroscopic observations: Pre and post-deposition....120
7.2.2 Microstructural analysis....123
7.2.3 Mechanical properties....127
7.3 Conclusions....134
CHAPTER 8 HIGH TEMPERATURE OXIDATION BEHAVIOUR OF LDED IN625....137
8.1 Experimental procedure....137
8.1.1 Materials & preparations....137
8.1.2 Oxidation experiment....139
8.1.3 Characterization of the oxidized samples....140
8.2 Results and discussion....140
8.2.1 Mass gain evaluations....140
8.3 Post oxidation characterization....144
8.3.1 Oxidation at exposure temperature of 800°C....144
8.3.2 Oxidation at exposure temperature of 1000°C....148
8.4 Mechanism of oxidation in IN625....153
8.5 Conclusions....155
CHAPTER 9 SUMMARY & FUTURE WORK....157
9.1 Summary of the thesis....157

9.2 Future work..159

REFERENCES...161

LIST OF PUBLICATIONS BASED ON PHD RESEARCH WORK 175

BIO-DATA...177

LIST OF FIGURES

Figure 1.1 Life cycle of a product through the process of part manufacturing, repair, reconditioning and remanufacturing (Partly reproduced from King et al. 2006)........2

Figure 1.2 Steps involved in the additive manufacturing process (Partly reproduced from Gibson et al., 2013) 4

Figure 1.3 Classification of additive manufaturing processes (ASTM 52900: 2021). 5

Figure 1.4. Additive manufacturing market share of different processes as of the year 2020 (Vafadar et al., 2021)........5

Figure 1.5 Schematic of Laser Powder Bed Fusion process (Partly reproduced from Gibson et al., 2013) 6

Figure 1.6 Schematic of Laser Directed Energy Deposition process (Partly reproduced from Gibson et al., 2013) 7

Figure 1.7 Deposition hierarchy in the Laser Directed Energy Deposition process (Gibson et al., 2013)........8

Figure 1.8 Process parameter involved in LDED process (Ahn, 2021) 10

Figure 1.9 Schematic illustrating deposition of two tracks with overlap (Sun et al., 2020b)........11

Figure 1.10 Schematic showing descritization of geometry (ANSYS Inc., 2022)..14

Figure 1.11 Schematic of element birth and death technique used to simulate material addition during LDED process (ANSYS Inc., 2022)........16

Figure 2.1 A thin wall fabricated (a), (b) without using closed loop and (c), (d) with a closed loop control system (Hu and Kovacevic, 2003)........28

Figure 3.1 Schematic of LDED setup used at RRCAT, Indore 34

Figure 3.2 Schematic of a typical nozzle used in LDED process 34

Figure 3.3 Furnace used to carry out high temperature oxidation experiments 35

Figure 3.4 Schematic of setup used for electrolytic etching of samples 37

Figure 3.5 Scanning electron microscopy facility at Central Researsh Facility, NITK Surathkal 38

Figure 3.6 Facility used for XRD analysis 38

Figure 3.7 Universal testing machine used for tensile testing 39

Figure 3.8 Dimensions of the sub-size and micro tensile specimen used in study 39

Figure 3.9 (a) Schematic of Vickers hardness test and (b) measurement of indent diagonals formed on the samlpe after hardness test 40

Figure 3.10 3D scanner facility used for scanning thin walls 41

Figure 4.1 Machine setup at LAML, RRCAT, Indore 45

Figure 4.2 (a) Schematic of experimental setup (b) Graphical representation of the melt pool width and depth obtained from the section z’-z’ 46

Figure 4.3 Peak temperature of all the investigated meshes in grid independency study 47

Figure 4.4 Numerical domain used in the study, related coordinate system and boundary conditions. 48

Figure 4.5. Magnitude and distribution of heat flux for laser powers 300, 400 and 500 W 52

Figure 4.6 Cross-section of the single laser tracks at different laser powers and scan speeds 55

Figure 4.7. Comparison of experimentally measured melt pool width with predictions from HCS and HCS-FD models 56

Figure 4.8. Comparison of experimentally measured melt pool depth with predictions from HCS and HCS-FD models 56

Figure 4.9. Melt pool shape predicted by the HCS-FD numerical model at a) negative value and b) positive value of temperature coefficient of surface tension 57

Figure 4.10. Side by side comparison of the cross section of the melt pool obtained from optical microscope images with a) HCS-FD model and b) HCS model at 500 W laser power and 100 mm/s scan speed 58

Figure 4.11. Comparison of peak temperatures obtained from HCS and HCS-FD models at different laser powers and scan speeds 60

Figure 4.12. Calculated velocity fields from the HCS-FD model at a laser power of 500 W and scan speed of 100 mm/s 60

Figure 4.13. Predicted cooling rate at different scan speeds and at constant laser power of 500 W 61

Figure 4.14. SEM Micrographs obtained at laser power of 500 W and scan speeds of (a) 100 mm/s, (b) 200 mm/s and (c) 300 mm/s 62

Figure 4.15. Effect of temperature gradient (G) and solidification velocity (R) on the grain size and morphology (Partly reproduced from, Kumara et al., 2019) 63

Figure 4.16. Numerically predicted cooling rate (G×R) and G/R from HCS-FD model at the traverse section 64

Figure 4.17. Experimentally obtained transverse section of (a) scanned track and microstructure at locations (b) 1 and (c) 2 65

Figure 5.1 Schematic of the LDED setup used at RRCAT, Indore for experimentation. 68

Figure 5.2. Schematic of laser directed energy deposition process and related terms. 70

Figure 5.3 Laser beam distribution used in present study. 71

Figure 5.4 Thermo-physical properties of IN625 used in present study 72

Figure 5.5 Schematic of the model used for numerical modelling........ 73

Figure 5.6 Meshed model used in present study........ 74

Figure 5.7 Process of element death and birth to obtain the bead shape 75

Figure 5.8 Flowchart of the process of element activation to predict the deposited track dimensions........ 76

Figure 5.9. Single track of Inconel 625 deposited at different process parameters using LDED process........ 77

Figure 5.10 Outline of the single tracks deposited at different laser powers and scan speeds 77

Figure 5.11 SEM images showing cross-section of the single tracks deposition at different laser powers and scan speeds 78

Figure 5.12 Topography of the single track deposited on IN625 substrate at different processing conditions 78

Figure 5.13 Single track dimensions predicted using enthalpy approach at different laser powers and scan speeds 80

Figure 5.14 Trend of the deposited track height and width from both experimental and predicted values at different laser powers and scan speeds........ 81

Figure 5.15. Comparison of the predicted track dimensions with the experimental observations 81

Figure 6.1 (a) SEM image of IN625 powder particles, (b) distribution of powder particles size and (c) cumulative percentage plot showing D_{10}, D_{50} and D_{90} particle size distribution 84

Figure 6.2 (a) Schematic of the LDED system used for deposition of thin walls, (b) deposition strategy used and (c) thin walls built at different process parameters 85

Figure 6.3. (a) 3D scanned model of thin wall, (b) section plane considered for measurements along the cross-section and (c) section plane considered for measurement along the laser travel direction 86

Figure 6.4. Schematic of tensile test coupon extraction and the dimensions of the tensile coupon 87

Figure 6.5. Macroscopic images showing cross-section of thin walls deposited at different laser powers and scan speeds 88

Figure 6.6. Thin wall height measured along its length and (b) range of variation in wall height and related normal distribution.. 89

Figure 6.7. (a) Macroscopic view of deposited thin wall (b), (c) evolution of dimensional instability along the length, (b1) and (c1) schemtic showing evolutionof diensionalm inconsistency 90

Figure 6.8: Thin wall thickness measured along the build height and (b) range of variation in wall thcinkess and related normal distribution 91

Figure 6.9. Relative density observed in thin walls fabricated at different process parameters 92

Figure 6.10. Effect of scan speed on surface roughness at different laser powers ... 93

Figure 6.11 (a) Change in surface quality along build direction and (b) graphical illustration showing the process of increase in surface roughness along the build height 94

Figure 6.12. Microstructure observed in thin walls at laser power of 1200W and scan speeds of (a) 0.4 m/min, (b) 0.6 m/min and (c) 0.8 m/min 95

Figure 6.13. Microstructure observed at different locations of fabricated thin wall 96

Figure 6.14. (a) (b) Yield strength, (c) (d)ultimate tensile strength and (e) (f) percentage elongation of samples extracted from thin walls 98

Figure 6.15. SEM images of the fractured surface of all the thin wall (vertical) 99

Figure 6.16 SEM images of the fractured surface of all the thin wall (horizontal) . 99

Figure 6.17. Elemental composition from EDS analysis observed on the fractured surface of the tensile coupon (W5-vertical samples) 100

Figure 6.18. Microhardness values observed along the build direction in different thin walls 101

Figure 6.19 Dimensions of the 3D model used in present study (all dimension in mm) 102

Figure 6.20 Results from mesh independent test carried at different mesh sizes .. 103

Figure 6.21 The finite element mesh used in present study 103

Figure 6.22. Various boundary conditions used in the numerical model 104

Figure 6.23 Temperature contours observed in thin wall at different layers 105

Figure 6.24 Peak temperatrure observed in different layers 106

Figure 6.25. Schematic showing difference of (a) heat transfer at layer – 1 and (b) higher layer numbers 106

Figure 6.26 Melt pool length and depth predictions at different layers................107

Figure 6.27 Predicted thermal history of five layer thin wall deposition.............108

Figure 6.28. Predicted (a) cooling rates and (b) thermal gradeints during the five layer thin wall deposition..109

Figure 6.29 Peak temperatures predicted at (a) 900 W and (b) 1200 W laser powers and different scan speeds..110

Figure 6.30 Melt pool depth predicted at (a) 900 W and (b) 1200 W laser powers and different scan speeds 110

Figure 6.31 Effect of process parameters on (a) cooling rates and (b) thermal gradients 112

Figure 7.1 (a) SEM image of the powder particles and (b) particle size distribution of IN625 powder used for deposition..115

Figure 7.2. Schematic representation of the methodology used in the present study. 117

Figure 7.3. Schematic representation of the four deposition strategies (a) deposition on top face, (b) deposition on both top and bottom faces, (c) deposition on one side and (d) deposition on both sides. 118

Figure 7.4. Tensile specimen after (a) fatigue, (b) deposition on top surface, (c) deposition on top and bottom surfaces, (d) deposition on one side surface and (e) deposition on both side surfaces. 121

Figure 7.5. Cross-sectional macroscopic view of the four deposition strategies (a) deposition on top surface, (b) deposition on both top and bottom surfaces, (c) deposition on one side surface and (d) deposition on both sides surfaces...122

Figure 7.6. Deposition of material at the edge of substrate (a) schematic layout and (b) macroscopic image. 122

Figure 7.7. Microstructure of the as-deposited samples (deposition on the top surface) at different locations in the deposited material. 123

Figure 7.8. Microstructural observations of the deposited material after solution treatment...124

Figure 7.9. EDS analysis of the as-deposited sample (deposition on top surface) at different locations..125

Figure 7.10. EDS analysis of solution treated sample (deposition on top surface) at different locations..125

Figure 7.11. (a) XRD peaks observed for wrought, as-deposited and heat-treated samples and (b) peak shift observed in heat treated sample. 127

Figure 7.12. Photographs of samples with different deposition strategies before and after tensile testing. 128

Figure 7.13. Stress-strain curves of (a) as-deposited and (b) solution treated samples at different deposition strategies considered in the study. 129

Figure 7.14. (a) Ultimate tensile strength, (b) yield strength and (c) elongation in of wrought, as-deposited and solution treated samples. 130

Figure 7.15. Fractographs of (a) as-deposited, (b) solution treated and (c) wrought alloy fractured samples..131

Figure 7.16. Elemental mapping of the fractured surface in case of (a) as deposited sample and (b) heat treated sample. 132

Figure 7.17. Vickers's microhardness measured from top of deposition toward substrate for different sample conditions. 134

Figure 8.1. Inconel 625 particles morphology and size distribution used for the deposition 138

Figure 8.2. IN625 thick block deposited on SS304 substrate using LDED process 139

Figure 8.3. (a, b, c, d) Procedure followed for oxidation study and (c1) actual samples placed on the refractory brick before oxidation study 140

Figure 8.4. Mass gain observed in the different sample conditions and time during isothermal oxidation at (a) 800 and (b) 1000 °C 141

Figure 8.5. Mass gain square observed in the different sample conditions and time at (a) 800 and (b) 1000 °C 143

Figure 8.6. Plot of ln k_p versus inverse of temperature used for calculation of the activation energy of oxidation at different sample conditions 143

Figure 8.7. Cross-setion images of the sample showing the oxide layer thickness in different sample conditions and exposure time at 800°C 145

Figure 8.8. Oxidation layer thickness measured for the samples at furnace explosure temperature 800 °C 146

Figure 8.9. Elemental maps of AD sample exposed for 100 hours at 800 °C 147

Figure 8.10. X-ray diffraction patterns collected at 800 °C for different samples 148

Figure 8.11. Cross-section images of the sample showing the oxide layer thickness in different sample conditions and exposure time at 1000 °C 149

Figure 8.12. Oxidation layer thickness measured for the samples at furnace exposure temperature 1000 °C 150

Figure 8.13. Chemical composition of the oxide layer observed in heat treated sample at 50 hours and 1000 °C 151

Figure 8.14. Chemical composition of the oxide layer observed in heat treated sample at 100 hours and 1000 °C 152

Figure 8.15. X-ray diffraction patterns collected at 1000°C for different samples 153

Figure 8.16 Mechanism of oxidation formation in IN625........ 155

LIST OF TABLES

Table 1.1 Steps involved in finite element modelling 15

Table 1.2. Typical composition of IN625 alloy (Special Metals Corp., 2013). 19

Table 4.1 Chemical composition of the IN625 alloy substrate. 44

Table 4.2 Combination of laser power, scan speed and related energy density used for single laser scan experiments. 45

Table 4.3. Reported Absorptivity coefficients (α) in literature for IN625. 52

Table 4.4 Material properties of IN625 used in numerical modelling 53

Table 4.5. Comparison of the experimentally measured dendrite size with the predictions from HCS-FD and HCS models at different scan speeds.. 63

Table 5.1 Combination of the laser power and scan speeds used for the experimentation. 68

Table 5.2 Experimental observation of the deposited tracks at different laser powers and scan speeds 79

Table 6.1 Chemical composition of IN625 powder obtained from EDS analysis 84

Table 6.2. Sample notation and process parameters used for deposition 85

Table 7.1 Chemical composition of Inconel 625 plate and powder used in the study. 116

Table 7.2. Process parameters used for the deposition....................................... 118

Table 8.1. Activation energy calculated of Inconel 625 at different sample conditions 144

ABBREVIATIONS

AM	Additive Manufacturing
RP	Rapid Prototyping
LAM	Laser Additive Manufacturing
SLS	Selective Laser Melting
SLM	Selective Laser Melting
PBF	Power Bed Fusion
DMLS	Direct Metal Laser Sintering
DED	Direct Energy Deposition
DMD	Direct Metal Deposition
LENS™	Laser Engineered Net Shaping
HAZ	Heat Affected Zone
PDD	Powder Deposition Density
ASTM	American Society for Testing and Materials
SEM	Scanning Electron Microscopy
WEDM	Wire-Electrical Discharge Machining
XRD	X-ray Diffraction

NOMENCLATURE

™	Trademark
R	Solidification rate (mm/sec)
G	Thermal gradient (K/sec)
P	Laser power (W)
v	Laser scanning velocity (mm/sec)
d	Laser beam diameter (mm)
R	Power feed rate (gm/s)
E	Energy density (J/mm^3)
t	Time (s)
T	Temperature (K)
α	Thermal diffusivity (m^2/s)
ρ	Density (kg/m^3)
k	Thermal conductivity (W/m-K)
C_p	Specific heat (J/kg-K)

CHAPTER 1
INTRODUCTION

1.1 Background

Nickel-based superalloy components are typically used in harsh environments in aerospace, marine, power and petrochemical industries. In these applications they are subjected to high temperature to highly corrosive environments (Donachie and Donachie, 2002; Shoemaker, 2012). During their long service, these components are subjected to non-uniform thermal cycling and complex state of repetitive stresses which cause thermo-mechanical fatigue cracking and other surface defects before their intended life (Xia et al., 2015). Components made out of Ni-based superalloys because of their application in critical areas, these components are usually scrapped and replaced with a new ones during the over-hauling process. However, nickel-based superalloys components have high intrinsic value due to the high cost of raw material and the number of manufacturing processes required to fabricate the components (Underhill, 2012). Also, the one-way use of material i.e., *"Take-Make-Use-Dispose"* is one of the major challenges moving forward with sustainable development (Colorado et al., 2020). Therefore, finding suitable techniques to repair and recycle these components without losing the actual characteristics is of great importance.

As defined by Steinhipler et al. (1998), remanufacturing is an industrial process where the degraded/worn-out components are restored to "*as good as new condition*". Remanufacturing also helps in eliminating a significant portion of the life cycle processes of a component which includes the acquisition of the raw material, casting, machining and huge involvement of human resources required to fabricate the part from scratch (Liu et al., 2016) (Figure 1.1). On the other hand, repairing is defined as a procedure where specific defects are corrected in a product. In general, the repaired part is inferior when compared to a remanufactured part (King et al., 2006). Essentially, a part usually goes out of its application due to two main reasons (*i*) Functional obsolescence, where a part fails to perform the desired function and needs repair or (*ii*) fashion obsolescence, where a part loses its value due to the new products/techniques appearing and need feature upgradations.

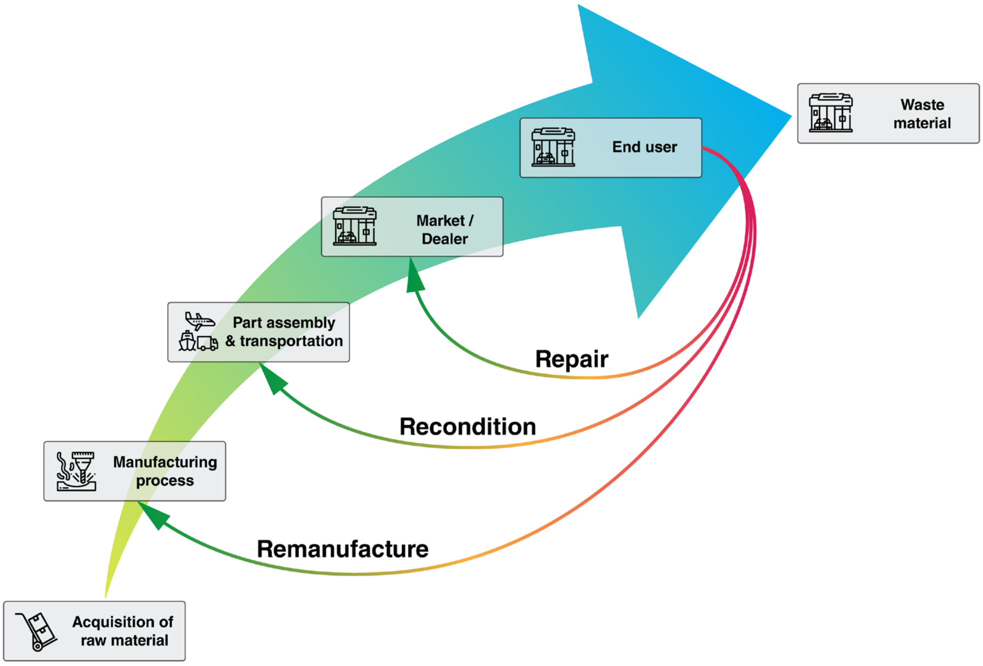
Waste material
End user
Market / Dealer
Part assembly & transportation
Manufacturing process
Acquisition of raw material
Repair
Recondition
Remanufacture

Figure 1.1 Life cycle of a product through the process of part manufacturing, repair, reconditioning and remanufacturing (Partly reproduced from King et al. 2006)

Feature addition is a process where either a new functionality is added or an existing functionality is improved for the part. Addition of the ribs on a part to improve its structural stiffness or addition of material on a part to improve its heat transfer capability are some of the examples of feature addition. Feature addition can either be done on the entire part or on a section of the part where a specific feature is required (www.beam-machines.com). The addition of a feature on a given part can be of similar, dissimilar, or functionally graded material, depending on the requirement of functionality.

Repair technologies being used currently include thermal spraying, cladding and welding. These repair technologies are ad hoc and do not provide tight control on the depth of penetration and the spread of the material deposited to repair the cracks (Meng et al., 2019; Tan et al., 1999; Tong et al., 2020). For over 60 years, Tungsten Inert Gas (TIG) welding is the industry go-to process for the repair of damage components (Chen et al., 2021). Despite its easy availability, lower cost and process simplicity, TIG welding results in a huge amount of heat signature, which alters the actual characteristics of the component to be repaired. The other downside of this process is its inability to repair complex shapes and corner sites (Piscopo and Iuliano, 2022). Alternatively, Plasma Transferred Arc Welding (PTAW) and Electron Beam welding (EBW) are processes which offer lower heat signature and thereby less distortion. However, the equipment for these processes is comparatively complex and expensive (Su et al., 1997). Therefore, there is a need for a technology/process which can perform repair for intricate shapes with ease.

Additive manufacturing (AM), as defined by the "*International Standards Organization/American Society for Testing and Materials (ISO/ASTM 52900:2021)*", *is a process of material joining to make parts from 3D model data, typically in layer upon layer as opposed to the formative and subtractive manufacturing processes* (ASTM 52900: 2021). The fabrication of a part using any additive manufacturing process involves several steps. Figure 1.2 show the various steps involved in an additive manufacturing process. The first step involves 3D CAD modelling of the part to be manufactured. For repair-related applications, the failed part is first 3D scanned and then a 3D model of the repair geometry is modelled. Next, using a slicing software, the 3D model is divided into several cross sections known as slices. The slicing data includes information on the cross-sections of each layer. This data is then forwarded to a CNC system (usually attached to a 3D printer) where it interprets the motion of the deposition head or the bed. After this, the part is built in a layer-by-layer fashion, which on completion, is removed from the base plate. In the last step, the build part goes through post-processing, where several operations, such as machining and surface finishing etc. are carried out to bring the part to the required shape and tolerances.

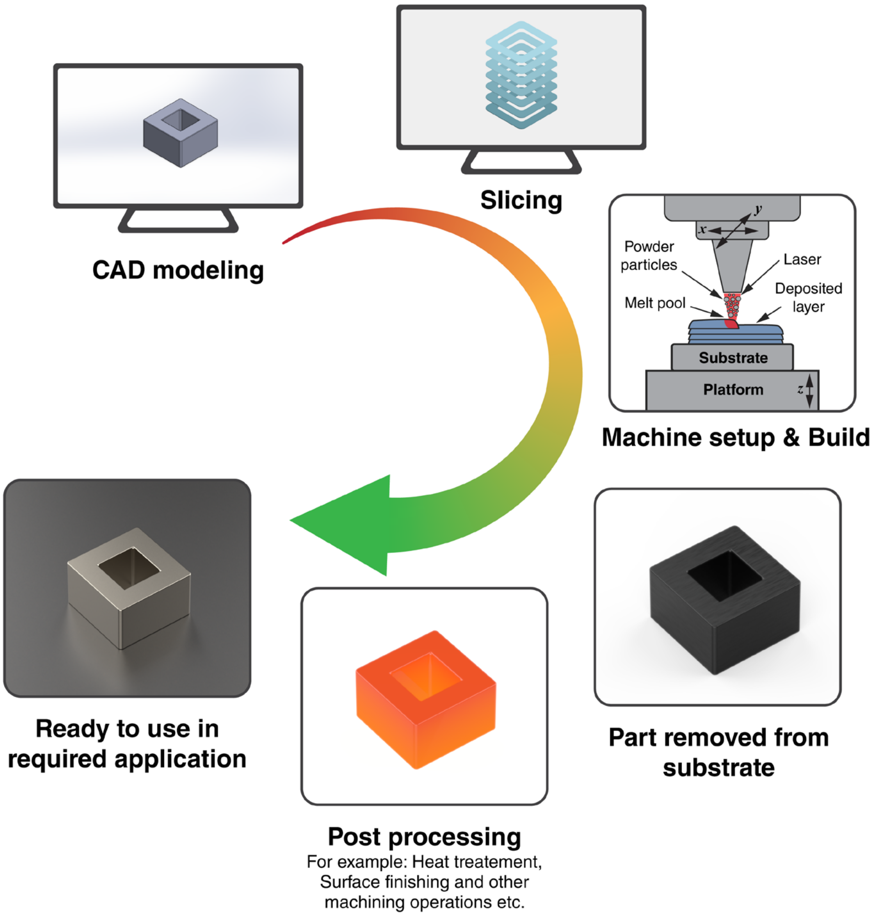
CAD modeling
Slicing
Powder particles
Laser
Deposited layer
Melt pool
Substrate
Platform
x
y
z
Machine setup & Build
Part removed from substrate
Post processing
For example: Heat treatement, Surface finishing and other machining operations etc.
Ready to use in required application

Figure 1.2 Steps involved in the additive manufacturing process (Partly reproduced from Gibson et al., 2013)

1.2 Metal additive manufacturing

At present, AM is classified into seven different categories as defined by the American Society for Testing and Materials (ASTM). These are Binder Jetting, Powder Bed Fusion, Directed Energy Deposition, Sheet Lamination, Material Extrusion, Vat Polymerization and Material Jetting (Figure 1.3). It should be noted that all the mentioned processes are being used for fabrication of metallic components (except Vat Polymerization) and their share in the AM market is shown in Figure 1.4 (Vafadar et al., 2021). According to figure 1.4, the dominant processes in metal AM industry are Powder Bed Fusion Process (PBF) and Directed Energy Deposition (DED) process. These two processes depending upon the kind of feedstock material (powder or wire) and heat source (laser, arc or electron beam) used can be further divided into different processes, as described in the subsequent section.

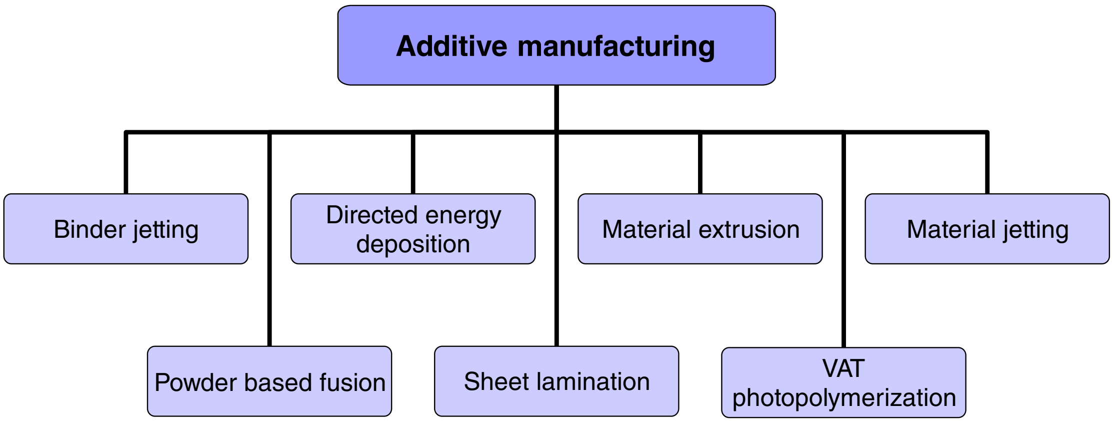
Additive manufacturing
Binder jetting
Directed energy deposition
Material extrusion
Material jetting
Powder based fusion
Sheet lamination
VAT photopolymerization

Figure 1.3 Classification of additive manufaturing processes (ASTM 52900: 2021).

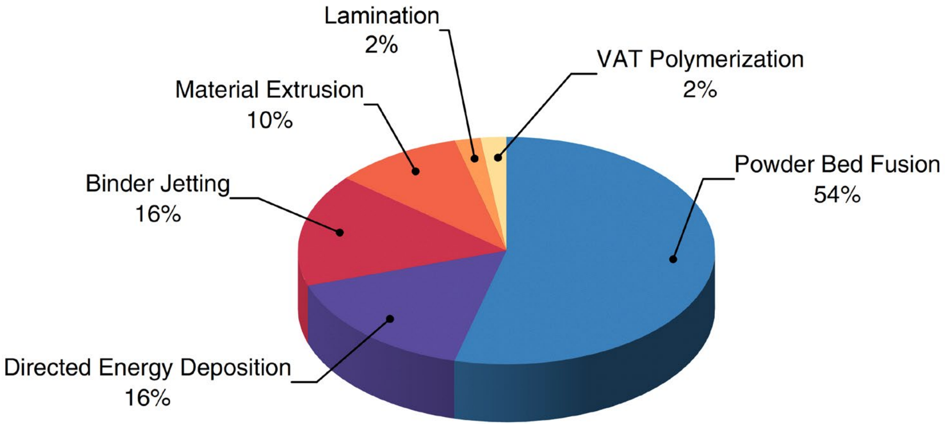

Figure 1.4 Additive manufacturing market share of different processes as of the year 2020 (Vafadar et al., 2021)

1.2.1 Powder bed fusion processes

Majority of PBF system uses metal powder as feed stock material. However, depending upon the kind of heat source used during fabrication, PBF process is further subdivided into two categories; (i) Laser Powder Bed Fusion (LPBF) process, where a laser is used for layer-by-layer scanning. This process is also known as Selective Laser Melting (SLM) and (ii) Electron Beam Melting (EBM), where an electron beam is used as a heat source. Between these two, LPBF is the more mature and widely used process. LPBF is now being used in the fabrication of commercial products, primarily in bio-medical and aerospace sectors (Yadroitsev et al., 2021). LPBF process holds a 54% market share in the metal AM industry. In this process, as shown in Figure 1.5, first, a micron level particle size powder is spread on a bed using a re-coater. Further, depending on the slicing data, a high-energy laser source selectively melts the powder. Next, the bed is lowered by the required layer thickness and again the powder is spread on the bed by the re-coater followed by laser scanning. This process continues until the required number of layers are built. By using LPBF process, one can easily fabricate parts with complete design freedom and fine details. Despite these advantages, the one aera where LPBF process really lags behind is the ability to repair components. LPBF process needs a flatbed to build parts. However, in majority of the cases the fractured/worn-out surfaces are complex and not flat.

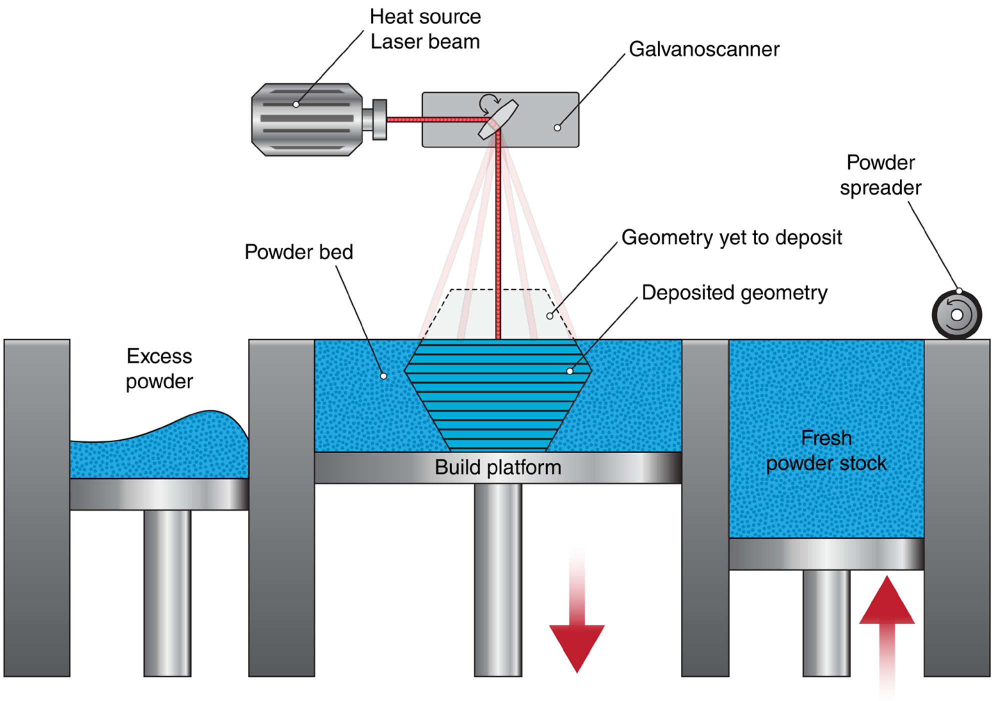
Heat source
Laser beam
Galvanoscanner
Powder spreader
Geometry yet to deposit
Deposited geometry
Powder bed
Excess powder
Build platform
Fresh powder stock

Figure 1.5 Schematic of Laser Powder Bed Fusion process (Partly reproduced from Gibson et al., 2013)

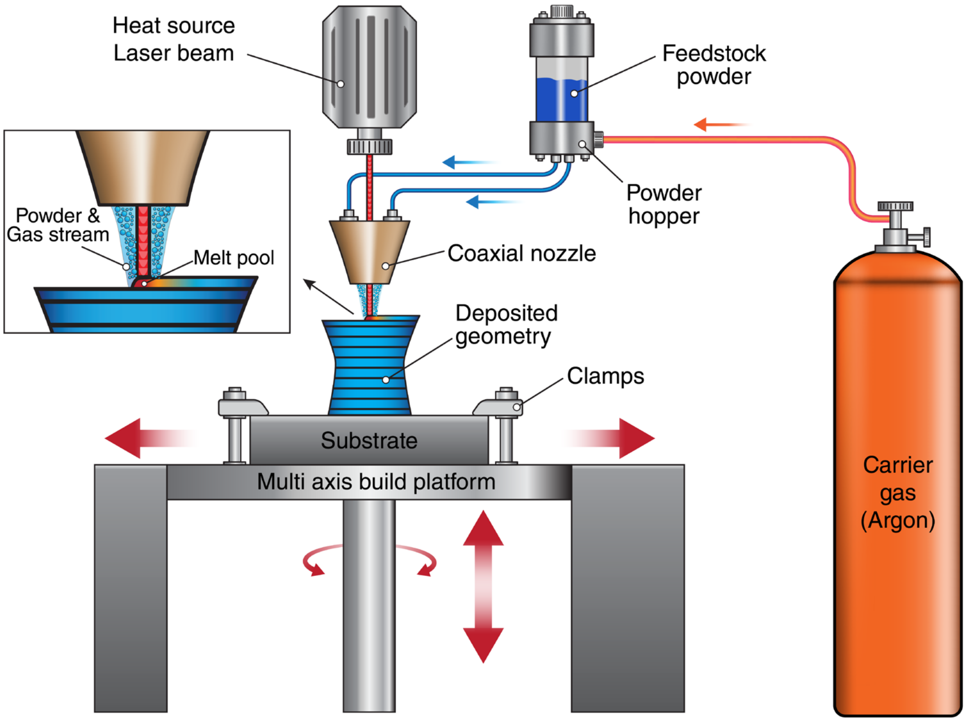
Heat source
Laser beam
Feedstock
powder
Powder &
Gas stream
Melt pool
Powder
hopper
Coaxial nozzle
Deposited
geometry
Clamps
Substrate
Multi axis build platform
Carrier
gas
(Argon)

Figure 1.6 Schematic of Laser Directed Energy Deposition process (Partly reproduced from Gibson et al., 2013)

1.2.2 Laser directed energy deposition process

Laser Directed Energy Deposition (LDED) is a metal additive manufacturing process. Like LPBF process, LDED process also uses a high intensity laser beam. However, unlike LPBF, where the powder bed is selectively melted, in the LDED process the powder is fed into the melt pool through a co-axial nozzle. Further, unlike LPBF process, where the feedstock material is limited to metallic powder, LDED process can use both metallic powders and wire as feedstock material. Figure 1.6 shows a schematic of the LDED process. The main components of a LDED system include a deposition head, 5 axes CNC controlled working table, nozzle, laser system, powder feeder and a computer system to control the motion of bed and other components.

In the LDED process as shown in fig 1.7, first a high intensity laser beam is focused on a substrate, forming a melt pool. Simultaneously, feedstock powder is fed into the melt pool through a co-axial nozzle creating a bead of the material. As the working table moves on the planned path, the feed stock material continues to deposit and solidify on the substrate forming a track. Further, several tracks are deposited with a pre-defined overlap to form a layer. Once a layer is deposited, either the bed is lowered or the deposition head is raised by an amount equal to the thickness defined during the slicing. In this way, multiple layers are deposited to obtain final shape of the part.

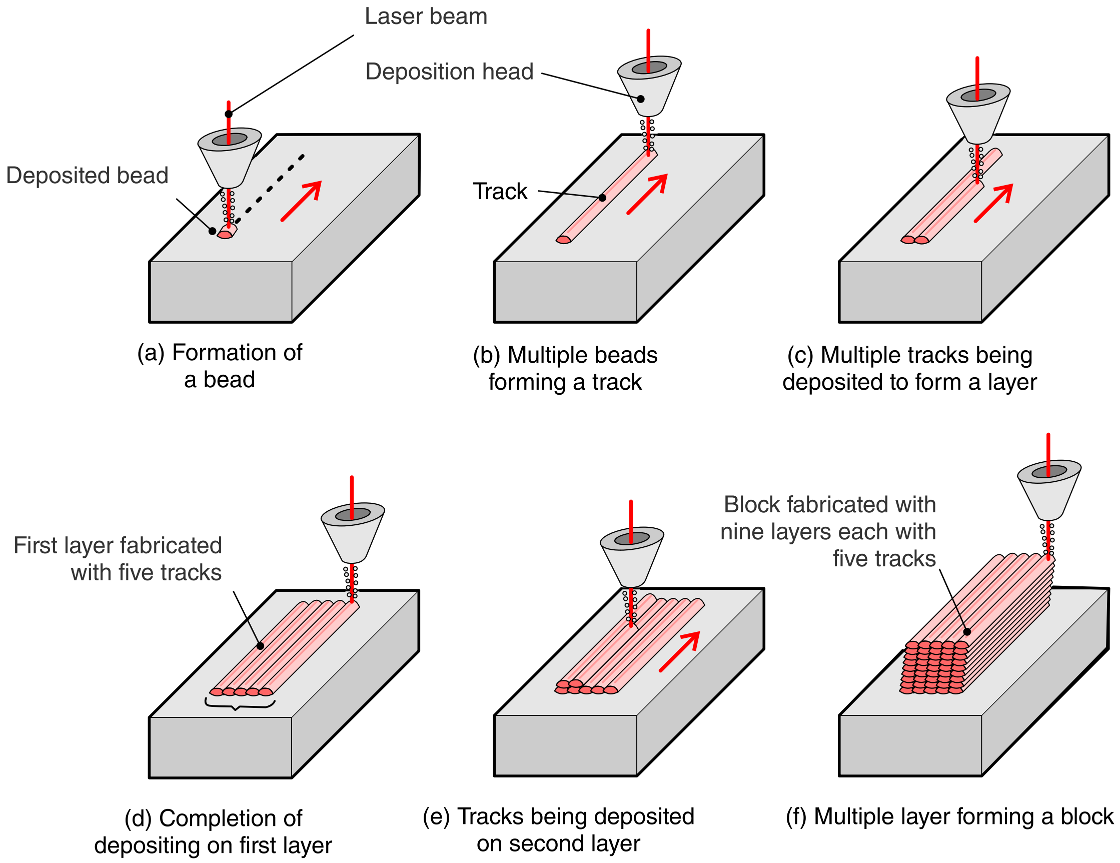
Laser beam
Deposition head
Deposited bead
Track
(a) Formation of a bead
(b) Multiple beads forming a track
(c) Multiple tracks being deposited to form a layer
First layer fabricated with five tracks
Block fabricated with nine layers each with five tracks
(d) Completion of depositing on first layer
(e) Tracks being deposited on second layer
(f) Multiple layer forming a block

Figure 1.7 Deposition hierarchy in the Laser Directed Energy Deposition process (Gibson et al., 2013)

1.2.2.1 Advantages of LDED process

LDED process offers several advantages as defined by ASTM 3413 standards (ASTM International, 2016), these include:

(a) High design freedom compared to conventional manufacturing techniques

(b) High deposition rates compared to LPBF process

(c) Large particle size compared to LPBF process (cost advantageous)
(d) Large build volume, especially in comparison with LPBF process
(e) Multi-material deposition capabilities (Functional Graded Materials (FGM's))
(f) High Technology Readiness Level (TRL) and Manufacturing Readiness Level MRL compared to other AM processes
(g) Broad range of feedstock materials
(h) Printing of either a complete part from scratch or addition of local features, cladding and repair capabilities in a single machine.
(i) Hybrid compatibility (Additive-subtractive manufacturing)

1.2.2.2 Limitations of LDED process

The following are the limitations of the LDED process:

(a) Low dimensional resolution compared to LPBF process.
(b) Large surface waviness and surface roughness due to high deposition rates.
(c) Due to large heat input, residual stress and distortion can occur.
(d) Limited complexity of the parts when compared to LPBF process.
(e) Post-processing, such as machining and surface finishing operations, are required.

The following subsections provide a detailed description of machine components, process parameters, mechanism of melting and solidification and common defects related to LDED process.

1.2.2.3 LDED process parameters

LDED is a complex process that involves different phenomena at different length scales. Therefore to achieve sound and defect-free deposits, it is very important to understand the effect of process parameters on the process outcomes (Ahn, 2021). Figure 1.8 show the various process parameters involved in the LDED process. It is important to note that all the process parameters shown in Fig 1.13 do not have the same influence on the quality of the deposit. Some of the most important process parameters are (ASM International, 2020):

- Laser power
- Scan speed
- Beam diameter
- Mass flow rate
- Carrier gas flow rate
- Interlayer delay
- Layer thickness
- Hatch spacing or overlap
- Stand-off distance
- Particle size distribution

- Laser power is the amount of energy provided by a given laser beam in watts. Insufficient laser power can lead to lack of fusion and less dilution. In contrast, high laser power can lead to issues such as high-temperature gradients, high residual stresses and loss of alloying elements due to vaporization at high temperatures.

- Scan speed defines the velocity of the laser head relative to the base plate. Scan speed is a very important process parameter and it is strongly interconnected with laser power and mass flow rate. For example, a low scan speed with high feed rate and high laser power will result in oversized beads and dimensional inaccuracy. Likewise, high scan speed and high feed rate should be compensated by increasing the laser power to obtain a quality deposit.

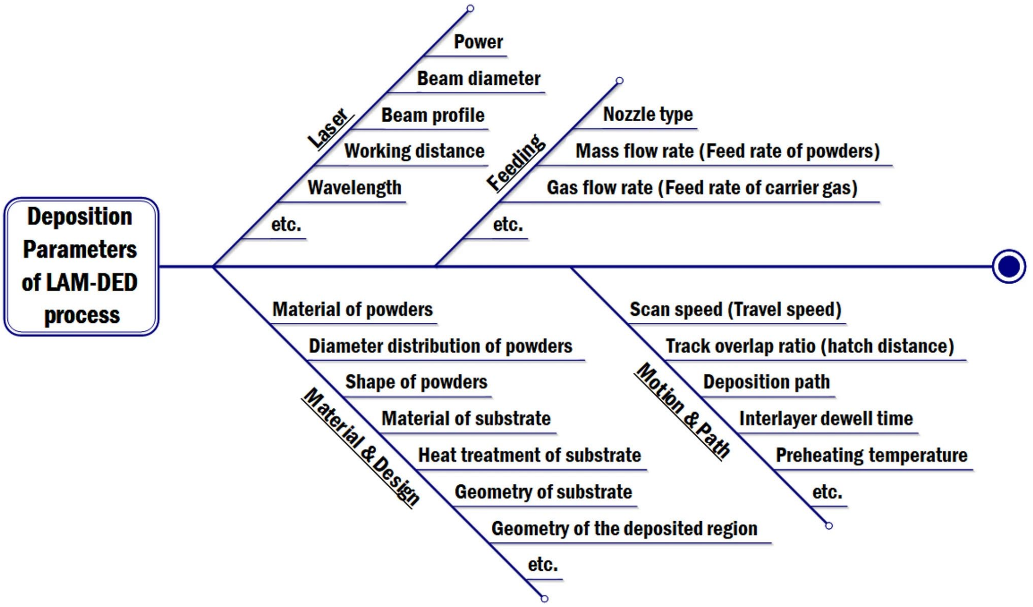
Deposition Parameters of LAM-DED process
Laser
Power
Beam diameter
Beam profile
Working distance
Wavelength
etc.
Feeding
Nozzle type
Mass flow rate (Feed rate of powders)
Gas flow rate (Feed rate of carrier gas)
etc.
Material & Design
Material of powders
Diameter distribution of powders
Shape of powders
Material of substrate
Heat treatment of substrate
Geometry of substrate
Geometry of the deposited region
etc.
Motion & Path
Scan speed (Travel speed)
Track overlap ratio (hatch distance)
Deposition path
Interlayer dwell time
Preheating temperature
etc.

Figure 1.8 Process parameter involved in LDED process (Ahn, 2021)

- Beam diameter, as the name indicates, is a measure of the size of the laser spot on the substrate. The beam diameter can be manipulated by means of defocusing to achieve higher deposition rates. However, a sufficient distance is required to be maintained between the nozzle and the substrate. This distance is often referred to as stand-off distance. Lower stand-off distance can lead to excessive heating of nozzle, which may result in the deposition of powder on the nozzle. A higher stand-off distance can lead to improper deposition.

- The mass flow rate of powder defines the amount of powder fed into the melt pool per unit of time. It is measured in gm/min. The powder is carried by a carrier gas to the deposition zone. The carrier gas flow rate is used to control the mass flow rate of powder. It is measured in litre/min. Interlayer delay is the time gap between the end of the previous layer to the start of next layer. This delay in deposition allows the build to cool down, reducing the risk of thermal cracking and residual stress.

- Layer thickness is the amount of z-shift defined after every successive layer during the slicing. Usually, it is monitored during the process and can be controlled by varying the laser power, scan speed and powder feed rate. Hatch spacing is the distance between two successive tracks of material. This parameter is also sometimes referred to as overlap and is defined in terms of percentage overlap.

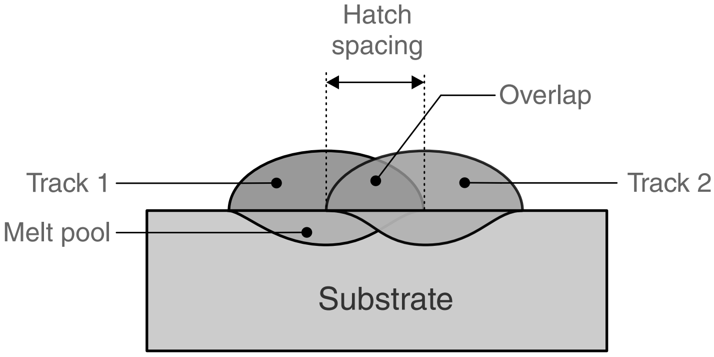

Figure 1.9 Schematic illustrating deposition of two tracks with overlap (Sun et al., 2020b)

1.3 LDED as repair technology

Parts during their service go through complex thermo-mechanical cycling which leads to wear, corrosion and cracking on the surface of the parts. Traditionally, damaged components are repaired using Gas tungsten arc welding (GTAW) also known as Tungsten Inert Gas (TIG) welding process (Jhavar et al., 2013). The simplicity of operation and ease of availability make GTAW process the most convenient process for repair. However, GTAW process has the following disadvantages: detrimental effects on the life of the repaired parts due to high heat input, inability to fill the corners and lack of control on the tolerances. Due to these reasons, the repaired part often fails well before the intended life (Wang et al., 2002). Alternatively, researchers have also used Plasma spraying (Kalfhaus et al., 2019; Rousseau et al., 2021), High-velocity oxy-fuel (HVOF) (Sahraoui et al., 2004; Tan et al., 1999) and friction stir process (FSP) (Maddela et al., 2021; Wang et al., 2021a) for repair related applications. Each of these processes has its own pros and cons, but one common limitation in all these processes is the inability to repair complex crack shapes in difficult to access locations.

In the last decade, several researchers have evaluated the potential of LDED process for repair (Barr et al., 2021; Kim and Shim, 2021; Liu et al., 2021a; Shinjo and Panwisawas, 2022; Wang et al., 2021c, 2022b; Zeng et al., 2022). The advantages of using the LDED process for repair and feature addition capabilities include precise deposition and narrow heat-affected zone. More discussion about the challenges and quality assessment of the conventional repair technology in comparison with LDED process is presented in Chapter 2.

1.4 Computational modelling

Computational modelling is a time-efficient and useful technique to understand the physical behaviour of a process. Computational modelling can provide useful insights on the how the process parameters influence the process outcomes. It is also a useful tool for determining an optimum/desired set of process parameters for a specific material in a short period of time. However, depending upon the complexity and the scale of physical problem, mathematical modelling can become computationally intensive. Mathematical modelling techniques are broadly classified into two categories: (i) Analytical and (ii) Numerical techniques.

An analytical model provides fast, stable, and exact solution for a problem. To obtain the solution, analytical models are usually simplified by making assumptions such as constant material properties, simple geometries that are generally infinite. Despite these simplifications, some analytical models give useful insights on the behaviour of the system. On the other hand, numerical methods provide an approximate solution to the physical problem. Finite Element Method (FEM), Finite Difference Method (FDM) and Finite Volume Method (FVM), Boundary Element Method (BEM) etc., are among some of the most widely used numerical methods. A numerical model consists of a set of algebraic equations (defined by the nature of physical problem) which are bound by the initial and boundary conditions on a geometry. Numerical methods offer capabilities to handle complex shapes, transient boundary conditions and temperature-dependent material properties. However, numerical modelling of complex physical phenomena is not easy to implement and the learning curve is steeper. Further, these techniques require high computational requirements for solving complex mathematical models.

FEM is the most widely used numerical technique to model additive manufacturing processes (Schoinochoritis et al., 2017). In FEM, firstly, a geometry is created either in the FE package or imported from an external CAD modelling software. The geometry is then discretised into a finite number of small domains (elements) of known shapes, typically square (quads) and triangles (triads) for two-dimensional geometries while cubes (hexahedron) and tetrahedron for three-dimensional geometries. The process of discretization is also referred to as meshing. Once a model is meshed, the geometry is defined by elements connected by nodes. An example of discretization is shown in Figure 1.10. During the solution stage, the corresponding degrees of freedom are evaluated at the nodes and then interpolated across the element depending on the order of the element (linear, quadratic etc.).

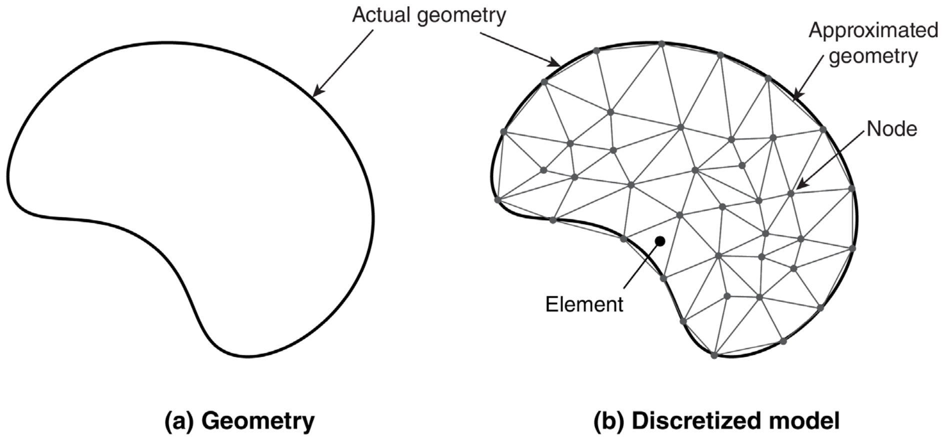

Figure 1.10 Schematic showing descritization of geometry (ANSYS Inc., 2022)

1.4.1 Steps involved in FEM

Any FEM problem consists of three major steps: Pre-processing, Solution and Post-processing. Table 1.1, lists the important steps involved in FEM. In the pre-processing phase, the first and most important step is to understand the physical nature of the problem to be solved i.e., thermal, structural, dynamic analysis etc. Next, the domain of interest with appropriate dimensions and units is either modelled within the FE software or an imported as a CAD model created using a 3rd party CAD modelling software. Depending upon the physical nature of the problem, a suitable type of element is selected, and then material properties are defined. The type of material properties required depends on the physical nature of the problem. For example, to solve a steady-state thermal analysis, only thermal conductivity (k) of the material needs to be define. In order to solve a transient thermal analysis, material properties such as thermal conductivity (k), specific heat (C_p) and density (ρ) need to be input. To improve the accuracy of numerical model, the material properties can be defined as a function of temperature. Next, the geometrical model is meshed with a specific mesh size. Usually, a mesh independency study is performed to ensure that the model has no error related to mesh size. Once the model is meshed, the geometry is discretised into elements and nodes. Thereafter, initial and boundary conditions are applied. Next, loads are applied. The next major and important step is to define the type of analysis. In this depending on the physical problem and the kind of output required, the analysis is set to either Static or Transient mode. Further, an appropriate time step and number of steps are defined. With these steps, pre-processing phase of FEM is done and now the model is ready to be solved. In the solution phase of FEM, the solver first establishes the system of equations/matrix depending on the type of problem defined in the pre-processing phase and solves it. The solver also saves the result files at a frequency defined by the user. The time required to solve the model depends on the complexity of the problem. Once the solution phase is over, the next step is post-processing. In this phase, the predictions are both analysed and visualised. The data at the nodes of interest is usually extracted and visualised in the form of line and bar graphs.

Table 1.1 Steps involved in finite element modelling

Steps involved in FE modelling		
1. Preprocessing	**2. Solution**	**3. Post processing**
• Understanding the nature of problem • Geometric modelling / Import an existing CAD model • Selection of a suitable element type • Define material properties required for a given analysis • Discretization / Meshing • Define initial and boundary conditions • Define loads and constraints	• Simulation type: Static or Transient analysis • Define time steps and selection of proper solver • Establishment of system of equations/ matrix • Solution of system of equations • Storing the results	• Visualization of the contours and plots • Analysis of results • Validation and verification

1.4.2 Element birth and death technique

One of the biggest challenges while simulating a deposition process is the addition of material. A viable technique to simulate the addition of material is called the "*Element birth and death technique*" (EBD). In this technique, the elements are turned active (alive) or inactive (dead) as and when required.

To set up a model with EBD technique, the ANSYS program uses a method to manipulate the stiffness values of the elements. When an element is set to be “*dead*”, the program does not remove the elements from the model; instead, it deactivates the elements by multiplying their properties with a severe reduction factor on the order of 10^{-6} so that elements contribution to the global equations is negligible. Similarly, whenever an element is set to be *alive* or *active* or *birth*, it is not that an element is added to the model; instead, the properties of the element are restored to their original values resembling as “*active*”. It is therefore must to mesh the model before activating or deactivating them(ANSYS Inc., 2022).

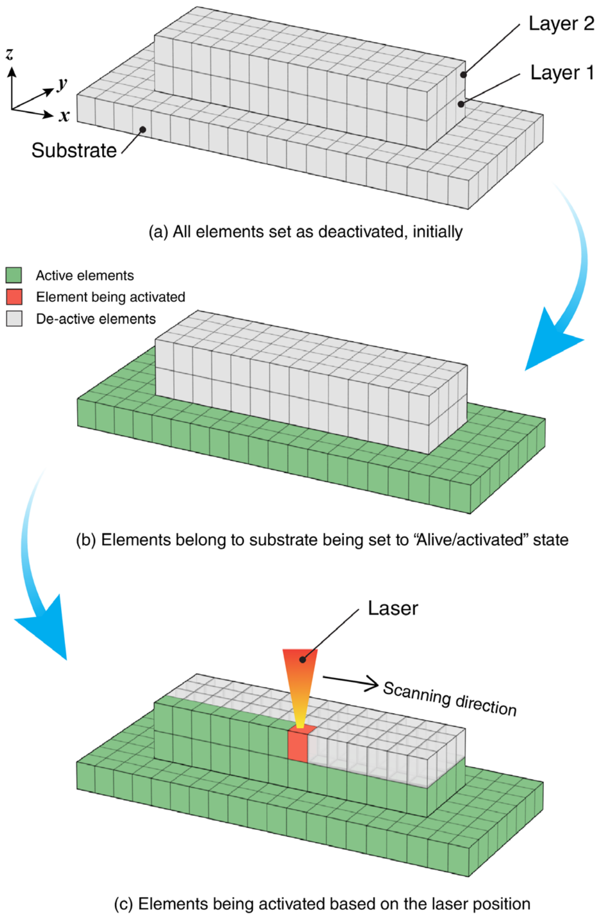
Layer 2
Layer 1
z
y
x
Substrate
(a) All elements set as deactivated, initially
🟩 Active elements
🟥 Element being activated
☐ De-active elements
(b) Elements belong to substrate being set to “Alive/activated” state
Laser
Scanning direction
(c) Elements being activated based on the laser position

Figure 1.11 Schematic of element birth and death technique used to simulate material addition during LDED process (Reproduced from ANSYS Inc., 2022)

1.4.2.1 Element birth and death technique for LDED process

Figure 1.11, shows the step-by-step implementation of EBD technique to simulate material addition during LDED process. At first, a geometry with both substrate and deposit is either modelled in the FE package or imported from a 3rd party CAD package. The geometry is then discretised into nodes and elements as shown in Figure 1.11 (a).

For EBD technique, it is preferred to discretise the geometry into hexahedron shapes, so that the elements can be easily selected by entering related coordinate values. Initial conditions, boundary conditions and loads are applied to the models, after which all the elements are set as dead. During the solution stage, elements belonging to substrate geometry are first set as alive (marked in green colour in Figure 1.11 (b)). In the first step of the solution, the elements from layer 1 are activated depending upon the position of the laser. As the laser moves in the planned direction, elements are activated accordingly. In this way, the entire geometry is simulated.

1.5 Nickel-based super alloys

In components where significant mechanical strength and corrosion resistance are required at elevated temperatures, especially above 800°C, the Nickel-based super alloys are always the choice of material (Betteridge and Shaw, 1987; Reed, 2006). Nickel-based super alloys offer good mechanical properties and corrosion resistance in harsh environments. Solid solution strengthened Ni based super alloys are strengthened by the addition of different alloying elements such as Cr, Fe, Mo etc. The addition of Nb in the Ni-Cr matrix results in extra solid solution strengthening to these alloys. Nb is primarily added to the matrix as a carbide former (Ni_3Nb) which further strengthens the material by means of precipitation hardening (DuPont et al., 2009). Because of the addition of several alloying elements, the Ni-rich, Face Centre Cubic (FCC) lattice expands, which further improves the strength of austenite phase. However, the addition of alloying element such as Nb, Ti and Mo also lead to the formation of carbides. Some of the most common carbides found in these alloys are MC, M_6C, M_7C_3 and $M_{23}C_6$. The presence of Mo and W in these alloys drives the formation of M_6C carbides, while the addition of Cr, stabilizes the formation of M_7C_3 carbides. (DuPont et al., 2009).

These carbides, when segregated on grain boundaries, have a detrimental effect on mechanical properties, especially plasticity. However, by using appropriate heat treatment techniques the formation of these carbides can be prevented.

For solid-solution strengthened Ni based super alloys, the most preferred heat treatment process is solution annealing, also known as Solution treatment (Hu et al., 2018b; Parizia et al., 2020). In solution treatment of Ni based super alloys, the materials are usually heated at temperatures ranging from 1000-1200 °C. The use of high temperature during solution treatment also ensures the dissolution of alloying elements in the austenite matrix. These materials are rapidly cooled by means of water quenching to prevent the formation of secondary brittle carbide phases such as $M_{23}C_6$ (DuPont et al., 2009). However, the use of high temperatures during solution treatment (1000-1200 °C) can lead to softening of the bulk due to recrystallization (Hu et al., 2018a).

In applications where corrosion behaviour (intergranular stress corrosion) is of more significance than structural properties, the heat treatment is carried out between 600-800 °C. As stable $M_{23}C_6$ carbides are formed between 600-800 °C, this range of temperature is often called the “carbide precipitation range”. These carbides have a unique, globular morphology and usually form at the grain boundaries (DuPont et al., 2009). The presence of these carbides also helps to prevent “sensitization” during fabrication. The use of conventional manufacturing techniques, such as machining on Ni-based super alloys is always challenging due to the work hardening. Ni-based super alloys are also well known for their good weldability characteristics, thus making Inconel® a prominent material for AM related research. Inconel 625 (IN625) and Inconel 718 (IN718) are among the most widely used Ni-based super alloy. These two alloys are also qualified and certified for engineering applications through AM process route (Cooke et al., 2020).

1.5.1 Inconel 625 alloy

Nickel-based IN625 alloy is known for its high temperature strength, excellent weldability and fabricability and excellent corrosion resistance. Service temperatures for IN625 alloy range from cryogenics to 900°C (Special Metals Corp., 2013). Standard chemical composition of IN625 is shown in Table 1.2. IN625 derives its strength from the stiffening effect provided by Mo and Nb in the Ni-Cr matrix. The presence of these elements also provides excellent protection in severe corrosive environments and against other thermal effects such as oxidation.

Compared to conventionally available wrought IN625, additively manufactured IN625 shows better mechanical properties because of the fine grain structure (Nguejio et al., 2019). Microstructure of LDED fabricated IN625 is mainly controlled by the solidification rate (*R*) and the temperature gradient (*G*). Faster solidification rates and high temperature gradients during the solidification stage lead to a mixed columnar and dendrite grain structure (Hu et al., 2018b). More discussion about the microstructure and phase transformations in IN625 is presented in Chapter 2.

Table 1.2. Typical composition of IN625 alloy (Special Metals Corp., 2013).

Element	**Ni**	**Cr**	**Mo**	**Nb**	**Fe**	**Co**	**Others**
Weight percentage (%)	58 min.	20-23	8 – 10	3.15 – 4.15	5 max.	1 max.	Balance

1.5.1.1 Applications of IN625 alloy

Characteristics of IN625, such as excellent corrosion resistance, high-temperature mechanical strength and thermal stability at elevated temperatures (up to 900°C), propel this alloy as an excellent material to use in the fields of marine, aerospace and nuclear power plants. In the marine industry, IN625 is used in propeller blades, exhaust ducts, steam line bellow and auxiliary propulsion motors casings. In aerospace sector, this alloy is being used in engine exhaust systems, aircraft ducts, honeycomb structures for housing engine controls, tubes of fuel delivery systems, heat exchanger tubes and turbine shroud rings. Some of the potential applications also include compressor vanes and turbine seals. In the petrochemical industry, because of its excellent corrosion resistance and mechanical strength, this alloy is mainly used to fabricate thin wall vessels, chemical transmission pipes and heat exchangers. Other applications include the control rod components in nuclear water reactors (Shankar et al., 2001; Special Metals Corp., 2013).

1.6 Layout of thesis

This thesis is divided into six chapters. The context discussed in each chapter is summarised as follows:

- **Chapter 1** presents an introductory remark to the need for repair and feature addition of Inconel based super alloys. The chapter also introduces the additive manufacturing process, its classification, metal additive manufacturing, the importance of numerical modelling approaches for additive manufacturing and the material of choice i.e., Inconel 625.

- **Chapter 2** presents a critical review of the literatures available related to the current research objectives. The literature review starts with a discussion on the conventional repair technology followed by LDED process as repair technology. Next, the discussion is focused on the literatures available on thin wall deposition using LDED process. Further, the literature review is focused on the IN625 deposited using LDED process. At last, the literature review is presented to show the status of oxidation behaviour of IN625.

- **Chapter 3** presents the experimental methods being used to accomplish the work presented in this thesis. In this section, a list of all facilities used to carry out the research is mentioned.

- **Chapter 4** presents a fundamental study where effect of process parameters on the melt pool geometry and microstructure was investigated during LSM. A FVM based numerical model was established to understand the effect of considering fluid dynamics on the thermal conditions while modelling LSM process.

- **Chapter 5** presents a fundamental study where the effect of process parameters (laser power and scan speed) on single track geometry (height and width) was investigated. The single tracks were categorised as tracks with no deposition, Inconsistent tracks and consistent tracks. A FEM based numerical model was established to predict the single-track geometry.

- **Chapter 6** presents a IN625 thin wall fabrication work, where the intention was to explore the feature addition capabilities of LDED process. Effect of process parameters on the build quality, surface roughness, microstructure and mechanical properties (in two orientations) was presented.

- **Chapter 7** presents a study where serviced IN625 samples were deposited to mimic repaired using LDED process. Four deposition strategies were used. Microstructure and mechanical properties were investigated. Effect of the post repair solution treatment was also studied.

- **Chapter 8** presented the oxidation behavior of IN625 samples repaired using LDED. The oxidation behaviors of LDED IN625 was also compared with the solution treated LDED 625 and wrought IN625.

CHAPTER 2

LITERATURE REVIEW

This chapter presents a critical review of the literature related to the current research objectives. The literature review starts with a discussion on the conventional repair technologies. The next section of this chapter discusses about the LDED process as a repair technology. Further, the literature is focused on the thin wall deposition followed by the status of work available on topic LDED of IN625. In the last section, a brief discussion the oxidation behaviour of IN625 is presented, followed by the summary from literature.

2.1 Repair using conventional techniques

From over 60 years, Tungsten Inert Gas (TIG), also known as Gas Tungsten Arc Welding (GTAW) is the most widely used technique for repair of metallic components, Chen et al. (2021). There are several studies reporting about the challenges and repair capabilities of GTAW. Hoyingchareon and Muangjunburee ((2016) used GTAW to repair v-grooves machine on an Aluminium 6082 substrate. The welding current was varied from 120A to 140A. It is reported that the weld region is high in porosity (4-6%) as a result of which the repaired test coupons show an inferior tensile property. Vahdatkhah et al. (2022) used pulsed GTAW to repair gas turbine discs made of Cr-Mo-V. The authors reported pulsed GTAW as an efficient process to repair worn components. Due to low input during the pulsed GTAW, lower segregation of carbides was observed after the repair. It also reported that pre heating the sample between 200-300 °C can help in reducing undesirable phase formation. Hapsoro et al., (2021) attempted to repair cracks on the rotor coupling of a 150MW high-pressure steam turbine by using GTAW. The authors proposed a procedure to repair the cracks as: (i) Coupling undercut, (ii) welding in the region of interest, (iii) post welding heat treatment and (iv) machining. Bhaduri et al. (2002) employed GTAW for the cracked steam turbine blades of Indian Pressurised Heavy Water Reactor (PHWR). Two different filler wires of ER316L and ER410 were used to fill the cracks. The welded cracks were found satisfactory for the intended service. AhgaAli et al. (2014) studied the effect of repeating repair welding on SS316L. The authors used Shielded Metal Arc

Welding (SMAW) to repair v-grooves with 90° opening for 1, 2, 3 and 4 times. The authors reported that SS316L can be repaired with no limits on the number of times in a chloride free environment. However, due to the damaging effect of chlorine on SS316L, the samples are reported to be repaired up to two times in the chloride rich environments. Repeating repair welding is reported to have a minimal effect on the tensile strength.

Xu et al. (2015) reported that the use of welding for repairing has a huge impact on substrate. Also, the repair zone is highly susceptible to have cracks during the repair using GTAW. The authors claims that laser cladding is an alternate repair technology which has higher positional accuracy, low heat affected zone and excellent mechanical properties. Liu et al. (2016) used laser cladding to repair cast iron cylinder head blocks. The authors claims that repair of single crack in a cylinder head block can reduce the environmental impact by 63%. However, due to the characteristics of some reactive powders the authors added that laser cladding may have negative emissions and adverse environmental impacts.

Alternatively, some researchers have used Cold Spray (CS) technique to repair cracks and worn surfaces. Faccoli et al. (2014) used CS technique to repair a trapezoidal groove machined on a CA6NM cast martensitic stainless-steel plate. A similar groove was also repaired using GTAW. The authors reported the presence of compressive residual stresses in the samples repaired using CS. Due to this, the fatigue life of repaired parts was improved. Micro-hardness of the repaired region was reported to be higher than the base materials. The authors do claim that a post-heat treatment is not required unlike welding repair techniques. Hattingh et al. (2016) used friction processing technique known as Friction Hydro-Pillar Processing (FHPP) to repair a crack observed on a steam turbine blades. It is reported that FHPP can be a cost-effective technique for the in-situ repairing of cracks. However, the cracks repaired using FHPP were reported to have a positive residuals stress. High-velocity Oxyfuel (HVOF) is a thermal spray process being used for repair components. Although, HVOF is advantageous over the conventional repair techniques because of the lower heat signature and less substrate distortion. HVOF required a good amount of secondary machining which is sometimes not possible for intricate shapes. Tan et al. (1999) used

HVOF to repair steel components. The authors reported a longer deposition time to repair using HVOF technique followed by a huge requirement of secondary machining.

2.2 LDED process as a repair technology

In the last couple of years, several studies have reported using LDED as an alternate technology for repair applications (Basak et al., 2018; Chen et al., 2020a; Liu et al., 2021b; Liu and Shu, 2021). Bennett et al. (2019) compared the life of LDED and GTAW repaired aluminium dies. The authors reported that the LDED repaired dies exhibited same service life as the original dies. Whereas the GTAW repaired dies were only able to perform up to 29% of the service life of original dies. The authors concluded LDED as the best process for automotive die repairing. Lie et al. (2021b) studied the repair capability of LDED process along with laser re-melting on a nickel-based superalloy IC10 using the same alloy stock powder. The authors observed a crack free thin wall on the substrate. For mechanical properties, nano-indentation tests were performed. The results reveal high micro hardness in the deposition zone compared to the substrate and HAZ. Chen et al. (2020a) employed LDED process to repair artificially made v-grooves on a DD5 superalloy substrate. The results indicate that LDED process is suitable for the repair of v-groove without any crack and epitaxial grain growth with controlled process parameters. Sun et al. (2019) repaired T-grooves milled on a SS316 alloys substrate. The study concludes that with the proper choice of laser power, scan speed and feed rate, T-grooves can be repaired without any micro-cracks and with good metallurgical bonding. However, due to rapid solidification in the melted zone, difference in the microstructure and the resulting mechanical properties were observed. Following up with the same route, several other studies have reported the repair capability of different alloys using LDED process (Fang et al., 2019; Sui et al., 2019). Ahn et al., (2022) used both LDED and TIG welding processes to repair a groove machined on Incoloy 901 substrate. The samples repaired with LDED were found to exhibit fine grain structure (3.42 μm). This is due to the high cooling rate associated with LDED ($\sim 6.17 \times 10^4$ K/s) process than TIG ($\sim 3.59 \times 10^3$ K/s). Authors reported that LDED repaired samples exhibited high mechanical properties when compared to TIG repaired samples. While the samples repaired using TIG welding found to exhibit (8.26 μm). The strength of the LDED repaired samples was found similar to the base plate of Incoloy. Liu et al. (2014) used Laser Engineered Net Shaping (LENS) (*equivalent technology name for LDED*) to repair casting and misplaced machining holes on Waspaloy and IN718. The authors drilled deep blind and through holes to simulate a defective part. IN718 was reported to have a good repair weldability. Solidification cracking was reported in the repaired Waspaloy samples. However, upon implementation of NDT techniques, lack-of-fusion was reported in the both the material systems. Zhu et al. (2022) used LDED process to repair 12Cr12Mo stainless steel, where cylindrical tensile specimens, half from the base plate and half from deposit (50/50 sample), were extracted. The deposition to was carried in both open and argon environment. No difference in microstructure of samples deposited in open and controlled environment was reported. The tensile test results of 50/50 samples were reported to have a similar strength as of the wrought plate. However, the author does report a heterogenous microstructure and suggests to use a suitable post-treatment technique for a long-term service life of the repaired components.

With the advancement in additive manufacturing techniques, researchers have also used Wire-arc Additive Manufacturing (WAAM) to repair parts of IN718 (Chen et al., 2022). The authors reported a sound deposit of the IN718 wires. The microstructure was found varying from the bottom to top of the deposited samples as a result of which the trends of micro-hardness in the repair zone were non-uniform. However, after the solution treatment of the repaired samples, the resulting micro-hardness was found uniform across the build. The solution treated samples are also reported to exhibit a balance of both strength and elongation. In a recent study on using WAAM to repair beds of machine tools made of Gray cast iron (Lee et al., 2022). The repaired slot was reported to have pores at the line of fusion. The hardness of the repaired zone was reported to be 17% higher than the base material. However, the study lacks information about the change in microstructure and tensile behaviour after the repair. In a similar study by Zhuo et al. (2020) where WAAM is used to repair titanium alloy (Ti–5Al–2Sn–2Zr–4Mo–4Cr). Despite the sound metallurgical bonding, the repaired samples were reported to have inferior mechanical properties than that of the base plate.

2.3 Thin wall deposition using LDED

Conventional techniques to fabricate thin walls are machining and forging, where a thick plate is machined/forged until the required thickness is achieved. However, these techniques being a plastic deformation processes, lead to several defects in the thin wall, such as sagging, buckling, poor surface quality and residual stresses due to the applied forces (Feng et al., 2021; Zawada-Michałowska et al., 2020). Peng et al. (2007) reported that the use of LDED process for thin wall fabrication can reduce 80% of machining time and 20-50% of the cost required by conventional manufacturing techniques. A thin wall study can also provide insights into the minimum possible feature that a given LDED setup can build (Kim and Saldana, 2020). Luzin and Hoye (2017) reported that the fabrication of thin walls using the LDED process with a consistent build is quite challenging because of several factors such as lack of material support on sides which results in the collapse of thin wall at higher heights and high-temperature gradients, which leads to distortion, cracking and delamination. Inconsistent build dimensions and uncontrolled surface roughness are some other challenges as reported by (Maleki et al., 2021). Ali et al. (2022) used a closed-loop monitoring system to control the melt pool width during thin wall deposition. Authors reported that the real-time control system (where melt pool width is controlled by varying laser power) can be used to fabricate geometrically sound thin walls but at the expense of reduced part density at lower laser power. Pacheco et al. studied the effect of build direction on the mechanical properties of SS316 deposited using LDED process Pacheco (2022). It was reported that the samples extracted along the laser travel direction (horizontal direction) exhibited high mechanical strength than the samples extracted along the build direction (vertical direction). Kim et al. (2020) deposited a thin wall on a plate thinner than the laser spot size. The work reported was to mimic a situation where the thickness of the part to be repaired less than the laser spot diameter. The author reported that while depositing a thin wall structure, laser power plays a vital role in controlling the geometry. Du et al. (2019) reported, geometrical instability in thin walls can be either process oriented or machine setup oriented. Process oriented geometrical instability occurs due to the selection of wrong or unoptimized process parameters for deposition. While fabricating a thin wall using LDED process, heat continues to accumulate in the wall. As a result of which, the melt pool size continues to increase which leads to increase in catchment efficiency and deposition. Use of closed-loop control for process monitoring is one solution to control process oriented geometrical instability, Figure 2.1 (Ali et al., 2022; Hu and Kovacevic, 2003). Machine setup oriented geometrical instabilities can either be due to wrong /inaccurate tool path or a misaligned nozzle-laser beam. Geometrical instability arising due to wrong machine setup can be corrected by performing a dry run prior to the actual deposition. Micro cracking is another defect in thin wall which usually arise due to the metallurgical change during the solidification. Segregation of the alloying element, and formation of brittle grain boundary phases such as carbides and borides are the reason which leads to micro-cracking after solidification. Micro cracking can be prevented by controlling the phase transition by means of controlling the cooling rates during solidification (Chakraborty et al., 2022).

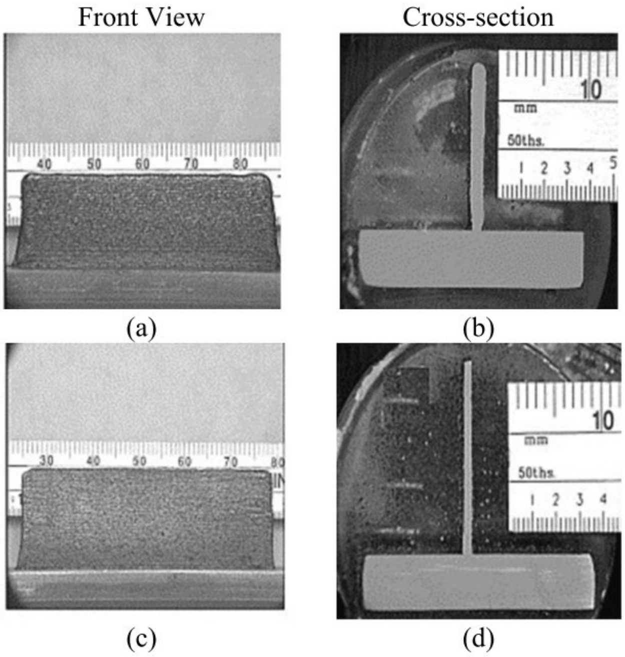

Figure 2.1 A thin wall fabricated (a), (b) without using closed loop and (c), (d) with a closed loop control system (Hu and Kovacevic, 2003)

2.4 Deposition of IN625 using LDED

There are several studies focusing on process parameter optimization for IN625. Fujishima et al. (2017) deposited to understand the effect of process parameters during single line tracks of IN625. The study suggests that low laser power is incapable of melting the stream of powder which leads to voids. At higher gas flow rates, high-volume voids were found due to the gas entrapment. The multilayer deposit of IN625 shows variability in hardness across different layers, which refers to the change in cooling rate across different layers. Hu et al. (2021) found that Inconel 625, because of the low content of Al and Ti, offer good resistance to hot cracking. This makes IN625 more favourable material for AM. However, during the rapid solidification which usually occurs in LDED process, IN625 becomes unstable. As a result, IN625 show columnar grain growth with fine dendrites. In a later study, Micro-segregation was found to be another issue in IN625, where the alloying elements Nb, Mo, Si and C segregate at the inter-dendrite regions (Hu et al., 2018a). Some studies have also reported the presence of brittle phases (Laves and carbides) at the inter-dendrite regions. The presence of these phases has detrimental effect on the mechanical properties, especially ductility and plasticity (Sui et al., 2017). Danielewski and Antoszewski (2020) deposited IN625 blocks using LENS technique. The authors reported anisotropy behaviour in the deposited block where the upper part show a lower value of hardness. This was referred to the annealing effect in the top layer due to heat accumulation during the deposition. The microstructure of the LDED IN625 samples was reported to compose of dendritic and columnar dendritic structure. The LDED IN625 was reported to exhibit a UTS of 690 MPa at room temperature and 610 MPa at elevated temperature (700 °C). Heat treatment LDED IN625 is reported to exhibit inferior tensile strength with up to 10% improvement in the elongation. The XRD results do not show any major change in phase between the base plate and the LDED IN625. (Wang et al., 2021b) used multiple powder to build in-situ alloyed IN625 by LDED. The authors reported that reducing the scan speed during the deposition increase the energy density which allow the in-situ alloying. The high temperature materials such as Nb and Mo were found fully melted. The authors concluded that both pre-alloyed and in-situ alloyed LDED IN625 exhibited similar tensile strength. The authors also reported the effect of scan speed on the micro-hardness of the LDED IN625. The results show an increase in the hardness value from 306 to 339 HV with the laser scanning speed increasing from 500 to 1100 mm/min, respectively. The solution treatment performed at 1200 °C on in-situ alloyed LDED IN625 sample were reported to be fully recrystallized. However, the solution treated sample were reported to have inferior tensile strength when compared to as-deposited sample. The solution treated samples exhibited an average tensile strength of 895 MPa whereas the as-deposited samples exhibited 1020 MPa. In some recent studies, IN625 has been manufactured by cold metal transfer (CMT-WAAM) Yangfan et al. (2019). Authors reported heterogenous microstructure where columnar dendrites were found at the bottom and equiaxed structure at the top layers. In addition, micro-hardness was reported to first increase (near substate), then decrease and finally increase (top layers). The results from tensile testing show an increase in yield strength, ultimate tensile strength and % elongation with the increase in travel speed.

2.5 Oxidation behaviour of IN625

With the AM technologies getting matured, the market is now demanding more alloy systems specifically tailored for 3D printing. So far, the research in Metal-AM is more focused towards the understanding of process physics where the intentions are to find the process-microstructure relation which should result in defect-free deposition, high tensile strength, fatigue life and creep strength etc. (Blakey-Milner et al., 2021). However, there is a lack of understanding towards the high temperature stability, i.e., the resistance of alloys to prevent oxidation and environmental degradation of the materials tailored for 3d printed (Sun et al., 2020a).

IN625 is widely used in the manufacturing of heat exchanger tubes, production of engine components dealing with high temperatures etc. In these environments, materials are expected to show both good mechanical properties and thermal stability. To this end, Ramenatte et al. (2020a) compared the wrought and Laser Beam Melted IN625. It is reported that the oxidation resistance being offered by the wrought alloy is systematically high by several folds than that of the as-built sample with significant internal oxidation at 1050 °C. Malafaia et al. (2020) compared the oxidation behaviour of cast forged bars of IN625 at 800 and 1000°C. Thickness of oxide for the sample tested at 1000°C was reported to be ten times higher than the sample tested at 800 °C at the same exposure time. This study paves the path to choose a suitable application temperature for IN625. Cr_2O_3 was reported as the primary oxide forming on the surface at 1000°C. At the same time, there are some studies available on IN625 fabricated using Selective Laser Melting (SLM) followed by post processing. The as-built samples are found to show poor oxidation resistance compared to the post processed (Laser shock peening) samples, which show two times better oxidation resistance (lower mass gain) (Chen et al., 2020b). From this study, it is evident that the as-built AM parts followed by post-processing can significantly improve oxidation resistance.

2.6 Conclusions from literature survey

From the literature discussed above, it is clear that one of the key areas for the concern of circular economy is the repair and refurbishment sector. Repair of components with high intrinsic value can bring down the wastage of material (sustainable development) as well the overall cost of replacing the wormed part with the new one. At the same time, feature addition is another area of improvement. Adding a feature to an existing part can improve its functionality, such as an increase in stiffness or heat transfer. Conventional repair technologies are limited to shape complexity and controlled deposition of material. Additive manufacturing processes are now evolved from the prototyping to the functional stage, and it is the right time to explore more capabilities of these processes. LDED is an additive manufacturing process which stands apart when it comes to repair and feature addition without any considerable defect. Ni based super alloys are high value components. These are generally employed in harsh environment; as a result, wear and tear are common and inevitable. IN625 is one alloy which is widely used in petrochemical, marine and other similar corrosive applications. This alloy goes through severe cracking, wear and tear and, therefore can be a good candidate for understanding the repairability using LDED process.

In a nutshell, it is known that AM is great manufacturing technique with a huge boom in the market now, but how good AM is at re-manufacturing, repairing and feature addition is the focus of this thesis.

2.7 Objectives

The objectives considered to understand the fundamentals of LDED process, factors affecting the deposition and the capabilities of LDED to repair and feature addition applications for IN625 are as follows.

- Understand the effect of fluid dynamics on melt pool geometry and thermal conditions governing microstructure during laser surface melting of IN625.
- Perform transient thermal finite element analysis to predict single track geometry during laser directed energy deposition of IN625 alloy and validate predictions with experimental measurements.
- Perform transient thermal finite element analysis of LDED IN625 thin walls to predict melt pool geometry, cooling rates and thermal gradients.
- Investigate microstructure and room temperature tensile properties of LDED IN625 thin walls in as-built condition along laser travel and build directions.
- To draw comparisons between microstructure and mechanical properties of LDED IN625 with wrought IN625 to establish repair quality.
- Investigate the effects of standard heat treatment on microstructure and mechanical properties of LDED IN625.
- Investigate isothermal oxidation behaviour of LDED IN625 in as deposited and heat-treated conditions.
- Compare oxidation behaviour of LDED IN625 with that of wrought IN625.

CHAPTER 3
EXPERIMENTAL METHODS

This chapter describes the experimental setup and characterization tools used in various studies mentioned in this thesis. The chapter also explains about various procedures such as sample cutting, mounting, grinding and polishing, required to characterize a material.

3.1 Experimental setups

3.1.1 LDED setup

In the present work, LDED setup available at Laser Additive Manufacturing laboratory, Raja Ramana Centre for Advanced Technology, Indore was used for depositing the samples. Figure 3.1 shows the schematic of the LDED setup available at RRCAT. The LDED setup consists of a 2-kW fibre laser of wavelength of 1070 nm having 2.5 mm spot diameter, build platform with 5-axes motion capabilities i.e., three linear axes (x, y, z) and two rotation axes (v, w). The build volume is 250 mm × 250 mm × 250 mm. The y-axis of the machine can be titled up ±110° (i.e., *v-rotation*) while the z-axis can be rotated continuously with 360° rotation (i.e., *w-rotation*). The machine's motion system offers repeatability of ± 5 μm, accuracy of ± 10 μm and resolution of 1 μm. The machine is equipped with a twin-powder feeder, an oxygen and moisture analyser. The powder feed rate can be varied between 2–40 g/min with reproducibility of up ±0.2 gm/min. A schematic representation of a typical co-axial nozzle is shown in Figure 3.2. The powder is fed through a co-axial nozzle consisting of a through hole at the centre and 3 concentric holes of 2 mm each at 120° inclination. The laser beam travels through the central hole while powder which is carried by a carrier gas, flows through the three concentric holes. During the deposition, argon gas, with a purity of 99.9933 % (O_2 and moisture level below 2 ppm) was used as carrier gas. The system has an environment-controlled deposition chamber with gloves ports, where the materials which are highly susceptible to oxidation, such as Ti-6Al-4V etc. can be deposited. Usually, an inert gas such as argon is used for purging the deposition chamber. A controlled chamber is not required for deposition of IN625. This is because IN625 exhibits good oxidation and corrosion resistance. Therefore, all the samples used in various studies of this thesis were fabricated in an open atmosphere.

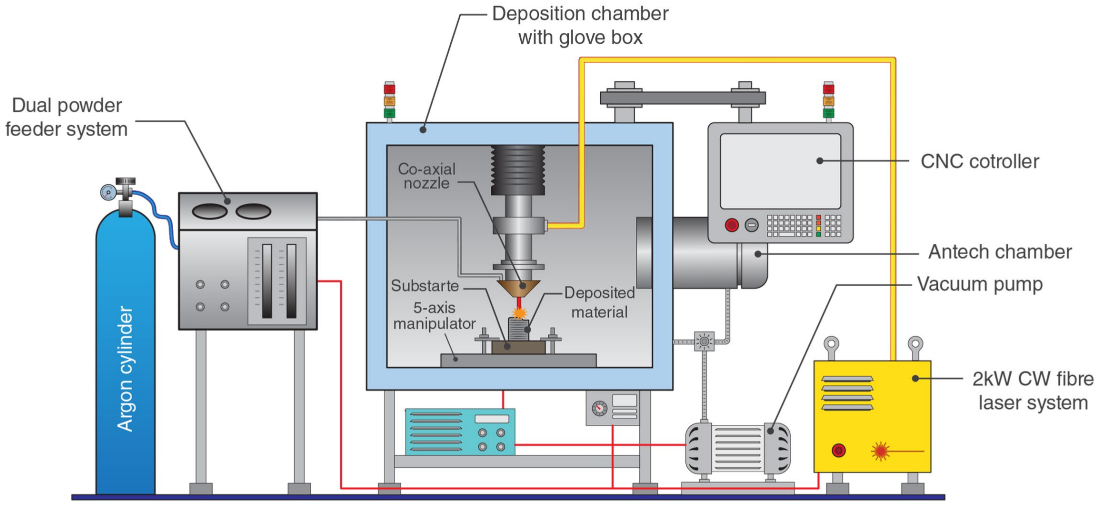
Deposition chamber
with glove box
Dual powder
feeder system
Argon cylinder
Co-axial
nozzle
Substarte
5-axis
manipulator
Deposited
material
CNC cotroller
Antech chamber
Vacuum pump
2kW CW fibre
laser system

Figure 3.1 Schematic of LDED setup used at RRCAT, Indore

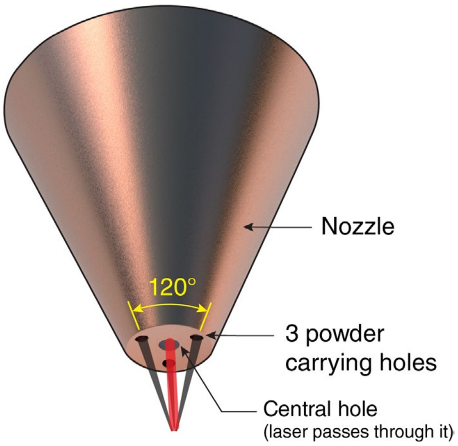
Nozzle
120°
3 powder
carrying holes
Central hole
(laser passes through it)

Figure 3.2 Schematic of a typical nozzle used in LDED process

3.2 Furnace

To study the effect of heat treatment on microstructure and mechanical properties of as-deposited samples, solution treatment was carried out in a muffle furnace available at RRCAT, Indore (Model: Bottom Loading Furnace; Make: Therelek). For IN625 standard solution treatment cycle was used, wherein the samples are heated to a peak temperature of 1200 °C at the rate of 5 °C/min. The sample is then held at the peak temperature for 90 mins, followed by water quenching (Hu et al., 2018b). To carry out the high temperature oxidation studies, a box furnace was used (Make: Indfurr, Chennai).

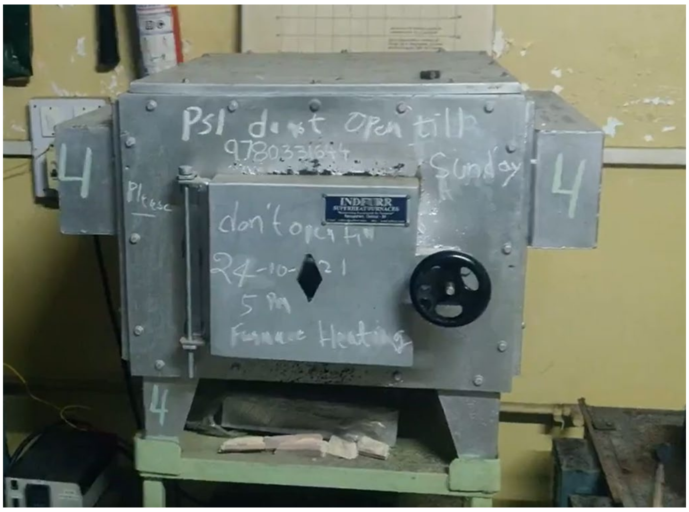

Figure 3.3 Furnace used to carry out high temperature oxidation experiments

3.3 Sample preparation

3.3.1 Sectioning and mounting

After the deposition, it is required to extract test coupons from the build. The dimensions of the test coupons extracted from the build were as per the ASTM standards. A Wire Electrical Discharge Machining (WEDM) setup was used to precisely cut the samples to the required dimensions. For microscopy and hardness tests, the test coupons were cold mounted to improve the handling of samples. Cold mounting the samples also helps in preserving the edges and corners of the samples during disc polishing. For cold mounting, the resin and hardener [Supplier: Chennai Metco, India] were mixed in the proportion of 2:1. In the next step, the sample to be mounted was placed inside a reusable rubber mounting cup, followed by pouring the mixture of resin-hardener. The mixture takes 15–20 minutes to cure. After the mixture is cured, mould is extracted from the cup and if required is subjected to facing operation on the lathe machine to make both top and bottom faces parallel.

3.3.2 Grinding and polishing

Grinding and polishing is carried on the sample to remove scratches and to obtain mirror surface finish, required for the metallography, porosity and hardness measurement studies. At first, a grinding operation was carried out on the samples using an automatic polishing machine [Model: Bainpol-auto; Make: Chennai Metco, India]. However, due to technical limitations, grinding was carried out in manual mode, where human intervention was required to apply pressure on the mould against the SiC sheet mounted on a rotating disc. SiC sheets of grit sizes 220, 400, 600, 800, 1000, 1200 and 1500 were used for grinding. The disc speed was set to 300 RPM. Further, to obtain a mirror surface finish, polishing was carried on a velvet cloth [Supplier: Chennai Metco, India] with fine abrasive particles usually dispersed in water. The studies mentioned in this thesis, involve the use of Alumina powder dispersed in water as an abrasive material to polish the samples. Finally, the samples were thoroughly cleaned in an ultrasonic bath.

3.3.3 Etching

Etching is a process of revealing microstructural information of a given sample. Depending upon the type of material, the process of etching varies, as explained in the ASTM standard for etching metals (ASTM E407, 2016). For Ni based superalloys, electrolytic etching is preferred. In electrolytic etching, as shown in Figure 3.4, the sample to be etched is connected with the anode (positive terminal) while the reference material is connected with the cathode (negative terminal) of a Direct Current (DC) power source [Model: PSD3005; Make: Scientific Mes-Technik Pvt. Ltd., India]. After the connections, both reference material and the sample to be etched are dipped in an electrolytic solution for a given time, voltage and current. For IN625, 10 gm of oxalic acid mixed in 100 ml of distilled water was used as an electrolyte. The samples were etched at 12V for 8-12 seconds. SS304L was used as the reference material.

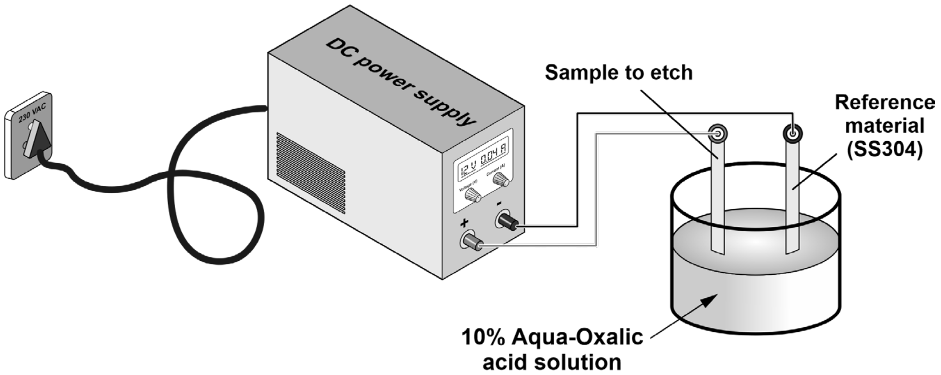
230 VAC
DC power supply
12 V
0.04 A
Voltage (V)
Current (A)
+
-
Sample to etch
Reference material (SS304)
10% Aqua-Oxalic acid solution

Figure 3.4 Schematic of setup used for electrolytic etching of samples

3.4 Characterization

3.4.1 Optical microscopy

The polished samples after etching were observed under an optical microscope (Make: Carl Zeiss). Images of the cross-sections were acquired at different magnifications between 50-500x. For macro-observations, such as measurement of single-track dimensions, stereo microscopy (Make: Leica) was used. A stereo microscope is a type of optical microscope which is used to acquire low-magnification images, usually up to 5x.

3.4.2 Scanning electron microscopy and energy dispersive spectroscopy

For high-resolution microscopy, Scanning Electron Microscopy (SEM) was used (Model: GEMINI 300; Make: Carl Zeiss, Germany) at CRF, NITK Surathkal (Figure 3.5). The EDS facility attached to the same machine was used to determine the elemental composition of the sample in different conditions, such as deposited or heat-treated.

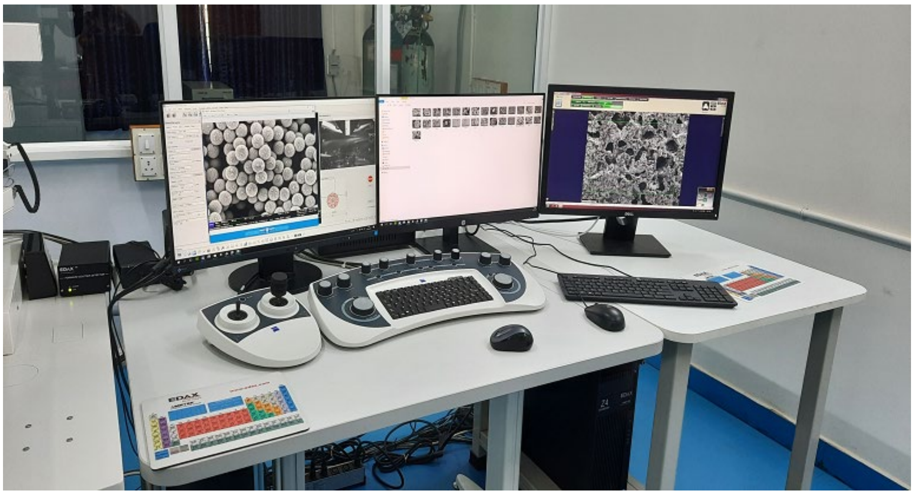

Figure 3.5 Scanning electron microscopy facility at Central Researsh Facility, NITK Surathkal

3.4.3 X-ray diffraction

For phase analysis, X-ray diffraction technique was used. (Model: Empyrean 3rd Gen, Make: Malvern PANalytical, Netherlands). X-ray diffraction technique makes use of the wave nature of X-rays to identify the crystal structure of a given sample. During the XRD analysis, the samples were scanned from 10° to 100° at a rate of 7°/min using Cu Kα radiation (λ=1.54 Å).

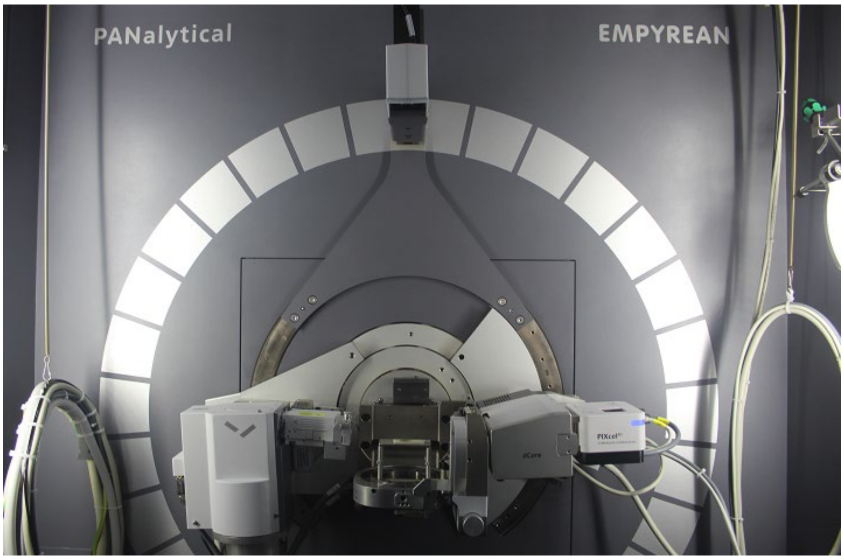

Figure 3.6 Facility used for XRD analysis

3.4.4 Tensile testing

The uniaxial tensile test was performed on standard sub-sized ASTM E8M samples at a strain rate of 1 mm/min using a Universal Testing Machine (Make: Instron), Figure 3.7. In the thin wall study, reported in chapter 6, due to the dimensional limitation of thin walls, micro-tensile specimens were extracted, and uniaxial tensile tests were carried out at a strain rate of 0.1 mm/sec (Model: Z020; Make: Zwick Roell, Germany). Dimensions of the ASTM sub-sized and micro tensile specimen is shown in Figure 3.8.

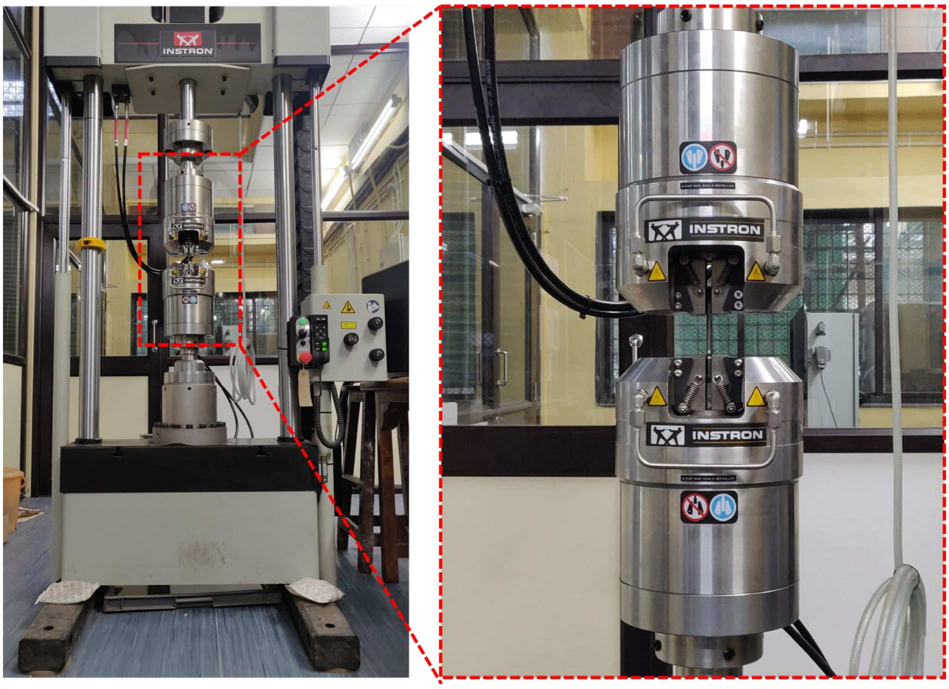

Figure 3.7 Universal testing machine used for tensile testing

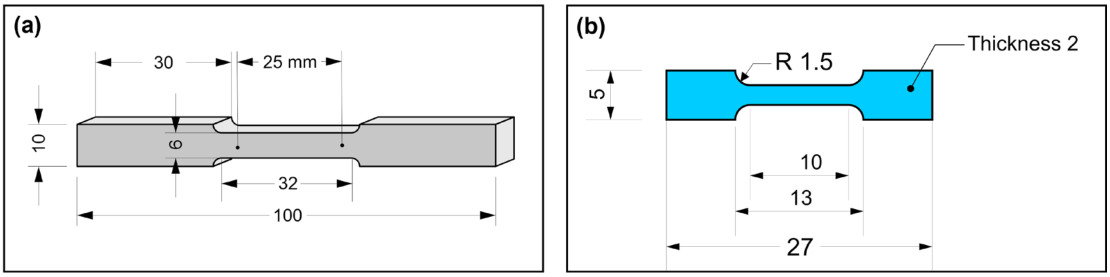

Figure 3.8 Dimensions of the (a) sub-size and (b) micro tensile specimen used in study

3.4.5 Microhardness

Vickers hardness test was conducted to measure the micro-hardness of the samples. Vickers hardness uses a diamond indenter, which is pressed against the sample at a given load and time (dwell time). After the dwell time, indenter is pulled back, and the dimensions of the indent are measured using optical microscopy (Figure 3.3). For the hardness tests reported in this thesis, the samples were first mirror polished. Then the hardness test was carried out at 300 gm-f and 10 second dwell time [Model: MVH- S Auto; Make: Omnitech]. The Vickers micro-hardness value can be estimated by using the equation given in eq. (3.1) and eq. (3.2):

$$HV = \frac{\text{Constant} \times \text{Test force}}{(\text{Average of indent diagonals})^2} = \frac{1.8544 \times f}{(d_{avg})^2}(kgf/mm^2); \qquad (3.1)$$

$$d_{avg} = \frac{d_1 + d_2}{2} \qquad (3.2)$$

where, f is the load applied and d_1 and d_2 are the diagonals of the indent formed on sample as shown in Figure 3.9.

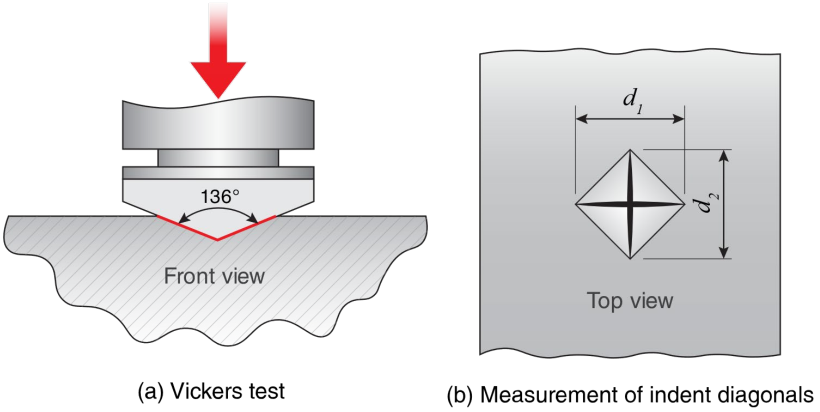

(a) Vickers test

(b) Measurement of indent diagonals

Figure 3.9 (a) Schematic of Vickers hardness test and (b) measurement of indent diagonals formed on the samlpe after hardness test

3.4.6 3D scanning

Thin walls built using LDED process were scanned using a 3D scanner. Figure 3.10 shows the picture of 3D scanner used (Model: Space spider Make: Artec, Europe). The scanner has a 3D point resolution of upto 50 μm. The point clouds were collected in a CSV file, which was then converted into a meshed model (STL file format). Next, dimensions such as thickness, height and length of the thin walls were measured using OEM-provided software (Artec Studio, Version-17).

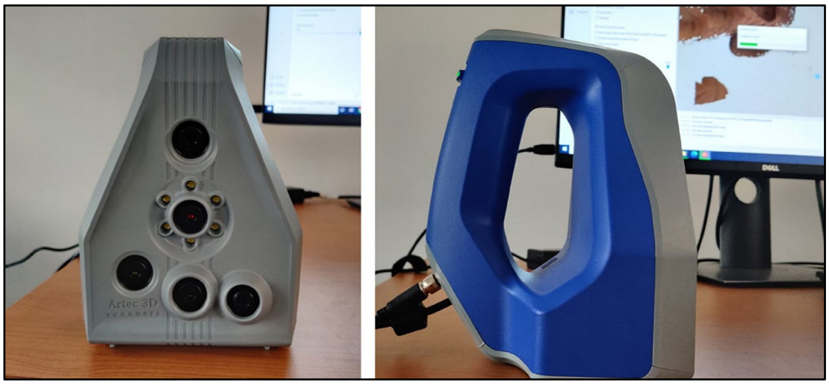

Figure 3.10 3D scanner facility used for scanning thin walls

CHAPTER 4

EFFECT OF FLUID FLOW ON MELT POOL GEOMETRY DURING LASER SURFACE MELTING OF IN625

The present study aims to understand the effect of considering fluid-dynamics and its effect on melt pool geometry while modelling a Laser Surface Melting (LSM) process. Nine tracks were melted on an IN625 plate at different laser powers and scan speeds. Melt pool geometry and grain morphology were evaluated using microscopy techniques. A 3-D finite volume model based on heat conduction solidification equation (HCS model) was used to simulate LSM process. Further, HCS model was expanded to include effects of fluid dynamics (HCS-FD model). Both the numerical models were used to predict melt pool geometry, peak temperatures, temperature gradients and cooling rates. The error in predictions of melt pool geometry from the HCS-FD model was lower when compared to the HCS model. The velocity vectors show a strong surface tension driven flow which has resulted in narrow and deeper melt pools in agreement with the cross-sectional images of the melted tracks. Further, solidification characteristics were interpreted to obtain inferences about grain size and morphology.

4.1 Materials and methods

4.1.1 Materials

For the single laser track studies, an IN625 plate of size 100 mm × 120 mm × 6 mm was used as the substrate. The plate was cleaned with acetone and dried prior to the experiments. Table 4.1, show the chemical composition of the IN625 plate used for the experimentation.

Table 4.1 Chemical composition of the IN625 alloy substrate.

Material	**Composition (wt. %)**
Nickel	58 %
Chromium	21 %
Molybdenum	6.3 %
Iron	4 %
Niobium	2.7 %
Manganese	0.67 %
Other	7.33 %

4.1.2 Experimental setup

The experiments were carried out at Raja Ramanna Centre for Advanced Technology (RRCAT), Indore, India. Figure 4.1 shows the machine setup used for experimentation at Laser Additive Manufacturing Laboratory (LAML), RRCAT, Indore. The system essentially consists of a 500 W fibre laser with 500 µm spot diameter (IPG Photonics, USA), Galvano-scanner for the laser movement in the x and z directions and a build platform. The IN625 plate was fixed on the build platform and single laser tracks were scanned at varying laser powers and scan speeds based on a full factorial experimental array. The laser power was varied from 300 to 500 W and scan speed from 100 to 300 mm/s, both in three levels. Hence, a total of 9 single track scan experiments (3×3) were performed as shown in Table 4.2. For the ease of discussion, the combination of laser power and scan speeds are also provided in terms of energy density (Dass and Moridi, 2019), as shown in Table 4.2.

$$\text{Energy density } (E) = \frac{P}{v \times d} (J/mm^2) \tag{4.1}$$

where E is the Energy density in J/mm², P is the Laser power in W, v is the scan speed in mm/s and d is the laser spot diameter in mm. The plate after the scan experiments was left to cool in the machine setup. Subsequently, the singe laser tracks were sectioned (along the z'-z' direction as shown in the Figure 4.2 (a), polished and etched

(Electrolytic etching at 12 V potential difference in 10 % Aqua-Oxalic solution for 10-12 seconds) for geometrical and metallographic studies. The samples were first characterised under an optical microscope (Primo Star, Zeiss) followed by Scanning Electron Microscope (SEM) (Gemini, Zeiss).

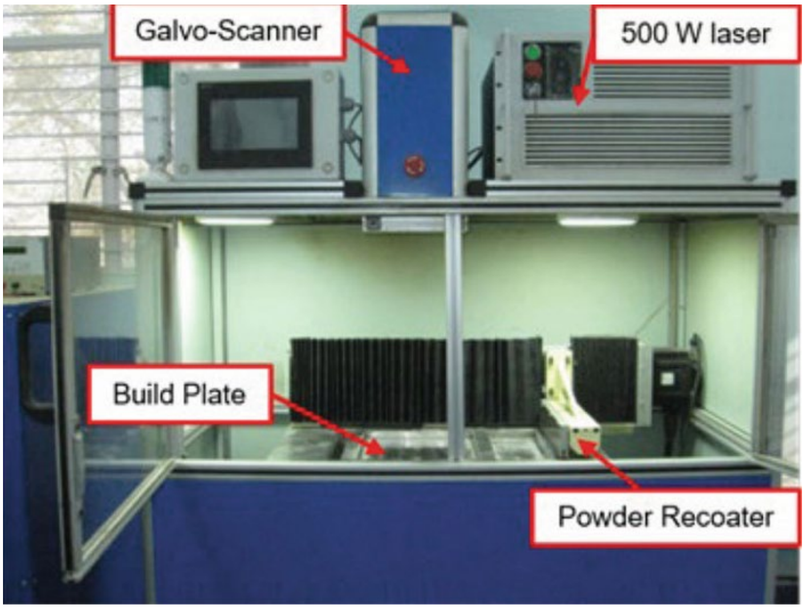

Figure 4.1 Machine setup at LAML, RRCAT, Indore

Table 4.2 Combination of laser power, scan speed and related energy density used for single laser scan experiments.

Experiment No.	Power (W)	Scan Speed (mm/s)	Energy density (J/mm²)
1	500	100	10
2	500	200	5
3	500	300	3.3
4	400	100	8
5	400	200	4
6	400	300	2.7
7	300	100	6
8	300	200	3
9	300	300	2

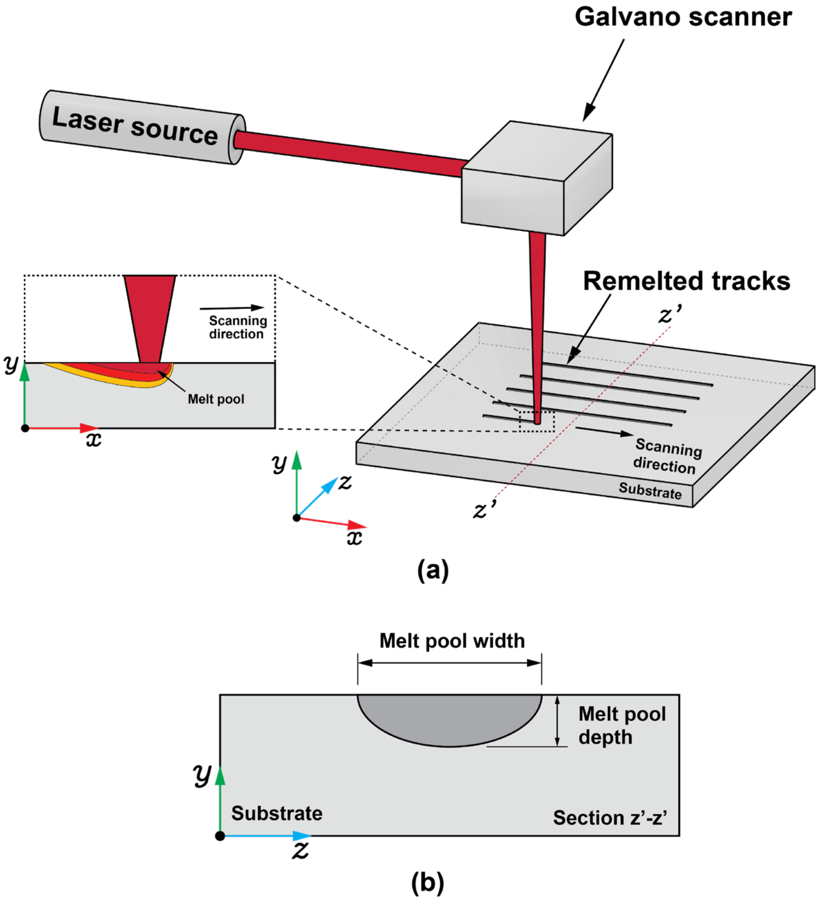
Galvano scanner
Laser source
Remelted tracks
z'
Scanning direction
Melt pool
y
x
z
Scanning direction
Substrate
z'
(a)
Melt pool width
Melt pool depth
y
Substrate
Section z'-z'
z
(b)

Figure 4.2 (a) Schematic of experimental setup (b) Graphical representation of the melt pool width and depth obtained from the section z'-z'.

4.2 Numerical modelling

A 3D cartesian coordinate system based finite volume model was established using the commercial software package, ANSYS Fluent. The domain used is a cuboid of dimensions 11 mm × 2 mm × 5 mm. To identify the grid density required to perform the simulations, grid independence study (Figure 4.3), was performed to predict the peak temperature at different grid densities. Based on the difference between the predicted results, the final domain was meshed with 50 μm grid size along depth and width and 100 μm along length, with a total of 4,39,560 cells. Further, the mesh was biased along the width direction in the vicinity of the heat source as shown in the Figure 4.4. A time dependent solver with a maximum time step based on Courant number was used (Aggarwal et al., 2023). The value of Courant number was kept constant as 1 for all the cases.

$$C = v\frac{\Delta t}{\Delta x} \tag{4.2}$$

where C is Courant number, v is the scan speed, Δt is time step and Δx is the dimension of the smallest computational grid cell.

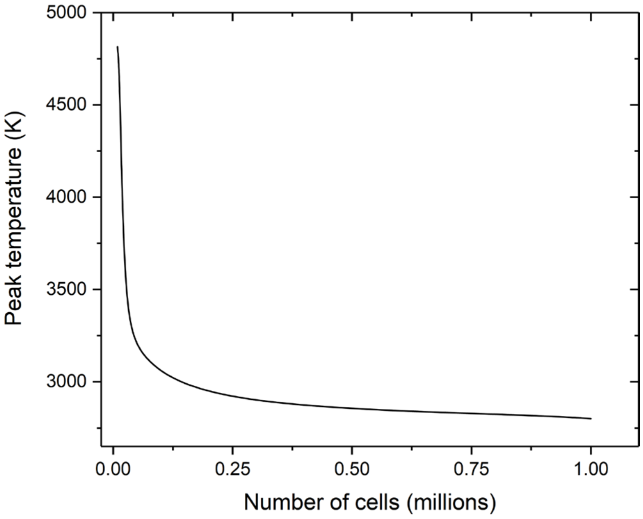

Figure 4.3 Peak temperature of all the investigated meshes in grid independency study

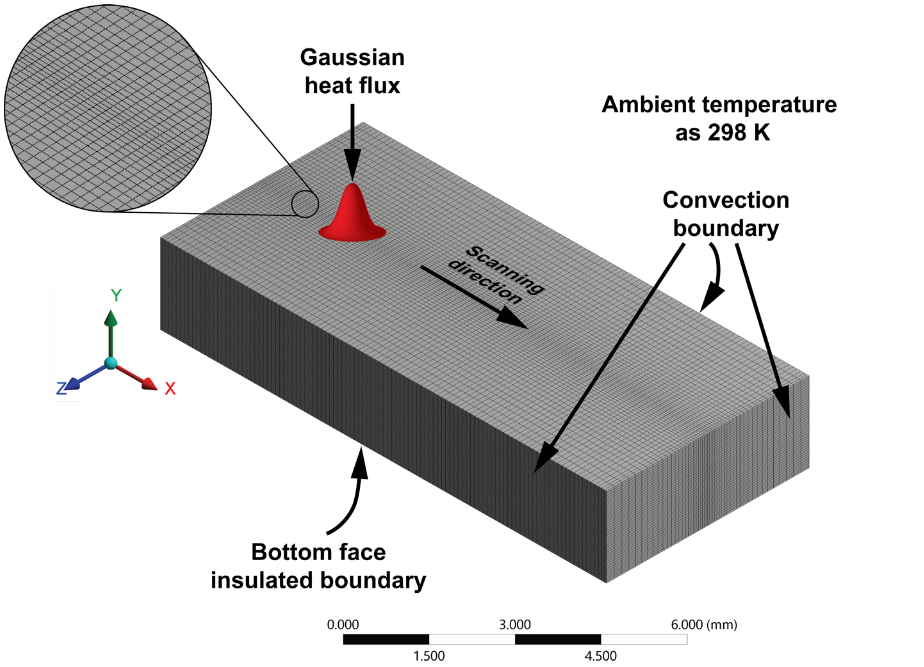
Gaussian heat flux
Ambient temperature as 298 K
Convection boundary
Scanning direction
Bottom face insulated boundary
Y
X
Z
0.000
1.500
3.000
4.500
6.000 (mm)

Figure 4.4 Numerical domain used in the study, related coordinate system and boundary conditions.

4.2.1 Assumptions

To simplify the modelling procedures following assumptions were made to the numerical model:

(a) The liquid flowing in the melt pool is assumed to be viscous incompressible Newtonian (Mukherjee et al., 2018) and the flow is laminar (Wu, 2010).

(b) The solid to liquid or liquid to solid transition region is described by the mushy zone model used in Ansys Fluent software (ANSYS Fluent Tutorial Guide 18, 2018).

(c) The moving heat source is a 2-D surface heat flux with a gaussian distribution (Balichakra et al., 2019; Li et al., 2018).

(d) Effect of composition change due to the loss of alloying elements during melting has not been included in the numerical model (Mukherjee et al., 2018).

4.2.2 Governing equations

The HCS-FD model considers both heat transfer and fluid dynamics, considering conservation of energy, mass and momentum (Chouhan et al., 2018a; Debroy and David, 1995; Manvatkar et al., 2015; Mukherjee et al., 2017) while on other hand, HCS model only considers heat conduction equation. Following governing equations were used to describe the heat transfer and fluid flow during the single laser track scanning.

4.2.3 HCS model

(i) Energy Conservation

Single track melting includes change of phase from solid to liquid and liquid to solid during the melting and solidification stages, respectively. These phase transformations require latent enthalpy of fusion which is included in the energy equation. It is important to note that for HCS model, only the conduction part of the energy equation (Chouhan et al., 2018a) was solved.

$$\rho c_p \frac{\partial T}{\partial t} + \rho c_p \vec{u} \cdot \nabla T = \nabla \cdot (k \nabla T) - \frac{\partial H}{\partial t} - \rho \vec{u} \cdot \nabla H \tag{4.3}$$

where, ρ, c_p and k are the density, specific heat and thermal conductivity, respectively. H is the latent enthalpy of fusion (Mukherjee et al., 2018) eq. (4.4),

$$\Delta H = L \times f_l \tag{4.4}$$

4.2.4 HCS-FD model

(i) Energy conservation

The governing equation for energy conservation considered for HCS-FD model is the same as the one used in HCS model (eq. (4.3))

(ii) Mass conservation

The continuity equation (Chouhan et al., 2018a) used for incompressible flow is,

$$\nabla.(\vec{u}) = 0 \tag{4.5}$$

(iii) Momentum conservation

The equations governing momentum conservation (Chouhan et al., 2018a), (Wu, 2010), are,

$$\frac{\partial(\rho\vec{u})}{\partial t} + \vec{u} \cdot \nabla(\rho\vec{u}) = -\nabla p + \mu(\nabla^2\vec{u}) + \vec{F} \tag{4.6}$$

$$\vec{F} = \vec{F}_s + \vec{F}_N \tag{4.7}$$

where, $\overrightarrow{F_s}$ is the momentum sink term, which helps in bringing down the velocity of the fluid in the melt pool and liquid-solid interface during solidification (Mukherjee et al., 2018).

$$\vec{F}_s = \frac{(1-f_l)^2}{f_l + b} C \cdot \vec{u} \tag{4.8}$$

f_l is the fraction of liquid in the melt pool which is mathematically expressed as eq. (4.9) , C is the mushy zone constant (10^6 in present study) and b is a very small number to avoid division by zero during solidification (10^{-3} in the present study).

$$f_l = \begin{pmatrix} 0 & T < T_L \\ \dfrac{T - T_S}{T_L - T_S} & T_S \le T < T_L \\ 1 & T \ge T_L \end{pmatrix} \tag{4.9}$$

where, T_L and T_S are the liquidus and solidus temperatures, respectively. The material flow in the region of melt pool was included in the model using the Boussinesq approximation. The term $\vec{F}_N$ accounts for the flow of melt pool due to natural convection ("Ansys Fluent 2020 R1 Theory Guide" 2021).

$$\vec{F}_N = \rho g \beta_T (T - T_{ref}) \tag{4.10}$$

where, ρ, g, β_T and T_{ref} are the density, acceleration due to gravity (g = 9.81 m/s²), thermal expansion coefficient and reference temperature (298 K) respectively. Also, to include the fluid flow due to temperature dependence of surface tension, the top surface of the substrate was assigned with slip condition defined by shear stress (Chouhan et al., 2018a) (eq.(4.11)).

$$\tau = \frac{d\gamma}{dT}\nabla_S T \tag{4.11}$$

where, $\frac{d\gamma}{dT}$ is the temperature coefficient of surface tension and $\nabla_S T$ is the surface temperature gradient.

4.3 Boundary conditions

4.3.1 Heat source model

The energy equation solved in the present study used a moving heat source as a boundary condition to represent the laser beam, as shown in the Figure 4.4. The laser beam was modelled as a heat source with a Gaussian distribution as given in eq.(4.12) (Chouhan et al., 2018a). Figure 4.5, show the energy intensity distribution at different laser powers used in the study.

$$I(x,z) = \frac{2\alpha Q}{\pi r^2}\cdot \exp\left(-2\frac{((x-vt)^2+z^2)}{r^2}\right) - h_c(T-T_0) \tag{4.12}$$

where *I(x, z)* is magnitude of heat flux applied to the surface of substrate measured in W/mm2, Q is the laser power in Watts, α is the laser absorption coefficient which represents the fraction of total laser energy absorbed by the substrate, r refers to the radius of the laser beam (m), v refers to the scan speed of the laser beam (m/s) and t is time (s). The coordinate variables *x* and *z* are the distance from the centre of the laser beam. From the eq. (4.12) it can be seen that the position of the heat sources is successively changed in the *x* direction with velocity *v* corresponding to the time *t*. The value of absorption coefficient for Inconel 625 has been reported in literature by various researchers. Table 4.3 documents the absorption coefficient (α) values used in different studies. Present study used an absorption coefficient of 0.3. The last term in eq. (4.12) accounts for the heat loss due to the convection on the top surface, where h = 10 W/m²·K, is the convective heat transfer coefficient (Chouhan et al., 2018b) and T_0 = 298 K, is the ambient temperature.

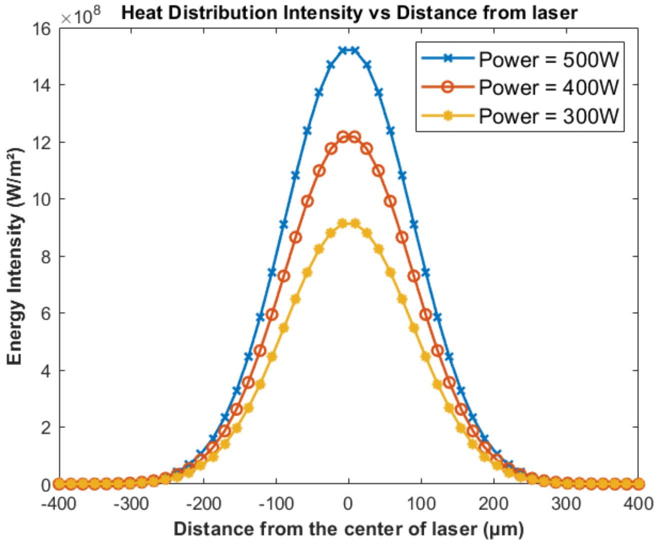

Figure 4.5. Magnitude and distribution of heat flux for laser powers 300, 400 and 500 W

Table 4.3. Reported Absorptivity coefficients (α) in literature for IN625.

Absorptivity value	Reference
0.5	(Ghosh et al., 2018)
0.30	(Sabau et al., 2020)
0.28	(Wang et al., 2017b)

4.4 Material properties

For both HCS and HCS-FD models, specific heat and thermal conductivity were assumed to be temperature dependent, while density was constant. Further, the HCS-FD model also uses properties related to fluid such as viscosity, temperature coefficient of surface tension and thermal expansion coefficient. The effect of latent heat involved during the liquid to solid and solid to liquid phase transformations was considered in both the models. Table 4.4, documents all the material properties and their values used in the numerical models of this study.

Table 4.4 Material properties of IN625 used in numerical modelling

Material Property	**Value**	**Reference**
Liquidus temperature, T_L [K]	1623	(Arisoy et al., 2019; Wang et al., 2020)
Solidus temperature, T_S [K]	1563	
Density ρ [kg/m^3]	8440	
Specific heat, Cp [J/kg-K]	338.98 + 0.2437 T (for $T \leq T_S$) 735 for ($T \geq T_L$)	
Thermal conductivity, k [W/m-K]	5.331 + 0.0015 T (for $T \leq T_S$) 30.05 (for $T \geq T_L$)	
Latent heat of fusion, L [J/kg]	227×10^3	
Dynamic viscosity, μ [kg/ms]	0.006	(Wang et al., 2020)
Temperature coefficient of surface tension, $d\gamma/dT$ [N/(m-K)]	-2×10^{-5}	
Thermal expansion coefficient, β_T [1/K]	1.28×10^{-5}	

4.5 Results and discussion

A comparison of melt pool geometry, peak temperatures and cooling rates obtained from HCS and HCS-FD models was carried out. Further, predictions of melt pool geometry obtained from the two numerical models were compared with optical microscopy measurements of the melt pool geometry from the scanned tracks. Next, cooling rates and thermal gradients obtained from the two numerical models were interpreted as G×R and G/R using a solidification map to obtain inferences on grain morphology which was then compared with the grain morphology shown by SEM images.

4.5.1 Comparison of melt pool dimensions at different laser powers and scan speeds

Figure 4.6 shows the optical microscope images of the cross-section of the single laser tracks that were used for the measurement of melt pool width and depth at different laser powers and scan speeds. The melt pool width and depth obtained from the HCS, HCS-FD models as well as from the experimental measurements are plotted in Figure 4.7 and Figure 4.8 respectively. It can be observed from Figure 4.7 and Figure 4.8, that both melt pool width and depth increase with increase in laser power and decrease with increase in scan speed. As the laser power increases from 300 to 500 W, melt pool width increases (Figure 4.7). This increase can be attributed to the melting of more material along the width direction due to the increase in energy density. However, the decrease in melt pool width with increase in scan speed is not uniform i.e., there is a 24% decrease in melt pool width with increase in scan speed from 100 to 200 mm/s and a 14% decrease melt pool width with increase in scan speed from 200 to 300 mm/s. This non-uniform decrease in melt pool width with increase in scan speed can be attributed to the non-uniform decrease in energy density i.e., energy density decreases by 100% when scan speed increases from 100 to 200 mm/s while it decreases by 50% with increase in scan speed from 200 to 300 mm/s. The trends in melt pool depth results (Figure 4.8) are analogous to that of melt pool width. Results also indicate that melt pool depth is more sensitive than melt pool width to changes in energy density *i.e.*, depth decreases by 38% for a decrease in energy density by 100%, while it decreases by 12% for a 50% decrease in energy density. The increased sensitivity of melt pool depth to changes in energy density can also be attributed to strong surface tension driven Marangoni flow at high energy density. Influence of surface tension on the melt pool dimensions is discussed in the subsequent paragraphs.

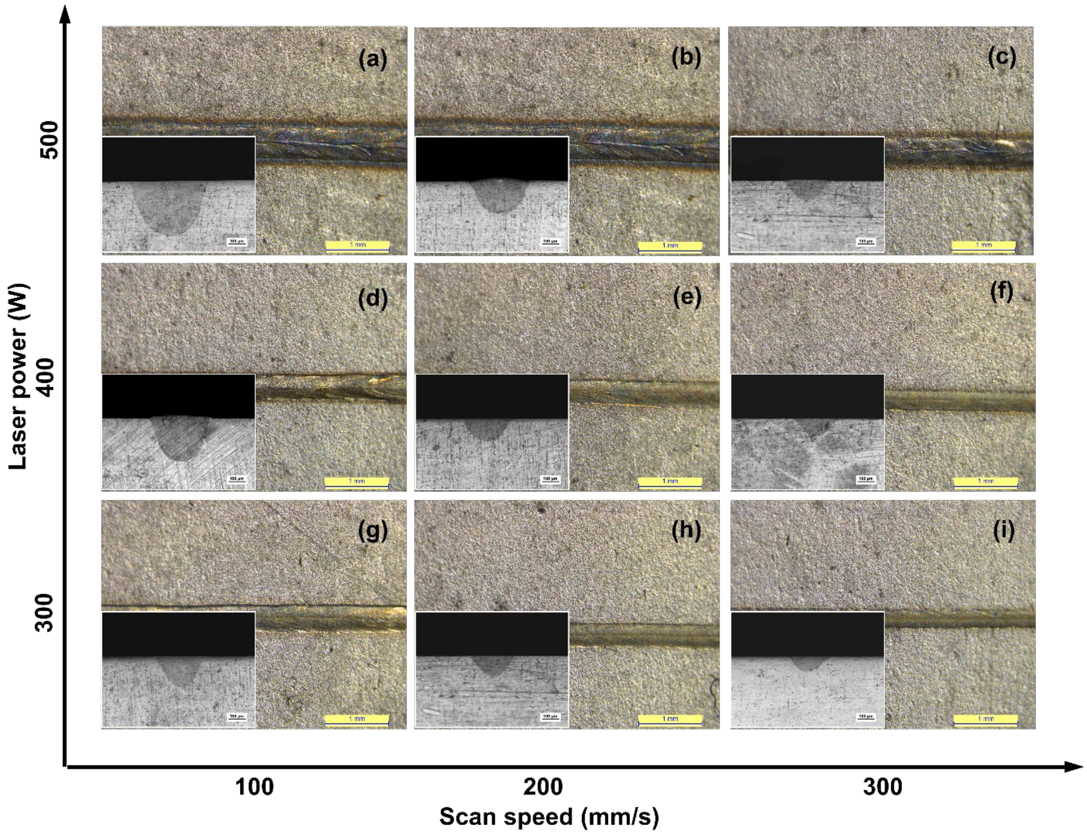

Figure 4.6 Cross-section of the single laser tracks at different laser powers and scan speeds

From the experimental results (Figure 4.6), it can also be observed that at high energy density (Figure 4.6 (a)), the melt pool is deep and narrow. While for low energy densities (Figure 4.6 (c), (f) and (i)) the melt pool is shallow and wide. These observations clearly demonstrate the influence of strong surface tension driven Marangoni's flow on melt pool shape and its dimensions. It has been reported in literature that a negative value of temperature coefficient of surface tension creates an outward flow resulting in a shallow and wide melt pool; while on the other hand a positive value of temperature coefficient of surface tension creates an inward flow resulting in a deeper and narrow melt pool (Fan et al., 2001; Zacharia et al., 1989).

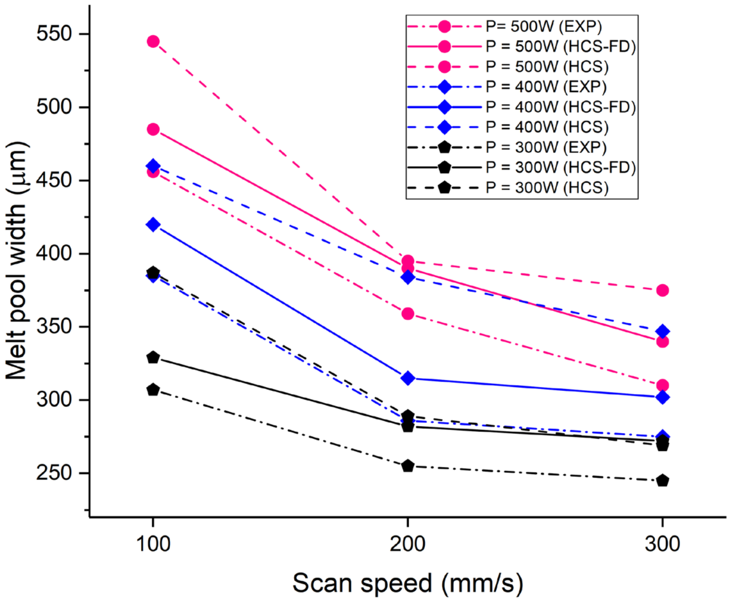

Figure 4.7. Comparison of experimentally measured melt pool width with predictions from HCS and HCS-FD models

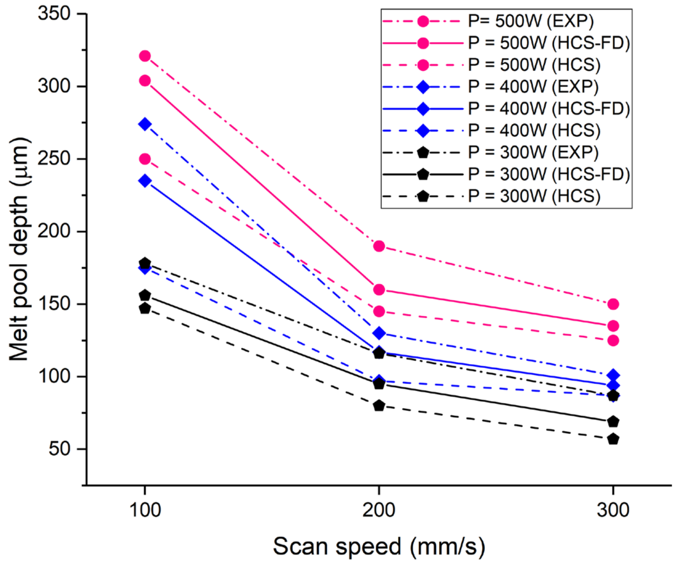

Figure 4.8. Comparison of experimentally measured melt pool depth with predictions from HCS and HCS-FD models

The melt pools at high energy densities (Figure 4.6 (a, d and g)) were found to be deep and narrow, indicating a positive value of temperature coefficient of surface tension. However, a negative value of temperature coefficient of surface tension has been reported in literature for IN625 (Wang et al., 2020). Further, it has also been reported that the presence of surface active elements such as oxygen and sulphur can alter the sign of temperature coefficient of surface tension from a negative to a positive value, thereby resulting in an inward flow (Lu et al., 2003; Wang et al., 2017a). Fig. 8, shows the comparison of the predicted melt pool shape at both negative and positive values of temperature coefficient of surface tension., The results of Figure 4.9 show that the negative value of temperature coefficient of surface tension has resulted in a shallow and wider melt pool; while a positive value of temperature coefficient of surface tension has resulted in a deep and narrow melt pool. Therefore, in the present study, a positive value of temperature coefficient of surface tension ($d\gamma/dT = 2\times10^{-5}$ N/m·K) has been considered for the numerical modelling of single laser tracks. Further, discussion on the surface tension driven Marangoni flow, its influence on the melt pool shape and peak temperatures is explained in subsequent sections.

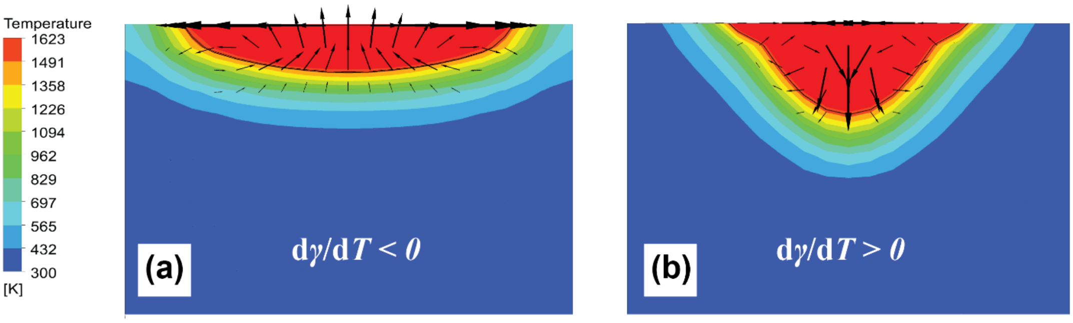

Figure 4.9. Melt pool shape predicted by the HCS-FD numerical model at a) negative value and b) positive value of temperature coefficient of surface tension

Results (Figure 4.7 & Figure 4.8) indicate that both the numerical models used in present work are overpredicting the melt pool dimensions. The average error in predictions from HCS-FD model (9 % error in melt pool width and 12 % error in melt pool depth) was lower when compared to average error in predictions obtained from HCS model (16 % error in melt pool width and 24 % error in melt pool depth). The error in predictions of both melt pool width and depth from the numerical models used herein are comparable to the error in predictions from similar numerical models used by other researchers for predicting melt pool geometry (Andreotta et al., 2017; de La

Batut et al., 2017; Paul et al., 2016). It can also be seen from Figure 4.7 and Figure 4.8 that the difference in the magnitude of the predictions made by the two numerical models is significantly large at high energy densities and less at low energy densities. This can be attributed to the fact that at high energy density, the temperature gradients are high in the melt pool resulting in significant change in surface tension from the melt pool to the solidification front leading to strong fluid flow within the melt pool. While for the cases with low energy density the temperature gradients are relatively lower and the magnitude of resulting fluid flow is also small. In summary, the predictions of numerical models which consider fluid flow (HCS-FD model) are found to be more accurate than that of HCS model. However, at low energy density, where fluid flow is not significant, the difference in magnitude of the predictions between the two numerical models is also small. Similar results have also been reported in literature (Lampa et al., 1997).

Figure 4.10 shows side by side comparison of the melt pool shape obtained from optical microscope images with the melt pool shape predicted from a) HCS-FD model and b) HCS model at a laser power of 500 W and scan speed of 100 mm/s. The visual comparison between the two images, *i.e.* Figure 4.10 (a) and (b), reveals that the melt pool shape predicted by HCS-FD model is comparable with the shape of melt pool obtained experimentally which is deep and narrow.

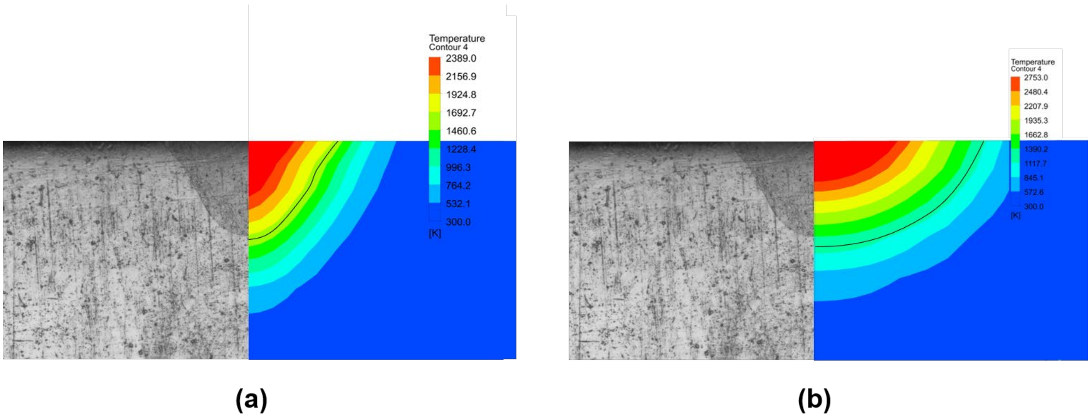

Figure 4.10. Side by side comparison of the cross section of the melt pool obtained from optical microscope images with a) HCS-FD model and b) HCS model at 500 W laser power and 100 mm/s scan speed

This can be attributed to convective fluid flow occurring due to the spatial variation of surface tension in the melt pool. These results (Figure 4.10) clearly demonstrate the importance of considering fluid dynamics while predicting melt pool geometry.

4.5.2 Peak temperatures and velocity fields

The results of Figure 4.11 indicate that the HCS model is overpredicting temperatures in particular at high values of energy density. This over prediction of the peak temperatures by the HCS model will result in inaccuracy in the prediction of cooling rates and temperature gradients in addition to inaccuracy in the prediction of melt geometry as discussed in the previous section (Mukherjee et al., 2018). Figure 4.12 shows the predicted velocity vectors from HCS-FD model at a laser power of 500W and scan speed of 100 mm/s. It can be observed that the liquid metal in the melt pool has an inward flow pattern with a maximum velocity of 0.7 m/s. This inward flow pattern as shown in Figure 4.12 is a clear effect of the surface tension driven Marangoni flow. Similar trends of velocity vectors were reported in literature (Burgardt and Heiple, 1986; Debroy, 1996; He et al., 2005; Kou, 2003). The inward flow behaviour in the melt pool can be attributed to the spatial variation of the surface tension due to large temperature gradients within the melt pool. The low value of surface tension associated with cooler liquid metal near the solidification front of the melt pool and high value of surface tension of the hotter liquid metal at the centre of melt pool create a strong shear stress which results in an inward pull of the liquid metal as shown in Figure 4.12. This inward flow pattern in the melt pool favours convective heat transfer from the surface through the depth of the melt pool resulting in a deep and narrow pool, as discussed prior in section (Kou, 2003).

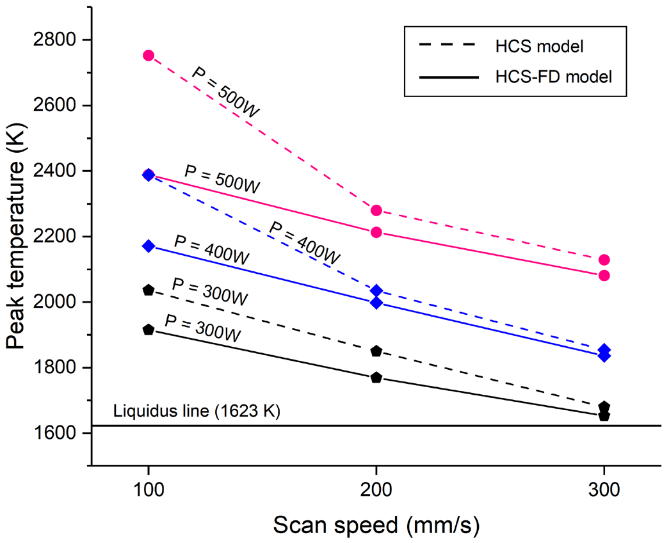

Figure 4.11. Comparison of peak temperatures obtained from HCS and HCS-FD models at different laser powers and scan speeds

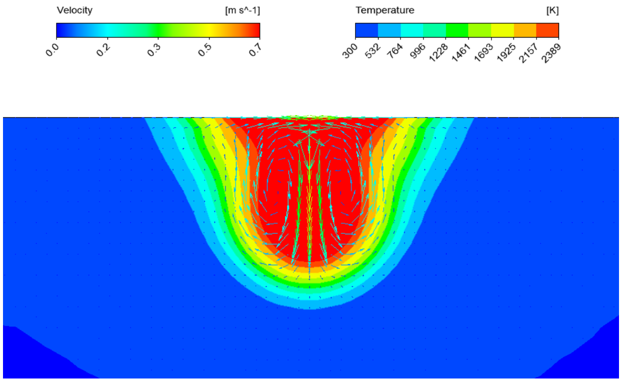

Figure 4.12. Calculated velocity fields from the HCS-FD model at a laser power of 500 W and scan speed of 100 mm/s

4.5.3 Solidification characteristics

The changes in the solidification parameters G×R (cooling rate) and G/R, were evaluated from both the numerical models and were corelated with dendrite size and morphology obtained from microscopy measurements. Figure 4.13 shows the predicted cooling rate (G×R) at the surface of the melt pool obtained from both the numerical models at different scan speeds and at a laser power of 500 W. It can be seen that cooling rate increases from 29407 K/s to 104588 K/s with increase of scan speed from 100 to

300 mm/s. The magnitude of predicted cooling rates from the HCS model were found to be less than that of HCS-FD model. This can be attributed to the higher peak temperatures predicted in the melt pool by the HCS model.

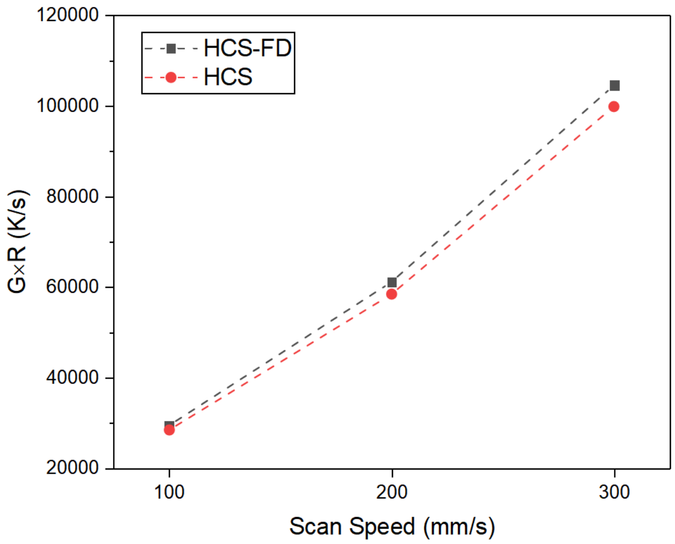

Figure 4.13. Predicted cooling rate at different scan speeds and at constant laser power of 500 W

Figure 4.14 (a), (b) and (c) show SEM images of the cross section of the single laser tracks at a laser power of 500 W and at scan speeds of 100, 200 and 300 mm/s respectively. Table 4.5 presents the comparison of the experimentally measured dendrite size from Figure 4.14 (a), (b) and (c) and the predicted dendrite size using the HCS-FD and HCS models. The images of Figure 4.14 and the results of Table 4.5 clearly show that dendrite size decreases with increase in scan speed due to increased cooling rates.

The predictions of microstructure from the numerical models were made by plotting the data of thermal gradient (G) and solidification velocity (R) (ratio of cooling rate to thermal gradient) obtained from the two numerical models on a solidification map (Figure 4.15). The solidification maps of Figure 4.15 shows a fine microstructure for a high value of GR (cooling rate) and a coarse microstructure for a low value of GR in agreement with SEM images presented at different scan speeds (Figure 4.14). Further dendrite sizes were computed using the analytical relationship as

$$d = a(\varepsilon^{-n}) \quad (4.13)$$

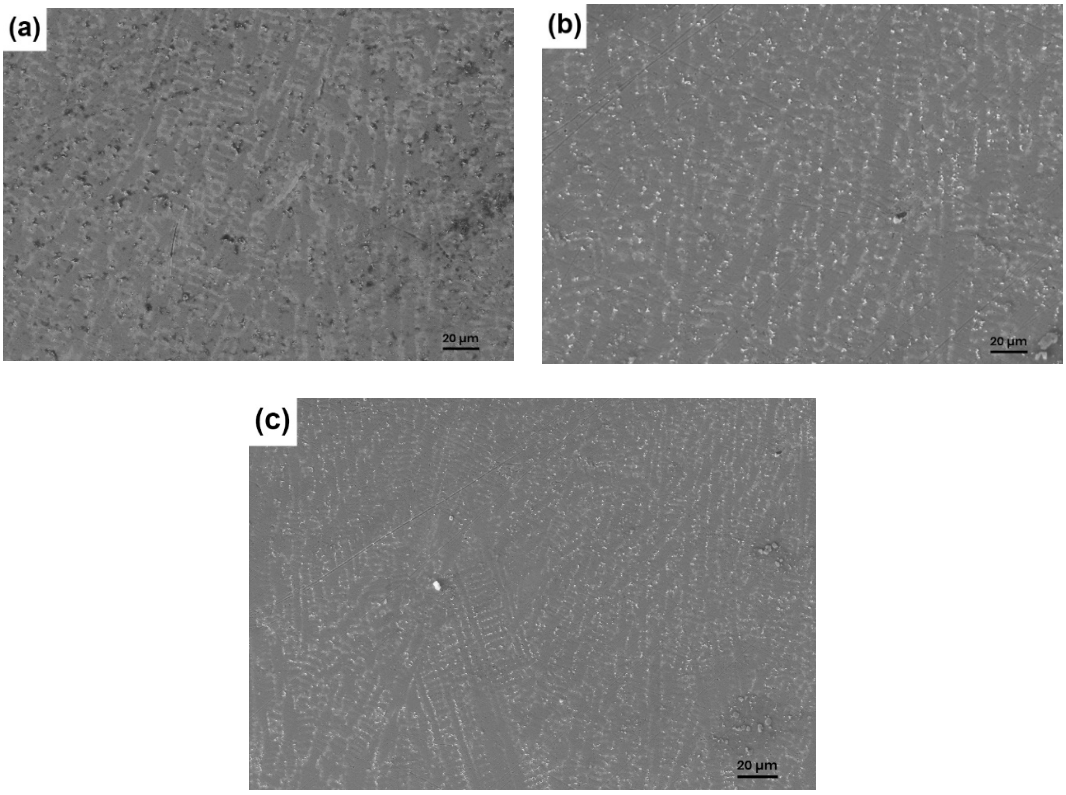

Figure 4.14. SEM Micrographs obtained at laser power of 500 W and scan speeds of (a) 100 mm/s, (b) 200 mm/s and (c) 300 mm/s

where, *d* is the secondary dendrite arm spacing (µm), ε is the cooling rate (Ks^{-1}), *a* and *n* are the fitting constants, which are taken from the literature as 79 and 0.3 respectively (Shao et al., 2019). In equation 4.13, the cooling rates are the inputs from the two numerical models.

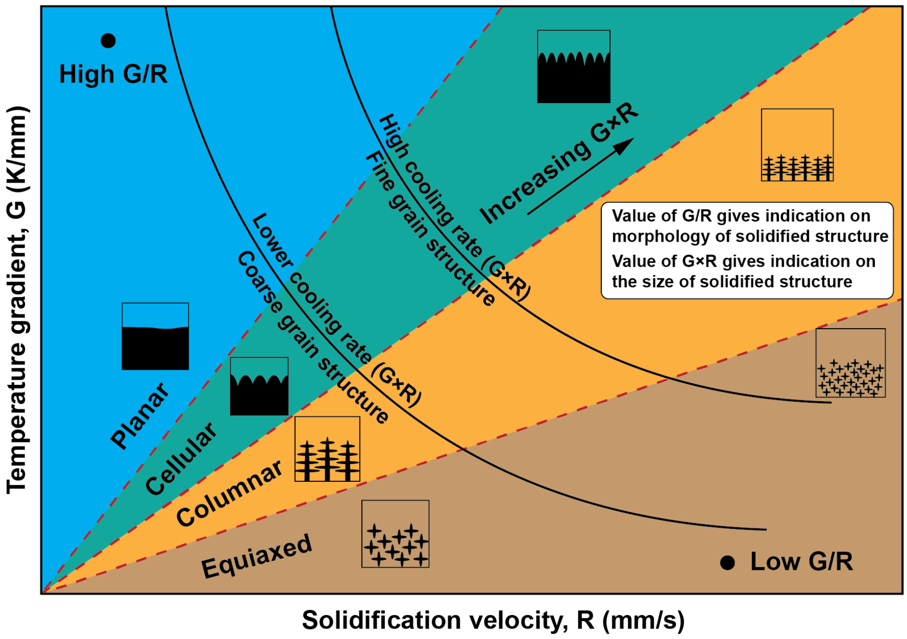
High G/R
Increasing G×R
High cooling rate (G×R)
Fine grain structure
Lower cooling rate (G×R)
Coarse grain structure
Value of G/R gives indication on morphology of solidified structure
Value of G×R gives indication on the size of solidified structure
Planar
Cellular
Columnar
Equiaxed
Low G/R
Temperature gradient, G (K/mm)
Solidification velocity, R (mm/s)

Figure 4.15. Effect of temperature gradient (G) and solidification velocity (R) on the grain size and morphology (Partly reproduced from, Kumara et al., 2019)

Table 4.5 presents the comparison of the experimentally measured dendrite size from Figure 4.14 (a), (b) and (c) and the predicted dendrite size by the HCS-FD and HCS models. The results of Table 4.5 indicates that there is no significant difference in the predictions of dendrite size from the two numerical models. Further, the predictions from both the HCS and HCS-FD models are reasonably close to the experimentally measured dendrite size. It can hence be concluded that solidification characteristics are not significantly affected by the consideration of fluid dynamics in the melt pool (Ghosh et al., 2018).

Table 4.5. Comparison of the experimentally measured dendrite size with the predictions from HCS-FD and HCS models at different scan speeds.

Laser power (W)	**Scan speed (mm/s)**	**Dendrite size (μm)**		
		Experimentally measured	**HCS-FD model**	**HCS model**
500	100	3.9	3.61	3.65
500	200	3.1	2.9	2.94
500	300	2.6	2.46	2.5

To enable predictions on grain morphology using data from the numerical models, cooling rates and thermal gradients were calculated through the depth of the melt pool. Figure 4.16, shows the change of solidification parameters (G×R and G/R) through the depth of the melt pool (presented in normalized form as h/h_{max}) at a laser power of 500 W and at a scan speed of 100 mm/s. It can be observed from Figure 4.16 that G/R increases while G×R (cooling rate) decreases with increase of melt pool depth. Figure 4.17 shows the microstructure at a laser power of 500 W and at a scan speed of 100 mm/s at two different locations (referred to as 1 and 2) through the depth of melt pool (Figure 4.17 (a)). The micrograph of Figure 4.17 (b) reveals equiaxed dendritic morphology near the surface (location -1) of the molten pool. The results of Figure 4.16 indicate low G/R value near the surface of the molten pool. The solidification map (Figure 4.15) predicts an equiaxed dendritic morphology for a low value of G/R in agreement with experimental observations (Figure 4.17(b)).

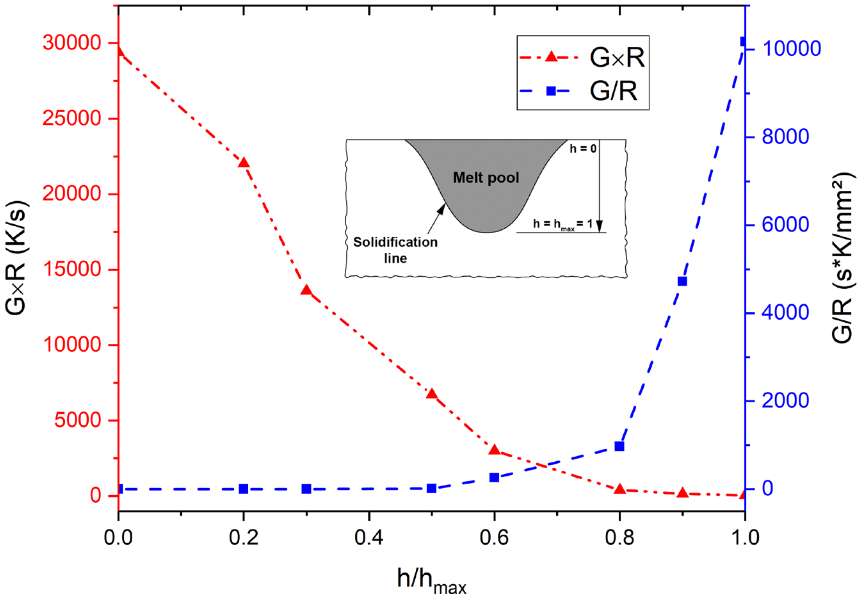

Figure 4.16. Numerically predicted cooling rate (G×R) and G/R from HCS-FD model at the traverse section

The regions close to the bottom of the melt pool (location - 2) resemble a planar front morphology (Figure 4.17(c)). From Fig. 15 a high value of G/R can be observed at the bottom of the melt pool ($h/h_{max}= \sim 1$). The solidification map predicts a planar front for a high value of G/R. These results indicate the agreement of numerical modelling predictions of grain morphology with experimental observations. Similar results for solidification characteristics were observed by (Shao et al., 2019) and (Geng et al., 2020).

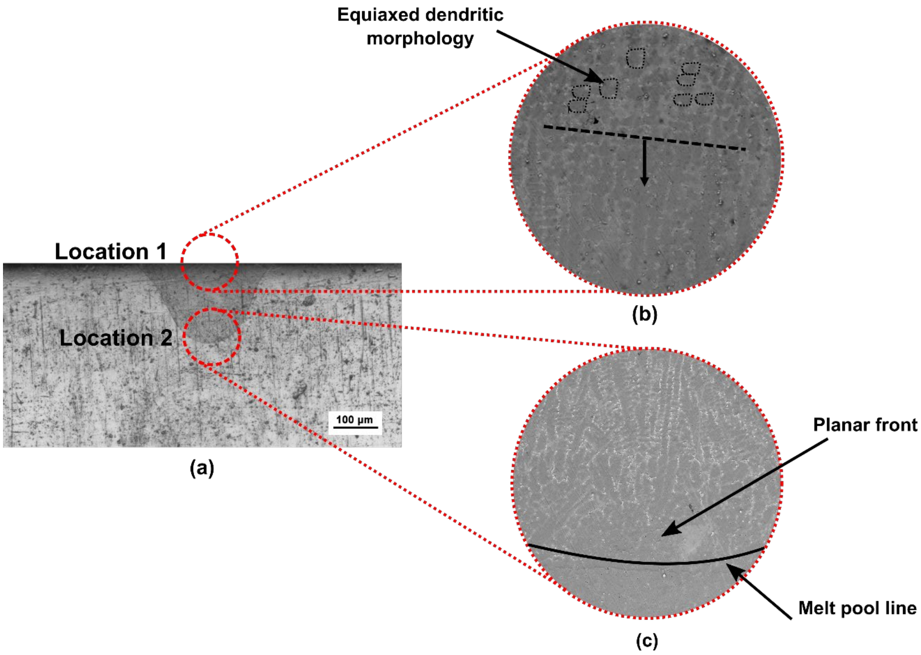

Figure 4.17. Experimentally obtained transverse section of (a) scanned track and microstructure at locations (b) 1 and (c) 2

4.6 Conclusions

A comparison of the finite volume based numerical models for the simulation of single laser track scans with and without fluid dynamics was carried out. Results obtained from both the numerical models were compared with the experimental observations. The outcome of the study clearly demonstrates the importance of considering fluid flow during laser processing. Numerical models considering only heat conduction equation have been found to over predict the peak temperature in the melt pool. The average error in predictions from HCS-FD model (9 % error in melt pool width and 12 % error in melt pool depth) was lower when compared to average error in predictions obtained from HCS model (16 % error in melt pool width and 24 % error in melt pool depth). Surface tension gradient driven Marangoni flow is found to have significant effect on the predicted melt pool shape and dimensions. A negative value of temperature coefficient of surface tension is found to result in a shallow and wider pool, while on the other hand a positive value of temperature coefficient of surface tension results in a deep and narrow melt pool. G×R and G/R predicted from the numerical models were interpreted using a solidification map to make inferences on the morphology and the size of the solidified structure. Effect of the solidification characteristics through the depth of melt pool was also observed. At regions near the top surface, of the melt pool where G/R is lower, grain morphology was observed to be equiaxed dendritic, which changes to planar front at the bottom where G/R is higher. The results of this work indicate that solidification characteristics are not significantly influenced by the consideration of fluid dynamics effects in the numerical models. However, this work clearly shows the importance of considering fluid dynamics for accurately predicting melt pool shape and dimensions.

CHAPTER 5
SINGLE-TRACK DEPOSITION USING LDED PROCESS

The objective of this study is to establish a numerical model to predict the single-track dimensions during LDED process on IN625. To this end, nine well separated single tracks of IN625 on a substrate of same material were deposited using LDED process at different laser power and scan speed combinations. Using a finite element-based approach, the track dimensions (track width and height) were predicted and validated with the experimental results. Detailed discussion on the methodology and results is presented in the subsequent sections.

5.1 Materials and methodology

5.1.1 Materials

Ni based superalloy, IN625 is a material with excellent corrosion resistance, high strength and excellent fabricability and weldability (Special Metals Corp., 2013). The high service temperature (ranging from the cryogenics to 982 *°C*), high corrosion fatigue offered by IN625 makes this alloy a perfect candidate for aerospace, marine and chemical industries (Shoemaker, 2012). The presence of chromium as an alloying element (20-23 %) in nickel imparts an excellent corrosion resistance to the matrix while the combination of two other major alloying elements molybdenum (8 %) and niobium (5 % to 4 %) adds additional stiffness to the Ni-Cr matrix. Commercially available IN625 alloy powder was used to deposit the single track on the substrate of same alloy.

5.1.2 Experimental setup

The experiments were carried out on an indigenously developed LDED system (Figure 5.1) is deployed in the present study. More details of the setup can be found in section 3.1.1 Nine well separated single tracks, each 20 mm long, were deposited on a $100\times100\times6$ mm^3 IN625 substrate at different laser powers and scan speeds listed in Table 5.1. The substrate was properly cleaned with acetone and dried prior to the deposition. For characterization, samples were sectioned using Wire-EDM process and taken further for standard metallographic preparations. Subsequently, the samples were electrolytically etched using a 10 gm Oxalic acid in 100 ml distilled water at a potential difference of 12 V for 10-15 seconds. These samples were than studied under Optical Microscope (OM) followed by scanning electron microscopy (SEM). Using an open-source image analyser software ImageJ, SEM images were analysed to measure deposited track height, width and heat affected zone (HAZ).

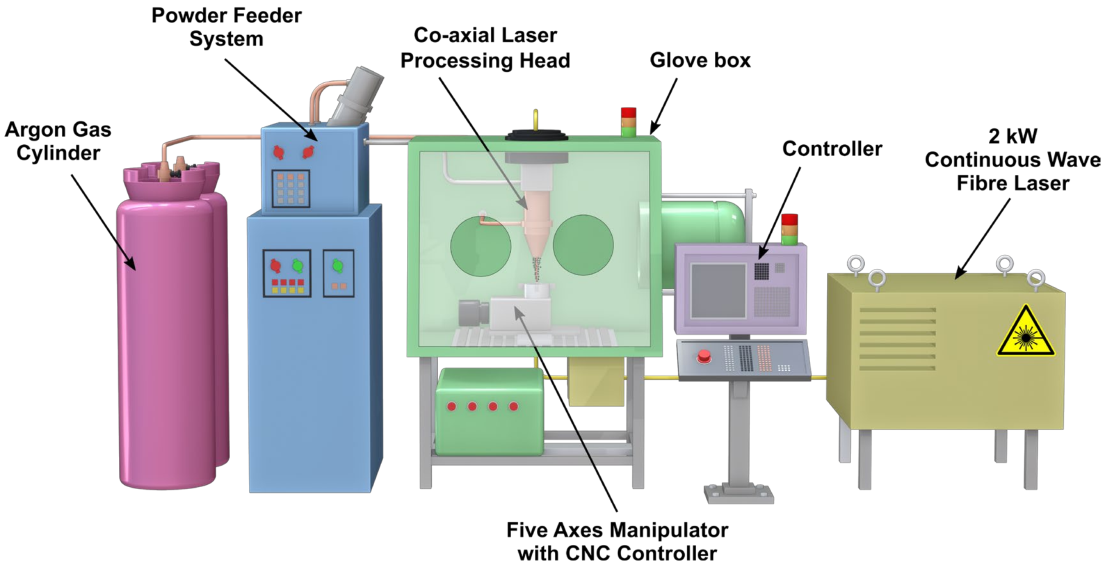
Powder Feeder System
Co-axial Laser Processing Head
Glove box
Argon Gas Cylinder
Controller
2 kW Continuous Wave Fibre Laser
Five Axes Manipulator with CNC Controller

Figure 5.1 Schematic of the LDED setup used at RRCAT, Indore for experimentation

Table 5.1 Combination of the laser power and scan speeds used for the experimentation

Case No.	Laser Power (W)	Scan speed (m/min)
(a)	600	0.4
(b)	600	0.6
(c)	600	0.8
(d)	900	0.4
(e)	900	0.6
(f)	900	0.8
(g)	1200	0.4
(h)	1200	0.6
(i)	1200	0.8

5.2 Numerical modelling description and approach

In this work, a two-dimensional transient thermal finite element model was established to predict the single-track dimensions of IN625 alloy during deposition using LDED process. The simulations were performed using a commercial finite element package ANSYS, where 4 node PLANE 13 elements were used to capture the thermal response. The relevant governing equations, boundary conditions, simplifications and material properties used are as follows:

5.2.1 Assumptions

1. Material properties such as density, specific heat and thermal conductivity are temperature dependent (Hernando et al., 2018). The variation of materials properties with temperature are shown in Figure 5.4

2. The effect of latent heat of fusion is incorporated in the model by modifying the specific heat capacity of the metal at melting point.

3. Marangoni phenomenon during melting is considered by modifying ($k_{\text{modified}} = 2.5\times k$ for $T > T_m$) the thermal conductivity of the metal for all temperatures above melting point in a particular direction. (Kumar et al., 2012; Lampa et al., 1997).

5.2.2 Governing equation

The finite element model solves a two-dimensional general heat transfer equation on the finite domain given as,

$$\frac{\partial(\rho C_p T)}{\partial t} - \nabla.(k \nabla T) = 0 \tag{5.1}$$

where, ρ = density of the material (kg/m^3) and C_p = specific heat (J/Kg-K), k = thermal conductivity (W/m-K), T = temperature of the body at the instance time t (K).

The process is modeled by using Eularian approach in which a specific location in the domain is considered to solve the equations and the corresponding boundary conditions are expressed as:

$$\begin{aligned} -K(\nabla T.n)\big|_{\Omega} &= [\alpha \cdot I(x,z,u) - h_c(T-T_0)]_{\Omega} \quad \text{if } \Omega \in \Gamma \\ &= [-h_c(T-T_0)]_{\Omega} \qquad\qquad\quad \text{if } \Omega \notin \Gamma \end{aligned} \tag{5.2}$$

Where n is the normal vector to the surface, β_e is the effective energy absorption factor, I (W/m^2) is laser energy distribution per unit length perpendicular to the cross-section of workpiece, u (m/s) is scan speed or the traverse velocity of laser beam perpendicular to the cross-section of the workpiece, h_c is heat convection coefficient (W/m^2·K), Ω (m^2) is the area of unit length workpiece surface, Γ (m^2) is the area of unit length workpiece surface where laser beam is irradiated, T_0 is the ambient temperature. The initial condition of the model was set to room temperature given as,

$$T\ (x,\ y,\ t)\big|_{t=0} = 25°C \tag{5.3}$$

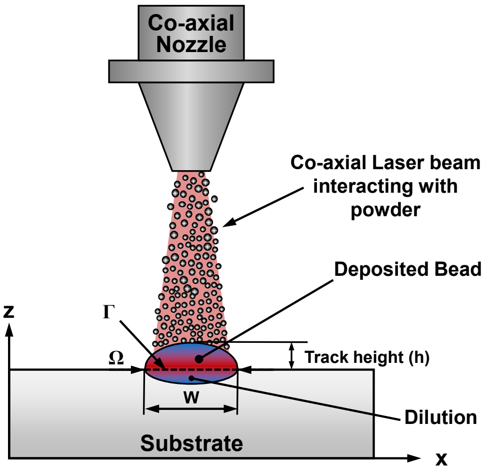

Figure 5.2. Schematic of laser directed energy deposition process and related terms.

5.2.3 Boundary conditions

For the simplification of laser additive manufacturing process, the proposed model assumes several assumptions. Following are the boundary conditions and related simplification/assumptions considered in the numerical model.

5.2.3.1 Combined heat transfer

To account for both convective and radiation heat transfer, a combined heat transfer coefficient (Yang et al., 2001) given in equation (5.4) has been used in the model. The purpose to combine both convective and radiation heat transfer is to simplify the problem and to reduce computation time.

$$h = 24.1\times 10^{-4} \times \varepsilon_t \times T^{1.61} \tag{5.4}$$

5.2.3.2 Laser energy density

The energy density of the laser beam is assumed to have a gaussian distribution, as shown in Figure 5.3. The intensity profile for the laser beam is given by (Kumar et al., 2012) as:

$$I_l(r) = \frac{2P_l}{\pi r_l^2} \exp\left[-\frac{2r^2}{r_l^2}\right] \tag{5.5}$$

Where r_l is the radius of the Gaussian beam component, r is the distance from the centre of the laser beam, and P_l is the laser average power.

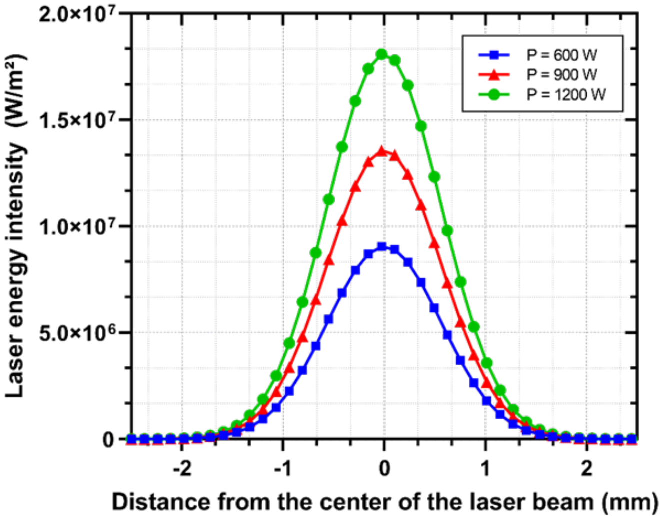

Figure 5.3 Laser beam distribution used in present study

5.2.3.3 Absorption Coefficient (*α*)

A part of the emitted power is absorbed by the substrate during the process. These losses are taken into account by providing a factor called absorption coefficient (Gedda, 2004). In present study, the absorption coefficient is considered to be as 0.3.

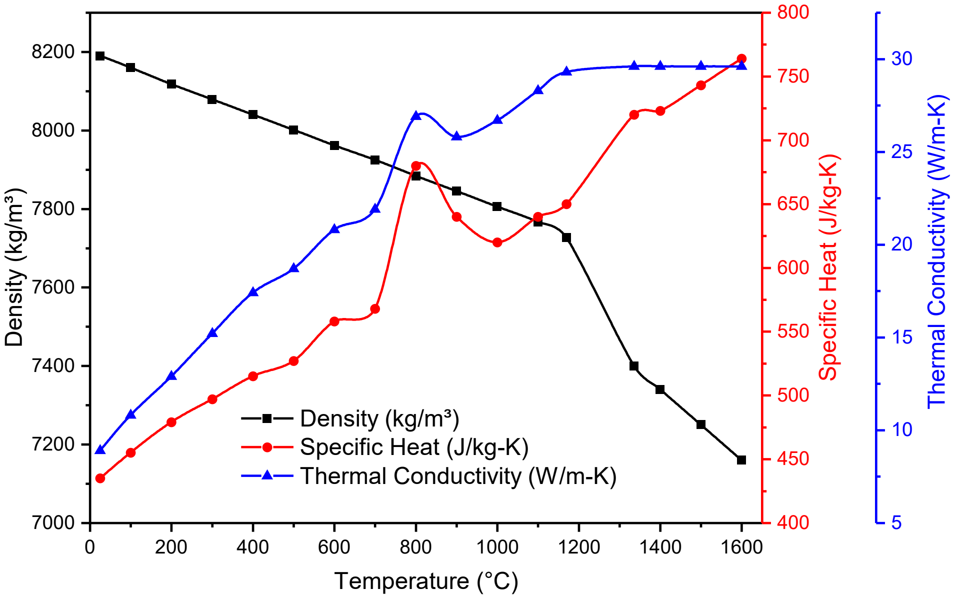

Figure 5.4 Thermo-physical properties of IN625 used in present study (Hernando et al., 2018)

5.2.4 Material properties

Material properties used in the present modelling approach considers temperature-dependent material properties. Figure 5.4, shows the temperature-dependent material properties for IN625 alloys used in numerical model.

5.2.5 Enthalpy approach

The enthalpy approach used in present study is based on the element birth and death technique of finite element methods. The process of solution in the numerical model is a two-way process. First, the numerical model is solved for a thermal solution which is used to obtain the melt pool dimensions. Secondly, to incorporate addition of material into the model, enthalpy is calculated at the nodal points interacting with the laser.

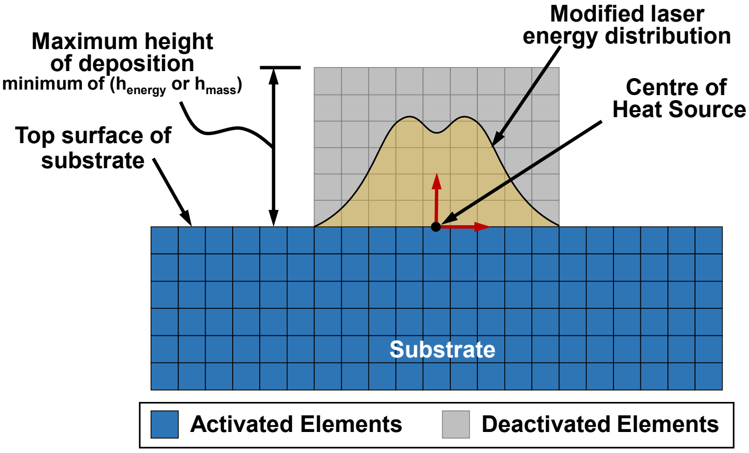
Maximum height of deposition
minimum of (h_{energy} or h_{mass})
Modified laser energy distribution
Centre of Heat Source
Top surface of substrate
Substrate
Activated Elements
Deactivated Elements

Figure 5.5 Schematic of the model used for numerical modelling

5.2.5.1 Step 1: Determination of melt pool geometry and calculation of excess enthalpy

Using the finite element approach the numerical model was solved and the dimensions of the melt pool were obtained. To compute the available enthalpy, calculations were performed on the nodes on the top surface of substrate interacting with the heat source. Subsequently, the obtained enthalpy at the nodes were compared with the enthalpy of material at melting point. This difference of enthalpy of top nodes and the enthalpy of material at melting, represents the excess energy available and is carried forward to the second step. Once the enthalpy at all the nodes were obtained, maximum track height based on both energy and mass balance was also calculated using equation (5.6) and (5.7). The localised height calculated as $h_{energy}(x)$ for all the nodes was calculated considering the energy balance of the molten pool available beneath those nodes.

$$h_{energy}(x) = \frac{h_{melt}(x)\rho_w\left(C_P(T(x)-T_m)+L_f\right)}{\rho_{jet}\left(C_{PP}(T_{mp}-T_i(x))+L_{fp}\right)} \tag{5.6}$$

$$h_{mass}(x) = \frac{\eta \dot{m} \Delta t}{A_{jet}^{melt}\rho_p} \tag{5.7}$$

Similarly, the height at all nodes was calculated, while accounting for the powder flow rate. To calculate the maximum height of deposit, while considering the mass balance a mathematical expression obtained from literature (Toyserkani et al., 2004) was used. For the purposes of modelling, minimum of the two heights *i.e.,* h_{energy} and h_{mass} was considered. Figure 5.5 shows the schematic of numerical model used in the study.

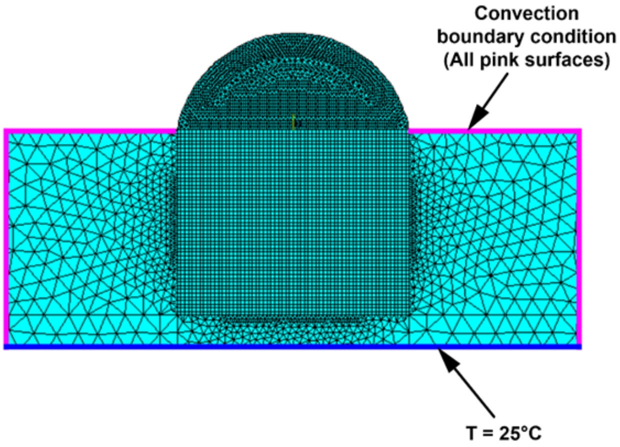

Figure 5.6 Meshed model used in present study

5.2.5.2 Step 2: Addition of material

To incorporate the addition of material in the finite element model, present study uses element death and birth technique. This technique allows the user to conditionally activate the elements in a finite domain. In this step, the height of deposition calculated in the previous step was initially set to dead state, *i.e.,* the deposition layer is actually present in the model, but will not participate during the solution stage. Figure 5.7 shows the process of activation and deactivation used in the present model. After the first-time step of the thermal analysis, the elements were activated based on the difference of enthalpy at the local node and the enthalpy of material at melting temperature.

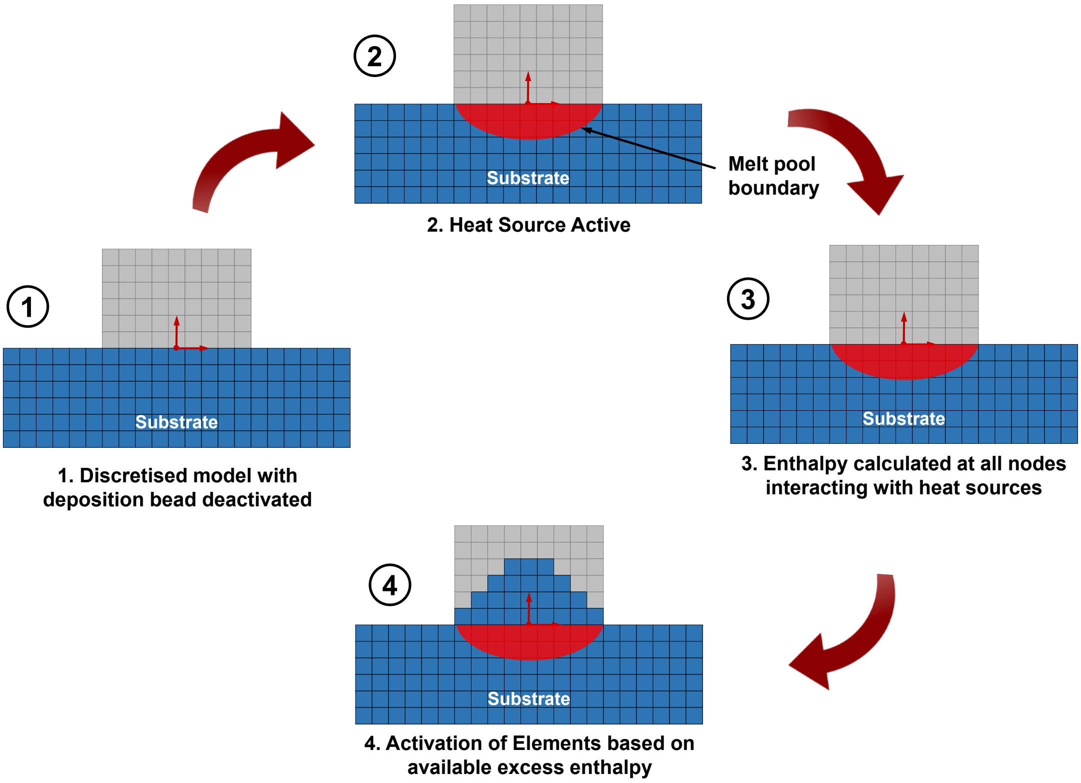
②
Substrate
2. Heat Source Active
Melt pool boundary
①
Substrate
1. Discretised model with deposition bead deactivated
③
Substrate
3. Enthalpy calculated at all nodes interacting with heat sources
④
Substrate
4. Activation of Elements based on available excess enthalpy

Figure 5.7 Process of element death and birth to obtain the bead shape

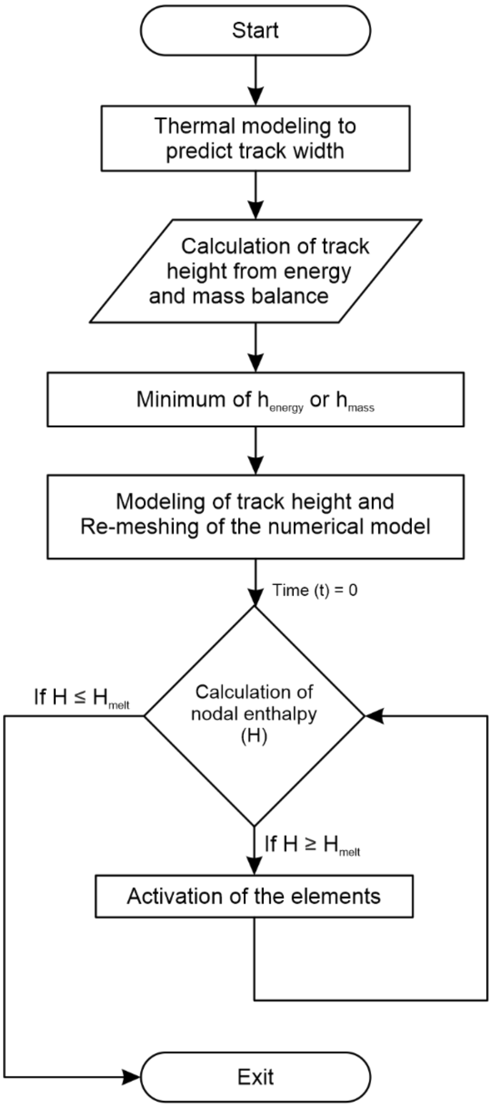
Start
Thermal modeling to predict track width
Calculation of track height from energy and mass balance
Minimum of h_{energy} or h_{mass}
Modeling of track height and Re-meshing of the numerical model
Time (t) = 0
Calculation of nodal enthalpy (H)
If $H \leq H_{melt}$
If $H \geq H_{melt}$
Activation of the elements
Exit

Figure 5.8 Flowchart of the process of element activation to predict the deposited track dimensions

5.3 Results and discussion

5.3.1 Track Geometry: Experimental observations

A total of nine single tracks were deposited using LDED to investigate the effect of processing parameters such as laser power and scan speeds on the deposited single-track geometry. Fig. 4 shows the macroscopic top view of the deposited single track at different laser powers and scan speeds, and their respective experiment number. The laser power and scan speed used for a particular experiment can be referred from table1.

Macro-examination of the deposited tracks reveals balling effect at lowest laser power (600W) and highest scan speed (0.8 m/min), which is due to the insufficient energy at the substrate to melt the powder. Moreover, the track (a), (b) and (f) are also found to have significant variation in the width along the track length as shown in Figure 5.9 and Figure 5.10 The cross-sectional SEM images of the single tracks is shown in Figure 5.11, it can be observed that the case (a) found to have un-melted power particles while some blow holes on the free surface in case (b). Other remarks observed from the OM and SEM images are listed in Table 5.2. Depositions at higher power (1200W) were found sound with consistent build throughout the track length (Figure 5.10 (g), (h) and (i)).

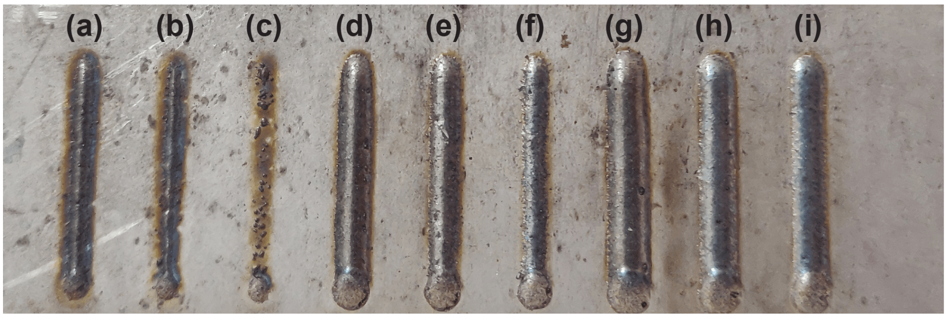

Figure 5.9. Single track of Inconel 625 deposited at different process parameters using LDED process

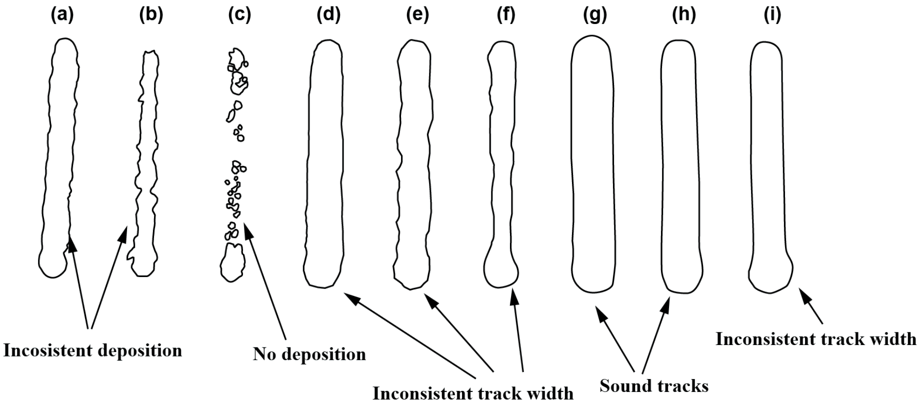
(a)
(b)
(c)
(d)
(e)
(f)
(g)
(h)
(i)
Incosistent deposition
No deposition
Inconsistent track width
Sound tracks
Inconsistent track width

Figure 5.10 Outline of the single tracks deposited at different laser powers and scan speeds

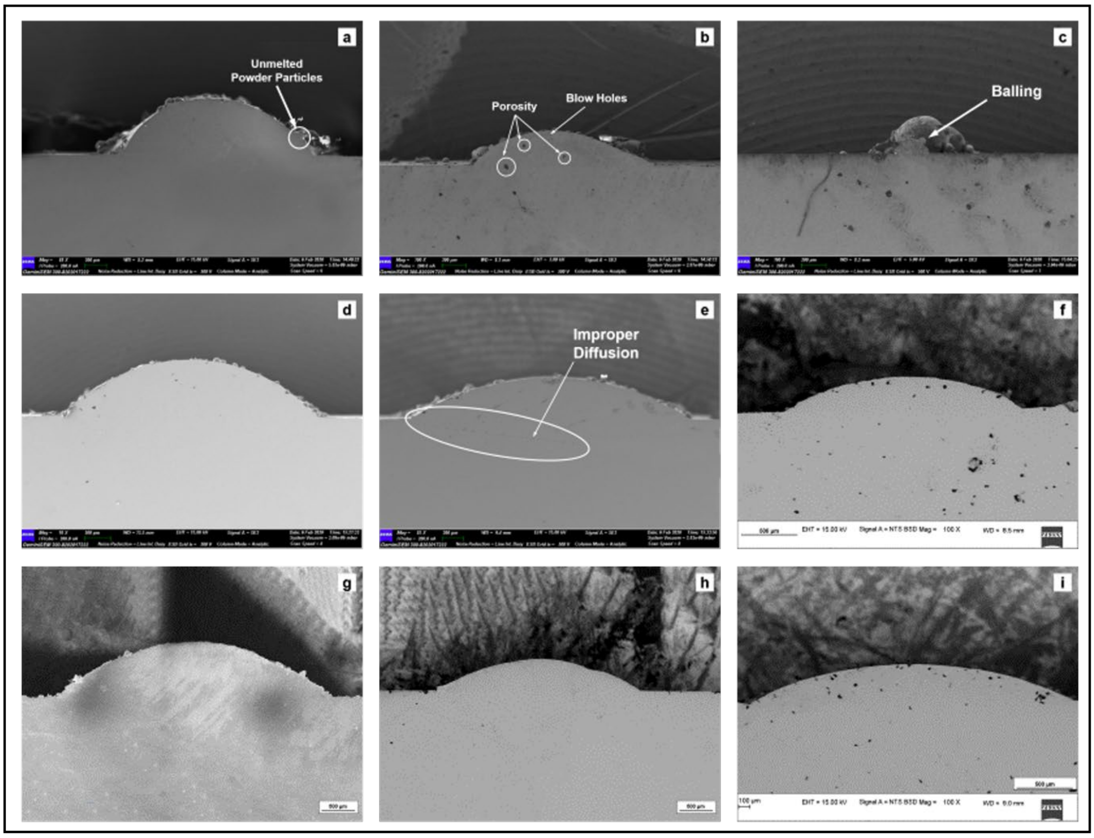
a
Unmelted Powder Particles
b
Porosity
Blow Holes
c
Balling
d
e
Improper Diffusion
f
g
h
i

Figure 5.11 SEM images showing cross-section of the single tracks deposition at different laser powers and scan speeds

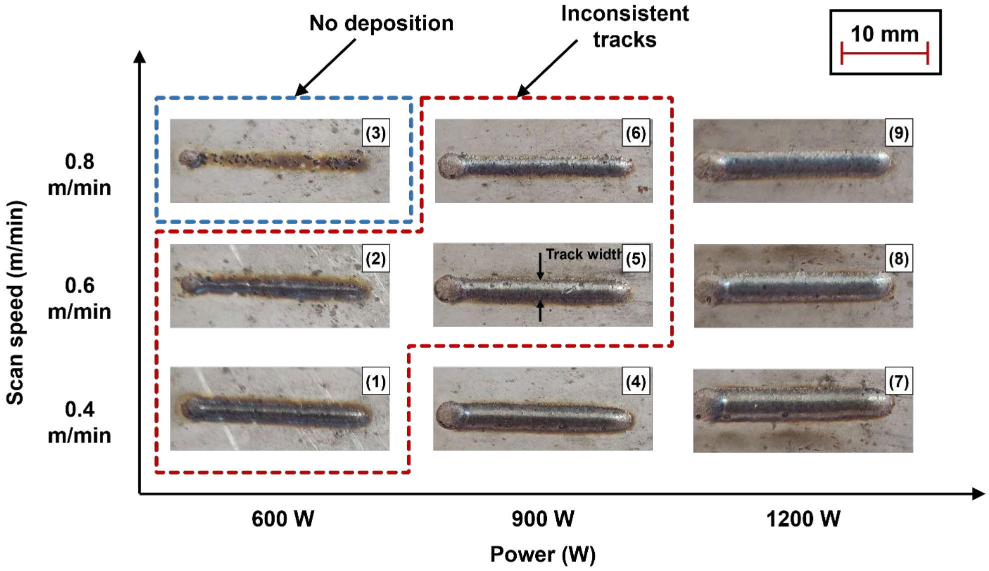
No deposition
Inconsistent tracks
10 mm
(3)
(6)
(9)
0.8 m/min
(2)
Track widt
(5)
(8)
0.6 m/min
(1)
(4)
(7)
0.4 m/min
Scan speed (m/min)
600 W
900 W
1200 W
Power (W)

Figure 5.12 Topography of the single track deposited on IN625 substrate at different processing conditions

Table 5.2 Experimental observation of the deposited tracks at different laser powers and scan speeds

Track No.	Laser Power	Scan speed	Track height	Track width	Remarks
	(*W*)	(*m/min*)	(*µm*)	(*µm*)	
1	600	0.4	530	1842	Line track with discontinues deposition
2	600	0.6	280	1495	Line track with no deposition
3	600	0.8	-	-	Line track with no deposition
4	900	0.4	668	2962	Continuous deposition with un-melted particles on the surface
5	900	0.6	386	2667	Continuous deposition with series of porosity at the junction of dilution
6	900	0.8	295	2097	Continuous deposition with inconsistent deposit width and high porosity
7	1200	0.4	733	3613	Continuous deposition
8	1200	0.6	490	3303	Continuous deposition
9	1200	0.8	354	2852	Continuous deposition

5.3.2 Prediction of track geometry using enthalpy approach

Figure 5.13, show the predicted track geometry using the enthalpy approach. The dimensions of the tracks are tabulated and their deviation from the experimental values were calculated. In Figure 5.13, the pool boundary is shown as the solidus temperature contour at 1563 K, the mushy zone is the small orange zone beneath the red zone with temperatures between solidus and liquidus (1623 K) temperatures and the fusion zone of the deposit is shown in red contour with temperature above 1623 K. The bead shape obtained follows similar trend from the experimental results as shown in Figure 5.14. It can be observed from Figure 5.13 (c), that at the low power and high scanning speed the predicted shape of the track is very small which is due to the reason of less interaction time available between the laser – powder particle and substrate. This is at par with the experimental observations.

The range of the percentage error predicted by the numerical model lies between 3 – 7 % in the track height and 7–13 % in the track width against the experimental values were observed. It was also observed that the track width changes linearly with the increase in the scan speed and for all the power considered in this study. Similar trends are observed from the prediction of the track width. At constant laser power (1200 W) and different scan speeds, the change in the track height was ~40% while track width was changed by 8%. Similarly, at constant scan speed (600 mm/min) and different laser power, the track height changes with a margin of 24 % while the track width changes 21%. These observations indicate that the track height is more influenced by the scan speed, while the track width is mainly affected by the laser power.

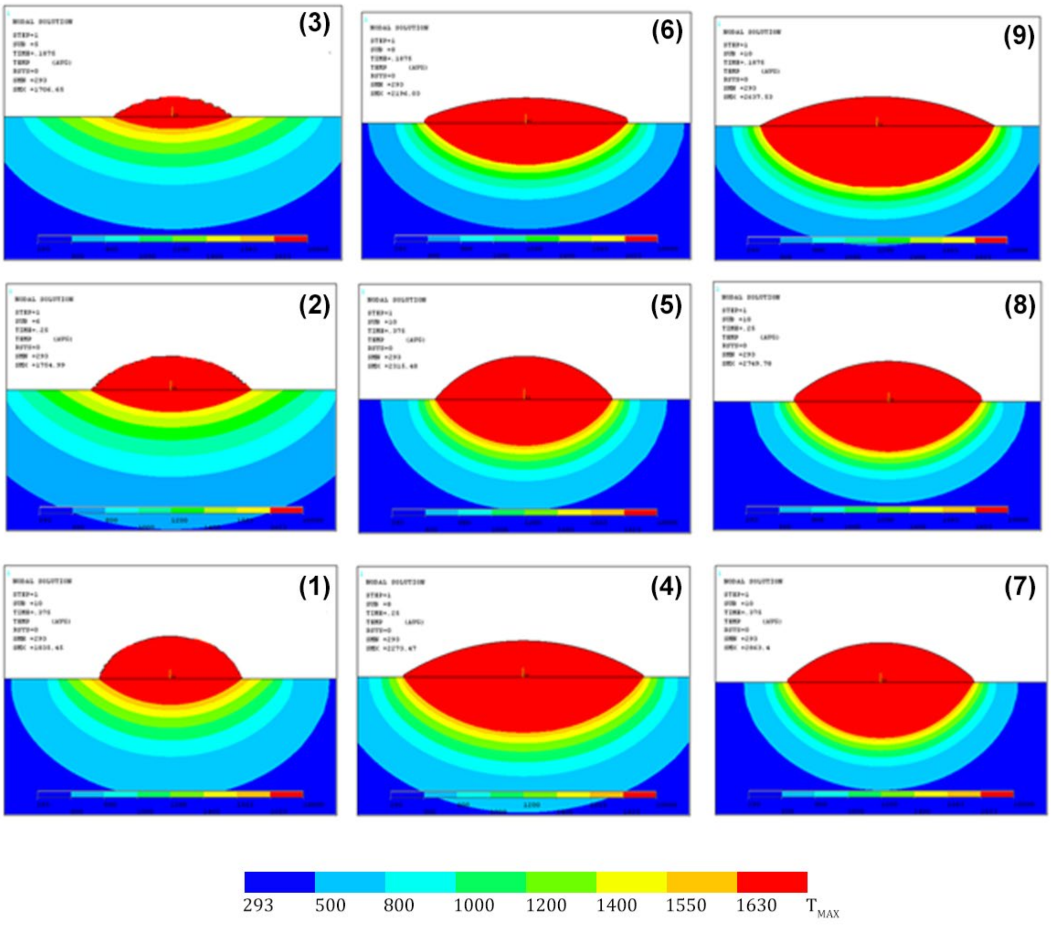

Figure 5.13 Single track dimensions predicted using enthalpy approach at different laser powers and scan speeds

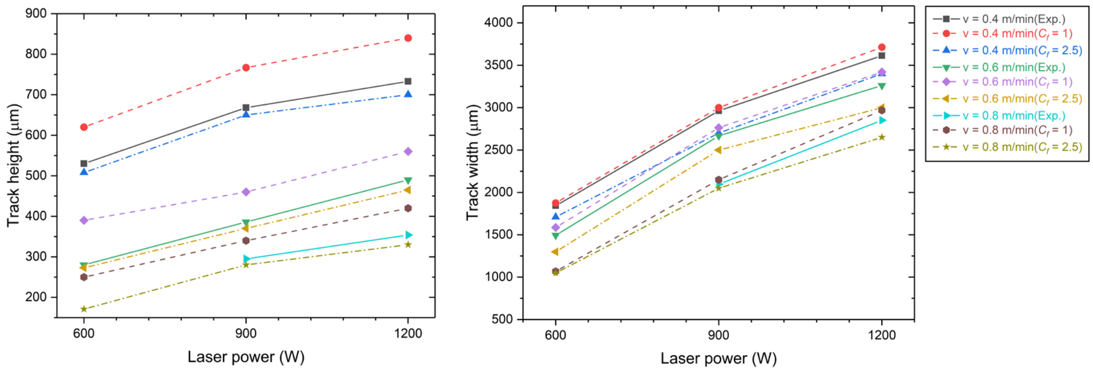

(a) **(b)**

Figure 5.14 Trend of the deposited track height and width from both experimental and predicted values at different laser powers and scan speeds

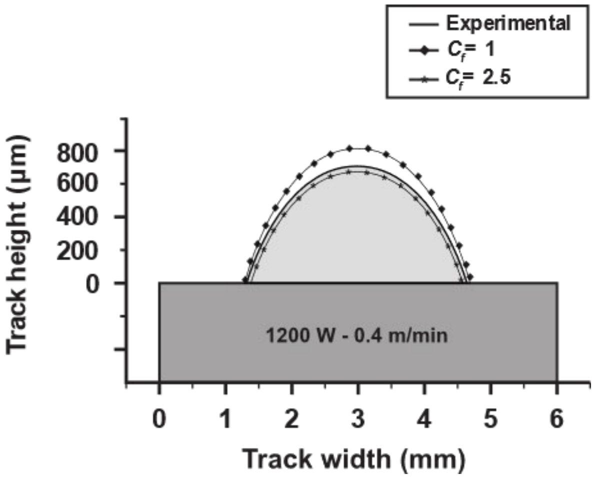

Figure 5.15. Comparison of the predicted track dimensions with the experimental observations

From the Figure 5.15 , it can be seen that enhancement of the thermal conductivity to incorporate the fluid dynamics effect has a significant effect on the prediction of melt pool dimensions. The predictions made by the numerical model considering C_f = 2.5 is found to have error percentage ranging between 2 to 5 % for track height and 5 to 9% for track width, while the numerical model with C_f = 1 have absolute percentage error ranging between 9 to 13%. In addition to the absolute percentage errors predicted by numerical model at both C_f = 1 and 2.5, it is also noted that the numerical model with

$C_f = 2.5$, is always found to under predict both track width and height. Whereas the numerical model with $C_f = 1$, is always found to over predict the track geometry. This is due to the multiplication of the enhancement factor ($C_f = 2.5$) to the thermal conductivity, which increases the overall heat transfer rate resulting in a lower track width and height compared to the numerical model with $C_f = 1$.

5.4 Conclusions

A finite element based transient thermal numerical model was proposed to predict the single-track dimensions in the present study. The numerical model accounts for the important physical characteristics of a LDED process such as heat source distribution, convection heat transfer and fluid dynamics effects in the melt pool by enhancing the thermal conductivity of the material above melting temperature. The numerical model at first uses a transient thermal analysis to predict the melt pool width and the depth. The melt pool width predicted from the thermal modelling was later used to mesh another model with track. Further, material addition was represented by strategic activation of the elements in the re-meshed track based on the excess enthalpy available at the nodes interacting with heat source. A comparison of the track height and width obtained from the numerical model at $C_f = 1$ and 2.5 with experimental measurements was done. The maximum absolute percentage error in the numerical model considering the fluid dynamics effects ($C_f = 2.5$) is 5% in track height and 9% in track width. While the percentage errors in the case of numerical model without fluid dynamics effects ($C_f = 1$) is 13% in track height and 16% in track width. The numerical model without considering the fluid dynamics effect is found to over predict the track dimensions in all the cases.

CHAPTER 6
THIN WALL DEPOSITION OF IN625: EXPERIMENTAL AND NUMERICAL INVESTIGATION

Thin wall structures are important engineering components with applications in the fields of aerospace (blades of impeller, heat exchanger walls), automobile and power sectors (heat exchanger fins). In this chapter, a detailed discussion on the effect of process parameters on the build quality, surface roughness, microstructure and mechanical properties of IN625 thin walls fabricated using laser directed energy deposition process. To this end, six thin walls were build using the optimized process parameters from the single-track study, as discussed in previous chapter. Effect of the laser power and scan speed on the dimensional stability, surface roughness and microstructure were examined. To understand the anisotropy in mechanical properties of thin walls were tested and compared in both vertical and horizontal directions. At the end of chapter, a FE based numerical model for thin wall deposition process is presented where melt pool geometry, time-temperature history, thermal gradients and cooling rates are compared for different laser powers and scan speed. The results from numerical models are interpreted with the experimental observations.

6.1 Materials and methods

6.1.1 Material

IN625 powder having spherical morphology Figure 6.1 (a)) with an average particle diameter of 55.3 μm was used for the deposition Figure 6.1 (b)). The measured D_{10}, D_{50} and D_{90} values for the powder particles used are 19, 51 and 69 μm, respectively as shown in Figure 6.1 (c). The chemical composition of the powder obtained from Energy Dispersive Spectroscopy (EDS) is shown in Table 6.1. The thin walls were deposited on a 10 mm thick SS316 substrate. Prior to the deposition, the plate was thoroughly cleaned using acetone.

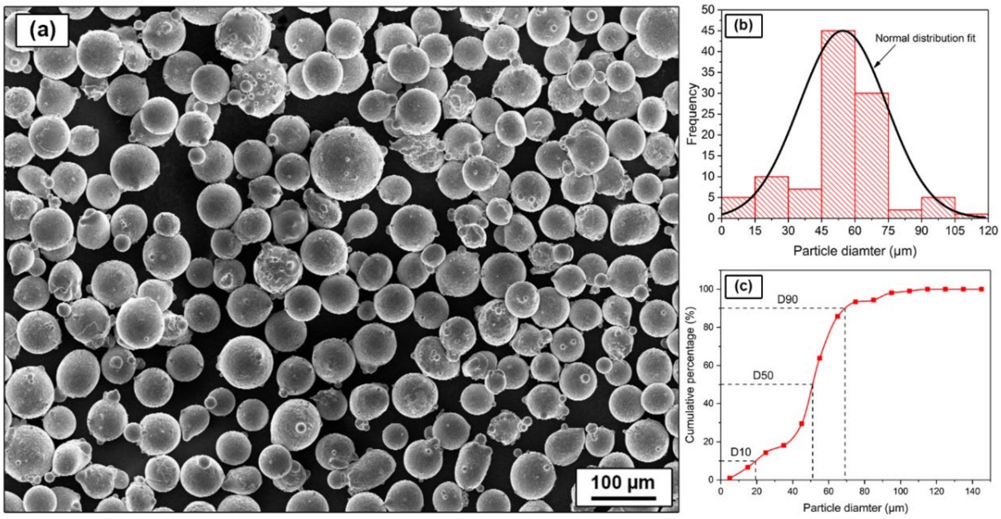

Figure 6.1 (a) SEM image of IN625 powder particles, (b) distribution of powder particles size and (c) cumulative percentage plot showing D_{10}, D_{50} and D_{90} particle size distribution

Table 6.1 Chemical composition of IN625 powder obtained from EDS analysis

Element	**Ni**	**Cr**	**Mo**	**Nb**	**Fe**	**Other**
Percentage (wt%)	54	22.2	5	3	4	12

6.1.2 Deposition of thin walls

In this work, the in-house developed LDED setup available at Raja Ramanna Centre for Advance Technology (RRCAT), Indore, India was used for the deposition of thin walls. The LDED setup as shown in Figure 6.2 (a), consists of a 2 kW continuous wave fibre laser, a coaxial powder feeding nozzle, a five-axis CNC control system and a twin powder feeder system. For shielding and carrying the powder, the argon gas supply was kept constant at 6 l/min. The spot size of the laser beam is 2.5 mm at the substrate surface. Using this LDED system, six thin walls 50 mm in length and 35 mm in height were fabricated at different combinations of laser power and scan speeds. The laser powers used for deposition are 900 and 1200 W while the scan speeds used are 0.4, 0.6 and 0.8 m/min, respectively. Sample notation and the process parameters used for deposition are listed in Table 6.2. The powder feed rate was kept constant at 8 gm/min for all the thin walls. Uni-directional strategy (from left to right), where the deposition takes place in one direction was used for deposition of thin walls, Figure 6.2 (b). The six fabricated thin walls are shown in Figure 6.2 (c).

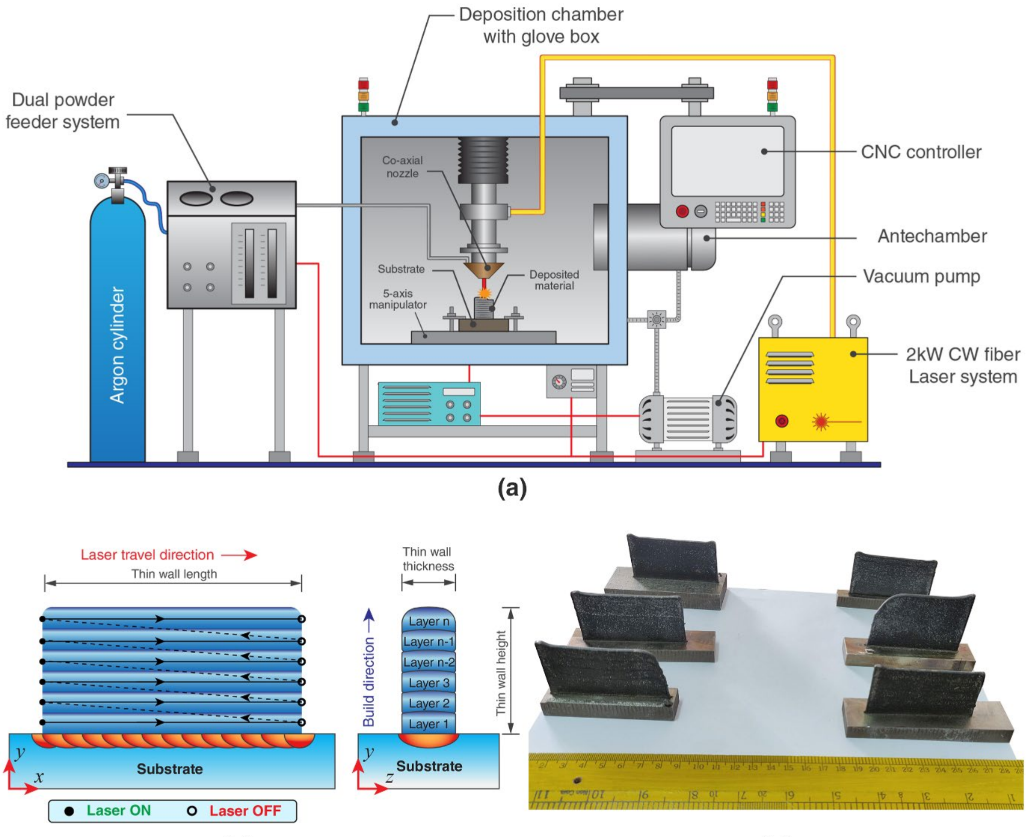
Deposition chamber
with glove box
Dual powder
feeder system
CNC controller
Co-axial
nozzle
Antechamber
Substrate
Deposited
material
Vacuum pump
5-axis
manipulator
Argon cylinder
2kW CW fiber
Laser system
(a)
Laser travel direction
Thin wall length
Thin wall
thickness
Build direction
Layer n
Layer n-1
Layer n-2
Layer 3
Layer 2
Layer 1
Thin wall height
Substrate
y
x
y
z
Substrate
● Laser ON
○ Laser OFF
(b)
(c)

Figure 6.2 (a) Schematic of the LDED system used for deposition of thin walls, (b) deposition strategy used and (c) thin walls built at different process parameters

Table 6.2. Sample notation and process parameters used for deposition

Wall name	Laser power (W)	Scan speed (m/min)
Wall – 1 (W1)	900	0.4
Wall – 2 (W2)	900	0.6
Wall – 3 (W3)	900	0.8
Wall – 4 (W4)	1200	0.4
Wall – 5 (W5)	1200	0.6
Wall – 6 (W6)	1200	0.8

6.1.3 Testing and characterization

Initially, all the fabricated thin walls were 3D scanned using a commercial 3D scanner (Model: Artec Space Spider, Make: Artec3D) with a resolution of up to 0.1 mm. The point cloud data obtained from the 3D scanner was processed using Artec Studio (Version: 17) to extract the dimensions of each thin wall. Figure 6.3 (a) (b) and (c) shows the 3D scanned model of a thin wall, the section planes considered for measuring the wall thickness and height, respectively.

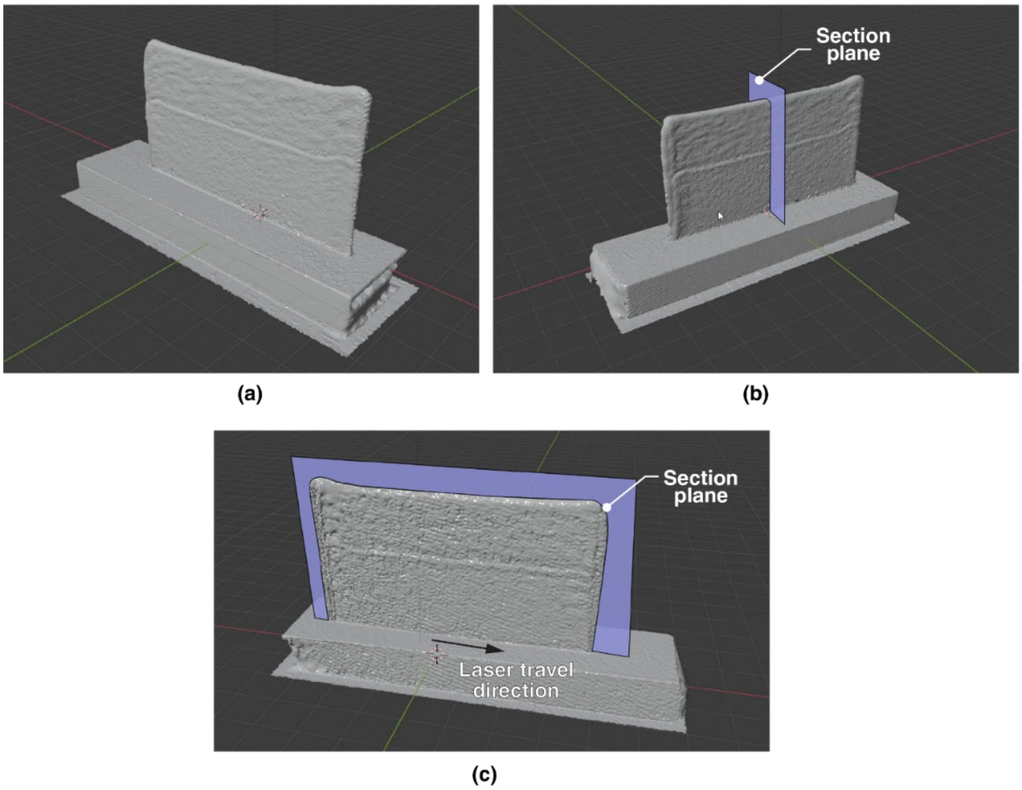

Figure 6.3. (a) 3D scanned model of thin wall, (b) section plane considered for measurements along the cross-section and (c) section plane considered for measurement along the laser travel direction

Further, thin walls were sectioned normal the laser travel direction to observe the change in microstructure along the build direction using Field Emission Scanning Electron Microscope (FE-SEM) (Model: Gemini 300; Make: Carl Zeiss, Germany). Prior to microscopy, the samples were polished and electrolytically etched using 10 wt% Oxalic acid in de-ionised water at 5 V for 10-12 secs. To understand the effect of laser power and scan speed on relative density, the samples were also subjected to density measurement tests using Archimedes' principle with five repetitions on each fabricated thin wall. Subsequently, uniaxial tensile test coupons were extracted from the thin walls by using Wire-Electrical Discharge Machining (W-EDM) process. The test coupons were cut from each wall in two orientations *i.e.,* vertical and horizontal as shown in Figure 6.4. The test coupons, where the tensile test axis is along the laser travel direction are referred to as horizontal specimen and the test coupons where the tensile test axis is parallel to the build direction are referred to as vertical test coupons. Tensile tests were conducted at a displacement rate of 0.3 mm/min (Model: Z020; Make: ZwickRoell). The fractured surfaces of each sample were analysed under FE-SEM (Model: 7610FPLUS; Make: Jeol, Japan) to obtain inferences about the mode of failure. Microhardness test was conducted (Model: MVH-S; Make: Omnitech, India) along the build direction using a load of 300 gm and a dwell period of 10 secs.

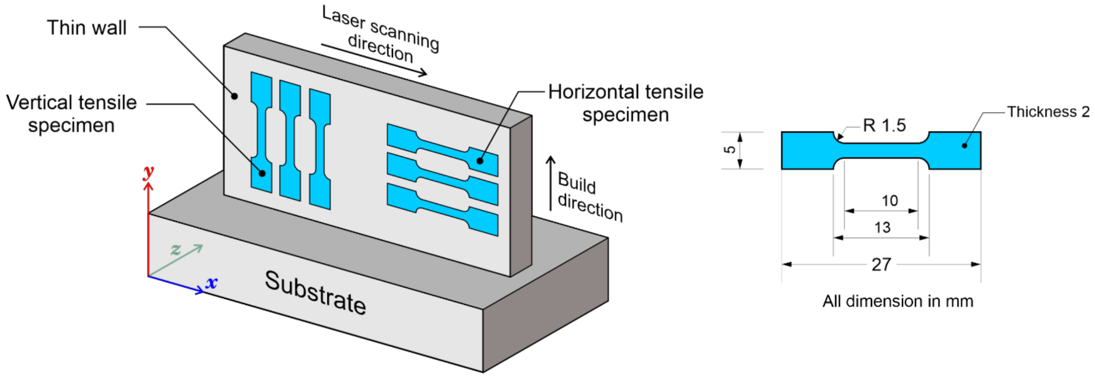

Figure 6.4. Schematic of tensile test coupon extraction and the dimensions of the tensile coupon

6.2 Results and discussion

6.2.1 Geometrical analysis of thin walls

Macroscopic cross-section images of the different thin walls obtained using stereo microscope were used to obtain quick qualitative inferences on the dimensional stability of the thin walls, especially in terms of build height and wall thickness. It is clearly evident from Figure 6.5, that thin wall height reduces as the scan speed increases at given laser power. It can be attributed to the combined effect of the smaller melt pool and low catchment efficiency at higher scan speeds. The interaction time between the laser and the material reduces at higher scan speeds, resulting in a smaller melt pool. Simultaneously, due to the reduced interaction time, the amount of powder captured by the melt pool also reduces leading to lower catchment efficiency. This results in lower layer thickness and overall, less deposition height. In addition to this, wall thickness was also found to be affected by the increase in scan speed at a given laser power (Figure 6.5). The thickness of the wall is mainly affected by the melt pool width which is controlled by process parameters such as laser power and scan speed. Therefore, it can be seen that as the laser power increase, a noticeable increase in the wall thickness (Wall-1 and Wall-4) can be observed.

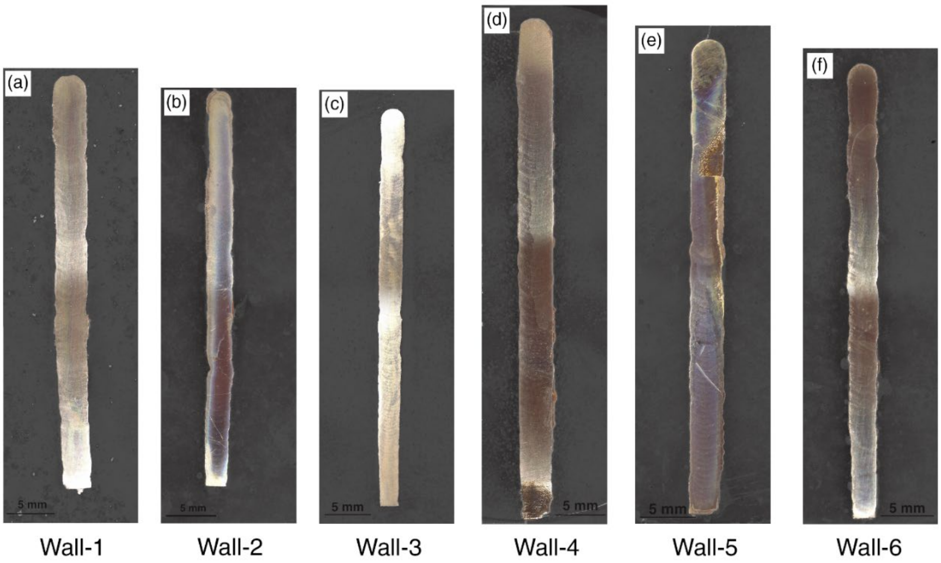

Figure 6.5. Macroscopic images showing cross-section of thin walls deposited at different laser powers and scan speeds

For quantitative analysis, the dimensions of thin walls (wall height and thickness) were extracted by post-processing the 3D scanned models. The variation in the height of the thin walls along its length is shown in Figure 6.6. From figure 6.6, it is evident that the wall height increases with the increase in laser power. For thin walls 1,2 and 3, where the deposition was carried out at a laser power of 900W, the wall height was found to be more or less the same, but comparatively lower than that of the thin walls 4, 5 and 6, where laser power of 1200W was used for deposition. This can be attributed to the fact that at higher laser power, a comparatively bigger melt pool is observed, which captures more powder, resulting in a higher layer thickness. It can be observed from Figure 6.6 that the height of thin walls is highly unstable at both the end (start and end point of deposition). This instability is seen in all the fabricated thin walls but at different magnitudes. Further the thin walls which were deposited at low scan speeds (W-1 and W-4) were found to exhibit maximum instability at the ends.

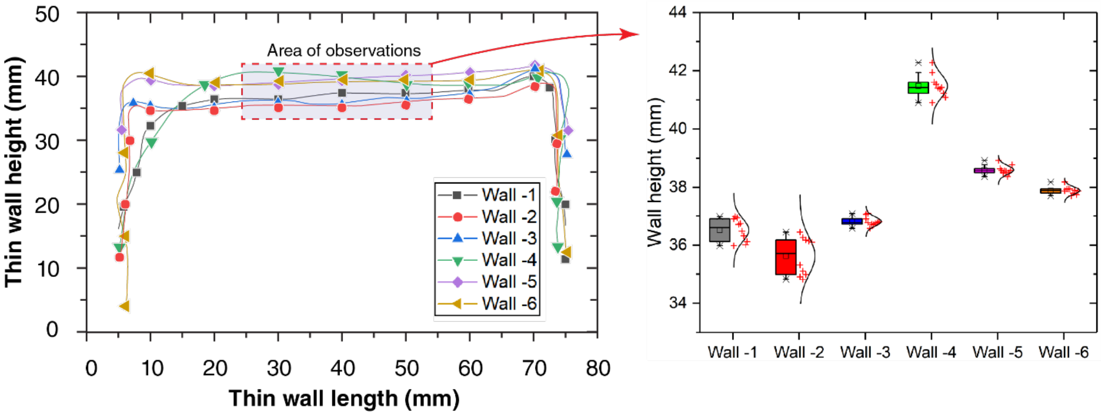

Figure 6.6. Thin wall height measured along its length and (b) range of variation in wall height and related normal distribution

At higher layers, the height of thin wall is found to be higher in all the cases. As a unidirectional depositional strategy was used for fabricating the thin walls, higher values of wall height were observed at the start point of deposition in many of the deposited thin walls. This is mainly due to more interaction time between the laser and the material at the beginning of the deposition. The laser, before it begins to move as per the planned path, goes through a transient motion, where it accelerates before achieving the desired scan speed. In this short time span where the laser is accelerating, there is an increase in the laser-material interaction time, creating a comparatively larger melt pool at the beginning of the deposition. Figure 6.7 (a), shows the macroscopic view of a thin wall. In the initial layers the layer thickness is found to be consistent, as can be seen from figure 6.7 (c). However, as the number of layers increases, more amount of material is deposited at the starting point of the laser, leading to inconsistent layer thickness. This is due to the higher Laser material interaction time that occurs during the acceleration period of the laser. The increase in the material deposition at the beginning also decreases the stand-off distance, because of which the effective laser energy is increased, leading to a bigger melt pool, higher catchment efficiency and higher deposition rate (figure 6.7(b)). A schematic illustration showing the evolution of inconsistency in wall height is shown in figures 6.7 (c1) and (b1).

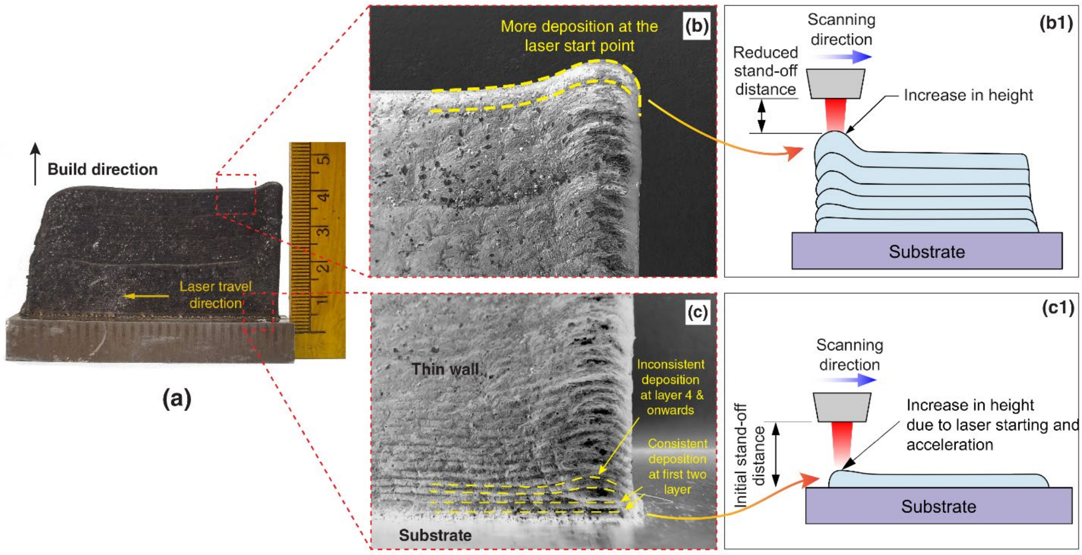
Build direction
Laser travel direction
(a)
More deposition at the laser start point
(b)
Scanning direction
(b1)
Reduced stand-off distance
Increase in height
Substrate
(c)
Thin wall
Inconsistent deposition at layer 4 & onwards
Consistent deposition at first two layer
Substrate
(c1)
Scanning direction
Initial stand-off distance
Increase in height due to laser starting and acceleration
Substrate

Figure 6.7. (a) Macroscopic view of deposited thin wall (b), (c) evolution of dimensional instability along the length, (b1) and (c1) schemtic showing evolutionof diensionalm inconsistency

The variation in the thickness of the thin walls along the build height is shown in Figure 6.8. Figure 6.8(a), presents the variation of wall thickness as a function of build height. The wall thickness was found to be varying from a minimum of 1.6 mm in Wall -3 (*P = 900W, v =0.8 m/min*) to a maximum of 3.54 mm in Wall – 4 (*P = 1200W, v =0.4 m/min*). Wall thickness was found to be significantly influenced by both laser power and scan speed.

Another important aspect of a stable thin wall is consistency in thickness. In the present study, a significant increase in the wall thickness was observed along the build direction. However, the amount of variation in wall thickness varies from case to case. For a better understating of the variation in wall thickness, Figure 6.8 (b) presents the wall thickness data with a normal distribution fitting. A narrow distribution represents the least change in thickness, while wider distribution represents higher variation. For a thin wall structure, a consistent thickness is always desired, therefore a thin wall with narrow distribution of thickness is always preferred. From Figure 6.8 (b), it can be observed that the normal distribution curve is narrow for wall-5 (P = 1200 W; v= 0.6 m/min) compared to all the other walls. Therefore, process parameters used for wall- 5 can be considered as the parameters of choice for depositing walls of consistent thickness. During the deposition of the initial layers, the substrate (which was at room temperature) acts as a heat sink dominates and extracts the heat through conduction due to which a smaller melt pool is generally observed in the initial layers. Further if the substrate is at room temperature, then the conduction of heat during the initial layers will be much higher. However, after the deposition of a certain number of layers, the effect of the substrate starts to diminish and heat transfer occurs through the thin wall which has a comparatively lower area (wall thickness × length) to conduct heat. This results in the accumulation of heat in the thin wall, by virtue of which melt pool size increases. Further, the temperature of the substrate also increases with time due to which, net heat transfer through conduction decreases.

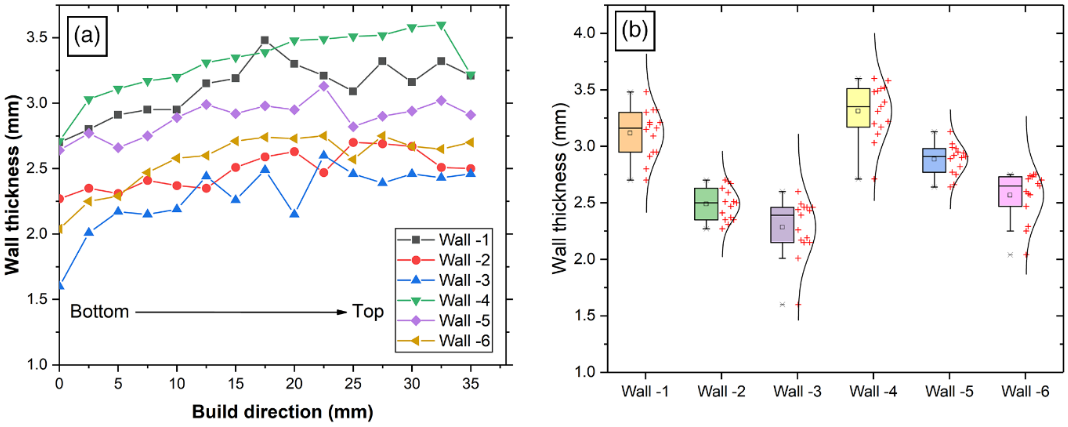

Figure 6.8: Thin wall thickness measured along the build height and (b) range of variation in wall thcinkess and related normal distribution

6.2.2 Density measurement

The density measurement analysis was carried out on all the thin walls using Archimedes' principle and is presented in Figure 6.9. From Figure 6.9, it can be seen that both scan speed and laser power have a significant effect on the relative density of the fabricated thin walls. For the thin wall fabricated at a laser power of 900 W, relative density was found to decrease with increase in scan speed from 0.4 to 0.8 m/min. This can be attributed to the reduced interaction time at higher scan speeds at constant laser power which leads to lack of fusion defect between the subsequent layers. As the laser power increases at a given scan speed, a clear increase in the relative density was observed. This can be attributed to the to larger melt pool which leads to greater penetration into the previous layer and possibly complete melting of powder. As the laser energy density increases, the relative density has an optimal value, which means that first relative density increases with the increase in laser energy and reaches to a maximum value and thereafter starts to decrease (du Plessis, 2019). At higher laser powers, the pores appear to be round, which usually occurs due to the vapour and gas entrapment (Figure 6.12). A high laser power creates a deeper melt pool with strong fluid dynamic forces, this causes entrapment of vapours and gases that comes between the powder particles, results in spherical pores during solidification.

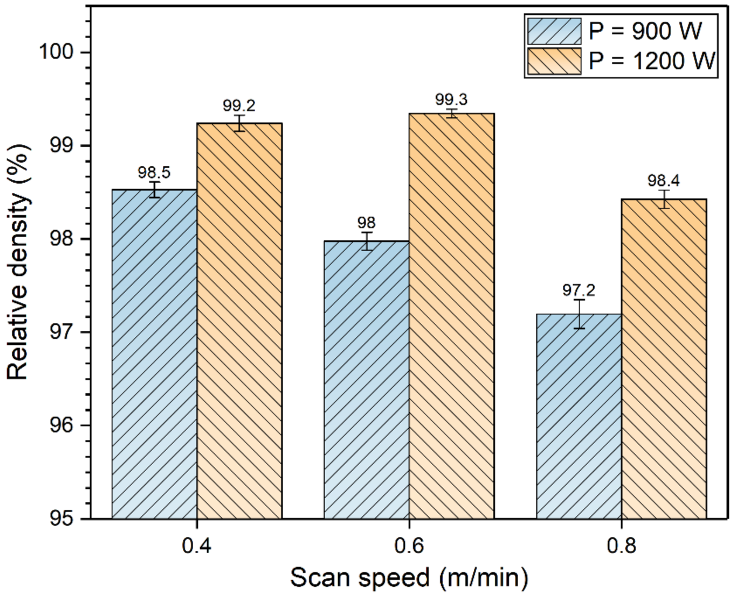

Figure 6.9. Relative density observed in thin walls fabricated at different process parameters

6.2.3 Surface quality analysis

Figure 6.10 presents the results of surface roughness measurements carried out on the fabricated thin walls. It can be seen from the Figure 12 that as the scan speed increases, the surface roughness of the thin walls increases. This increase in surface roughness with increase in scan speed can be attributed to the reduced laser-powder interaction time at higher scan speeds. Due to the reduced laser-powder interaction time, small partially melted particles were found on the surface of thin walls (Craig et al., 2021; Mahamood and Akinlabi, 2017). The thin walls fabricated at higher laser power exhibit a higher surface roughness as compared to the thin walls fabricated at lower laser powers mainly due to higher turbulence and outward flow at higher laser power.

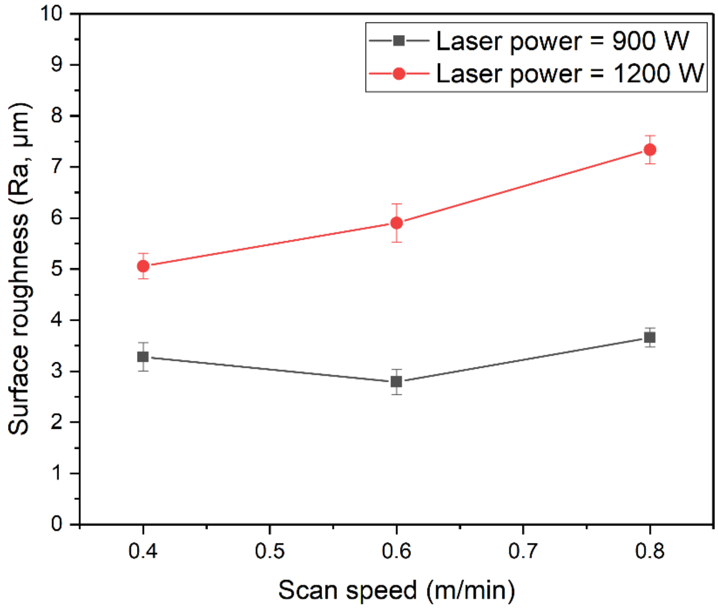

Figure 6.10. Effect of scan speed on surface roughness at different laser powers

Figure 13 shows the surface roughness along the build direction. Figure 6.11 (a) shows the peaks and valleys obtained after scanning the surface of the thin wall sample under a profilometer. It is observed that the surface roughness of the thin wall is lower in the initial layers of deposition. However, after certain layers are deposited, a clear increase in the surface roughness can be observed. The increase in surface roughness may be attributed to the increase in waviness at higher layers. As the deposition height increase, more amount of heat accumulates in the wall because of which the temperature in the melt pool increases, leading to a bigger melt pool with a low contact angle, creating a wavier surface (Figure 6.11 (b)).

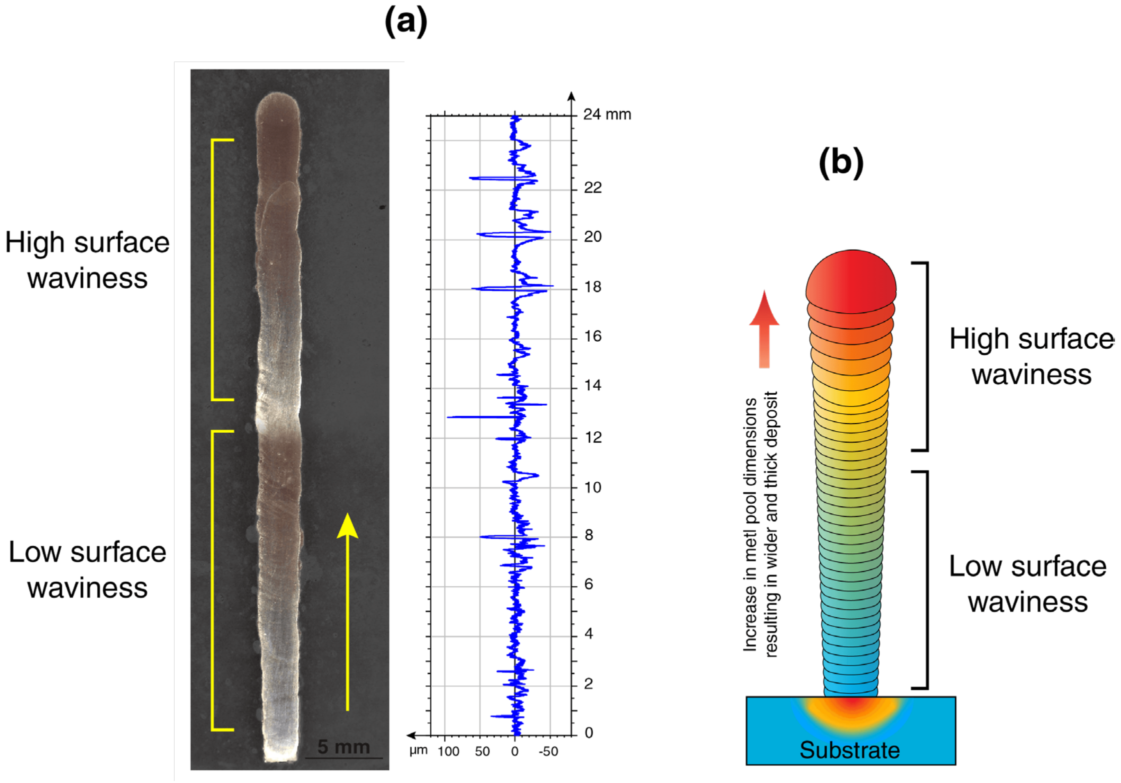
(a)
High surface waviness
Low surface waviness
5 mm
24 mm
22
20
18
16
14
12
10
8
6
4
2
0
µm 100 50 0 -50
(b)
Increase in metl pool dimensions resulting in wider and thick deposit
High surface waviness
Low surface waviness
Substrate

Figure 6.11 (a) Change in surface quality along build direction and (b) graphical illustration showing the process of increase in surface roughness along the build height

6.2.4 Microstructural analysis

Figure 6.12 and 6.13 show the change in microstructure with the change in process parameters and along the build direction of fabricated thin walls. Figure 6.12 (a), (b) and (c), show the microstructure obtained at a constant power of 1200W and three scan speed values of 0.4, 0.6 and 0.8 m/min. It can also be observed that the microstructure for all scan speeds is columnar dendritic in nature. This indicates directional solidification that usually occurs during LDED process (Jinoop et al., 2021b; SAFARZADE et al., 2020; Yangfan et al., 2019). The grains grow in a preferential direction following the maximum thermal gradients i.e. against the heat transfer

(Yangfan et al., 2019). From Figure 6.12 (a), (b) and (c) it can be observed that grain size is significantly affected by scan speed. Increasing scan speed results in a gradual decrease in the dendrite spacing. At higher scan speeds, the low interaction time leads to a decrease in net energy supplied to create melt pool. The reduction in laser energy reduces the peak temperature and the size of the resulting melt pool which increases the overall cooling rate in the melt pool. As a result of which the grain size decreases (Chai et al., 2021).

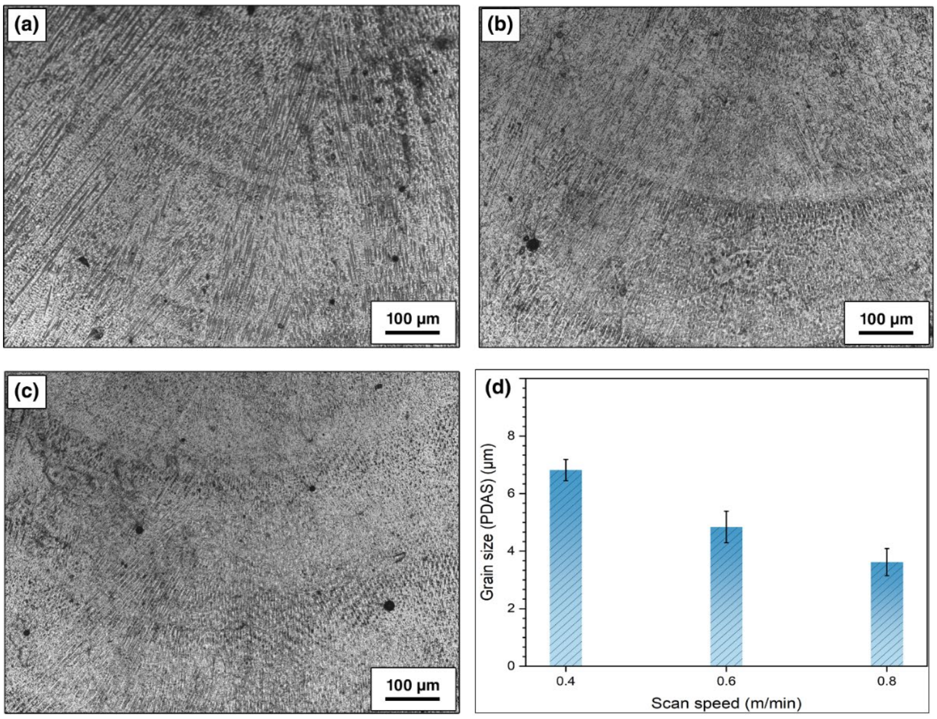

Figure 6.12. Microstructure observed in thin walls at laser power of 1200W and scan speeds of (a) 0.4 m/min, (b) 0.6 m/min and (c) 0.8 m/min

Figure 6.13 shows the microstructure of the thin wall (W5) along the build direction. The microstructure was captured at three locations, referred to as top, middle and bottom. From the Figure 6.13 (b) and (b1), the microstructure at the initial layer of thin walls is dendritic in nature. The dendrites were found to have a small secondary arm growth. However, as the number of layers increases, transition from dendritic to columnar structure can be seen (Figure 6.13 (c) and (c1)). Further, increase in the layer number (top), cellular microstructure can be seen (Figure 6.13 (d) and (d1)).

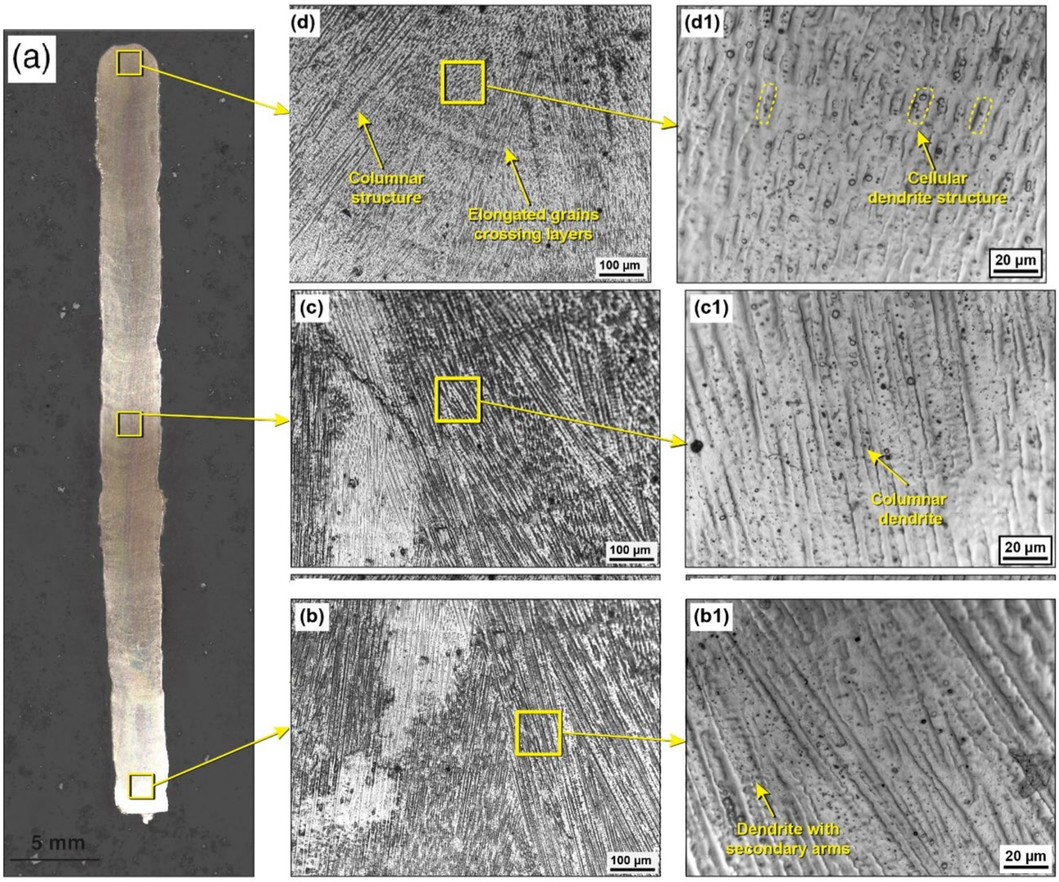
(a)
5 mm
(d)
Columnar structure
Elongated grains crossing layers
100 µm
(d1)
Cellular dendrite structure
20 µm
(c)
100 µm
(c1)
Columnar dendrite
20 µm
(b)
100 µm
(b1)
Dendrite with secondary arms
20 µm

Figure 6.13. Microstructure observed at different locations of fabricated thin wall

6.2.5 Tensile properties & fractography

The tensile property of a part is indicated by Yield Strength (YS), Ultimate Tensile Strength (UTS) and elongation obtained from uniaxial tensile test. Figure 6.14 (a) and (b) show the YS observed at laser power 900 W and 1200 W, respectively. The results indicate an increase in the YS with the increase in scan speed. This is due to the fine microstructure that occurs as a result of high cooling rates during high scan speeds, as discussed in section 3.3. Grain size plays an important role in controlling YS which is expressed by the Hall-Petch relation (N., 2004).

$$\sigma_y = \sigma_0 + k/d^{0.5} \tag{6.1}$$

where, σ_y is the yield strength, d is the grain size, σ_0 and *k* are the material constants. It can be observed from the eqn. (6.1) that grain size (*d*) and yield strength (σ_y) are inversely proportional to each other, which means as the grain size decreases, yield strength increases. Fine grain structure brings more grain boundaries and dislocation density. This contributes to the strengthening of alloy by hindering the movement of dislocation when subjected to loading. In LDED process, the cooling rates usually varies in the order of 10^4 to 10^6 K/sec, as a result of which finer grain structures are formed leading to higher yield strength compared to conventional manufacturing techniques (Wang et al., 2022a). However, it is worth noting that the YS, after a certain laser power and scan speed starts to decrease, as in the case of laser power of 900W and scan speed of 0.8 m/min. This reduction in yield strength can be attributed to the lack of fusion porosity defect that usually occurs at a combination of low laser and high scan speeds. The effect of laser power of YS is found to be insignificant. However, there is a slight decrease in the YS when laser power is changed from 900 W to 1200 W. Increasing the laser increase the maximum temperature in a given sample. At higher laser power, the resulting melt pools are usually bigger which takes more time to cool (slow cooling rates) as a virtue of which grain with larger dimensions are formed. Since the horizontal samples, were extracted from the different locations of a given thin wall, an inconsistent trend in their mechanical properties can be observed.

The results of Figure 6.14 (b) show that horizontal and vertical samples exhibit different values of yield strength indicating anisotropy in mechanical properties in the fabricated thin walls. The samples extracted along the horizontal direction were found to exhibit higher strength than the samples extracted along the vertical direction. LDED samples exhibit large thermal gradients exist because of the layer-by-layer deposition, as a result of which the parts usually have anisotropic mechanical properties. In vertical samples, where the direction of columnar grains and tensile test axis is parallel, the dislocations need to cross fewer grain boundaries as a result of which both yield and tensile strength reduce. However, in the case of horizontal samples, the tensile axis is perpendicular to the columnar grains, due to which dislocations during movement need to cross several grains leading to an increase in mechanical strength. Similar results were reported in other material systems such as Ti-6Al-4V and SS304 (Beese and Carroll, 2016; Carroll et al., 2015; Wang et al., 2016) processed by LDED and LPBF process. The samples are found to exhibit ductility ranging between 60-70% in different cases. There is no clear trend in the percentage elongation with the change of process parameters and sample orientation. Fractography results of thin walls fabricated different process parameters are shown in Figure 6.15 and Figure 6.16. The fractographs show several dimples on the fractures surface, in all combination of laser powers and scan speeds, indicating a ductile mode of failure. However, a good amount of porosity can be seen at higher scan speeds. The elemental maps of the fractured do not show segregation of elements (Figure 6.17).

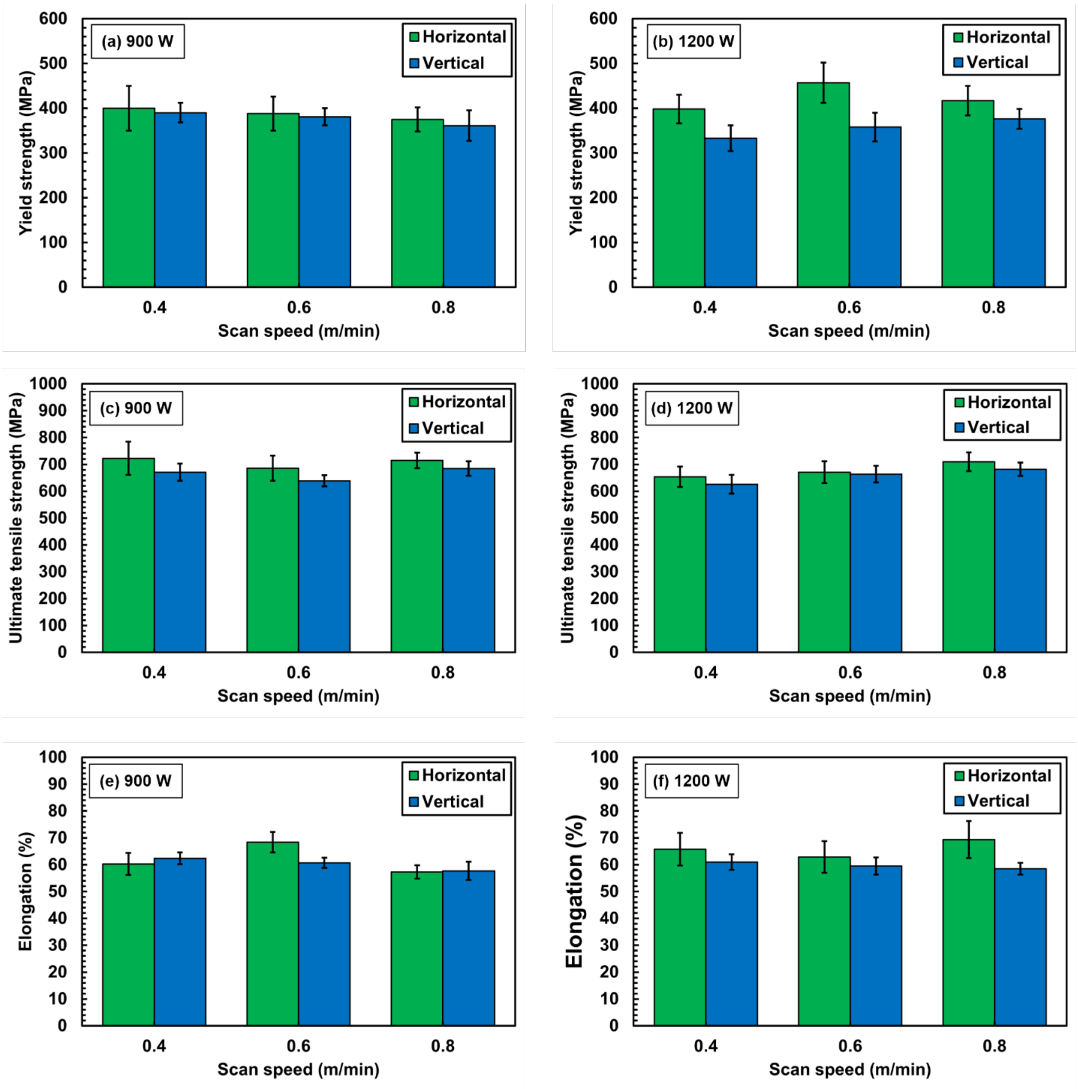

Figure 6.14. (a) (b) Yield strength, (c) (d)ultimate tensile strength and (e) (f) percentage elongation of samples extracted from thin walls

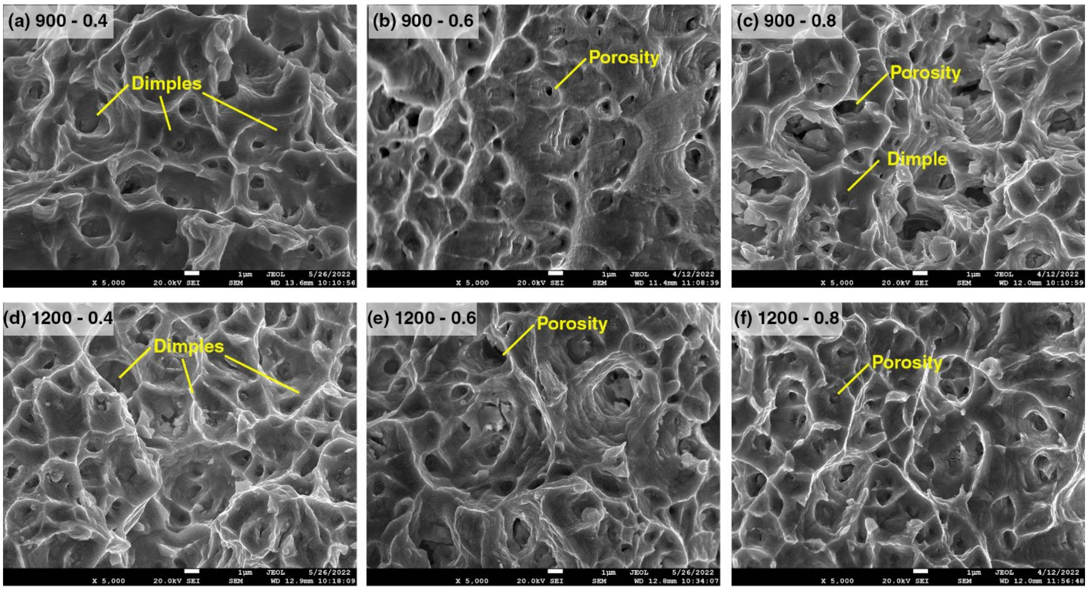
(a) 900 - 0.4
Dimples
(b) 900 - 0.6
Porosity
(c) 900 - 0.8
Porosity
Dimple
(d) 1200 - 0.4
Dimples
(e) 1200 - 0.6
Porosity
(f) 1200 - 0.8
Porosity

Figure 6.15. SEM images of the fractured surface of all the thin wall (vertical)

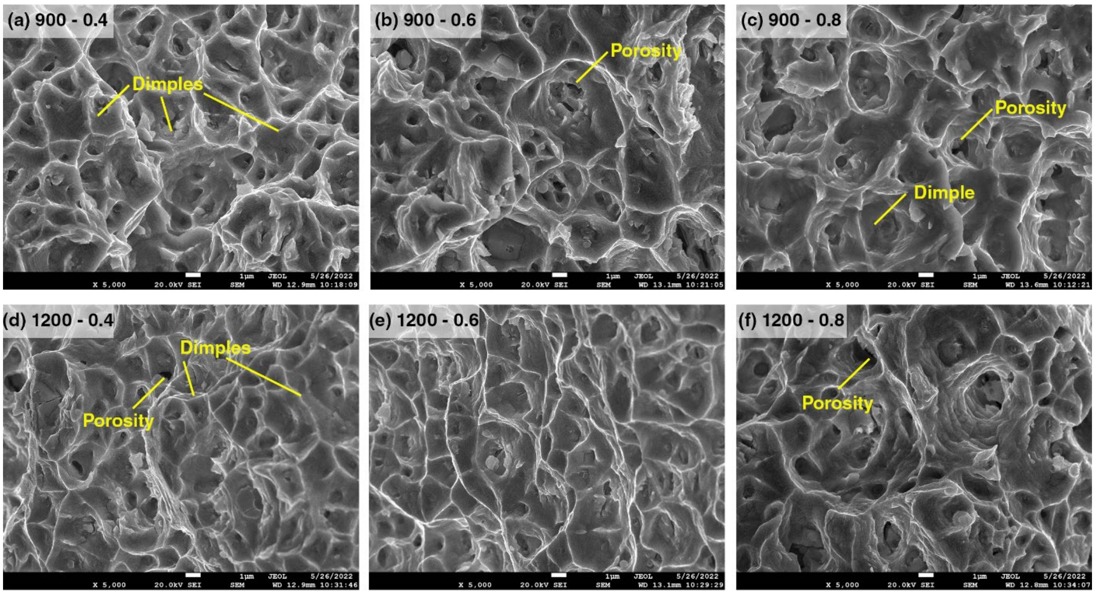
(a) 900 - 0.4
Dimples
(b) 900 - 0.6
Porosity
(c) 900 - 0.8
Porosity
Dimple
(d) 1200 - 0.4
Dimples
Porosity
(e) 1200 - 0.6
(f) 1200 - 0.8
Porosity

Figure 6.16 SEM images of the fractured surface of all the thin wall (horizontal)

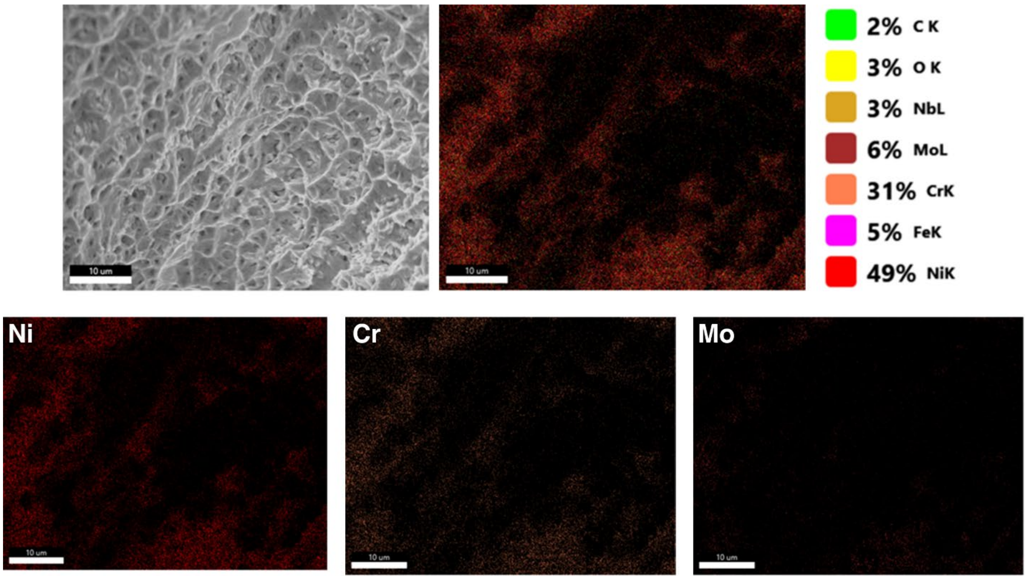

Figure 6.17. Elemental composition from EDS analysis observed on the fractured surface of the tensile coupon (W5-vertical samples)

6.2.6 Microhardness

Microhardness test starting from the bottom to the top of each thin wall was carried out and the results of same are shown in Figure 6.18. The thin walls are found to exhibit a maximum of 315 HV hardness at laser power 1200W and scan speed 0.8 m/min (wall -6). It is also worth noting that, as the scan speed increases at laser power of 1200W, the hardness values are found to be increasing (W4, W5 and W6). This increase can be attributed to the decrease in the grain size at higher scan speeds. However, for the thin wall deposited at 900W, the increase in scan speed is found to not follow a similar trend. The hardness of the thin wall deposited at 900 W-0.4 m/min is found to exhibit more hardness than that of the thin wall deposited at the same laser power but 0.8 m/min. This may be due to the increase in the lack of fusion porosity defect that usually occurs at low power high scan speeds.

The hardness test for all the thin walls was also carried out from the bottom to top. The thin walls, irrespective of the laser power and scan speed used, are found to follow a similar trend of hardness variation along the build (Figure 6.18). It can be seen that the hardness value, after depositing a few layers increases to a maximum value, then decrease and again increases. The variation in the hardness values can be attributed to the different microstructures observed at different build heights, as discussed in section

6.2.3 (Figure 6.13). During the initial layers, the substrate which acts as a heat sink is usually at room temperature. As a result of which, heat transfer rates are higher, resulting in a small melt pool, high thermal gradient and faster cooling rates, leading to a fine microstructure. As described in the last section, a fine microstructure will have more associated grain boundaries which hinder the dislocation movement leading to a high hardness value in the initial layer. However, as the number of layer increases, the substrate effect starts to diminish as a virtue of which heat starts to accumulate in the thin wall, resulting in a larger melt pool, small thermal gradient and slow cooling rates. Because of this the grain size in the middle of the wall is comparatively larger which results in a low hardness value.

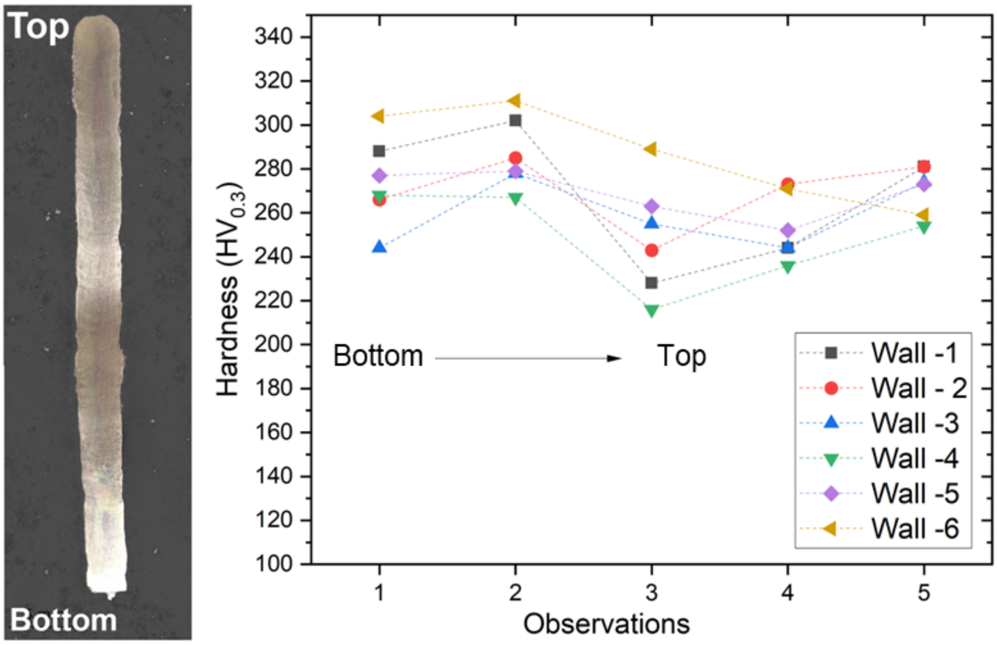

Figure 6.18. Microhardness values observed along the build direction in different thin walls

6.3 Numerical modeling thin walls

To understand the physical nature of the thin wall deposition process, a 3D transient thermal finite element model was established in ANSYS Mechanical. Here, laser power and scan speeds were varied to understand their effect on peak temperature, melt pool geometry, cooling rates and thermal gradients.

6.3.1 Description of the numerical model

6.3.1.1 Assumptions

a) Material properties such as density, specific heat and thermal conductivity are temperature dependent (Hernando et al., 2018). Material properties used in present study are shown in Figure 5.4.

b) The effect of latent heat of fusion is incorporated in the model by modifying the specific heat capacity of the metal at melting point (Eq. 5.7).

c) The moving heat source is a 2-D surface heat flux with a gaussian distribution (Balichakra et al., 2019; Li et al., 2018).

d) Effect of composition change due to the loss of alloying elements during melting has not been included in the numerical model (Mukherjee et al., 2018).

e) Marangoni phenomenon during melting is considered by modifying ($k_{\text{modified}} = 2.5 \times k$ for $T > T_m$) the thermal conductivity of the metal for all temperatures above melting point in a particular direction. (Kumar et al., 2012; Lampa et al., 1997).

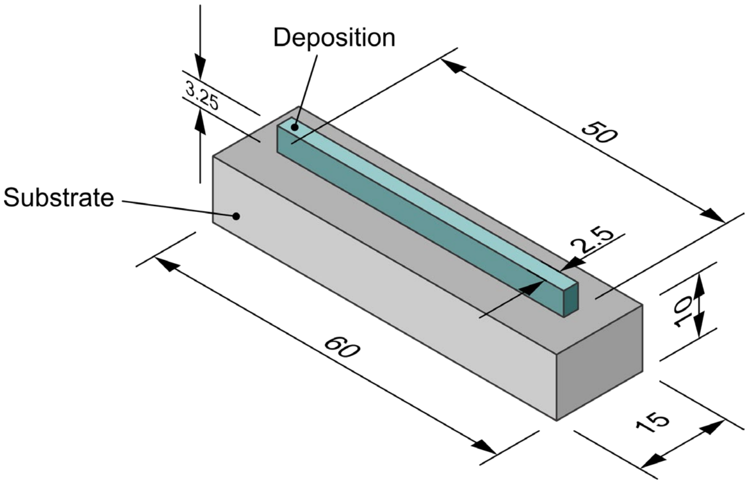

Figure 6.19 Dimensions of the 3D model used in present study (all dimension in mm)

6.3.1.2 Modelling and meshing

Initially, a 3D model of dimensions shown in Figure 6.19 was created using ANSYS Mechanical. Both substrate and deposit models were created separately and glued together to build one FE model. Next, the 3D model was meshed using SOLID70 element type available in ANSYS APDL. The deposit part of the model was meshed with a finer mesh size (0.3125 mm) while the substrate part was meshed with a coarse mesh size (1 mm). These dimensions were identified after conducting a mesh independence test. Results of the mesh independence test are shown in Figure 6.20. The present FE model consists of 1.78 lakhs nodes.

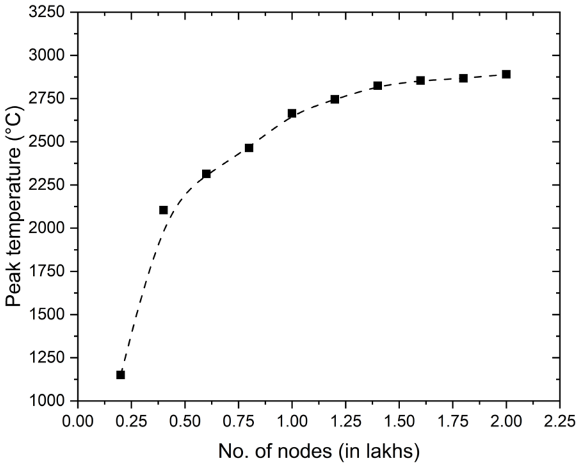

Figure 6.20 Results from mesh independent test carried at different mesh sizes

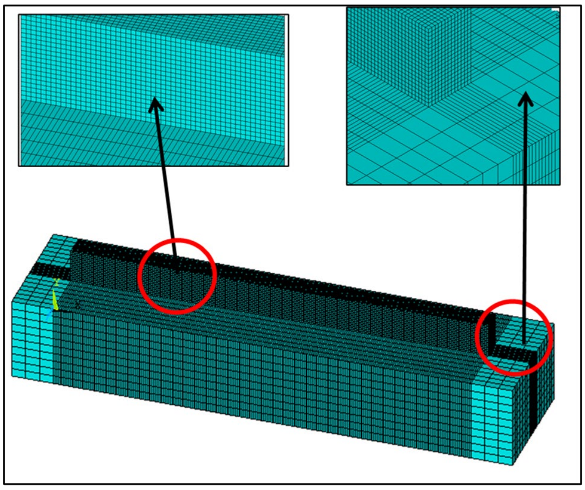

Figure 6.21 The finite element mesh used in present study

6.3.1.3 Boundary conditions

To define the physical conditions boundary conditions are to be defined. Figure 6.22 shows the various boundary conditions assigned to the numerical model. All the surface which are exposed to air have been defined by a convection boundary conditions with a convective heat transfer coefficient value of 10 W/m²K and ambient temperature of 25°C. The bottom of the substrate is assigned with a uniform temperature boundary condition. This boundary condition defines bottom as an infinite heat sink, which is to mimic the deposition of thin wall on a big substrate (semi-infinite geometry). Rest of the numerical model was set to an initial temperature of 25°C.

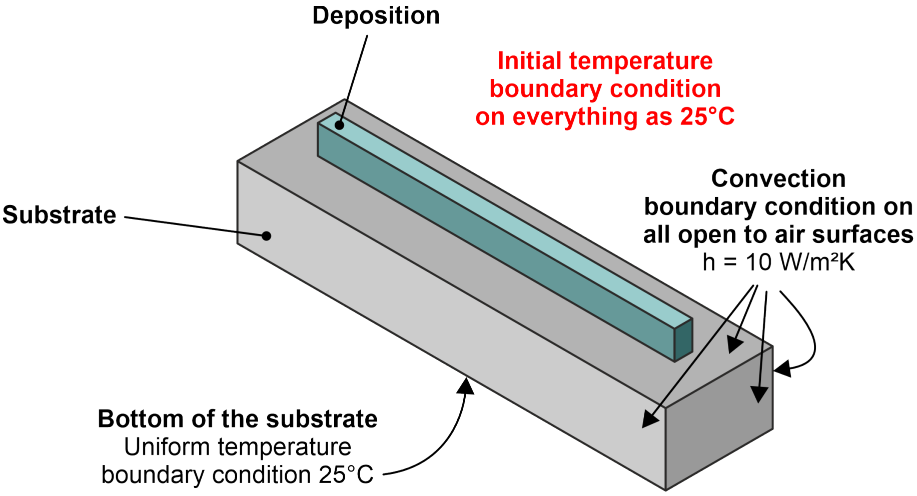
Deposition
Initial temperature boundary condition on everything as 25°C
Convection boundary condition on all open to air surfaces
h = 10 W/m²K
Substrate
Bottom of the substrate
Uniform temperature boundary condition 25°C

Figure 6.22. Various boundary conditions used in the numerical model

6.3.2 Results & discussion

6.3.2.1 Variation of melt pool geometry with number of layers

During the deposition of thin wall structures, it is known that the heat accumulates over the time which leads to a net increase in temperature in progressive layers. To capture this phenomenon, temperature contours were obtained at the center of thin wall at different layer numbers. The predicted temperature contours at different layers are presented in Figure 6.23. The data from numerical model was post-processed to extract results relating the change in peak temperature and dimensions of melt pool over the five layers. The change in peak temperature over the layers is presented in Figure 6.24.

The graphs clearly show an increase in the temperature over the five layers. The temperature predicted at the first layer is 2875 °C at a laser power of 1200 W and scan speed of 0.4 m/min which continue to increase till 3125 °C over the five layers. The increase in temperature with the increasing layers can be attributed the heat accumulation over the time. While depositing the first layer, the substrate acts as heat sink which takes a major amount of heat through the conduction mode of heat transfer. Also, the substrate during the first layer deposition is at room temperature as a result the peak temperature in the first layer is less. However, while depositing the 2^{nd} layer, the base is now the first layer, which is already at a higher temperature, leading to a higher peak temperature in 2^{nd} layers. Similar phenomena occur for rest of the layers, thereby temperature continues to increase. At the same time, while depositing the first layer, the area available to conduct heat is more (product of width and length of substrate), whereas, while depositing the higher number layers, the area available to conduct heat also goes down (product of thickness and length of thin wall), as shown in Figure 6.25. This reduced heat conduction also leads to the accumulation of heat and thereby results in increase of peak temperature in successive layers.

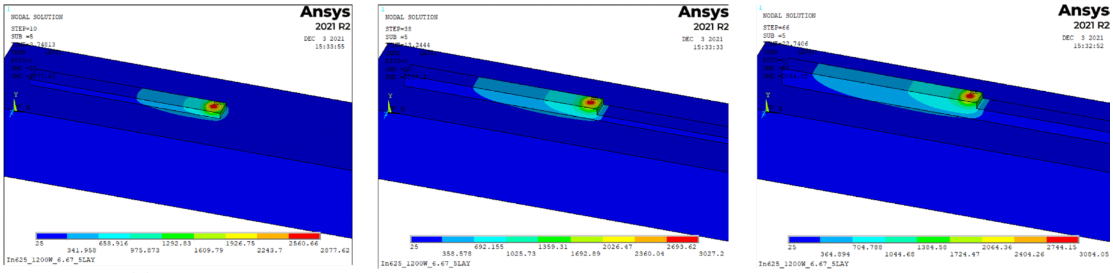
NODAL SOLUTION
Ansys
2021 R2
25
341.958
658.916
975.873
1292.83
1609.79
1926.75
2243.7
2560.66
2877.62
In625_1200W_6.67_5LAY
NODAL SOLUTION
Ansys
2021 R2
25
358.578
692.155
1025.73
1359.31
1692.89
2026.47
2360.04
2693.62
3027.2
In625_1200W_6.67_5LAY
NODAL SOLUTION
Ansys
2021 R2
25
364.894
704.788
1044.68
1384.58
1724.47
2064.36
2404.26
2744.15
3084.05
In625_1200W_6.67_5LAY

(a) Layer - 1 (b) Layer - 2 (c) Layer - 3

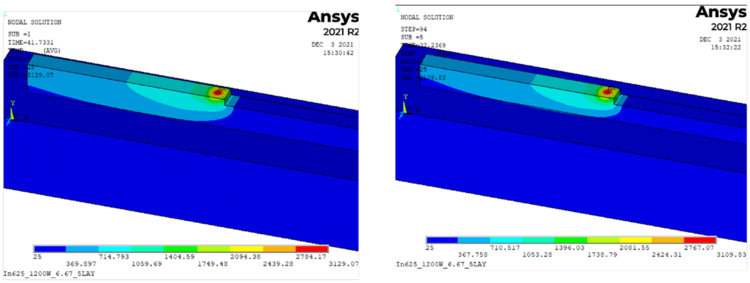
NODAL SOLUTION
SUB =1
TIME=41.7331
Ansys
2021 R2
DEC 3 2021
25
369.897
714.793
1059.69
1404.59
1749.48
2094.38
2439.28
2784.17
3129.07
In625_1200W_6.67_5LAY
NODAL SOLUTION
STEP=94
SUB =5
Ansys
2021 R2
DEC 3 2021
15:32:22
25
367.758
710.517
1053.28
1396.03
1738.79
2081.55
2424.31
2767.07
3109.83
In625_1200W_6.67_5LAY

(d) Layer - 4 (e) Layer - 5

Figure 6.23 Temperature contours observed in thin wall at different layers

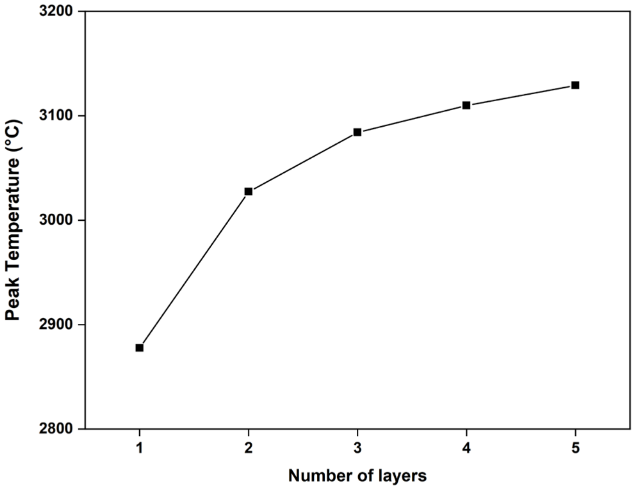

Figure 6.24 Peak temperatrure observed in different layers

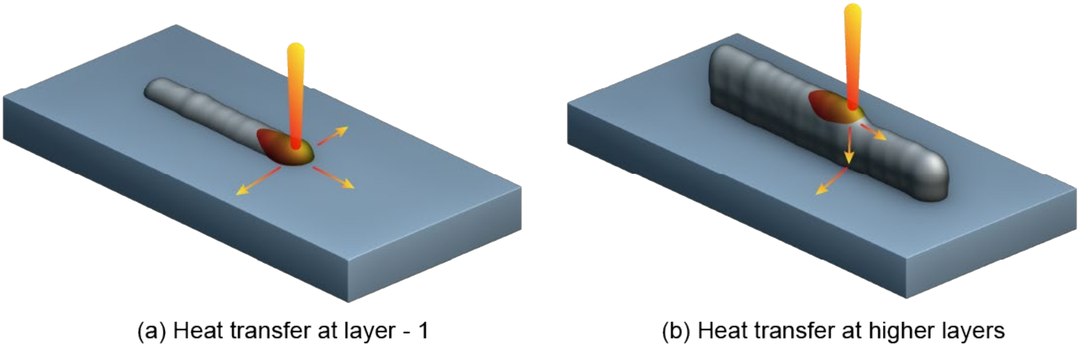
(a) Heat transfer at layer - 1
(b) Heat transfer at higher layers

Figure 6.25. Schematic showing difference of (a) heat transfer at layer – 1 and (b) higher layer numbers

6.3.2.2 Variation of peak temperature with number of layers

Figure 6.26 (a) shows the temperature contours at different layer numbers. The grey coloured areas in Figure 6.26 (a) indicate a melt pool, where the temperature is higher than 1350°C. From the Figure 6.26 (a), it can be observed that both length and depth of the grey portion increases over the layers, indicating an increase in the melt pool length and depth. The increase in the melt pool dimensions can be attributed to the increase in the peak temperature, as discussed previously. Qualitative representation of the same is presented in Figure 6.26 (b). It can be seen that from layer 1 to layer 5, the melt pool length increases from 2.44 mm to 2.76 mm. Similarly, the melt pool depth is found increasing 0.7 mm to 0.94 mm from layer 1 to layer 5.

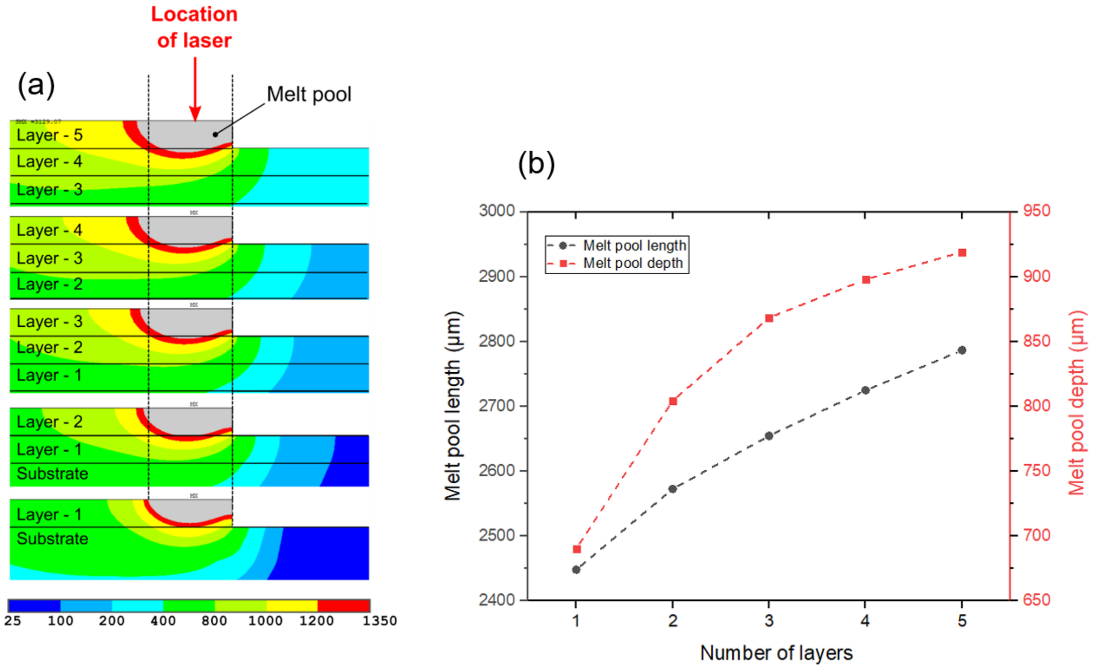

Figure 6.26 Melt pool length and depth predictions at different layers

6.3.2.3 Thermal history of five layers

Temperature vs time plots of the five layers deposition process is shown in Figure 6.27. The plots shown in Figure 6.27 helps in understand the process of both cyclic heating and cooling of a given layer over the time of deposition. From Figure 6.27 (a), an overall increase in the peak temperature can be observed in all the layers. Magnified plots of Time vs Temperature plots are shown in Figure 6.27 (b, c, d & e). It can be observed that during the deposition of second layer, the temperature on the first layer reaches very close to the melting temperature (1350 °C). This outcome indicates the remelting of the previous layer during the deposition of successive layer. Remelting of previous layer also gives an indication of a proper bonding between the layers. Similarly, while the third layer is being deposited, the temperature in 2nd layer reaches to a value of 1400 °C, indicating remelting of 2nd layer. In addition, the temperature of 1st layer again increases to a value close to 800 °C. This cycle of reheating and cooling continues over the layers.

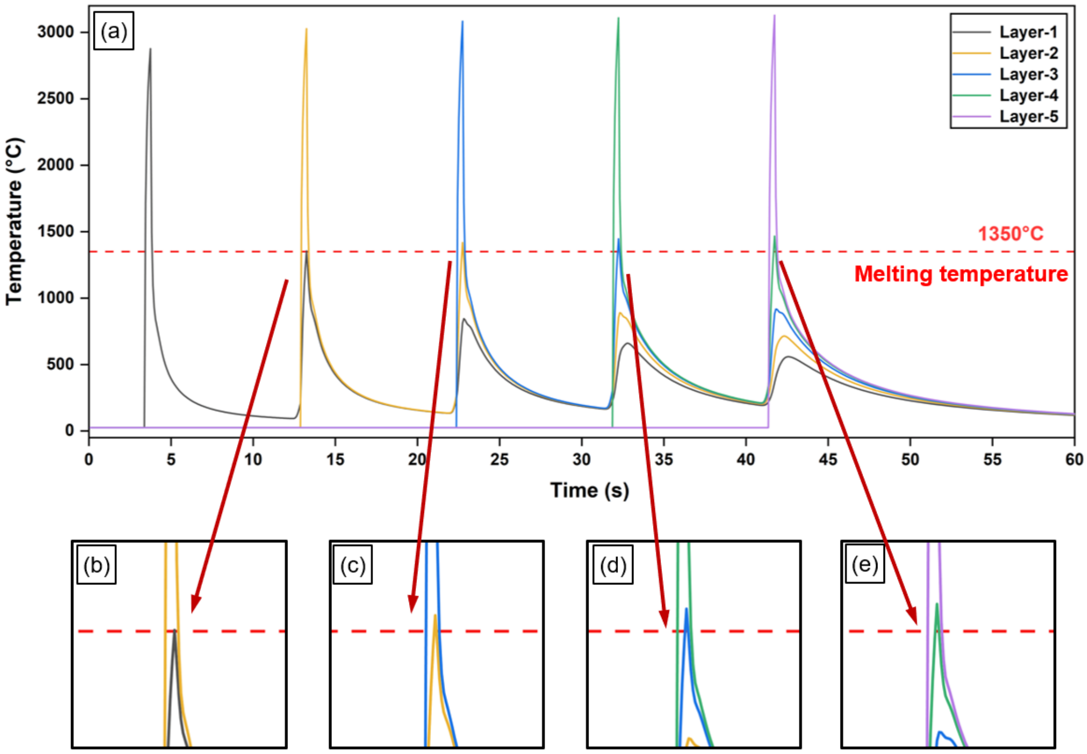

Figure 6.27 Predicted thermal history of five layer thin wall deposition

6.3.2.4 Variation of cooling rates and thermal gradient in five layers

Cooling rates (CR) and thermal gradients (G) in the five layers were measured from the numerical model. Results of CR and G across the fives layers are shown in Figure 6.28. The results of CR from Figure 6.28 (a) show that the CR is higher at the initial layer which continues to fall with the increase in layer numbers. This can be attributed to the high heat transfer during the initial layers. During the deposition of first layer, the substrate acts as heat sink, because of which the material cools faster. However, as the layer increases, the substrate effect reduces due to which the cooling rate comes down. These results are found in line with the experimental observations of thin walls (Figure 6.13), where a fine microstructure is observed at lower layers followed by coarse microstructure). However, as shown in Figure 6.13, the grain morphology is found changing over the height of thin wall, which is governed by the ration of *G/R*, where *R* is the solidification velocity. Figure 6.28 (b), shows the thermal gradient in different layers. It can be seen that the *G* falls with the increase in layer numbers. At higher G value, the ratio *G/R* is higher, indicating a dendritic microstructure. However, at higher layer where the value of *G* is less, the ratio of *G/R* also goes down, indicating an equiaxed morphology. The trends of both cooling rates and thermal gradients are found in agreement with the microstructural results shown in Figure 6.13.

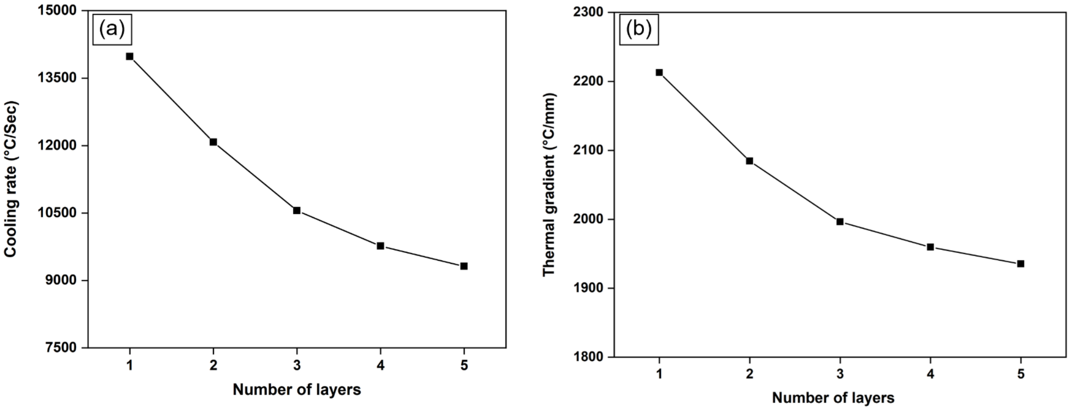

Figure 6.28. Predicted (a) cooling rates and (b) thermal gradeints during the five layer thin wall deposition

6.3.2.5 Effect of process parameters on peak temperature and melt pool depth

Figure 6.29 show the peak temperatures at different laser powers, scan speeds and layers. The predictions from the numerical model are found to follow the physical behavior of the LDED process where, increasing the laser power is found to increase the peak temperature. The increase in temperature is due to the increase of laser energy being provided. Similarly, it can also be observed that the with the increase of scan speed at a given laser power, the peak temperature is going down. At higher scan speeds, the interaction time between the laser and material goes down, as a result of which the predicted peak temperature goes down. Qualitative analysis of these results show that laser power has more influence on the peak temperature followed by scan speed.

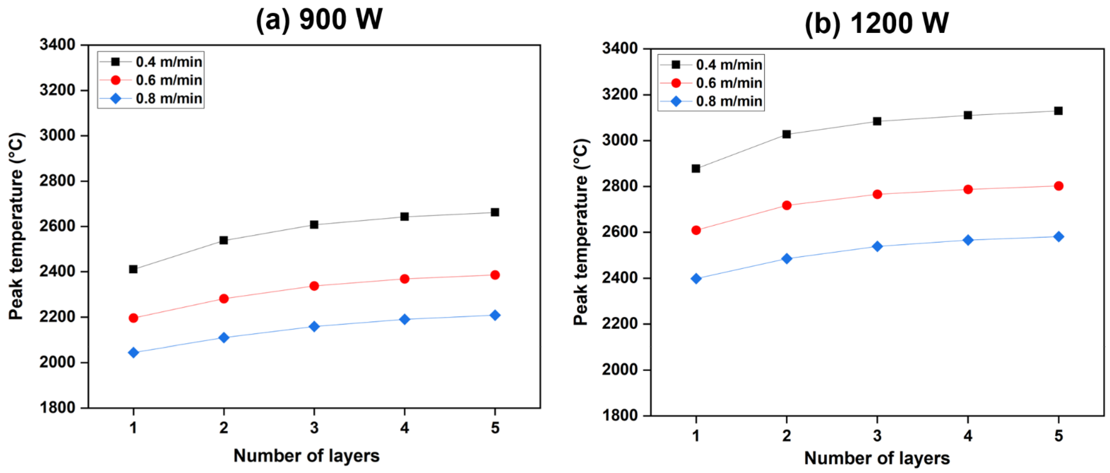

Figure 6.29 Peak temperatures predicted at (a) 900 W and (b) 1200 W laser powers and different scan speeds

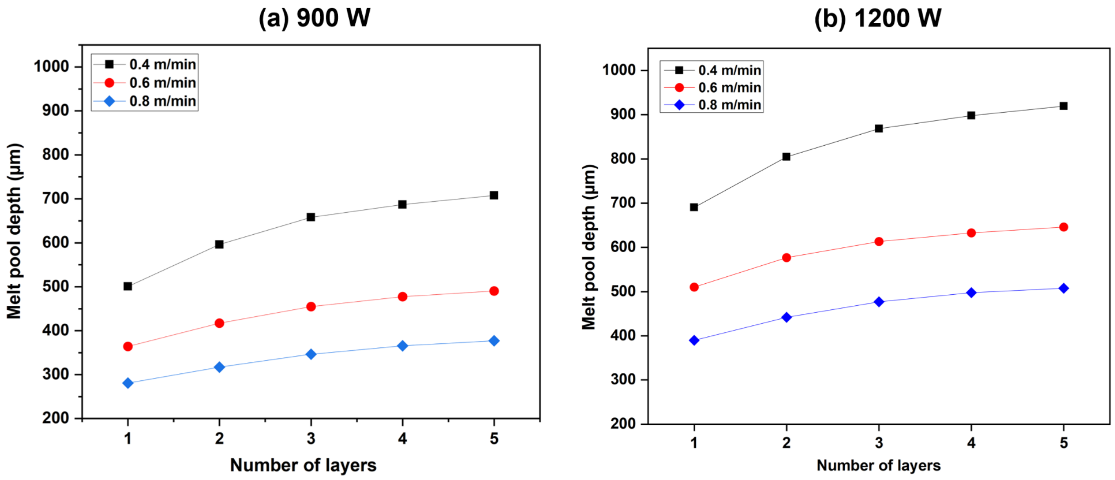

Figure 6.30 Melt pool depth predicted at (a) 900 W and (b) 1200 W laser powers and different scan speeds

Similarly, the predicted temperature contours at different laser powers and scan speeds were post processed to analyze the melt pool depth during the thin wall deposition. Results of melt pool depth are different laser powers and scan speeds are show in the Figure 6.30. The results of melt pool depth were found in line with the predicted peak temperature results. The melt pool depth is found increasing with the increase of laser power at all scan speeds. This is due to the increase of laser energy at higher powers, leading to increase the peak temperature and thereby the melt pool depth. Similarly with the increase of scanning speed, melt pool depth is also decreasing. This can be attributed to the lower interaction time between the laser and substrate or previous layer at high scan speeds. In addition, the melt pool depth is found increasing with the increase of number of layers. This is due to the accumulation heat in the thin wall, as discussed in the previous sub-section. The qualitative analysis of these results show that laser power has more influence on the melt pool depth followed by scan speed.

6.3.2.6 Effect of process parameters on peak temperature and melt pool depth

Results of cooling rates and thermal gradient at different laser power and scan speeds is shown in Figure 6.31. The predictions from numerical model show an increase in the cooling rates with the increase in scan speed at both the laser powers, Figure 6.31 (a). At higher scan speeds, the resulting melt pool is small which cools down quickly leading to an increase in the cooling rate. Cooling rate affects the grain size during the solidification. A higher cooling rate indicate a finer grain structure whereas a lower cooling rate indicate a coarse grain structure. The experimental results of grain size obtained from the microscopy are shown in Figure 6.12, and were found in agreement with the cooling rate predictions made by the numerical model. In addition, the cooling rate is found to be affected by the laser power also. It is found that increasing the laser power increases the peak temperature, thus the melt pool takes more time to reach solidus temperature which in turn results in a decreased cooling rate.

Thermal gradients were measured in the melt pool at different laser powers and scans speeds and the predictions are shown in Figure 6.31 (b). It is found that thermal gradient increases with increase in laser power whereas it decreases with increase in scan speed. At higher laser power, the peak temperature increases which results in higher temperature difference within the melt pool. Hence, it leads to increase in thermal gradient. The predictions of thermal gradients give an information about the thermal stresses (residual stresses). A higher thermal gradient leads to increase in thermal stresses. In this thesis, the scope of the work presented is limited to the thermal analysis.

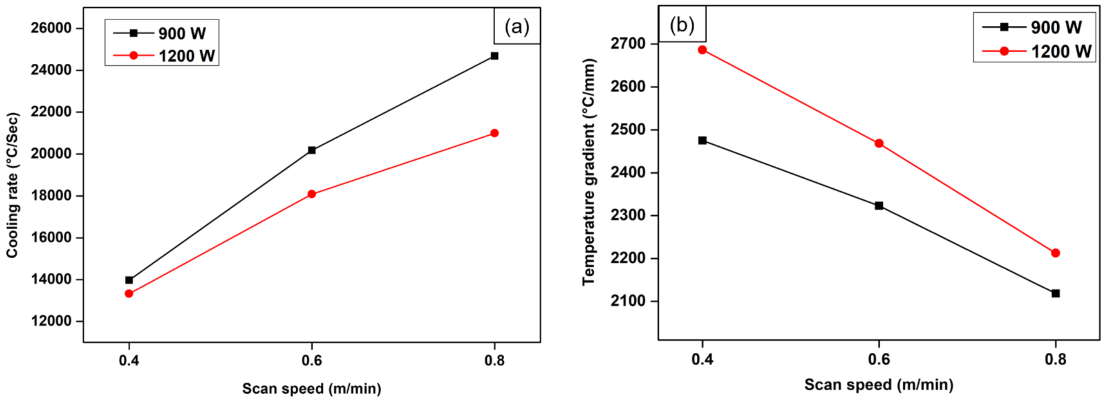

Figure 6.31 Effect of process parameters on (a) cooling rates and (b) thermal gradients

6.4 Conclusions

This paper aims to fabricate six thin walls of IN625 using LDED process to elucidate the effect of process parameters on the build geometry, porosity, microstructure, surface roughness and mechanical properties in two orientations. The key conclusions from this study are as follow:

- For the thin walls, where the scan speed is low (W-1 and W-4, *v*= 0.4 m/min), the geometry is found to be highly unstable at both beginning and end. This may be attributed to increase in the laser energy density at lower scan speed and high laser material interaction at starting due to laser acceleration. However, by using an optimised process parameter, a stable geometry can be obtained.

- Thin walls are found to exhibit a maximum relative density of 99.3%. However, for the thin walls deposited at lower power and high scan speed, low relative density of 97% is observed due to the presence of lack of fusion porosities.

- Microstructure in the thin walls is found to reducing with the increase in scan speed. In addition, the microstructure is also found to be varying along the build direction, which is due to the inhomogeneous heat transfer through the build height.

- Surface roughness is found to be varying with both process parameter and along the build height. Roughness is found to be increasing with the increase in scan speed which can be attributed to the reduced laser-particle interaction time at higher scan speeds, as a result of which a small, unmelted particles can be found on the surface of thin walls, adding roughness.

- Surface roughness is also found to be varying through the build height. At the initial layers, surface roughness was low which was found to increase along the build height.
- The horizontal samples were found to exhibit high mechanical strength compared to the vertical samples.
- Hardness test results show an increase in the hardness values with the increase in scan speed. However, for the case where low power and higher scan speed are used, the resulting hardness value is less. This is due to the increase in lack of fusion porosity at low power and high scan speeds.

CHAPTER 7

LASER DIRECTED ENERGY DEPOSITION AS A REPAIR TECHNOLOGY FOR SERVICED INCONEL 625 PARTS

One of the key advantages where LDED stands apart from other metal AM techniques is the capability to repair parts. In this study, an attempt has been made to repair an IN625 serviced part with four different deposition strategies using the LDED process. The repaired samples were subsequently post-treated using solution heat treatment to obtain consistent microstructure and mechanical properties for all the sample conditions. Further, the repair capabilities in all four deposition strategies are compared using macrostructure, microstructure, tensile properties, and micro-hardness studies in the wrought, as deposited, and heat-treated conditions.

7.1 Materials and methods

7.1.1 Materials

Tensile specimens extracted from a wrought plate of IN625 alloy and subjected to fatigue loading (to mimic a serviced component) were selected as specimens for repair using the LDED process. IN625 powder having a particle size in the range of 40-105 m with spherical morphology (Figure 7.1) was used for the deposition. The chemical composition of both Inconel 625 plate and powder obtained from elemental analysis using Energy Dispersive Spectroscopy (EDS) is shown in Table 7.1.

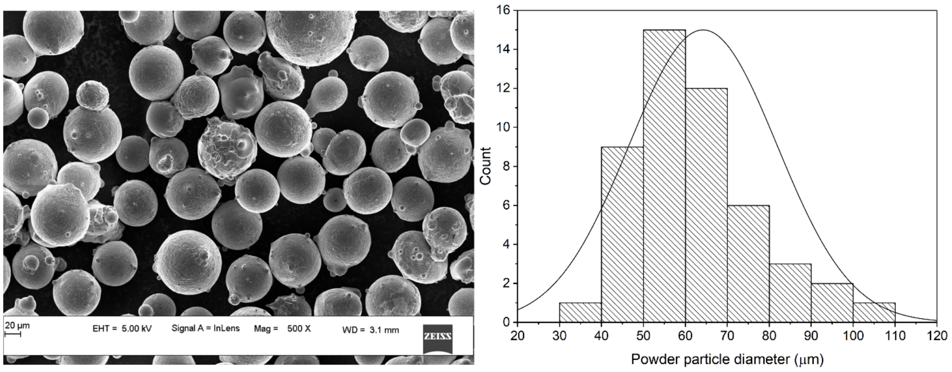

(a) (b)

Figure 7.1 (a) SEM image of the powder particles and (b) particle size distribution of IN625 powder used for deposition

Table 7.1 Chemical composition of Inconel 625 plate and powder used in the study

Form of Feedstock	Weight percentage (%)									
	Ni	Cr	Mo	Nb	Fe	Ti	Mn	Si	C	Other
Inconel 625 plate	54.3	23.5	6.2	2.69	3.73	0.22	0.36	0.01	0.057	Bal.
Inconel 625 powder	55.2	23.4	5.3	2.9	4.4	0.29	0.45	0.01	0.082	Bal.

7.1.2 Experimental setup

IN625 depositions were carried out using an in-house developed LDED system at Raja Ramanna Centre for Advanced Technology, Indore, India. More information about the system can be found in chapter 3. Argon gas at a flow rate of 6 lpm was used as a carrier gas and shielding gas to deliver the powder through coaxial nozzles. The depositions were carried out in ambient atmosphere.

7.1.2.1 Pre-processing

Figure 7.2 shows the schematic representation of the experimental procedure followed in the present study. Sub-size tensile test specimens as per ASTM E8M (ASTM E8 / E8M-16ae1, 2013) were extracted from Inconel 625 alloy plates. The dimensions of all the tensile specimens were reduced by approximately 900 µm (close to the deposition height) to match the actual dimensions of the standard tensile test coupon after deposition (Figure 4). Further, to physically simulate a component in service, the tensile specimens were subjected to fully reversed fatigue loading. It has been documented in published literature that for a service life of 15,000 cycles the strain amplitude should be around 0.004 (Chou and Earthman, 1997; Dodaran et al., 2022). Therefore, the tensile specimens were subjected to fully reversed fatigue loading ($R = -1$) for 15000 cycles at a frequency of 5 Hz and strain amplitude of 0.4%. After the completion of fatigue cycling, all the test samples were visually inspected for any significant plastic deformation and presence of defects such as cracks. After which, the samples were thoroughly cleaned to remove any oil and dust from the surface by dipping in a bath of Ethanol.

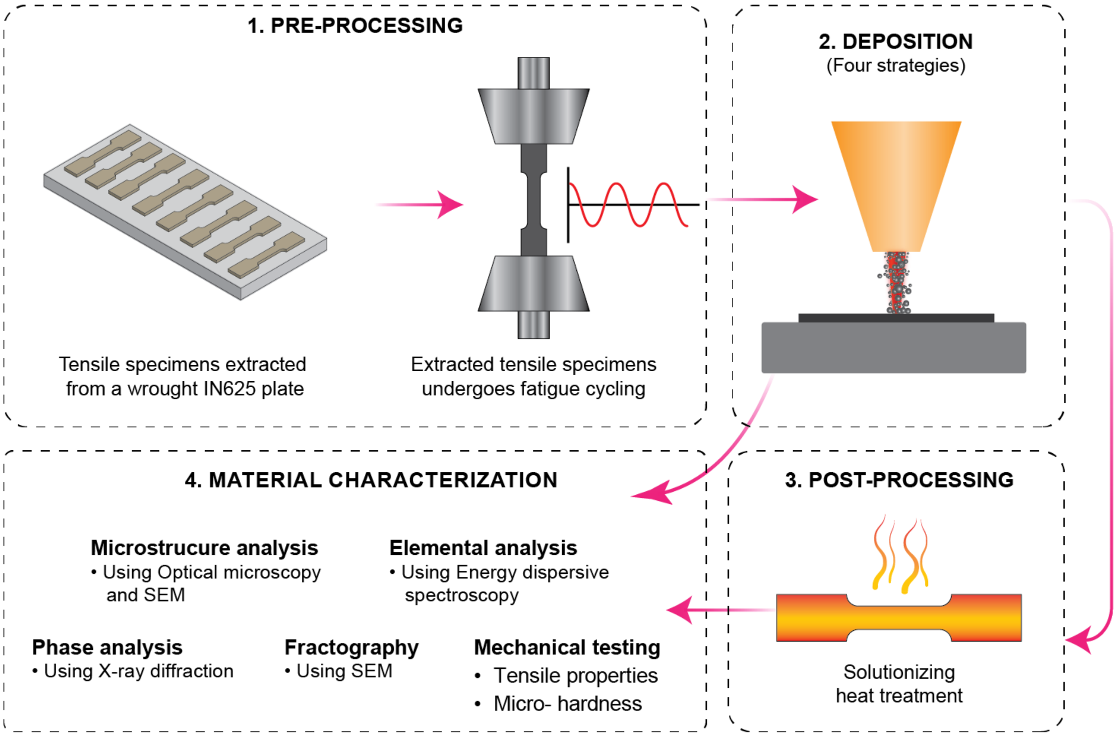
1. PRE-PROCESSING
Tensile specimens extracted from a wrought IN625 plate
Extracted tensile specimens undergoes fatigue cycling
2. DEPOSITION
(Four strategies)
3. POST-PROCESSING
Solutionizing heat treatment
4. MATERIAL CHARACTERIZATION
Microstrucure analysis
• Using Optical microscopy and SEM
Elemental analysis
• Using Energy dispersive spectroscopy
Phase analysis
• Using X-ray diffraction
Fractography
• Using SEM
Mechanical testing
• Tensile properties
• Micro- hardness

Figure 7.2. Schematic representation of the methodology used in the present study

7.1.2.2 Deposition using LDED process

Subsequently, deposition was carried out on the tensile specimens to mimic the repair of fatigued specimens using the LDED process. IN625 was deposited on the (a) top face, (b) top and bottom faces, (c) one side face and (d) both side faces, as shown in Figure 7.3. These depositions will henceforth be referred to as the four deposition strategies in the manuscript. Table 7.2 presents the LDED process parameters used for deposition. The process parameters used for the deposition were optimised by depositing single tracks prior to the actual deposition. The process parameters, as identified in the single-track study in chapter 5, yielding minimum porosity and a sound/ continuous track were selected for the deposition to repair serviced components. The samples were left to cool in the machine setup after the deposition process.

Table 7.2. Process parameters used for the deposition

Sl No.	Process Parameters	Value
1	Laser power [W]	1200
2	Scan speed [m/min]	0.6
3	Powder feed rate [g/min]	8
4	Laser beam diameter [mm]	2.5

7.1.2.3 Post-processing

To study the effect of heat-treatment, solution treatment was carried out using a high temperature muffle furnace with quenching facility (Make: Therelek; Model: Bottom Loading Furnace). The maximum temperature at which the furnace can operate is 1400°C. To achieve complete static recrystallization, solution treatment was carried out by increasing the temperature of the samples from room temperature to 1200° C at a rate of 5 °C/min in an open atmosphere (Hu et al., 2020a). The samples were soaked for a duration of 90 minutes followed by water quenching to room temperature.

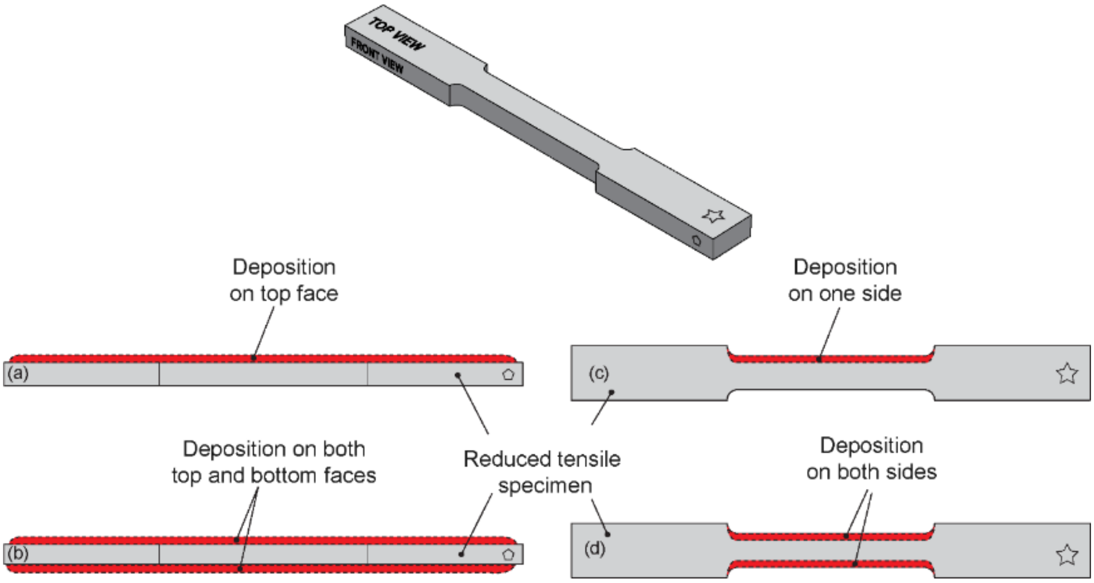
TOP VIEW
FRONT VIEW
Deposition on top face
Deposition on one side
(a)
(c)
Deposition on both top and bottom faces
Reduced tensile specimen
Deposition on both sides
(b)
(d)

Figure 7.3. Schematic representation of the four deposition strategies (a) deposition on top face, (b) deposition on both top and bottom faces, (c) deposition on one side and (d) deposition on both sides

7.1.3 Material characterization

After deposition, the specimens were sectioned for metallographic studies using the Wire-Electric Discharge Machining (WEDM) process. Next, the samples were fixed in an acrylic mount and subsequently polished with SiC sheets of grit size varying from 200-2000. Next, the samples were subjected to cloth polishing in a dispersed aqua-alumina solution. Samples after mirror polishing were electrolytically etched using a 10% aqua–oxalic acid solution at 10–15 V potential difference for 10–20 s. The cross-section of the samples was observed under a stereomicroscope (Make: Leica) for macroscopic observations. The microstructure was then characterised using both Optical Microscope (OM) (Make: Carl-Zeiss) and Scanning Electron Microscope (SEM) (Make: Zeiss Gemini). For elemental and phase analysis, Energy Dispersive Spectroscopy (EDS) (Make: EDAX, AMETAK) and X-ray diffraction (XRD) (Make: Empyrean, Malvern Panalytical), were respectively used. The XRD analysis was performed using a CuKα source at a speed of 7°/min for a 2θ range of 10°-90°. To experimentally validate the change in crystallite size between as-deposited and solution treated conditions, Scherrer equation (Suryanarayana and Norton, 1998) as given below was used.

$$L = \frac{K\lambda}{\beta \cos\theta} \tag{7.1}$$

Where, L is the mean crystallite size (in nm), K is a dimensionless shape factor = 0.94, λ is the X-ray wavelength (Cu-Kα radiation of wavelength 1.5406 Å), β is the FWHM in radians and θ is the Bragg angle (in degrees). Further, lattice parameter (a) was calculated using equations (7.2) and (7.3)

$$d = \frac{n\lambda}{2\sin\theta} \tag{7.2}$$

$$d = \frac{a}{\sqrt{h^2 + k^2 + l^2}} \tag{7.3}$$

Where, n is the "order" of reflection, which is usually considered as unity, λ is the wavelength of the incident X-rays (1.5406 Å), d is the interplanar spacing of the crystals, θ is the angle of incidence, a is the lattice parameter, h, k and l are the corresponding miller indices.

The tensile tests were conducted at room temperature on a UTM machine (Make: Instron) at a constant strain rate of 10^{-3}/sec. The dimensions of the tensile specimen dimensions were based on the ASTM E8M standard (ASTM E8 / E8M-16ae1, 2013). To determine statistical significance in mechanical properties between as-deposited and solution treated samples, a student's t-test was conducted (Myers and Myers, 2007). Vickers micro-hardness tests (Make: Omnitech) were also carried out at a force of 300 g and a dwell time of 10 s to evaluate the change in the mechanical properties between as-deposited, heat-treated and wrought alloy samples.

7.2 Results and discussion

7.2.1 Macroscopic observations: Pre and post-deposition

Photographs of the tensile samples after undergoing (a) fatigue, (b) deposition on the top surface, (c) deposition on top and bottom sides, (d) deposition on one side and (e) deposition on both sides are shown in Figure 7.4. It can be observed from Figure 7.4 (a) that the tensile test specimen extracted from the IN625 plate does not show any substantial deformation after undergoing fatigue cycling. Similar observations were noticed on the other fatigued tensile specimens. Dimensions of all the samples were measured before and after the deposition to obtain inferences on any distortion that may occur in LDED processed samples due to cyclic heating and cooling. Subsequently, the deposited samples were cut using the WEDM process to measure the thickness and consistency of deposition at different locations on the samples. Figure 7.5 shows the macroscopic images of the cross-section as well as the measured thickness of deposition for various deposition strategies. The height of deposition was found to be consistent at ~1.02 mm with a maximum deviation of ±0.25 mm at the centre of all the samples.

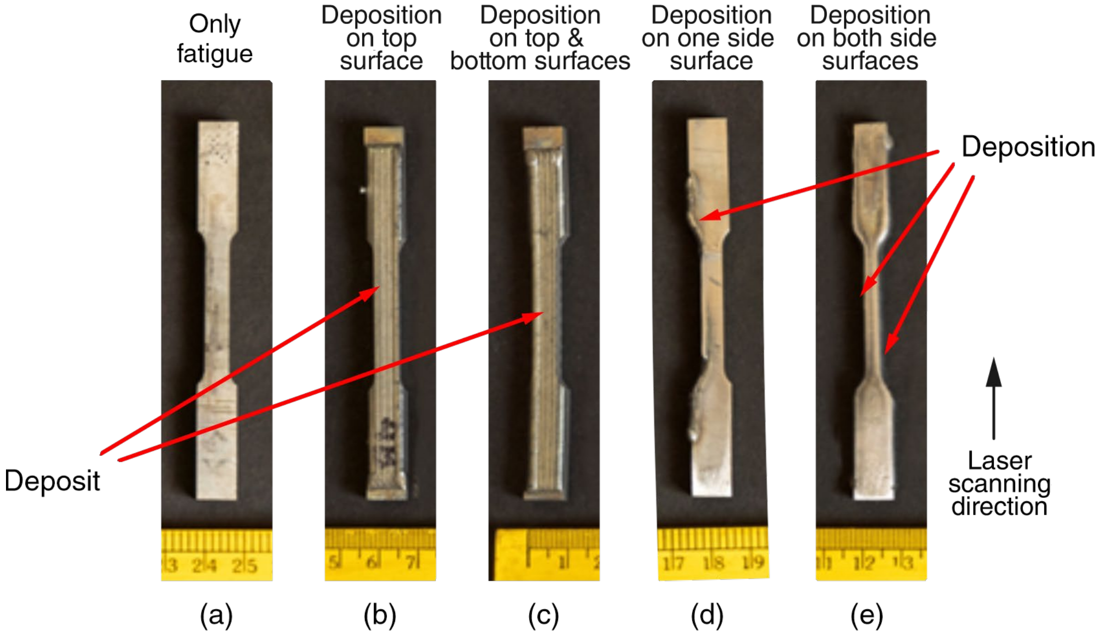
Only fatigue
Deposition on top surface
Deposition on top & bottom surfaces
Deposition on one side surface
Deposition on both side surfaces
Deposition
Deposit
Laser scanning direction
(a)
(b)
(c)
(d)
(e)

Figure 7.4. Tensile specimen after (a) fatigue, (b) deposition on top surface, (c) deposition on top and bottom surfaces, (d) deposition on one side surface and (e) deposition on both side surfaces

However, at the edges of the samples, the height of deposition was found to be comparatively lower than that of the height at the centre. This can be attributed to the reduction in the catchment efficiency and increase in the melt pool depth due to the decreased area available for heat conduction (Figure 7.6). The reduction in catchment efficiency can be due to more amount of metal powder falling outside the melt pool while depositing at the edges of the substrate (Figure 7.6 (a)). Further, the temperatures in the melt pool tend to increase at the edge due to the decreased area available to conduct heat. This results in a deeper melt pool, melting more material of both substrate and powder at the edges (Liu et al., 2021c). Thus, a competing phenomenon can take place at the edges and the lower deposit height at the edge can be attributed to the dominating effect of reduction in the catchment efficiency when compared to increased melt pool size due to the decreased area available for heat conduction.

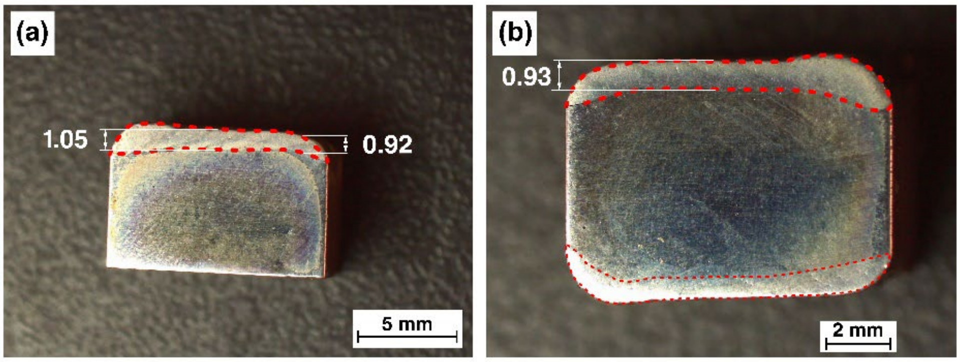
(a)
1.05
0.92
5 mm
(b)
0.93
2 mm

Top repair

Top and Bottom

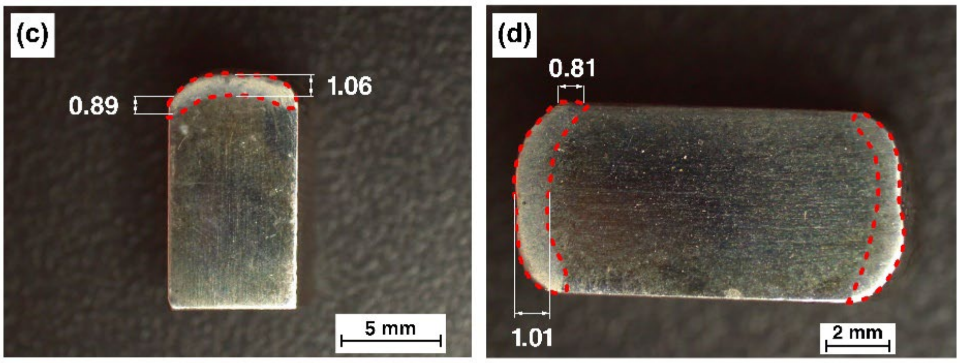
(c)
0.89
1.06
5 mm
(d)
0.81
1.01
2 mm

One side

Both sides

Figure 7.5. Cross-sectional macroscopic view of the four deposition strategies (a) deposition on top surface, (b) deposition on both top and bottom surfaces, (c) deposition on one side surface and (d) deposition on both sides surfaces

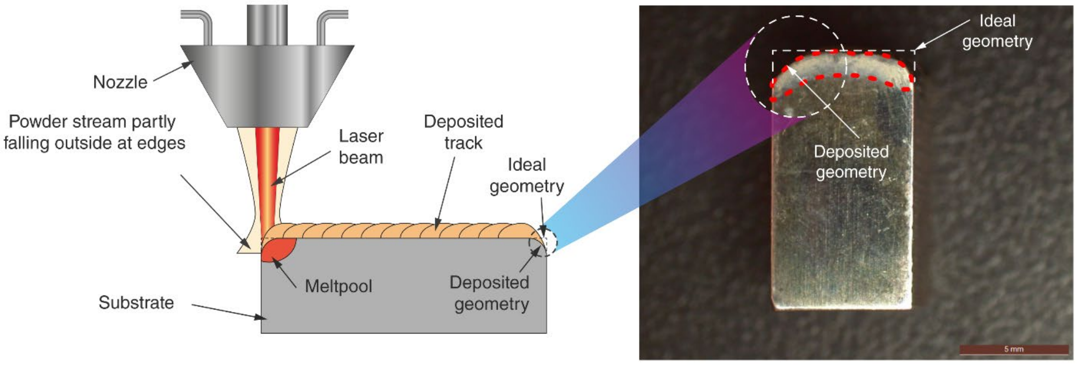
Nozzle
Powder stream partly falling outside at edges
Laser beam
Deposited track
Ideal geometry
Substrate
Meltpool
Deposited geometry
Ideal geometry
Deposited geometry
5 mm

(a)

(b)

Figure 7.6. Deposition of material at the edge of substrate (a) schematic layout and (b) macroscopic image

7.2.2 Microstructural analysis

The observed microstructures from the as-deposited sample are shown in Figure 7.7. The microstructure observed in all the deposition strategies was found to be similar, as same process parameters were used for all depositions. It can be seen from Figure 7.7 (a), that the microstructure in the deposition zone exhibits a dendritic morphology. It is well documented that rapid cooling is observed in samples processed using LDED (Nair et al., 2020). These high cooling rates lead to a columnar structure with a dendritic morphology (Wang et al., 2021b), as observed in Figure 7.7 (a) & (b). As can be seen from Figure 7.7 (b), the grain growth is towards the top of the melt pool in the direction opposite to the heat transfer. In order to quantify the prevailing thermal conditions in different deposition strategies, the Primary Dendrite Arm Spacing (PDAS) was measured. It was found that PDAS values are low for deposition on top as well as for deposition on top-&-bottom faces (4.12 ± 1.39 μm) when compared to the PDAS values for deposition on both one side as well as two-sides (7.21 ± 2.95 μm). This may be due to the increase in temperature due to the lower area available for heat conduction in the case of one side and two-sided depositions. The increase in temperature leads to slow cooling which results in coarse grains.

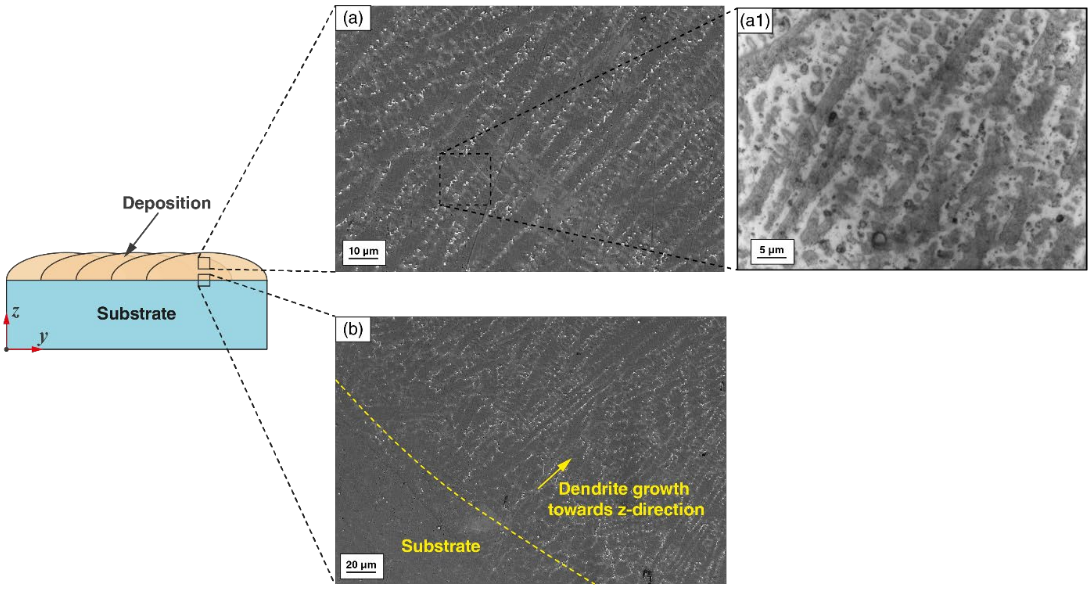

Figure 7.7. Microstructure of the as-deposited samples (deposition on the top surface) at different locations in the deposited material

Figure 7.8 show the microstructure of the solution heat-treated samples. It can be observed from these micrographs that the melt pool boundaries have completely disappeared after the solution heat treatment. Further, the dendritic structure present in the as-deposited samples (

Figure 7.7) was also found to disappear/dissolve after the heat treatment. However, the microstructure of the heat-treated samples reveals the presence of recrystallized equiaxed grains (Figure 7.8 (a)). This indicates static recrystallization after heat-treatment as observed by Hu. et al (Hu et al., 2019). It can also be seen that the microstructure obtained post heat treatment is rich in twin boundaries (Figure 7.8(b)) which usually occur after heat treatment of IN625 alloy at higher temperatures (Gao et al., 2021). Figure 7.9 & Figure 7.10 present the elemental analysis carried out using EDS for the as deposited and solution treated samples, respectively. From Figure 7.9, it can be observed that there exists an NbC rich phase (Spot-1) at the inter-dendritic zones of the as-deposited samples (Carrozza et al., 2023; Dubiel and Sieniawski, 2019; Hu et al., 2020c). However, after the heat treatment, the volume fraction of the NbC phase reduces. This indicates that NbC gets partly dissolved into the γ matrix after heat treatment. This is in line with the observations reported in the literature by Hu et al. (Hu et al., 2019).

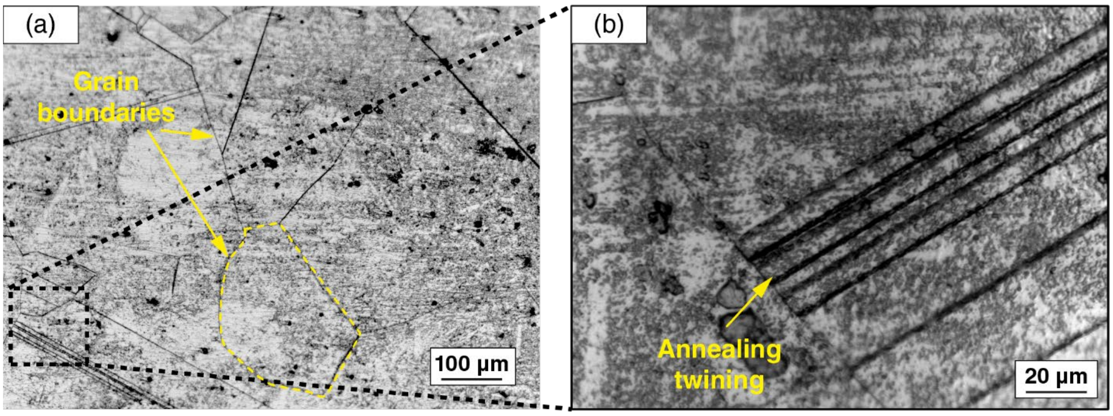

Figure 7.8. Microstructural observations of the deposited material after solution treatment

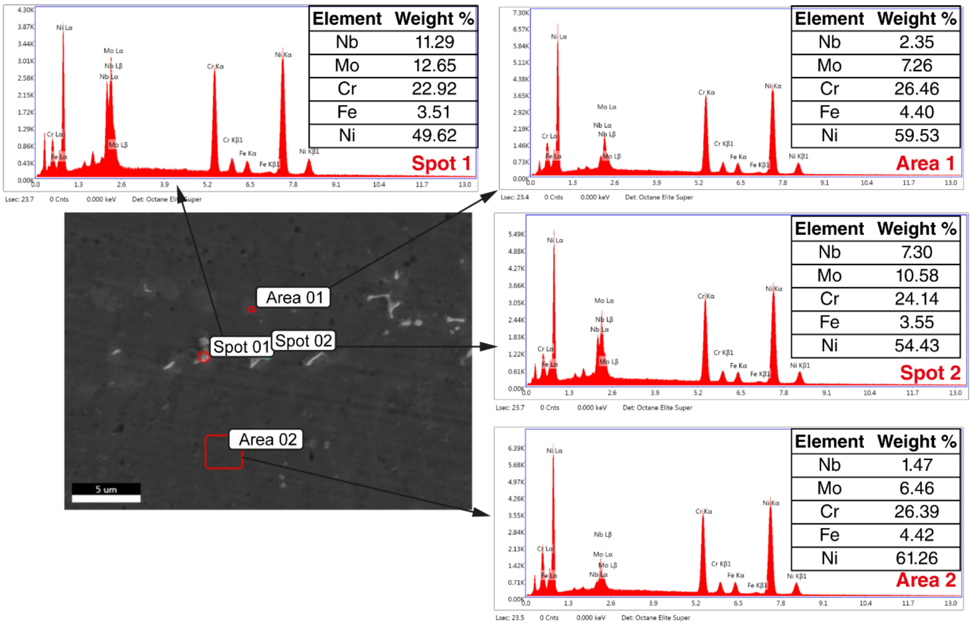

Spot 1

Element	Weight %
Nb	11.29
Mo	12.65
Cr	22.92
Fe	3.51
Ni	49.62

Area 1

Element	Weight %
Nb	2.35
Mo	7.26
Cr	26.46
Fe	4.40
Ni	59.53

Spot 2

Element	Weight %
Nb	7.30
Mo	10.58
Cr	24.14
Fe	3.55
Ni	54.43

Area 2

Element	Weight %
Nb	1.47
Mo	6.46
Cr	26.39
Fe	4.42
Ni	61.26

Figure 7.9. EDS analysis of the as-deposited sample (deposition on top surface) at different locations

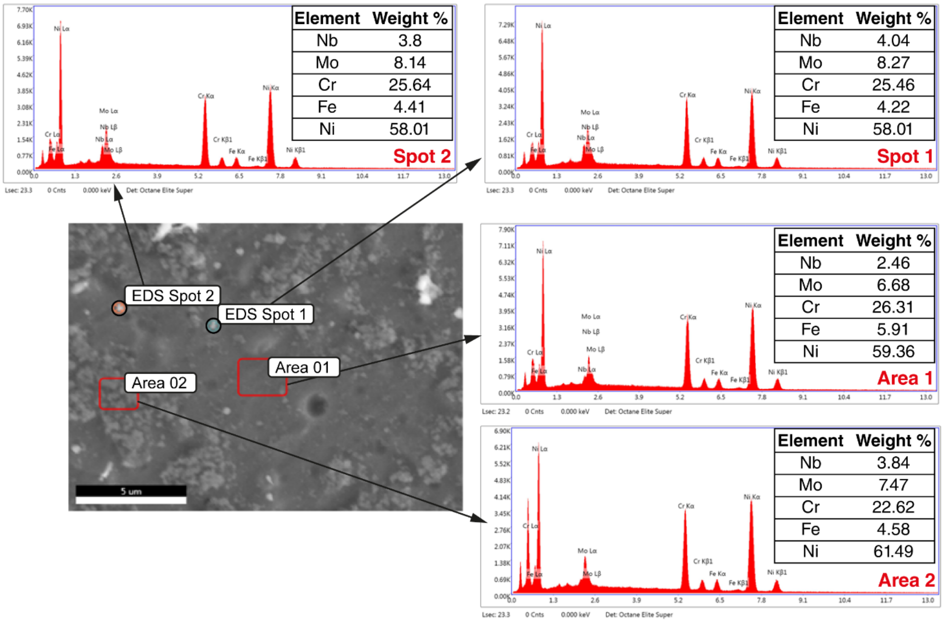

Spot 2

Element	Weight %
Nb	3.8
Mo	8.14
Cr	25.64
Fe	4.41
Ni	58.01

Spot 1

Element	Weight %
Nb	4.04
Mo	8.27
Cr	25.46
Fe	4.22
Ni	58.01

Area 1

Element	Weight %
Nb	2.46
Mo	6.68
Cr	26.31
Fe	5.91
Ni	59.36

Area 2

Element	Weight %
Nb	3.84
Mo	7.47
Cr	22.62
Fe	4.58
Ni	61.49

Figure 7.10. EDS analysis of solution treated sample (deposition on top surface) at different locations

Figure 7.11 presents the X-ray diffraction (XRD) analysis of as deposited and heat-treated IN625 samples which are compared with the wrought IN625. XRD was carried out on the section perpendicular to the build direction. As reported in several studies (Ferreri et al., 2020; Wang et al., 2021b), the XRD spectrum of additively manufactured Ni-based superalloy samples is mainly composed of γ-FCC matrix. Results obtained from the XRD analysis are in agreement with previously published literature i.e. FCC (111) γ and (200) γ peaks were observed for all the cases discussed in the study as shown in Figure 7.11 (Ferreri et al., 2020; Wang et al., 2021b) (PDF number: 00-004-0850). The presence of dendrite microstructure in the case of as-deposited samples and its orientation towards the top of deposition contributes to a strong (200) γ peak. These results fall in line with the existing literature wherein (200) γ planes were found to orient along the build direction (Vikram et al., 2020). In contrast to as-deposited samples, a comparatively low (200) γ peak was observed in samples subjected to solution heat treatment. This can be attributed to the dissolution of dendrites and the lack of preferred microstructural growth in heat-treated samples. It can also be observed that the width of the peak is comparatively lower in the heat-treated samples when compared to as-deposited samples (Jinoop et al., 2021b). This indicates that there is static recrystallization of the grains, and an increase in crystallite size (Hu et al., 2020c). The calculated crystallite sizes are 26.6 nm and 32.87 nm respectively for as deposited and solution treated conditions. The fine crystallite observed in the as-deposited samples can be attributed to the high cooling rates during the deposition process. However, after post processing, an increase in the crystallite size can be observed. This can be attributed to the coalescence of the particles during heat-treatment resulting in an increase in the crystallite size.

Lattice parameter values of 3.5968 Å and 3.5795 Å were obtained upon solving equations (2) and (3), in as deposited and solution treated samples. The reduction in the lattice parameter of heat-treated samples can be attributed to the reduction in tensile stresses in these samples. Therefore, it can be seen that the residual stresses present in the as-deposited samples are reduced after solution treatment at 1200 °C, which is indicated by the shift in peak-positions, as seen in Figure 12 (b) (Hu et al., 2020b). The variation in the lattice strain can also be due to minor changes in the composition that may occur during processing (Maimaitiyili et al., 2019).

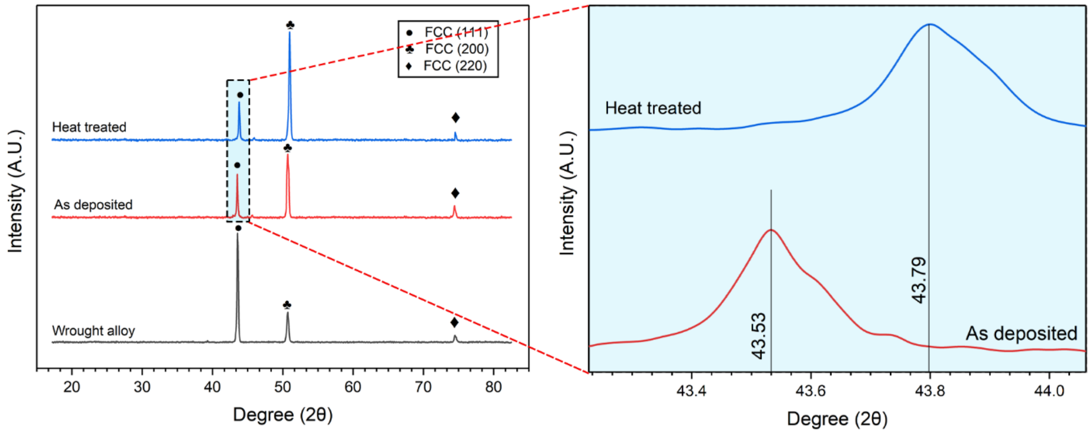

(a) (b)

Figure 7.11. (a) XRD peaks observed for wrought, as-deposited and heat-treated samples and (b) peak shift observed in heat treated sample

7.2.3 Mechanical properties

7.2.3.1 Tensile test & fractography

Variation in the Ultimate Tensile Strength (UTS), Yield Strength (YS) and elongation between various deposition strategies in both as deposited and solution treated conditions were investigated. Figure 7.12 shows the condition of the specimens before and after room temperature tensile test for different deposition strategies and wrought IN625 samples captured using a digital camera. Figure 7.13 shows the stress-strain curves of samples with different deposition strategies at both (a) as-deposited and (b) solution treated conditions. The observations drawn from the stress-strain curves are presented in Figure 7.14. (a) Ultimate tensile strength, (b) yield strength and (c) elongation in of wrought, as-deposited and solution treated A significant variation (as inferred from student's t-test, p-value = 0.0000835) in the UTS can be seen between the as-deposited and solution treated samples. A maximum ultimate tensile strength of 843 MPa was observed in the case of the wrought sample, while a minimum strength of 719 MPa was observed in the sample with one side deposition. The reduction in the UTS value can be attributed to the heat input given to the substrate. In a study on IN625 alloy by Salarian et. al. (Salarian et al., 2020), it was found that the UTS value increases with the increase in heat input during laser powder bed fusion process. In the samples where the deposition was carried out on the top or top and bottom surfaces, the area available for heat transfer (10 × 100 mm²) is higher than that of the samples where the deposition is carried out either on one side or both the sides (6 × 100 mm²). This leads to an increase in the temperature of the melt pool resulting in a slow cooling and coarser grains, as discussed in section 3.2.

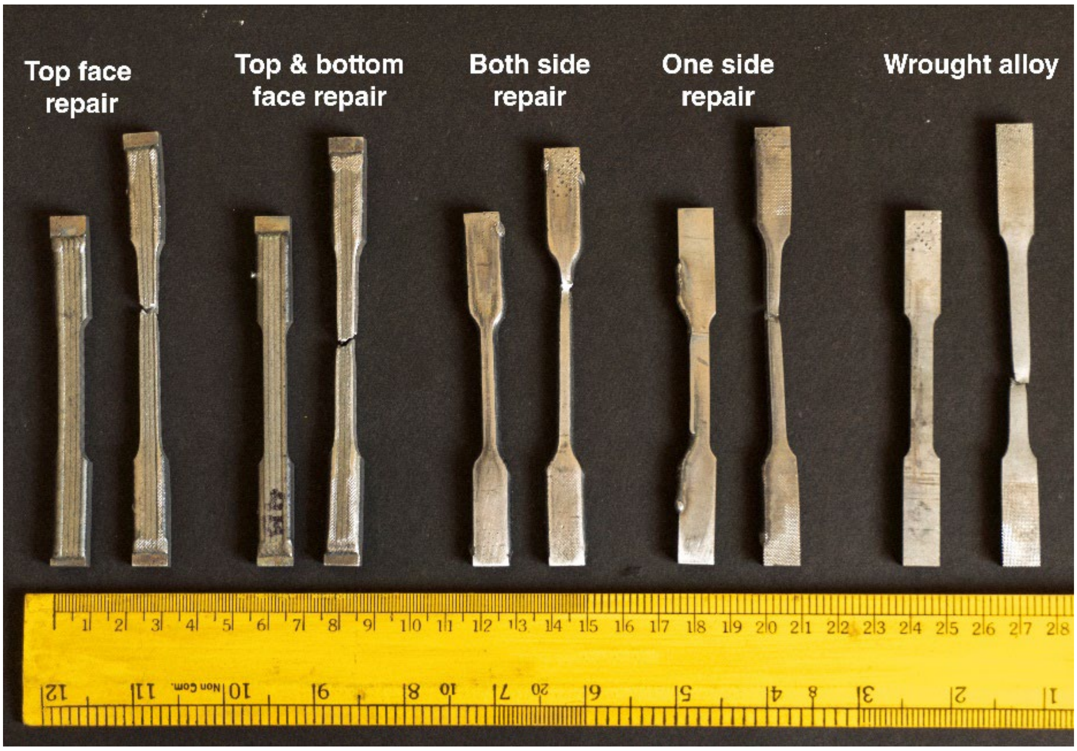
Top face repair
Top & bottom face repair
Both side repair
One side repair
Wrought alloy

Figure 7.12. Photographs of samples with different deposition strategies before and after tensile testing

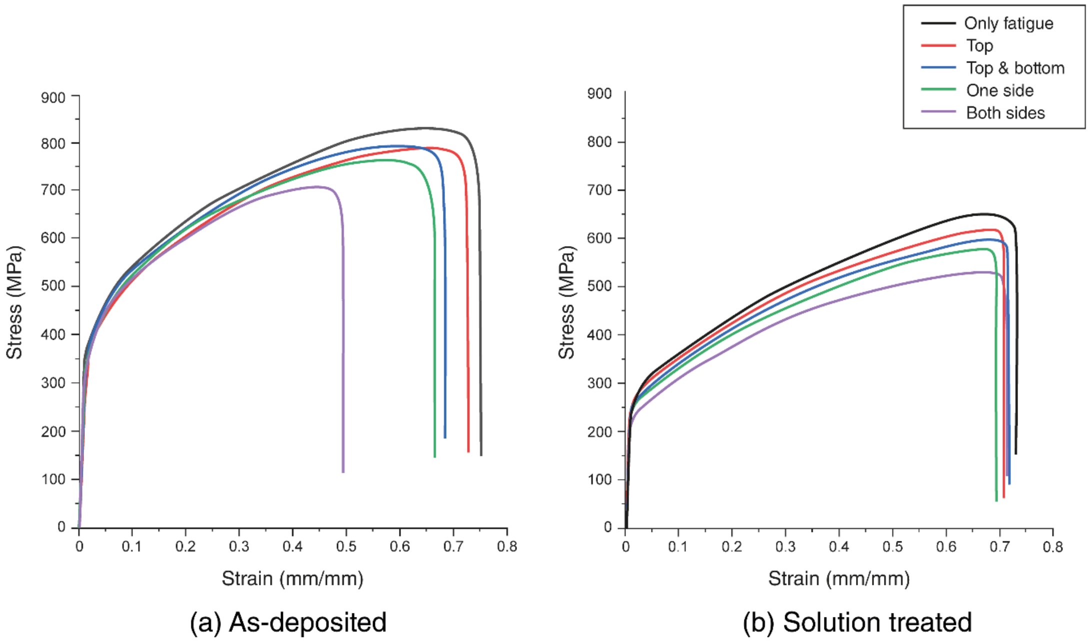

Figure 7.13. Stress-strain curves of (a) as-deposited and (b) solution treated samples at different deposition strategies considered in the study

Additionally, it was found that the magnitude of UTS is comparatively lower in the case of solution treated samples, but the order of the strength across the different deposition strategies is similar. The reduction in the strength after solution treatment is mainly due to the competing nature of the increase in grain size, reduction in dislocation density and formation of twins. Yield strength values for different deposition strategies in the case of the as-deposited condition vary between 300-350 MPa. For the solution-treated samples, yield strength values are in the range of 230-270 MPa. This observation indicates that the deposition strategies have a minimal influence on the YS. However, a significant difference (as inferred from student's t-test, p-value = 0.00021) in the YS value can be observed between the as-deposited and solution treated conditions, indicating a strong influence of solution treatment on the YS. In the solution treated samples the YS reduction can be attributed to grain coarsening and reduction in dislocation density after the heat treatment process (Wong et al., 2019). Therefore, the solution treated samples were easy to deform when compared to as-deposited samples. Similar results were observed in previous studies carried out on Inconel 625 (Wong et al., 2019; Yang et al., 2020).

It can be observed from Figure 7.14 that the elongation varies in a wide range for all the deposition strategies in the as-deposited condition. In the as-deposited samples, a maximum elongation of 72% was observed for the sample where deposition was carried out on the top surface. A minimum elongation of 50% was observed for the sample where deposition was carried on both sides. However, in contrast, the samples after solution treatment show a minimal variation in elongation (maximum elongation is 73% and minimum elongation is 69%). This can be attributed to the fact that post-solution treatments, the resulting microstructure and state of residual stress in all the samples become similar, which leads to comparable mechanical properties in all samples subject to solution treatment.

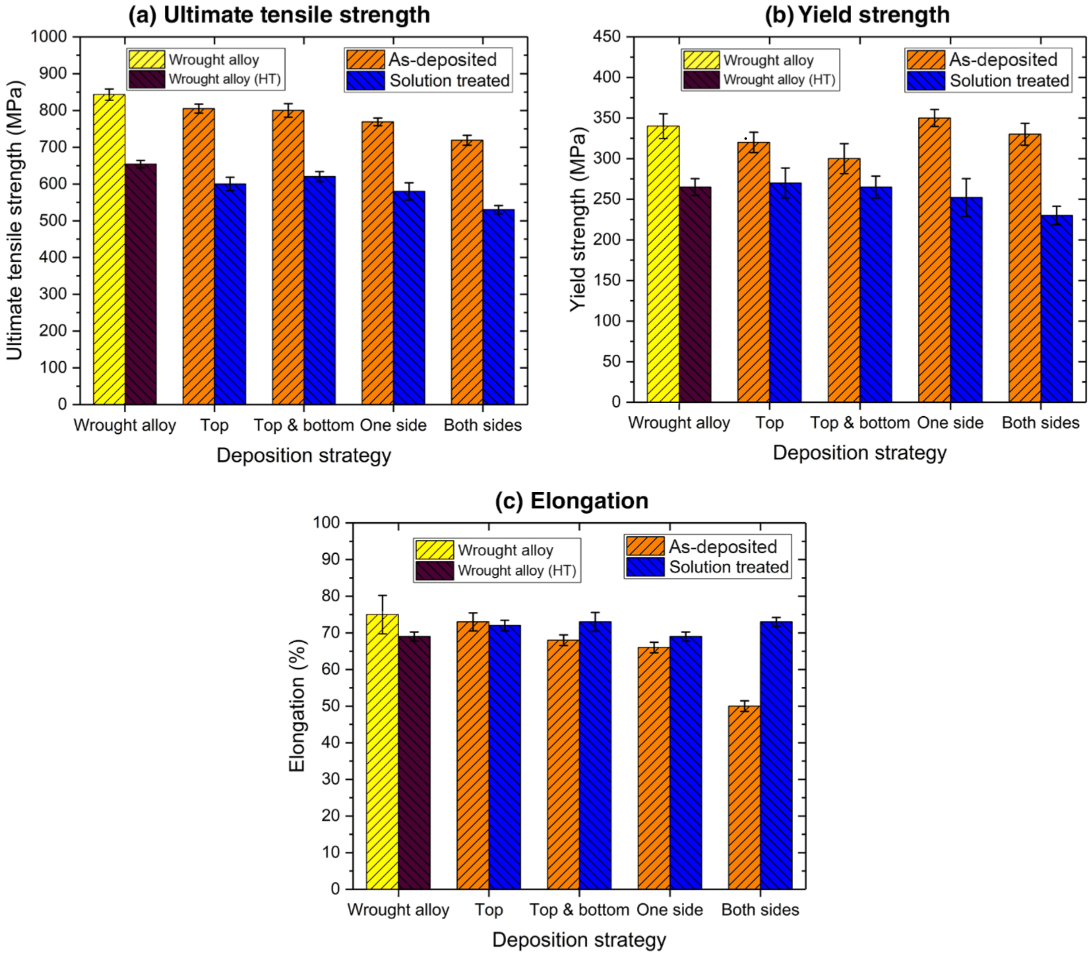

Figure 7.14. (a) Ultimate tensile strength, (b) yield strength and (c) elongation in of wrought, as-deposited and solution treated samples

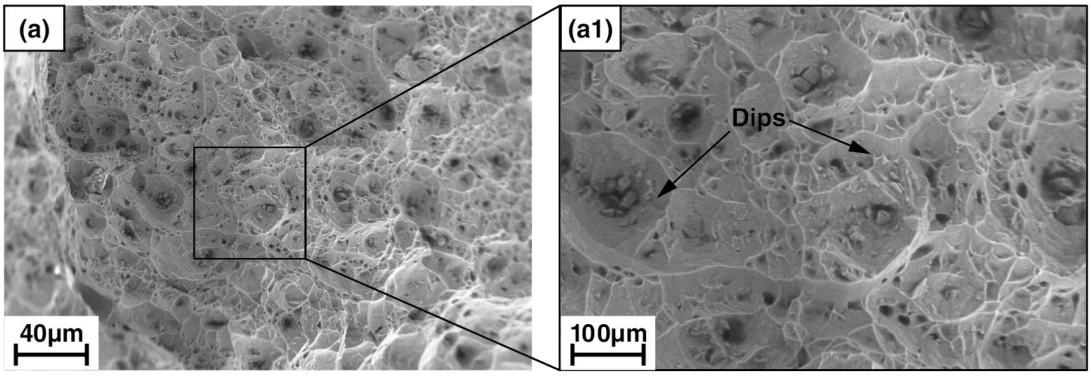
(a)
40µm
(a1)
Dips
100µm

Before solution treatment (Top repair)

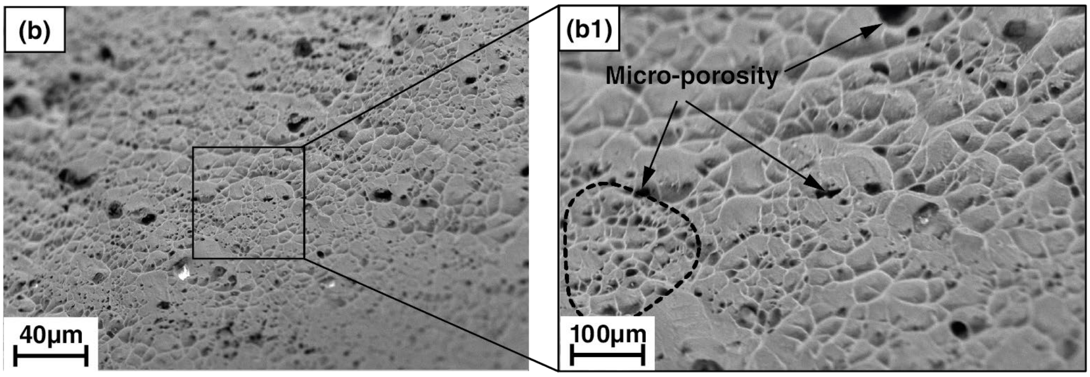
(b)
40µm
(b1)
Micro-porosity
100µm

After solution treatment (Top repair)

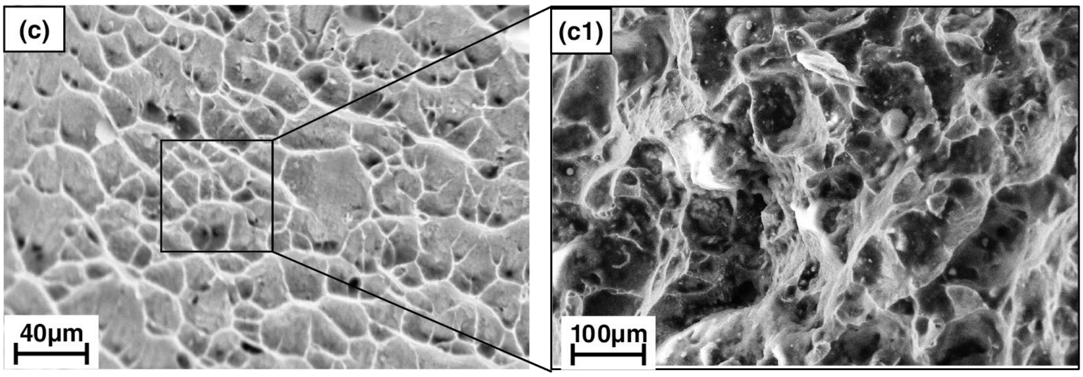
(c)
40µm
(c1)
100µm

Wrought alloy

Figure 7.15. Fractographs of (a) as-deposited, (b) solution treated and (c) wrought alloy fractured samples

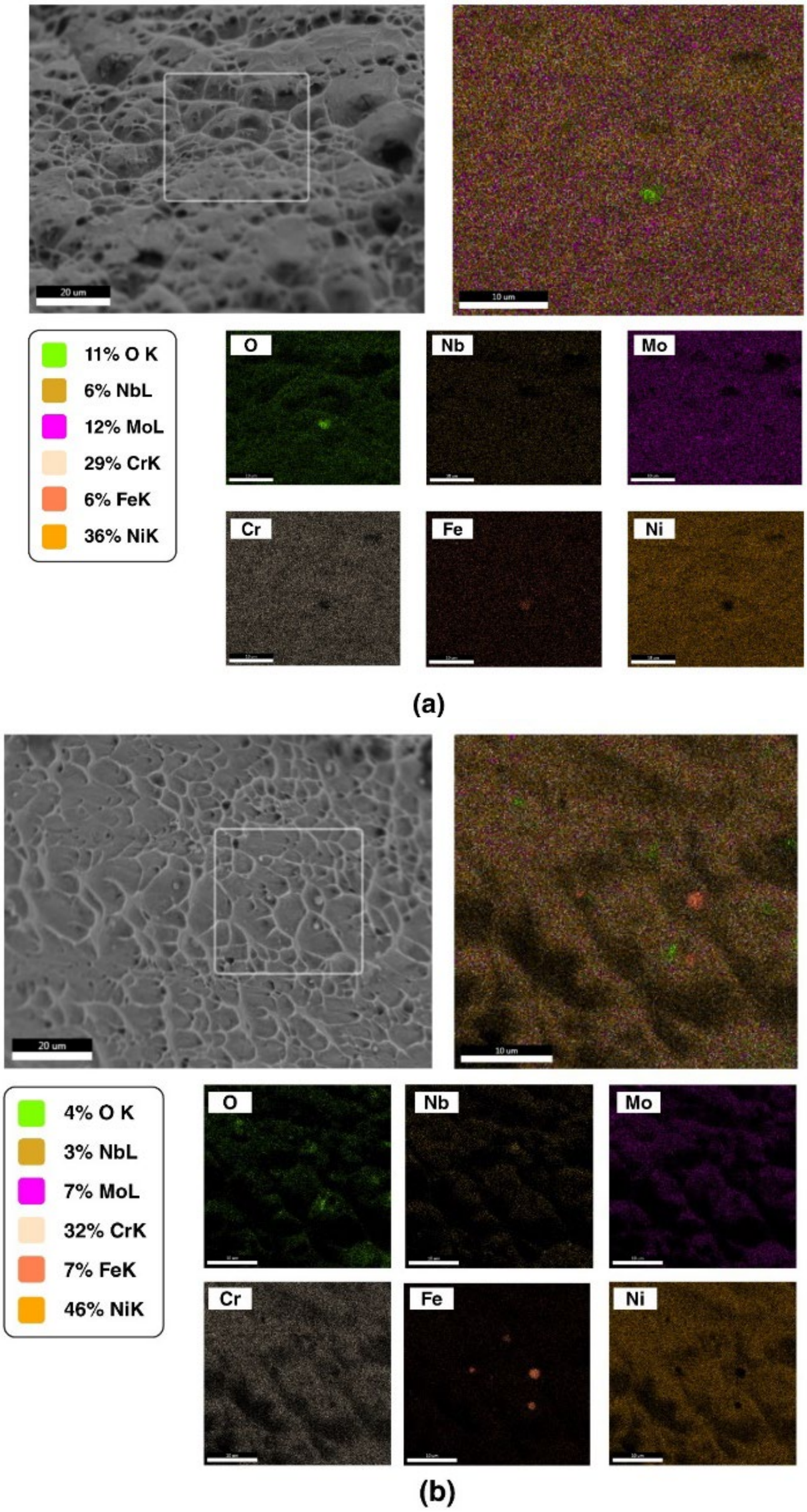
20 um
10 um
11% O K
6% NbL
12% MoL
29% CrK
6% FeK
36% NiK
O
Nb
Mo
Cr
Fe
Ni
(a)
20 um
10 um
4% O K
3% NbL
7% MoL
32% CrK
7% FeK
46% NiK
O
Nb
Mo
Cr
Fe
Ni
(b)

Figure 7.16. Elemental mapping of the fractured surface in case of (a) as deposited sample and (b) heat treated sample

The fracture surfaces of as-deposited, solution treated and wrought samples were analysed using SEM and the images are presented in Figure 7.15. The samples in all the conditions (wrought, as deposited and solution treated) primarily show a ductile mode of failure with the presence of clear dimples on the fractured surface. This observation falls in good agreement with the value of strain observed after the tensile testing (Figure 7.13 & Figure 7.14). Elemental maps of the fractured surface obtained from the EDS analysis are shown in Figure 7.16. Elemental maps of the as-deposited samples (Figure 7.16 (a)) show an increase in MoC-NbC rich phase on the fractured boundaries. The presence of the MoC-NbC phase might have resulted in an increase in strength due to restrictions to the dislocation movement (Hu et al., 2020c). However, in the EDS analysis of the solution treated samples, the amount of the MoC-NbC was found to be lower than the as-deposited samples (Figure 7.16 (b)). This is due to the dissolution of the MoC-NbC phase during the solution treatment process (Hu et al., 2020c).

7.2.3.2 Hardness results

Figure 7.17 presents the microhardness values observed in wrought, as deposited and solution treated samples. A maximum hardness value of 282 HV was observed in the as-deposited sample. This can be attributed to the high cooling rates in the LDED process resulting in finer microstructures and higher dislocation density thereby leading to higher hardness. The other reason that can be attributed to the increase in hardness in the as-deposited sample is the accumulation of Mo rich carbides at the grain boundaries as shown in Figure 7.16 (a). The MoC-NbC rich phase at the grain boundary restricts the dislocation movement during the loading resulting in high hardness. Comparing these results with that of the solution treated samples, it can be observed that the hardness value drops by approximately 12%. This drop in the hardness value in the case of solution treated samples can be attributed to the relief of thermal stress, increase in grain size and dissolution of hard MoC, NbC phase due to the prolonged solution treatment time, as well as the reduction in dislocation density. However, the

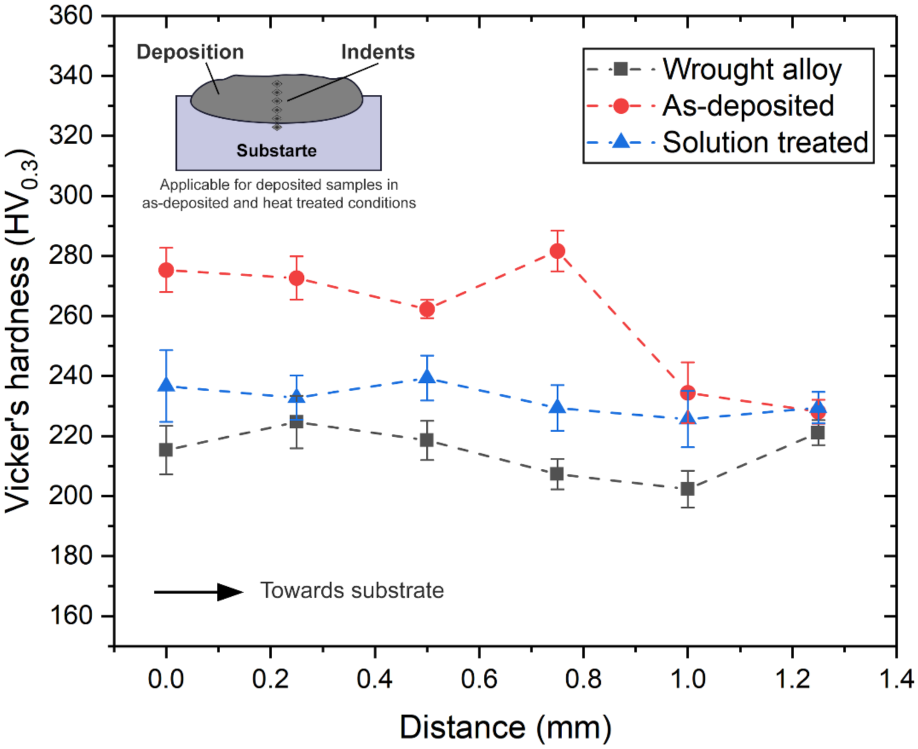

Figure 7.17. Vickers's microhardness measured from top of deposition toward substrate for different sample conditions

hardness value after solution treatment is comparatively higher than that of the initial wrought alloy sample used for repair. The improvement in the hardness value of the solution treated sample in comparison with the wrought alloy sample is on the order of 11%. This clearly shows a significant improvement in hardness after the repair of the samples.

7.3 Conclusions

In this study, an attempt has been made to explore the opportunity of repairing serviced Inconel 625 parts using the LDED process. Microstructure and mechanical properties at different deposition strategies and heat treatment were compared with wrought alloy. The following observations can be made:

1. Sound deposition with minimal porosity was observed in all the four deposition strategies using the LDED process with a mean deposit height of 1.02 mm. The height of the deposit was found to be maximum at the centre and minimum at the

edges of the samples. This is due to both increase in the temperature and a decrease in the catchment efficiency at the edge of the samples.

2. Microstructural study revealed dendritic morphology with columnar structure in the case of as-deposited samples. This is due to the high rates of cooling rate and thermal gradient in the LDED process. The dendrites grow towards the top of the melt pool. Microstructure after solution treatment shows complete static recrystallization. The columnar-dendrite structure observed in the as-deposited samples was found to disappear/dissolve after solution treatment. However, the microstructure in the solution treated condition was found to be rich in annealing twin boundaries, which usually occurs after solution treatment of IN625 alloy.

3. All the fractured samples show a ductile mode of failure with clear dimples. A maximum UTS value of 843 MPa was observed in the case of the wrought IN625 sample and a minimum UTS value of 719 MPa was seen in the case of one-sided deposition strategy. Yield strength values for different deposition strategies in the case of as-deposited condition varied between 300-350 MPa, while they varied between 230-270 MPa in the solution treated condition. This indicates that the deposition strategies have a minimal influence on the YS. A significant difference in the YS value can be observed between the as deposited and solution treated conditions.

4. The hardness values of the as-deposited samples were found to be higher by 12% than that of the solution treated samples. This can be attributed to the presence of fine dendrite structure and MoC-NbC rich phase in as-deposited condition. Further, the as-deposited condition was found to exhibit better hardness (11% high), than the wrought alloy and solution treated samples.

CHAPTER 8

HIGH TEMPERATURE OXIDATION BEHAVIOUR OF LDED IN625

The study in this chapter is focused to understand the oxidation behaviour of LDED IN625. To this end, a block of IN625 was fabricated on a similar substrate using Laser Directed Energy Deposition (LDED) process. Samples were extracted from the deposited block to understand the high temperature isothermal oxidation behaviour. The oxidation studies were carried out at 800 and 1000 ºC in a furnace with static air. Weight gain of each sample was recorded at four-time intervals i.e., 25, 50, 75 and 100 hours. The oxidation behaviour of the as-deposited sample was also compared with the solution treated LDED IN625 and wrought IN625.

8.1 Experimental procedure

8.1.1 Materials & preparations

IN625 powder used for the deposition was of spherical morphology and the particle size distribution majority varying between 40-60 µm was calculated from the analysis of SEM image shown in Figure 8.1. The deposition was done using an in-house developed LDED setup available at Laser Additive Manufacturing Laboratory, Raja Ramana Centre for Advance Technology (RRCAT), Indore, India. Process parameters such as laser power (*P*) of 1200 W, scan speed (*v*) of 0.6 m/min and powder feed rate (*f*) of 8 gm/min were used for the deposition of a thick block of dimensions 110 mm × 25 mm × 6 mm on a SS304 substrate of dimensions 120 mm × 35 mm × 20 mm (Figure 8.2). More details of the machine setup can be found in chapter 3. The values of *P*, *v* and *f* were chosen after conducting a single-track deposition study. The best track, where consistent deposition and minimum porosity was observed, and is considered for the deposition of a block.

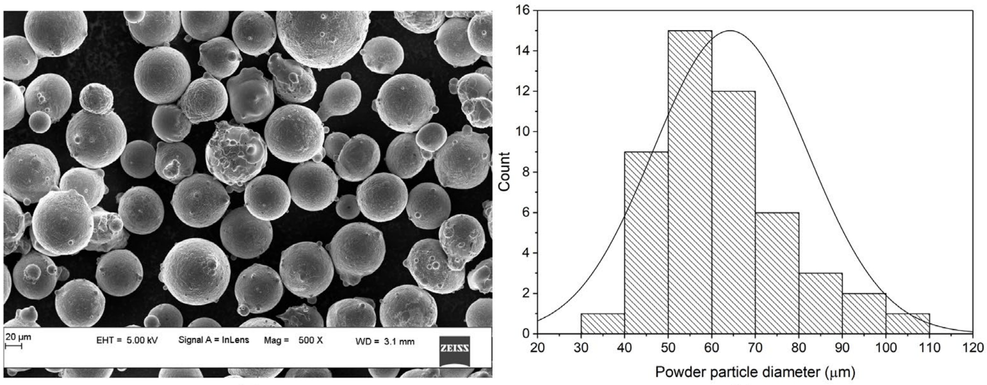

(a) (b)

Figure 8.1. Inconel 625 particles morphology and size distribution used for the deposition

Subsequently, after cooling, the deposited block was separated from the substrate and cut into two halves using Wire-EDM process. One half was retained as it is, while the other half of block was solution heat treated at 1200 °C for 2 hours (5°C/s heating rate – 2 hours hold time) in an open environment followed by water quenching. Further, oxidation samples of dimension 10 mm × 10 mm × 2 mm were extracted from both the as-deposited and heat treated blocks (ASM International, 1996). For the purpose of comparing the oxidation behaviour of LDED samples in both as deposited and heat-treated conditions with the wrought IN625 alloy, samples of the same dimensions were extracted from a 6 mm thick IN625 wrought plate. Now onwards, the as built, solutionized and wrought alloy samples will be abbreviated as AD, ST and WA, respectively. To bring similar surface conditions, all the samples were polished using SiC sheets from 400 to 1200 grit size prior to the oxidation study.

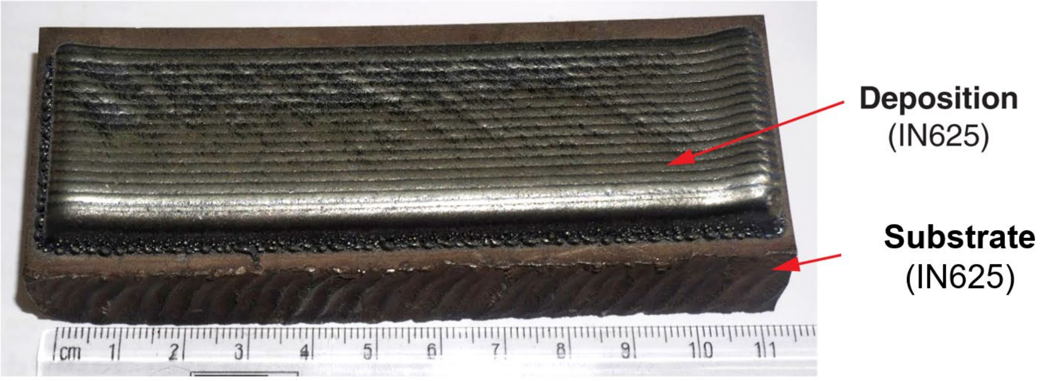

Figure 8.2. IN625 thick block deposited on SS304 substrate using LDED process

8.1.2 Oxidation experiment

Figure 8.3, show the procedure followed for oxidation study. First, initial weight measurement was carried out on each sample using a five-digit precision weighing balance. To avoid/reduce any measurement error, the reading was observed three times in three sets which are the mass of individual sample, mass of the crucible alone and mass of both crucible and sample together. After measurements, samples were placed on the refractory brick (as shown in Fig 8.3(c1)) and placed in a furnace. The oxidation study was carried out at two temperatures i.e., 800 and 1000 ºC in static air. Oxidation rate was measured at four-time intervals i.e., 25, 50, 75 and 100 hours. Samples at their respective time were taken out from the furnace and left to cool in open environment. After cooling, final weight measurement was done on all the samples.

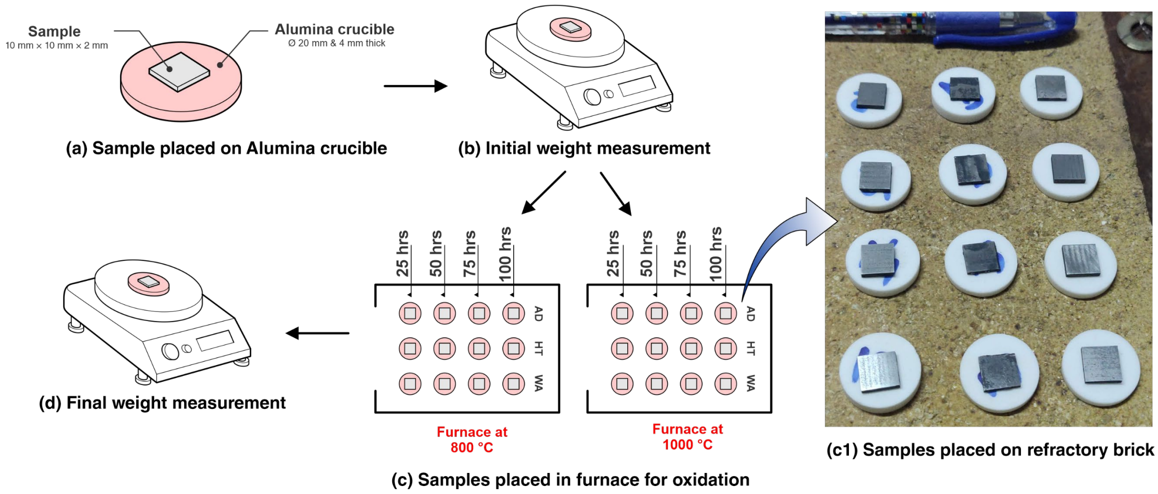
Sample
10 mm × 10 mm × 2 mm
Alumina crucible
Ø 20 mm & 4 mm thick
(a) Sample placed on Alumina crucible
(b) Initial weight measurement
25 hrs
50 hrs
75 hrs
100 hrs
AD
HT
WA
Furnace at 800 °C
Furnace at 1000 °C
(c) Samples placed in furnace for oxidation
(c1) Samples placed on refractory brick
(d) Final weight measurement

Figure 8.3. (a, b, c, d) Procedure followed for oxidation study and (c1) actual samples placed on the refractory brick before oxidation study

8.1.3 Characterization of the oxidized samples

The samples, after weighing, were immediately taken for Scanning Electron Microscopy (SEM) (Make: Carl Zeiss Model: Gemini300), Energy Dispersive Spectroscopy (EDS) and X-ray Diffraction (XRD) (Make: Malvern PANalytical, Netherlands; Model: Empyrean 3rd Gen) to identify the sample topography and elemental composition. XRD analysis was conducted using CuKα radiation with θ ranging from 10° to 100°. Further, samples were sectioned through-thickness to understand the depth of oxidation penetration and kinetics. The samples were grounded and mirror polished using SiC sheets of grit size varying from 200-2000, followed by cloth polishing in dispersed alumina solution. The thickness and elemental composition of the oxide layer were analysed using SEM and EDS.

8.2 Results and discussion

8.2.1 Mass gain evaluations

Figure 8.4 (a) & (b) show the isothermal weight gain per unit area with respect to different sample conditions, observation time and temperatures. IN625 alloy in all the sample conditions as well as both temperature conditions, is found to exhibit a gain in weight behaviour during isothermal oxidation. From figures 8.4 (a) and (b), it is evident that the weight gained per unit area for a given sample condition has increased by up to four times with the change in temperature from 800 to 1000 °C.

At 800°C, the weight gain of AD sample after 25 hours is 0.13235 mg/cm², while for the ST and WA sample is 0.05744 and 0.03631 mg/cm², respectively. It can be observed that the ST sample shows 57% less weight gain than that of AD samples. This result clearly shows the improvement in the oxidation resistance after post processing of as-build samples. In addition, WA sample shows a 36% lower weight gain than that of ST sample, indicating wrought alloy as the best performing condition during high temperature isothermal oxidation. Similar trends of results were observed in the samples at 1000 °C as well. In both temperature conditions, the AD samples are found to show poor oxidation resistance. It can also be observed that the rate of weight change in HT and WA samples is quite similar at both temperatures. The weight gain in WA sample is found to be significant for up to 50 hours, after which the weight gain slows down (Figure 4(a)). However, at 1000°C, irrespective of the sample condition, there is a continuous increase in weight gain.

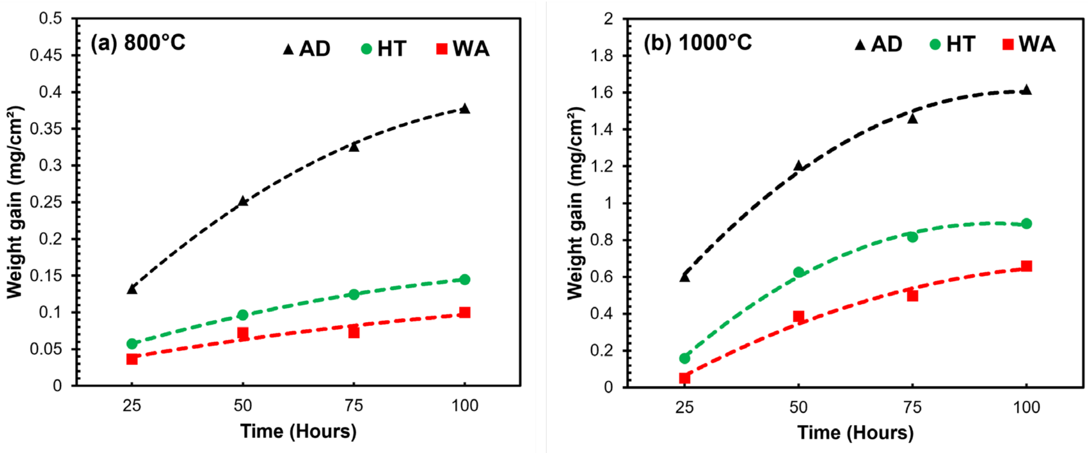

Figure 8.4. Mass gain observed in the different sample conditions and time during isothermal oxidation at (a) 800 and (b) 1000 °C

Materials with continuous and adherent oxidation scales effectively prevent diffusion from the environment, as a result of which material offer resistance to high-temperature oxidation. This process of controlled diffusion is called the parabolic rate constant, defined as k_p, expressed as

$$k_p = \frac{(\Delta m)^n}{t} \tag{8.1}$$

where, Δm is the weight gain per unit area (g/cm^2), k_p is the parabolic rate constant and t is the exposure time (s).

The exponential term 'n' in the equation (8.1) gives an indication of the oxidation mechanism. In the present study, the non-linear fitting (dotted lines), as shown in figures 4 (a) and (b), of the weight gain for sample conditions show a good fit with R^2 values ranging between 0.98 to 0.99 while considering n as 2. The good fitting of the weight gain data in all the sample conditions indicates that samples are following a parabolic growth law.

In addition, the parabolic rate constant (k_p) can be used to determine the activation energy by applying the Arrhenius equation given as,

$$k_p = A \exp\left\{\frac{-Q}{RT}\right\} \tag{8.2}$$

Which can be simplified as

$$\ln k_p = \ln A - \left\{\frac{Q}{RT}\right\} \tag{8.3}$$

Where, A is temperature-independent constant, Q is the activation energy for the reaction, R is the universal gas constant (8.31 J/(mol-°K).

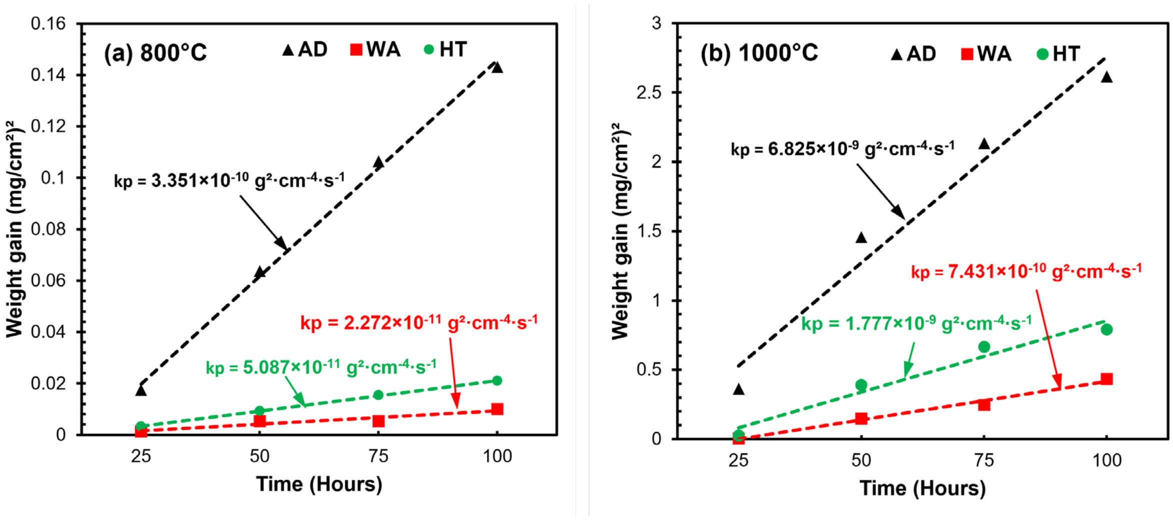

Figure 8.5. Mass gain square observed in the different sample conditions and time at (a) 800 and (b) 1000 °C

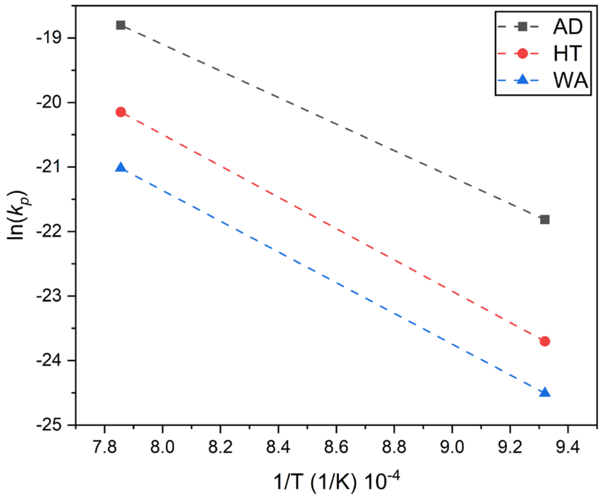

Figure 8.6. Plot of ln k_p versus inverse of temperature used for calculation of the activation energy of oxidation at different sample conditions

The plot of ln k_p versus the inverse of temperature is shown in figure 8.6. The slope of the lines divided by the Universal Gas constant, R (8.31 J/mol-K) in Figure 8.6 will give the activation energy, *Q*. The activation energy values for oxidation obtained for in the different sample conditions between 800 and 1000 °C are listed in Table 8.1. Activation energy values give an indication of the minimum energy required to execute the oxidation reaction. It can be observed that the AD sample requires minimum activation energy for an oxidation reaction to occur. However, the activation energy for both HT and WA samples is almost similar.

Table 8.1. Activation energy calculated of Inconel 625 at different sample conditions

Sample condition	**Activation energy (kJ/mol)**
AD	248
HT	292
WT	287

8.3 Post oxidation characterization

8.3.1 Oxidation at exposure temperature of 800°C

For the purpose of qualitative analysis, Figure 8.7 and 8.8, show the thickness of the oxide scale formed on each sample condition at different furnace exposure times and temperatures observed from scanning electron microscopy. Comparing the different sample conditions at time 25 hours (figures 8.7 (a, e and i)), it can be seen that AD sample is quite reactive at the exposed temperature (800 °C) as compared to the HT and WA samples. This result is found in line with the weight gain results observed in the previous section. The HT and WA samples at 25 hours show a very thin oxidation scale formation. However, as the furnace exposure time increases from 25 to 100 hours, a significant increase in the oxide scale can be observed in all the sample conditions. Comparing the figure 8.7 (a, b, c & d), it can be noted that the oxide scale formation is limited to the top of exposed surface for up to 25 hours of exposure time. However, the oxide scale is found to penetrate (*also known as internal oxidation*) into the sample after 50 hours of furnace exposure. The penetration in AD sample condition is found to be severe in 75 and 100 hours exposure time. Similarly, for the exposure temperature of 800 °C, the HT and WA samples are found to hold a good oxidation resistance for up to 25 hours. However, a noticeable oxidation scale can be found at 50 hours of furnace exposure in both HT and WA samples (Figure 8.7 (f, j)). At 800°C, there are no trace of internal oxidation found in both HT and WA samples in the entire duration of exposed time (Figure 8.7 (g, k, h, l)). In addition, in all the sample conditions after

50 hours of exposure time, voids were observed between the oxide scale and the sample surface. As reported by Rolland et. al., the oxide scale in case of IN625 alloy mainly consists of chromia (Cr_2O_3) (Rolland, 2012). The resulting chromia scale is known to have poor adherence (Ramenatte et al., 2020b). As a result of this, a significant number of voids can be seen between the oxide scale and sample surface. Another reason which leads to high void formation could be due to the vacancy injection and the well-known Kirkendall effect. The details of the mechanism behind the void formation is comprehensively explained by Desgranges et al. (2013). More discussion on the element composition will be discussed in further sub-sections.

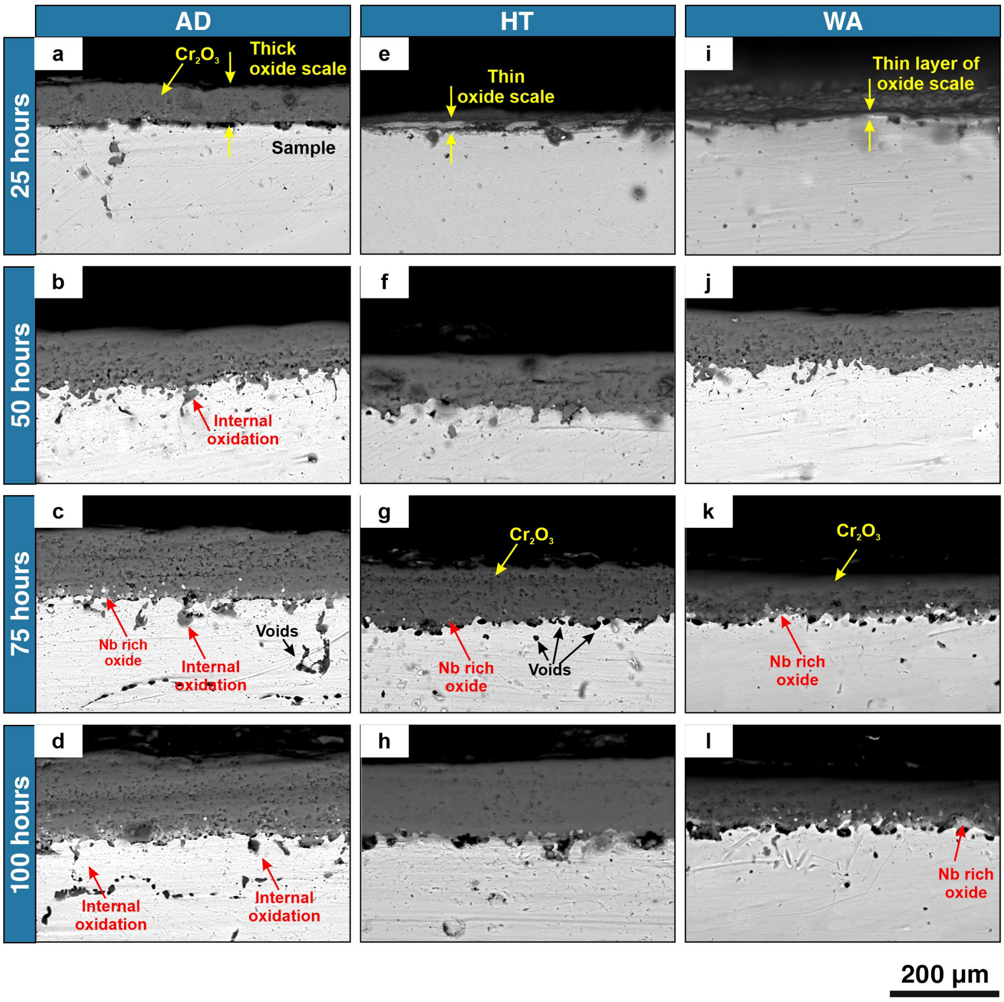
AD
HT
WA
25 hours
50 hours
75 hours
100 hours
a
Cr_2O_3
Thick oxide scale
Sample
e
Thin oxide scale
i
Thin layer of oxide scale
b
Internal oxidation
f
j
c
Nb rich oxide
Internal oxidation
Voids
g
Cr_2O_3
Nb rich oxide
Voids
k
Cr_2O_3
Nb rich oxide
d
Internal oxidation
Internal oxidation
h
l
Nb rich oxide
200 μm

Figure 8.7. Cross-setion images of the sample showing the oxide layer thickness in different sample conditions and exposure time at 800°C

For quantitative analysis, thickness of each sample was measured using image analysis software ImageJ. The results of measurements are presented in Figure 8.8. At 25 hours, the minimum thickness the WA and HT samples have the least oxide layer thickness which ranges between 15 to 30 µm. However, at the same exposure time, the average oxide scale thickness in AD sample is 70 µm, which is almost 133% and 350% higher than that of HT and WA samples, respectively, indicating a poor high temperature oxidation resistance of AD samples. It can also be observed that in WA and HT samples, increase in oxide thickness is quite significant from 25 to 50 hours. However, thereafter the change in oxide scale thickness is comparatively insignificant.

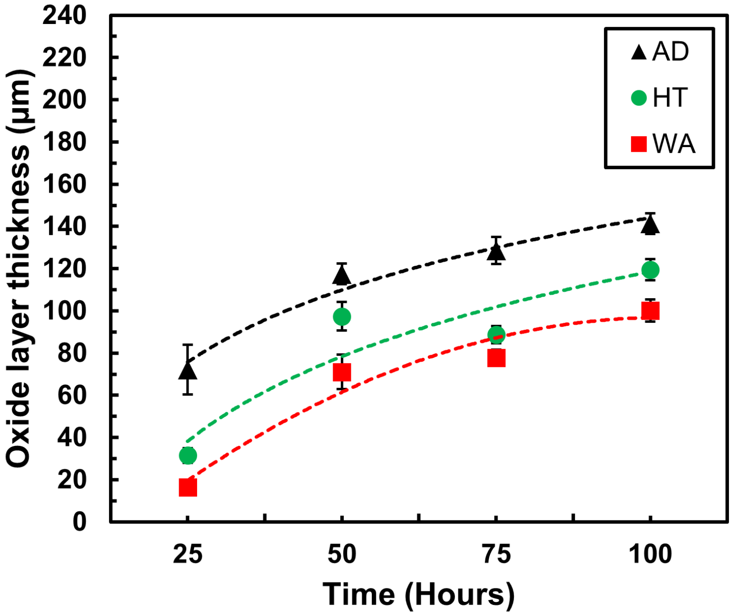

Figure 8.8. Oxidation layer thickness measured for the samples at furnace explosure temperature 800 °C

To identify the chemical composition of the oxide thickness, elemental mapping was done using Energy Dispersive Spectroscopy (EDS). In general, all the samples are found to show a similar characteristic of elements forming during the oxidation test. For ease of discussion, the sample where oxidation is much more severe is presented. Therefore, elemental area maps observed in the AD sample at 800 °C and 100 hours is shown in Figure 8.9. It is evident that the oxide scale is primarily composed of Chromium and Oxygen. A small amount of Nb can also be traced just above the surface of the sample. The elemental map of Mo shows no trace of Mo in the oxide scale. The

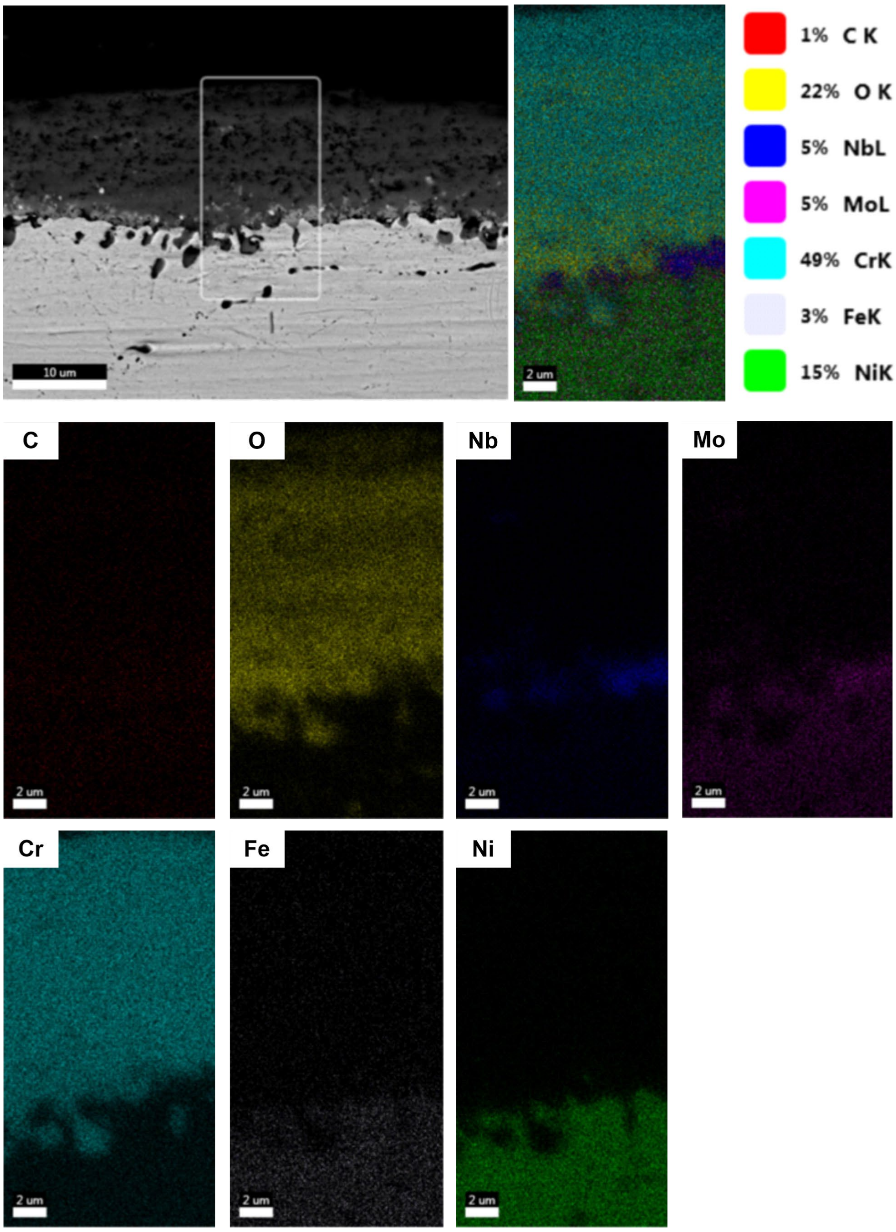

Figure 8.9. Elemental maps of AD sample exposed for 100 hours at 800 °C

internal voids formed during the oxidation confirm the presence of chromium. These results fall in line with the existing literatures. The strong presence of Cr:O atomic rate of 2:1 could possibly reassemble the Cr_2O_3 phase formed during the oxidation. In a similar fashion, the presence of Ni:Cr:O atomic ratio in 1:3:2 possibly implies the presence of $NiCr_2O_3$. However, the presence of this phase will be confirmed by performing the x-ray diffraction study on the oxidized surface.

X-ray diffraction patterns observed in the different sample conditions and exposure time at 800 °C are shown in Figure 8.10. The peak patterns observed in all the sample confirm the presence of γ-Ni, Cr_2O_3, Ni_3Nb, $NbCrO_4$ and $NiCr_2O_4$ phases. The AD sample shows a strong Cr_2O_3 peak which is the prime constituent of the oxide scale. The possible reason of γ-Ni phase detected on the top surface of all the samples could be due to the depth of penetration of x-rays, which usually can go up to 100 µm. The XRD results are found in line with the SEM and EDS results discussed early in this section.

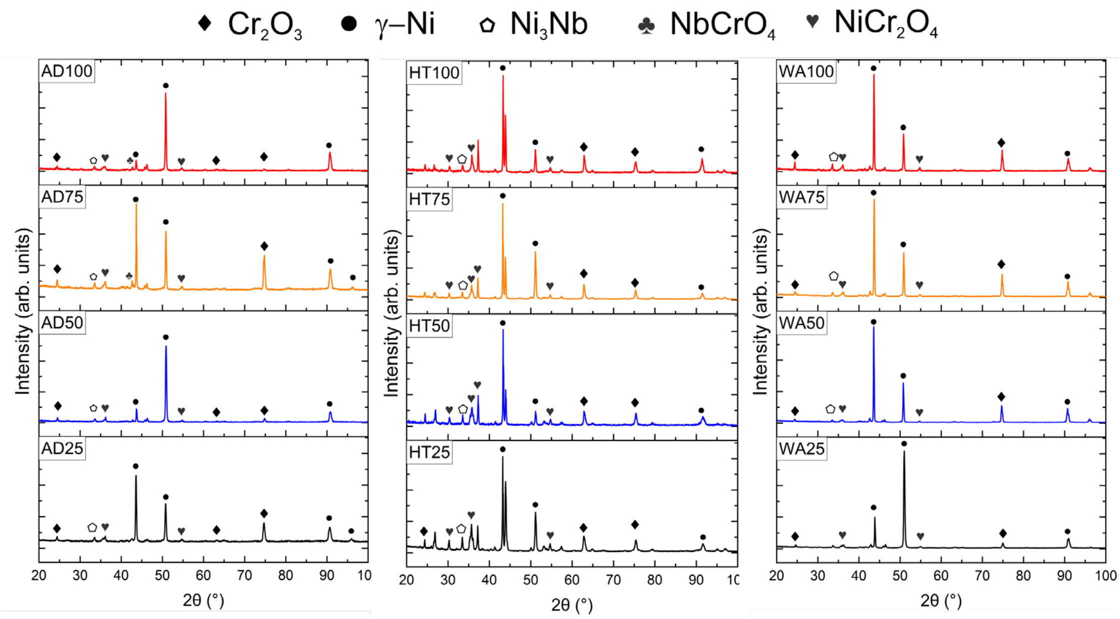

Figure 8.10. X-ray diffraction patterns collected at 800 °C for different samples

8.3.2 Oxidation at exposure temperature of 1000°C

The cross-section images of different sample conditions and exposure time obtained from the scanning electron microscopy is shown in Figure 8.11. The observations at 25 hours for samples exposed to 1000 °C reveals the presence of oxide scale in all the sample, unlike the sample exposed to 800 °C, where scaling was observed after 50 hours, especially in HT and WT samples. In addition, severe internal oxidation can be observed in all the sample conditions are all times. At 1000 °C, the sample also shows both interfacial voids and bulk voids. In the AD sample at 100 hours, the oxidation is found to be severe, where the inward-growing oxidation is found growing in the interfacial voids as well (Svensson et al., 2009). Another phenomenon which can be observed in almost all the samples is the presence of bulk spherical voids. These spherical voids are more abundant in all sample with more exposure time. These spherical bulk voids are the result of Cr depletion, as reported by Sachitanand et al. (2015). In WA samples at 50 hours figure 8.11 (j), a series of small size voids originating from the surface can be seen. It is expected that this series of small voids, when exposed for a longer time, form a big void leading to severe internal oxidation as shown in figure 8.11 (k).

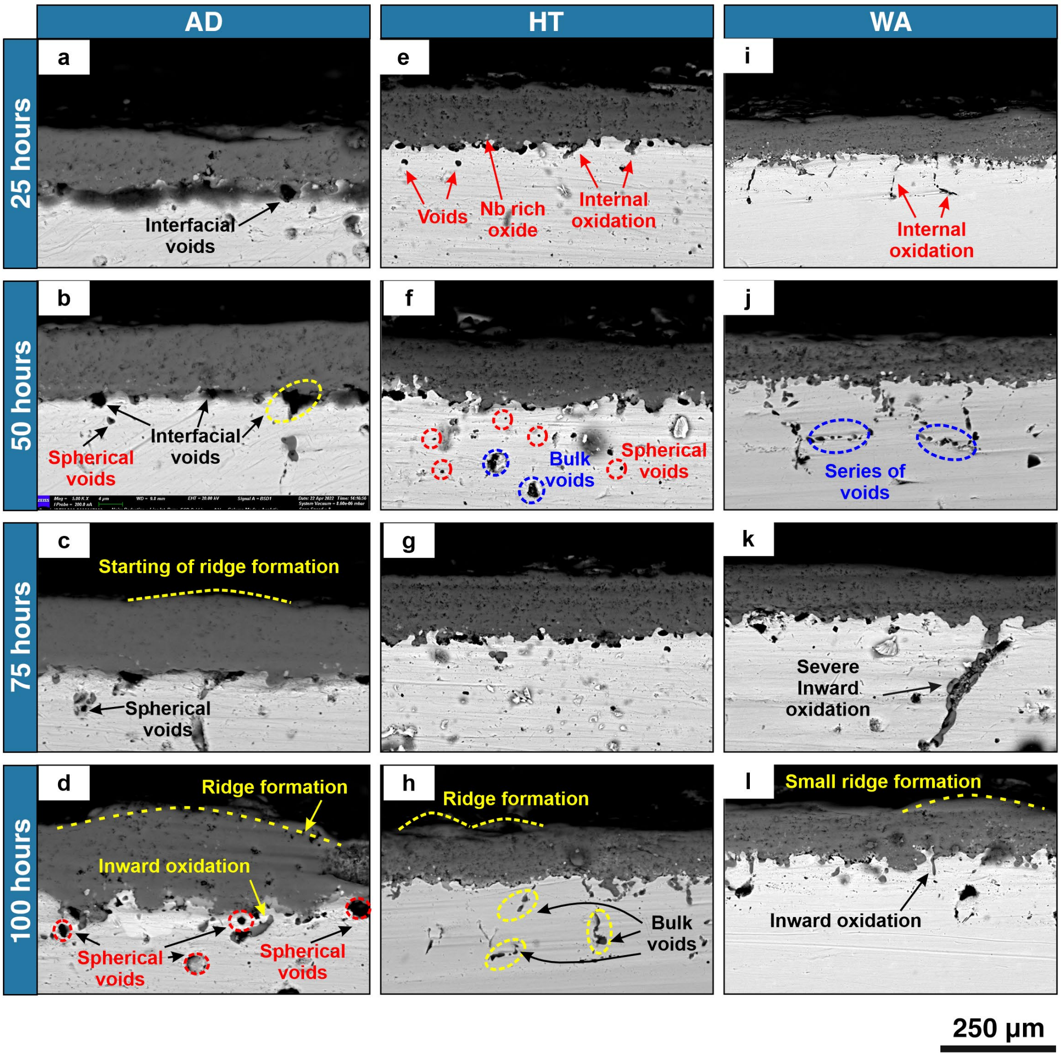
AD
HT
WA
25 hours
50 hours
75 hours
100 hours
a
Interfacial voids
e
Voids
Nb rich oxide
Internal oxidation
i
Internal oxidation
b
Spherical voids
Interfacial voids
f
Bulk voids
Spherical voids
j
Series of voids
c
Starting of ridge formation
Spherical voids
g
k
Severe Inward oxidation
d
Ridge formation
Inward oxidation
Spherical voids
Spherical voids
h
Ridge formation
Bulk voids
l
Small ridge formation
Inward oxidation
250 µm

Figure 8.11. Cross-section images of the sample showing the oxide layer thickness in different sample conditions and exposure time at 1000 °C

Quantitative results of oxide scales observed in different samples conditions are presented in Figure 8.12. A maximum oxide scale thickness of 185±3 is observed in the AD sample at 100 hours of exposure. At 25 hours of exposure time, the thickness of the oxide scale is quite similar (varying between 80-100 µm) in all the sample conditions. However, as the exposure time increase further, a significant increase in the thickness can be observed in the AD samples. Similar to exposure temperature 800 °C, both HT and WA samples are found to show a similar trend of increase in oxide scale thickness. The thickness in AD samples is found to increase with respect to time, indicating thermal instability at high temperatures. On the other side, in WA and HT samples, the increase in the mass is significant in the initial hours, which continue to slow down over time.

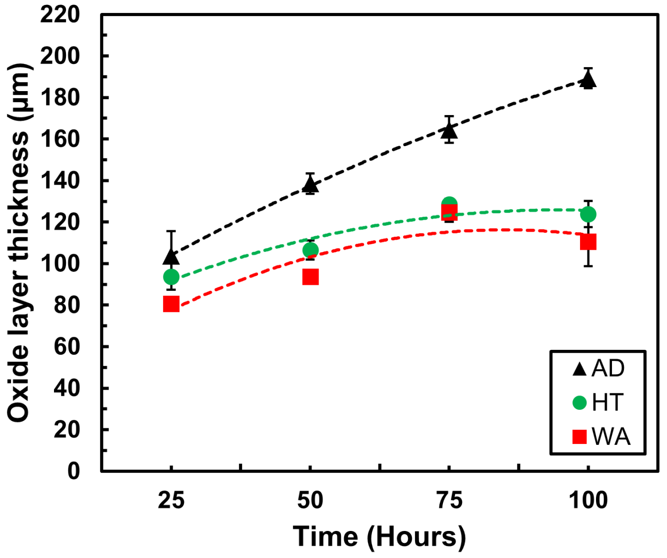

Figure 8.12. Oxidation layer thickness measured for the samples at furnace exposure temperature 1000 °C

EDS area maps of the AD sample exposed to 1000 °C for 50 hours is shown in Figure 8.13. The maps show the presence of chromium and oxygen in the oxide scale which indicate the possibility of Cr_2O_3 as observed in the sample exposed to 800 °C. At the junction of the scale and the sample, traces of Nb are observed. However, the trace of Nb is limited to 4%.

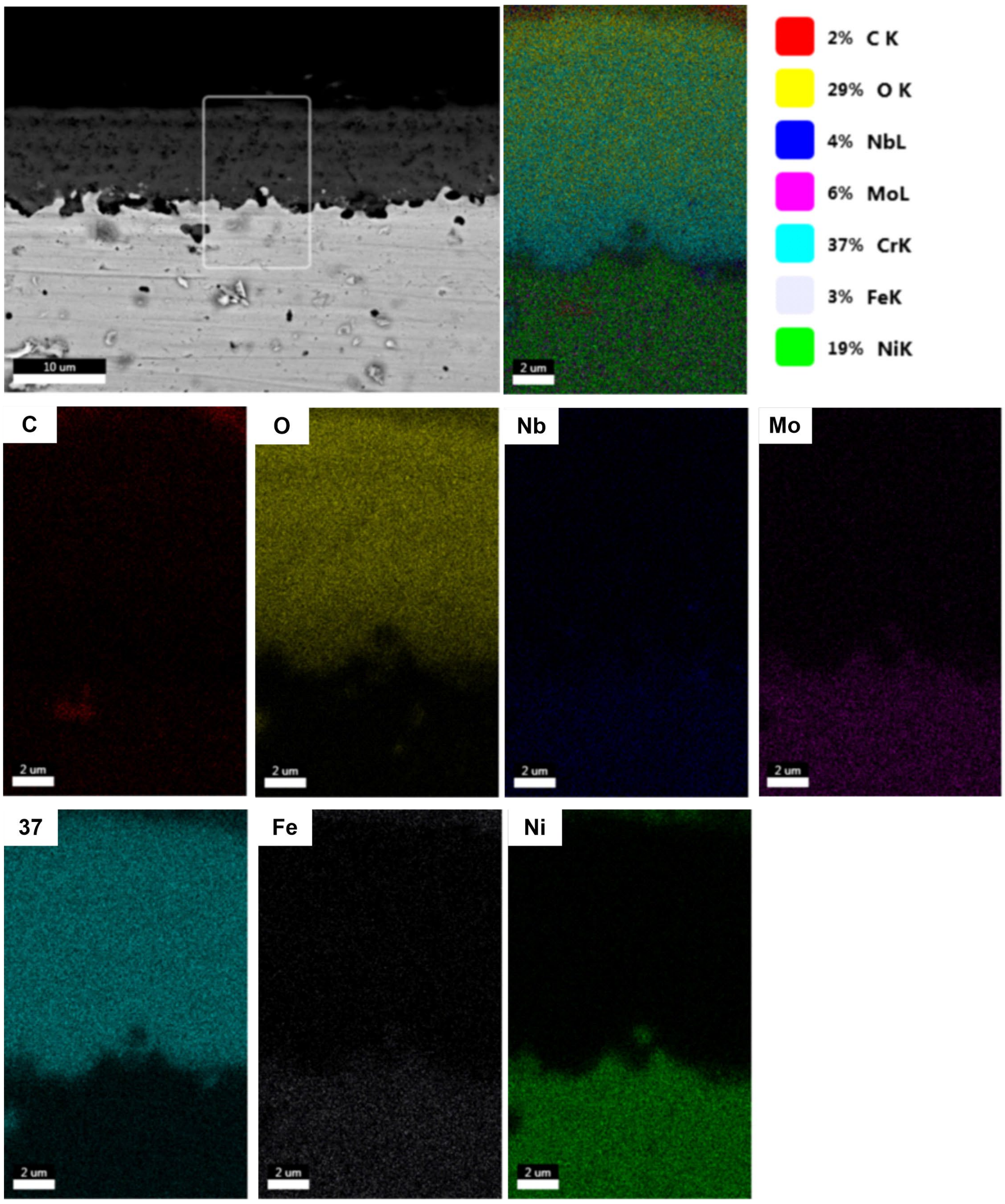

Figure 8.13. Chemical composition of the oxide layer observed in heat treated sample at 50 hours and 1000 °C

EDS elemental area maps of AD sample at 100 hours of exposure time is shown in Figure 8.14. At higher temperatures also majority of the trace elements in the oxide scale are Cr and O. However, a good increase in the Nb (7% at 50 hours and 10% at 100 hours) can be seen at the junction of the oxide scale and sample surface. As reported by Chyrkin et al. (2011), the increase in chromium depletion during long exposure hours leads to an increase in Nb flux, as a result of which strong Nb enrichment can be seen on the sub-surface regions of oxide scale. No traces of Fe, Mo and C is observed in the oxide scale.

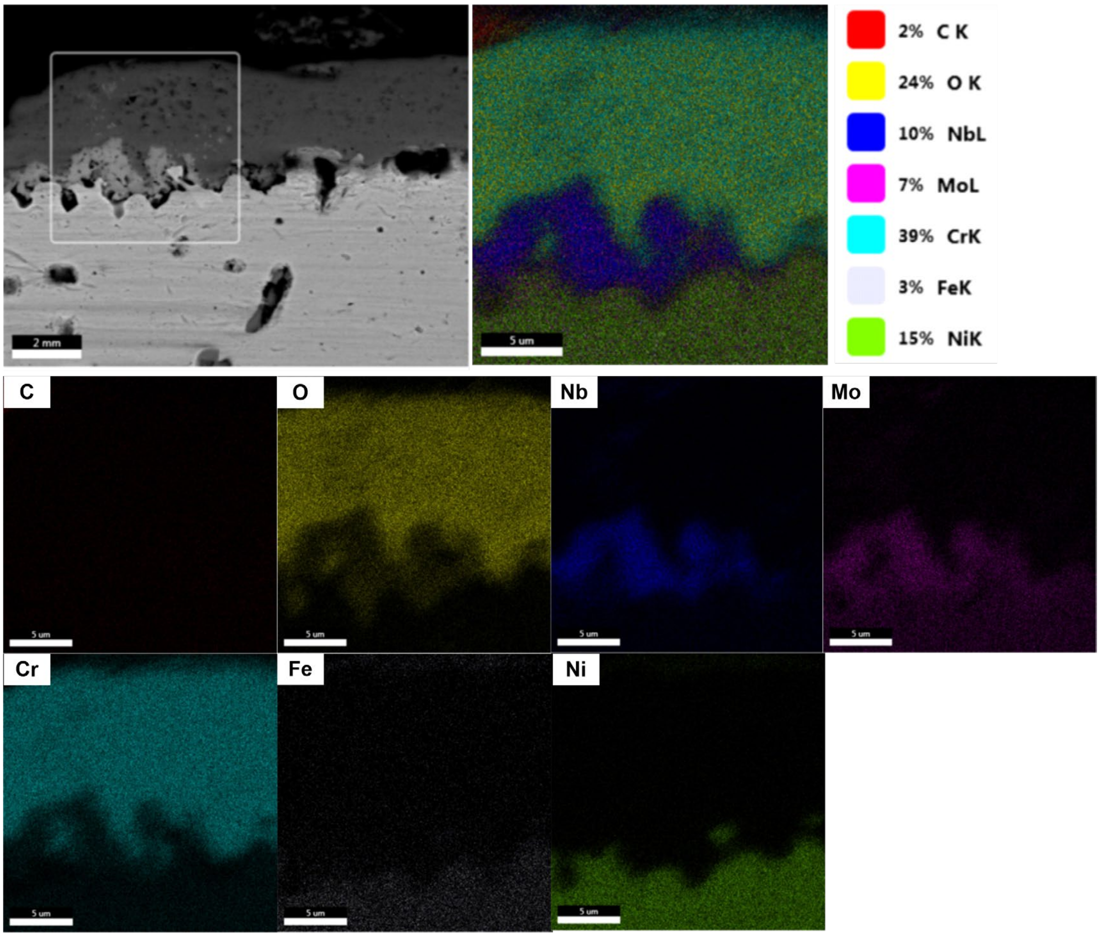

Figure 8.14. Chemical composition of the oxide layer observed in heat treated sample at 100 hours and 1000 °C

XRD patterns collected for the samples exposed to 1000 °C are shown in Figure 8.15. At first instance, it can be observed that the intensity of γ-Ni (111) peaks in the AD samples are weak, indicating the presence of other phases. The XRD pattern of samples at 1000°C show Cr_2O_3, Ni_3Nb, $NbCrO_4$ and $NiCr_2O_4$. Unlike 800 °C, where the $NbCrO_4$ was mainly present in the as-deposited sample, at 1000 °C, this $NbCrO_4$ can be found in all the cases. As reported by Huczkowski et al. (2017), the Nb enrichment occurs at the interface of the sample surface and oxide scale. The scale being rich in Cr and O tends to react with the Nb and forms $NbCrO_4$.

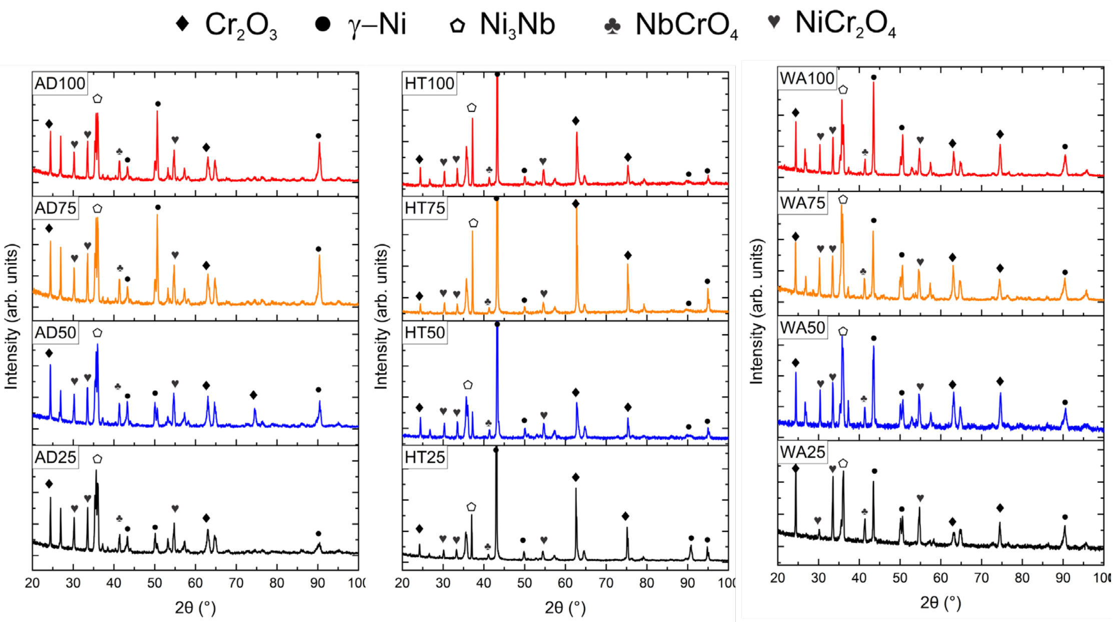

Figure 8.15. X-ray diffraction patterns collected at 1000°C for different samples

8.4 Mechanism of oxidation in IN625

The mechanism of oxidation can be explained by the Wagner theory of the oxidation diffusion process. According to the Wagner theory, the external oxide layer is primarily formed by the selective oxidation of active elements present in the matrix, such as Cr in case of IN625 (Figure 8.16) [13]. At high temperatures, the rate of oxidation is rapid in the initial hours of exposure. The abundant oxygen present in the atmosphere gets excited and starts colliding with the sample surface and breaks down into oxygen atoms. Due to this breakdown of atoms, a process of chemical absorption between the oxygen atoms and the free electrons available with the active elements starts. In IN625, a chemical absorption between Cr and O takes place, leading to the formation of Cr_2O_3 as a reaction product. The product of chemical absorption creates an oxide scale on the exposed surface. This process also causes a rapid weight gain in the samples, as observed in this study. However, after a certain period of exposure time, the second stage of oxidation starts, which is usually known to follow a parabolic rate growth law (Hou and Chou, 2009). In this stage of oxidation, the primary mode of oxidation is by means of atomic diffusion, as of result of which Kirkendall pores are observed (Figure 8.7 and Figure 8.11). The voids formed during the oxidation are the result of grain boundary sliding. As oxidation advances, it is reported that compound stresses, which include both thermal and growth stresses, are induced on the surface. To achieve the stress equilibrium on the surface, plastic deformation occurs where grain boundaries slide. This leads to the formation of intergranular voids (Clarke, 2002). These voids in some weak areas also lead to the formation of internal cracks, as observed by Clarke et al. (Clarke, 2002). LDED samples, because of the high cooling rates, usually have a fine microstructure and more grain boundaries in a given volume. Also, the LDED samples are known to have tensile thermal stress on the surface originating due to the non-uniform heating and cooling during LDED. It is expected that because of the thermal stresses, severe grain boundary sliding samples as a result of which a poor oxidation resistance can be seen. The IN625 AD samples, after heat treatment at 1200°C are known to have a full recrystallized stress-free microstructure with comparably large grain size. As of result of which, the oxidation rate in HT sample goes down significantly. Moving forward, as the oxidation at higher temperatures continues to enhance further, the stresses exceed the carrying capacity of the oxide layer, as a result of which spallation occurs in the weak areas. Due to the spallation, Cr depletes from the surface and the Ni is exposed to O. This leads to the formation of Ni-rich oxides, such as Ni_3Nb, as seen in the XRD patterns. The possible reaction that forms Cr_2O_3 and Ni-rich oxides from the Ellingham-Richardson diagram are (Robino, 1996):

$$2\mathrm{Cr} + \frac{3}{2}\mathrm{O_2} \rightarrow \mathrm{Cr_2O_3} \tag{8.4}$$

$$\mathrm{Ni} + \frac{1}{2}\mathrm{O_2} \rightarrow \mathrm{NiO} \tag{8.5}$$

$$\mathrm{NiO} + \mathrm{Cr_2O_3} \rightarrow \mathrm{Ni_2Cr_2O_4} \tag{8.6}$$

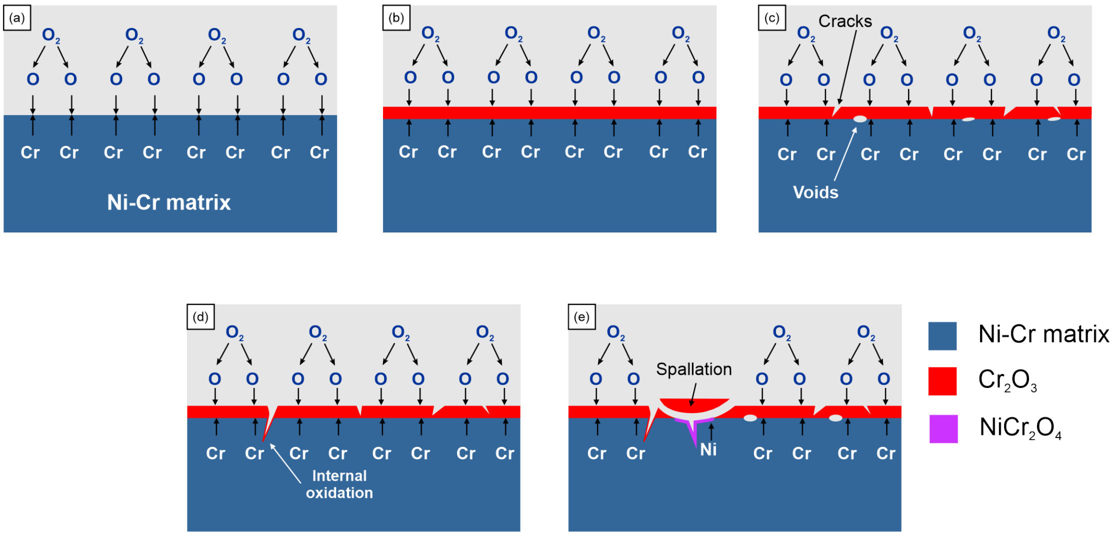

Figure 8.16 Mechanism of oxidation formation in IN625

8.5 Conclusions

In this work, oxidation behaviour of as deposited and heat treated LDED IN625 was compared with that of wrought alloy. Weight gain, oxide scale thickness and phases were compared for all the sample conditions at 25, 50, 75 and 100 hours under thermal exposure of 800 and 1000 °C. The conclusions drawn from the study are as follows:

- At both the test temperatures i.e., 800 and 1000 °C, the AD condition sample show a poor resistance toward oxidation followed by HT and WA.
- HT sample shows a 2-3 times better oxidation resistance, indicating the effect of post processing on AD samples.
- Chromium oxide is found as the primary scale formed during the oxidation at both the temperatures.
- At 800°C, the HT and WA samples show a good resistance for up to 25 hours while AD shows poor oxidation resistance well before 25 hours.
- The weight gain in all the samples is found to follow a parabolic growth law.
- The results from the study show the importance of using post processing for LDED IN625 to improve oxidation resistance.

CHAPTER 9
SUMMARY & FUTURE WORK

9.1 Summary of the thesis

Repair technologies being used currently include thermal spraying, cladding and welding. These repair technologies are ad hoc and do not provide tight control on the depth of penetration and the spread of the material deposited to repair the cracks. For over 60 years, TIG welding is the industry go-to process for the repair of damage components (Chen et al., 2021). Despite its easy availability, lower cost and process simplicity, TIG welding results in a huge amount of heat signature, which alters the actual characteristics of the component to be repaired. The other downside of this process is its inability to repair complex shapes and corner sites (Piscopo and Iuliano, 2022).

LDED is an emerging additive manufacturing technology which is best suitable for repair and refurbishment applications. The advantages of using the LDED process for repair and feature addition applications include precise deposition and narrow heat-affected zone. To this end, the work presented in this thesis is focused to understand the fundamental of LDED process and explore its potential as a technique for repair and feature addition of IN625 components. The summery of the different studies presented in this thesis are as follows.

- Chapter 4 presented a fundamental study where effect of process parameters on the melt pool geometry and microstructure was investigated during LSM. A FVM based numerical model was established to understand the effect of considering fluid dynamics on the thermal conditions while modelling LSM process. The results of this work indicate that solidification characteristics are not significantly influenced by the consideration of fluid dynamics effects in the numerical models. However, this work clearly shows the importance of considering fluid dynamics for accurately predicting melt pool shape and dimensions.

- Chapter 5 presented a fundamental study where the effect of process parameters (laser power and scan speed) on single track geometry (height and width) was investigated. The single tracks were categorised as tracks with no deposition, Inconsistent tracks and consistent tracks. A FEM based numerical model was established to predict the single-track geometry. The predictions of the numerical model were found in agreement with the experimental results with acceptable error.

- Chapter 6 presented a IN625 thin wall fabrication work, where the intention was to explore the feature addition capabilities of LDED process. Effect of process parameters on the build quality, surface roughness, microstructure and mechanical properties (in two orientations) was presented. The results indicate that the selection of an optimum process parameters is must to build sound & consistent thin walls using LDED process. The thin walls were found to exhibit superior strength in horizontal direction when compared to vertical direction. A FEM based numerical model was presented to understand the effect of process parameters on melt pool geometry, cooling rates and thermal gradients. The predications from numerical model were found in agreement with the experimental observations.

- Chapter 7 presented a study where serviced IN625 samples were deposited to mimic repair using LDED process. Four deposition strategies were used. Microstructure and mechanical properties were investigated. Effect of the post repair solution treatment was also studied. The results show sound deposition with minimal porosity in all the four deposition strategies. The repaired samples after the solution treatment were found to exhibit similar tensile strength. This highlights the importance of post repair heat treatment.

- Chapter 8 presented the oxidation behavior of IN625 samples repaired using LDED. The oxidation behaviors of LDED IN625 was also compared with the solution treated LDED 625 and wrought IN625. The LDED IN625 samples were found to show a poor oxidation resistance followed by solution treated and wrought alloy. The solution treated samples were found to exhibit a 2-3 times better oxidation resistance than the LDED IN625 samples. These findings highlight the importance of using post processing for LDED IN625 to improve oxidation resistance.

9.2 Future work

The motivation of this study was to explore the repair and feature addition capabilities of LDED process. When this work started, the LDED process was in the initial stages and the primary objectives of the available literature were to optimize process parameters for sound deposit and study the effect of process parameters on the microstructure and mechanical properties. This work gives a comprehensive idea about using LDED process as a repair technology. Despite all the progress reported in thesis, the work can be further extended. The following gaps have been identified as future research directions.

- The numerical modelling work presented in chapter 4, presents the effect of fluid flow on the melt pool dimensions and characteristics during laser surface melting. However, this work can be further extended with mass addition to represent a metal additive manufacturing / deposition process.

- The numerical modelling work presented in chaper-5 predicts the single-track dimensions during the LDED process. In future, this model be further extended to understand the thermal response, melt pool characteristics and dimension during the multi-track and multi-layer deposition.

- The repair candidates in the study mentioned in chapter 7, are the samples extracted from an IN625 substrate. In future, actual failed component(s) can be identified with industrial collaboration and similar study can be performed.

- In this thesis, the assessment of mechanical properties of the repaired samples is limited to the tensile strength. This can be further extended to understand the change in fatigue and creep life of the repaired parts.

- The repair work presented in thesis do not assess the number of times a given part can be repaired. A study focusing on identifying the effect of repeating repair on the microstructure and mechanical properties of the repaired samples can be investigated in future.

- LDED process is known to have positive residual stresses due to non-uniform cooling and heating during layer-by-layer deposition. Therefore, a study comparing the residual stresses in repaired zone and the base plate can be done.

REFERENCES

Aggarwal, A., Shin, Y. C., and Kumar, A. (2023). “Investigation of the transient coupling between the dynamic laser beam absorptance and the melt pool - vapor depression morphology in laser powder bed fusion process.” *Int. J. Heat Mass Transf.*, 201.

AghaAli, I., Farzam, M., Golozar, M. A., and Danaee, I. (2014). “The effect of repeated repair welding on mechanical and corrosion properties of stainless steel 316L.” *Mater. Des.*, 54, 331–341.

Ahn, D. G. (2021). “Directed Energy Deposition (DED) Process: State of the Art.” *Int. J. Precis. Eng. Manuf. - Green Technol.*, 8(2), 703–742.

Ahn, J., Kim, C., Lee, D., Kim, B., Hong, H.-U., and Lee, J.-H. (2022). “Superior tensile and fatigue properties of Incoloy 901 repair welds produced by direct energy deposition.” *J. Mater. Res. Technol.*, 19, 3554–3567.

Ali, N., Tomesani, L., Ascari, A., and Fortunato, A. (2022). “Fabrication of Thin Walls with and without Close Loop Control as a Function of Scan Strategy Via Direct Energy Deposition.” *Lasers Manuf. Mater. Process.*, 9(1), 81–101.

Andreotta, R., Ladani, L., and Brindley, W. (2017). “Finite element simulation of laser additive melting and solidification of Inconel 718 with experimentally tested thermal properties.” *Finite Elem. Anal. Des.*, 135, 36–43.

“Ansys Fluent 2020 R1 Theory Guide.” (2021). .

ANSYS Fluent Tutorial Guide 18. (2018). “ANSYS Fluent Tutorial Guide 18.” *ANSYS Fluent Tutor. Guid. 18*, 15317(April), 724–746.

ANSYS Inc. (2022). *ANSYS Advanced Analysis Techniques Guide*.

Arisoy, Y. M., Criales, L. E., and Özel, T. (2019). “Modeling and simulation of thermal field and solidification in laser powder bed fusion of nickel alloy IN625.” *Opt. Laser Technol.*, 109(June 2018), 278–292.

ASM International. (1996). *Heat Treater’s Guide: Practices and Procedures for Nonferrous Alloys*. *ASM Int.*, ASM International.

ASM International. (2020). *ASM Handbook, Volume 24: Additive Manufacturing Processes*. ASM International.

ASTM 52900. (2021). *Standard Terminology for Additive Manufacturing – General Principles – Terminology*. *ASTM Int.*, 1–9.

ASTM E407, A. (2016). “Standard Practice for Microetching Metals and Alloys ASTM E-407.” 07(Reapproved 2015), 1–22.

ASTM E8 / E8M-16ae1. (2013). “Standard Test Methods for Tension Testing of Metallic Materials.” *ASTM Int.*

ASTM International. (2016). “Standard Guide for Directed Energy Deposition of Metals.” *ASTM Stand.*, 1–22.

Balichakra, M., Bontha, S., Krishna, P., and Balla, V. K. (2019). “Laser surface melting of γ-TiAl alloy: An experimental and numerical modeling study.” *Mater. Res. Express*, 6(4).

Barr, C., Rashid, R. A. R., Sun, S. Da, Easton, M., Palanisamy, S., Orchowski, N., Matthews, N., Walker, K., and Brandt, M. (2021). “Role of deposition strategy and fill depth on the tensile and fatigue performance of 300 M repaired through laser directed energy deposition.” *Int. J. Fatigue*, 146.

Basak, A., Acharya, R., and Das, S. (2018). “Epitaxial deposition of nickel-based superalloy René 142 through scanning laser epitaxy (SLE).” *Addit. Manuf.*, 22, 665–671.

BeAM. (2022). “What is a Feature Addition?” <https://www.beam-machines.com/faq/what-is-a-feature-addition#:~:text=A Feature addition is adding,to significantly reduce the cost.> (Mar. 7, 2022).

Beese, A. M., and Carroll, B. E. (2016). “Review of Mechanical Properties of Ti-6Al-4V Made by Laser-Based Additive Manufacturing Using Powder Feedstock.” *Jom*, 68(3), 724–734.

Bennett, J., Garcia, D., Kendrick, M., Hartman, T., Hyatt, G., Ehmann, K., You, F., and Cao, J. (2019). “Repairing Automotive Dies with Directed Energy Deposition: Industrial Application and Life Cycle Analysis.” *J. Manuf. Sci. Eng. Trans. ASME*, 141(2).

Betteridge, W., and Shaw, S. W. K. (1987). “Development of superalloys.” *Mater. Sci. Technol.*, 3(9), 682–694.

Bhaduri, A. K. (2002). “Repair welding of cracked steam turbine blades using austenitic and martensitic stainless-steel consumables.” *Fuel Energy Abstr.*, 43(4), 282.

Blakey-Milner, B., Gradl, P., Snedden, G., Brooks, M., Pitot, J., Lopez, E., Leary, M., Berto, F., and Plessis, A. du. (2021). “Metal additive manufacturing in aerospace: A review.” *Mater. Des.*, 209.

Burgardt, P., and Heiple, C. R. (1986). “Interaction Between Impurities and Welding Variables in Determining Gta Weld Shape.” *Weld. J. (Miami, Fla)*, 2(6).

Carroll, B. E., Palmer, T. A., and Beese, A. M. (2015). “Anisotropic tensile behavior of Ti-6Al-4V components fabricated with directed energy deposition additive manufacturing.” *Acta Mater.*, 87, 309–320.

Carrozza, A., Lorenzi, S., Carugo, F., Fest-Santini, S., Santini, M., Marchese, G., Barbieri, G., Cognini, F., Cabrini, M., and Pastore, T. (2023). “A comparative analysis between material extrusion and other additive manufacturing techniques: Defects, microstructure and corrosion behavior in nickel alloy 625.” *Mater. Des.*, 225.

Chai, R., Zhang, Y., Zhong, B., and Zhang, C. (2021). “Effect of scan speed on grain and microstructural morphology for laser additive manufacturing of 304 stainless steel.” *Rev. Adv. Mater. Sci.*, 60(1), 744–760.

Chakraborty, A., Tangestani, R., Batmaz, R., Muhammad, W., Plamondon, P., Wessman, A., Yuan, L., and Martin, É. (2022). “In-process failure analysis of thin-wall structures made by laser powder bed fusion additive manufacturing.” *J. Mater. Sci. Technol.*, 98, 233–243.

Chen, H., Lu, Y., Luo, D., Lai, J., and Liu, D. (2020a). “Epitaxial laser deposition of single crystal Ni-based superalloys: Repair of complex geometry.” *J. Mater. Process. Technol.*, 285.

Chen, J., Tatman, J., Feng, Z., Miller, R., Curlin, S., Dai, T., Mao, K., Sutton, B., and Frederick, G. (2021). “Suppression of Helium Induced Cracking in Laser Repair Welding of Highly Irradiated Stainless Steels.” *J. Nucl. Mater.*, 556.

Chen, L., Sun, Y., Li, L., and Ren, X. (2020b). “Improvement of high temperature oxidation resistance of additively manufactured TiC/Inconel 625 nanocomposites by laser shock peening treatment.” *Addit. Manuf.*, 34(April), 101276.

Chen, Y., Yang, C., Fan, C., and Wang, M. (2022). “Microstructure evolution and mechanical properties of a nickel-based superalloy repaired using wire and arc additive manufacturing.” *Mater. Charact.*, 193.

Chou, K. J. C., and Earthman, J. C. (1997). “Characterization of low-cycle fatigue damage in Inconel 718 by laser light scanning.” *J. Mater. Res.*, 12(8), 2048–2056.

Chouhan, A., Aggarwal, A., and Kumar, A. (2018a). “Model Development in OpenFOAM for Laser Metal Deposition-based Additive Manufacturing Process.” *Trans. Indian Inst. Met.*, 71(11), 2833–2838.

Chouhan, A., Aggarwal, A., and Kumar, A. (2018b). “Model Development in OpenFOAM for Laser Metal Deposition-based Additive Manufacturing Process.” *Trans. Indian Inst. Met.*, 71(11), 2833–2838.

Chyrkin, A., Huczkowski, P., Shemet, V., Singheiser, L., and Quadakkers, W. J. (2011). “Sub-scale depletion and enrichment processes during high temperature oxidation of the nickel base alloy 625 in the temperature range 900-1000 °c.” *Oxid. Met.*, 75(3–4), 143–166.

Clarke, D. R. (2002). “Stress generation during high-temperature oxidation of metallic alloys.” *Curr. Opin. Solid State Mater. Sci.*, 6(3), 237–244.

Colorado, H. A., Velásquez, E. I. G., and Monteiro, S. N. (2020). “Sustainability of additive manufacturing: the circular economy of materials and environmental perspectives.” *J. Mater. Res. Technol.*, 9(4), 8221–8234.

Cooke, S., Ahmadi, K., Willerth, S., and Herring, R. (2020). “Metal additive manufacturing: Technology, metallurgy and modelling.” *J. Manuf. Process.*, 57, 978–1003.

Craig, O., Bois-Brochu, A., and Plucknett, K. (2021). “Geometry and surface characteristics of H13 hot-work tool steel manufactured using laser-directed energy deposition.” *Int. J. Adv. Manuf. Technol.*, 116(1–2), 699–718.

Danielewski, H., and Antoszewski, B. (2020). “Microstructure and properties of laser additive deposited of nickel base super alloy inconel 625.” *Arch. Foundry Eng.*, 20(3), 53–59.

Dass, A., and Moridi, A. (2019). “State of the art in directed energy deposition: From additive manufacturing to materials design.” *Coatings*, 9(7), 1–26.

Debroy, T. (1996). “Numerical Prediction of Fluid Flow and Heat Transfer in Welding with a Moving Heat Source.” (February).

Debroy, T., and David, S. A. (1995). “Physical processes in fusion welding.” *Rev. Mod. Phys.*, 67(1), 85–112.

Desgranges, C., Lequien, F., Aublant, E., Nastar, M., and Monceau, D. (2013). “Depletion and voids formation in the substrate during high temperature oxidation of Ni-Cr alloys.” *Oxid. Met.*, 79(1–2), 93–105.

Dodaran, M. S., Muhammad, M., Shamsaei, N., and Shao, S. (2022). “Synergistic effect of microstructure and defects on the initiation of fatigue cracks in additively manufactured Inconel 718.” *Int. J. Fatigue*, 162.

Donachie, M. J., and Donachie, S. J. (2002). “Superalloys: a technical guide.” 439.

Du, F., Zhu, J., Ding, X., Zhang, Q., Ma, H., Yang, J., Cao, H., Ling, Z., Wang, G., Duan, X., and Fan, S. (2019). “Dimensional characteristics of Ti-6Al-4V thin-walled parts prepared by wire-based multi-laser additive manufacturing in vacuum.” *Rapid Prototyp. J.*, 25(5), 849–856.

Dubiel, B., and Sieniawski, J. (2019). “Precipitates in additively manufactured inconel 625 superalloy.” *Materials (Basel).*, 12(7).

DuPont, J. N., Lippold, J. C., and Kiser, S. D. (2009). *Welding Metallurgy and Weldability of Nickel-Base Alloys. Weld. Metall. Weldability Nickel-Base Alloy.*

Faccoli, M., Cornacchia, G., Maestrini, D., Marconi, G. P., and Roberti, R. (2014). “Cold Spray Repair of Martensitic Stainless Steel Components.” *J. Therm. Spray Technol.*, 23(8), 1270–1280.

Fan, H. G., Tsai, H. L., and Na, S. J. (2001). “Heat transfer and fluid flow in a partially or fully penetrated weld pool in gas tungsten arc welding.” *Int. J. Heat Mass Transf.*, 44(2), 417–428.

Fang, J. X., Dong, S. Y., Li, S. B., Wang, Y. J., Xu, B. S., Li, J., Liu, B., and Jiang, Y. L. (2019). “Direct laser deposition as repair technology for a low transformation temperature alloy: Microstructure, residual stress, and properties.” *Mater. Sci. Eng. A*, 748(December 2018), 119–127.

Feng, B., He, J., Li, S., Gu, B., and Lin, Z. (2021). “Sheet Metal Forging Process for Thin-Walled Structures With Crossed Ribs: Process Design, Simulation and a Forming Experiment.” *Met. 2021 - 30th Anniv. Int. Conf. Metall. Mater. Conf. Proc.*, 217–222.

Ferreri, N. C., Vogel, S. C., and Knezevic, M. (2020). “Determining volume fractions of γ, γ′, γ″, δ, and MC-carbide phases in Inconel 718 as a function of its processing history using an advanced neutron diffraction procedure.” *Mater. Sci. Eng. A*, 781.

Fujishima, M., Oda, Y., Ashida, R., Takezawa, K., and Kondo, M. (2017). “Study on factors for pores and cladding shape in the deposition processes of Inconel 625 by the directed energy deposition (DED) method.” *CIRP J. Manuf. Sci. Technol.*, 19, 200–204.

Gao, Y., Ding, Y., Ma, Y., Chen, J., Wang, X., and Xu, J. (2021). “Evolution of annealing twins in Inconel 625 alloy during tensile loading.” *Mater. Sci. Eng. A*, 831(October 2021), 142188.

Gedda, H. (2004). “Laser Cladding: An Experimental and Theoretical Investigation.” *PhD Thesis, Luleå Univ. Technol. 2004*.

Geng, S., Jiang, P., Shao, X., Guo, L., and Gao, X. (2020). “Heat transfer and fluid flow and their effects on the solidification microstructure in full-penetration laser welding of aluminum sheet.” *J. Mater. Sci. Technol.*, 46, 50–63.

Ghosh, S., Ma, L., Levine, L. E., Ricker, R. E., Stoudt, M. R., Heigel, J. C., and Guyer, J. E. (2018). “Single-Track Melt-Pool Measurements and Microstructures in Inconel 625.” *Jom*, 70(6), 1011–1016.

Gibson, I., Rosen, D., and Stuker, B. (2013). “Additive Manufacturing Technologies: 3D Printing, Rapid Prototyping, and Direct Digital Manufacturing.” *Rapid Manuf. Assoc.*, 10–12.

Hapsoro, A., Hanipa, H., and Grebinnyk, K. (2021). “Repair of Cracked 150 MW High-Pressure Steam Turbine Rotor Coupling.” *IOP Conf. Ser. Mater. Sci. Eng.*, 1096(1), 012124.

Hattingh, D. G., James, M. N., Newby, M., Scheepers, R., and Doubell, P. (2016). “Damage assessment and refurbishment of steam turbine blade/rotor attachment holes.” *Theor. Appl. Fract. Mech.*, 83, 125–134.

He, X., Elmer, J. W., and Debroy, T. (2005). “Heat transfer and fluid flow in laser microwelding.” *J. Appl. Phys.*, 97(8).

Hernando, I., Renderos, M. A., Cortina, M., Ruiz, J. E., Arrizubieta, J. I., and Lamikiz, A. (2018). “Inconel 718 laser welding simulation tool based on a France moving heat source and phase change.” *Procedia CIRP*, 74, 674–678.

Hou, X. M., and Chou, K. C. (2009). “Quantitative interpretation of the parabolic and nonparabolic oxidation behavior of nitride ceramic.” *J. Eur. Ceram. Soc.*, 29(3), 517–523.

Hoyingchareon, K., and Muangjunburee, P. (2016). “Welding repair of aluminium alloy 6082 T6 by TIG welding process.” *Mater. Sci. Forum*, 872, 3–7.

Hu, D., and Kovacevic, R. (2003). “Sensing, modeling and control for laser-based additive manufacturing.” *Int. J. Mach. Tools Manuf.*, 43(1), 51–60.

Hu, Y. L., Li, Y. L., Zhang, S. Y., Lin, X., Wang, Z. H., and Huang, W. D. (2020a). “Effect of solution temperature on static recrystallization and ductility of Inconel 625 superalloy fabricated by directed energy deposition.” *Mater. Sci. Eng. A*, 772(July 2019).

Hu, Y. L., Li, Y. L., Zhang, S. Y., Lin, X., Wang, Z. H., and Huang, W. D. (2020b). “Effect of solution temperature on static recrystallization and ductility of Inconel 625 superalloy fabricated by directed energy deposition.” *Mater. Sci. Eng. A*, 772.

Hu, Y. L., Lin, X., Li, Y. L., Wang, J., Zhang, S. Y., Lu, X. F., and Huang, W. D. (2019). “Effect of heat treatment on the microstructural evolution and mechanical properties of GH4099 additive-manufactured by directed energy deposition.” *J. Alloys Compd.*, 800, 163–173.

Hu, Y. L., Lin, X., Li, Y. L., Zhang, S. Y., Gao, X. H., Liu, F. G., Li, X., and Huang, W. D. (2020c). “Plastic deformation behavior and dynamic recrystallization of Inconel 625 superalloy fabricated by directed energy deposition.” *Mater. Des.*, 186.

Hu, Y. L., Lin, X., Lu, X. F., Zhang, S. Y., Yang, H. O., Wei, L., and Huang, W. D. (2018a). “Evolution of solidification microstructure and dynamic recrystallisation of Inconel 625 during laser solid forming process.” *J. Mater. Sci.*, 53(22), 15650–15666.

Hu, Y. L., Lin, X., Zhang, S. Y., Jiang, Y. M., Lu, X. F., Yang, H. O., and Huang, W. D. (2018b). “Effect of solution heat treatment on the microstructure and mechanical properties of Inconel 625 superalloy fabricated by laser solid forming.” *J. Alloys Compd.*, 767, 330–344.

Hu, Y., Lin, X., Li, Y., Zhang, S., Zhang, Q., Chen, W., Li, W., and Huang, W. (2021). “Influence of heat treatments on the microstructure and mechanical properties of Inconel 625 fabricated by directed energy deposition.” *Mater. Sci. Eng. A*, 817.

Huczkowski, P., Lehnert, W., Angermann, H. H., Chyrkin, A., Pillai, R., Grüner, D., Hejrani, E., and Quadakkers, W. J. (2017). “Effect of gas flow rate on oxidation behaviour of alloy 625 in wet air in the temperature range 900–1000 °C.” *Mater. Corros.*, 68(2), 159–170.

Jhavar, S., Paul, C. P., and Jain, N. K. (2013). “Causes of failure and repairing options for dies and molds: A review.” *Eng. Fail. Anal.*, 34, 519–535.

Jinoop, A. N., Nayak, S. K., Yadav, S., Paul, C. P., Singh, R., Kumar, J. G., and Bindra, K. S. (2021a). “Effect of scan pattern on Hastelloy-X wall structures built by laser-directed energy deposition-based additive manufacturing.” *J. Micromanufacturing*, 4(2), 179–188.

Jinoop, A. N., Paul, C. P., Nayak, S. K., Kumar, J. G., and Bindra, K. S. (2021b). “Effect of laser energy per unit powder feed on Hastelloy-X walls built by laser directed energy deposition based additive manufacturing.” *Opt. Laser Technol.*, 138.

Kalfhaus, T., Schneider, M., Ruttert, B., Sebold, D., Hammerschmidt, T., Frenzel, J., Drautz, R., Theisen, W., Eggeler, G., Guillon, O., and Vassen, R. (2019). “Repair of Ni-based single-crystal superalloys using vacuum plasma spray.” *Mater. Des.*, 168.

Kim, M. J., and Saldana, C. (2020). “Thin wall deposition of IN625 using directed energy deposition.” *J. Manuf. Process.*, 56, 1366–1373.

Kim, T. G., and Shim, D. S. (2021). “Effect of laser power and powder feed rate on interfacial crack and mechanical/microstructural characterizations in repairing of 630 stainless steel using direct energy deposition.” *Mater. Sci. Eng. A*, 828.

King, A. M., Burgess, S. C., Ijomah, W., and McMahon, C. A. (2006). “Reducing waste: Repair, recondition, remanufacture or recycle?” *Sustain. Dev.*, 14(4), 257–267.

Kou, S. (2003). “Fluid Flow and Metal.” *Weld. Metall.*, John Wiley & Sons, Ltd, 97–122.

Kumar, A., Paul, C. P., Pathak, A. K., Bhargava, P., and Kukreja, L. M. (2012). “A finer modeling approach for numerically predicting single track geometry in two dimensions during Laser Rapid Manufacturing.” *Opt. Laser Technol.*, 44(3), 555–565.

Kumara, C., Segerstark, A., Hanning, F., Dixit, N., Joshi, S., Moverare, J., and Nylén, P. (2019). “Microstructure modelling of laser metal powder directed energy deposition of alloy 718.” *Addit. Manuf.*, 25(23), 357–364.

La Batut, B. de, Fergani, O., Brotan, V., Bambach, M., and Mansouri, M. El. (2017). “Analytical and Numerical Temperature Prediction in Direct Metal Deposition of Ti6Al4V.” *J. Manuf. Mater. Process.*, 1(1), 3.

Lampa, C., Kaplan, A. F. H., Powell, J., and Magnusson, C. (1997). “An analytical thermodynamic model of laser welding.” *J. Phys. D. Appl. Phys.*, 30(9), 1293–1299.

Lee, J. H., Lee, C. M., and Kim, D. H. (2022). “Repair of damaged parts using wire arc additive manufacturing in machine tools." *J. Mater. Res. Technol.*, 16, 13–24.

Li, T., Zhang, L., Chang, C., and Wei, L. (2018). "A Uniform-Gaussian distributed heat source model for analysis of residual stress field of S355 steel T welding." *Adv. Eng. Softw.*, 126, 1–8.

Liu, D., Lippold, J. C., Li, J., Rohklin, S. R., Vollbrecht, J., and Grylls, R. (2014). "Laser engineered net shape (LENS) technology for the repair of Ni-base superalloy turbine components." *Metall. Mater. Trans. A Phys. Metall. Mater. Sci.*, 45(10), 4454–4469.

Liu, G., Du, D., Wang, K., Pu, Z., Zhang, D., and Chang, B. (2021a). "High-temperature oxidation behavior of a directionally solidified superalloy repaired by directed energy deposition." *Corros. Sci.*, 193.

Liu, G., Du, D., Wang, K., Pu, Z., Zhang, D., and Chang, B. (2021b). "Microstructure and nanoindentation creep behavior of IC10 directionally solidified superalloy repaired by laser metal deposition." *Mater. Sci. Eng. A*, 808.

Liu, M., Kumar, A., Bukkapatnam, S., and Kuttolamadom, M. (2021c). "A Review of the Anomalies in Directed Energy Deposition (DED) Processes & Potential Solutions - Part Quality & Defects." *Procedia Manuf.*, 53, 507–518.

Liu, Z., Jiang, Q., Li, T., Dong, S., Yan, S., Zhang, H., and Xu, B. (2016). "Environmental benefits of remanufacturing: A case study of cylinder heads remanufactured through laser cladding." *J. Clean. Prod.*, 133, 1027–1033.

Liu, Z., and Shu, J. (2021). "Control of the microstructure formation in the near-net-shape laser additive tip-remanufacturing process of single-crystal superalloy." *Opt. Laser Technol.*, 133.

Lu, S., Fujii, H., Sugiyama, H., Tanaka, M., and Nogi, K. (2003). "Effects of Oxygen Additions to Argon Shielding Gas on GTA Weld Shape." *ISIJ Int.*, 43(10), 1590–1595.

Luzin, V., and Hoye, N. (2017). "Stress in Thin Wall Structures Made by Layer Additive Manufacturing." *Residual Stress. 2016*, 2, 497–502.

Maddela, N., Aluri, M., and M.d., J. (2021). "Study on defects repairing using Friction Stir technologies." *Mater. Today Proc.*, 44, 2373–2379.

Mahamood, R. M., and Akinlabi, E. T. (2017). "Scanning speed and powder flow rate influence on the properties of laser metal deposition of titanium alloy." *Int. J. Adv. Manuf. Technol.*, 91(5–8), 2419–2426.

Maimaitiyili, T., Woracek, R., Neikter, M., Boin, M., Wimpory, R. C., Pederson, R., Strobl, M., Drakopoulos, M., Schäfer, N., and Bjerkén, C. (2019). "Residual lattice strain and phase distribution in Ti-6Al-4V produced by electron beam melting." *Materials (Basel).*, 12(4).

Maleki, E., Bagherifard, S., Bandini, M., and Guagliano, M. (2021). "Surface post-treatments for metal additive manufacturing: Progress, challenges, and opportunities." *Addit. Manuf.*, 37.

Manvatkar, V., De, A., and DebRoy, T. (2015). "Spatial variation of melt pool geometry, peak temperature and solidification parameters during laser assisted additive manufacturing process." *Mater. Sci. Technol. (United Kingdom)*, 31(8), 924–930.

Meng, D. H., Zhou, B., Wu, D., Ma, Y. Q., Chen, R. S., and Li, P. J. (2019). "Parameter Optimization of Gas Tungsten-Arc Repair Welding Technique in Mg–6Gd–3Y–0.5Zr Alloy." *Int. J. Met.*, 13(2), 345–353.

Mukherjee, T., Wei, H. L., De, A., and DebRoy, T. (2018). "Heat and fluid flow in additive manufacturing—Part I: Modeling of powder bed fusion." *Comput. Mater. Sci.*, 150, 304–313.

Mukherjee, T., Zhang, W., and DebRoy, T. (2017). "An improved prediction of residual stresses and distortion in additive manufacturing." *Comput. Mater. Sci.*, 126, 360–372.

Myers, R. H., and Myers, S. L. (2007). *Probability & Statistics for Engineers Scientists Probability & Statistics for Engineers & Scientists*. *Prentice Hall*.

N., H. (2004). "Hall-Petch relation and boundary strengthening." *Scr. Mater.*, 801.

Nair, A. M., Muvvala, G., Sarkar, S., and Nath, A. K. (2020). "Real-time detection of cooling rate using pyrometers in tandem in laser material processing and directed energy deposition." *Mater. Lett.*, 277, 128330.

Nguejio, J., Szmytka, F., Hallais, S., Tanguy, A., Nardone, S., and Godino Martinez, M. (2019). "Comparison of microstructure features and mechanical properties for additive manufactured and wrought nickel alloys 625." *Mater. Sci. Eng. A*, 764.

Pacheco, J. T., Meura, V. H., Rafael, P., Bloemer, A., Veiga, M. T., Moura, O. C. De, and Cunha, A. (2022). "Laser directed energy deposition of AISI 316L stainless steel : The effect of build direction on mechanical properties in as-built and heat-treated conditions." 4(February).

Parizia, S., Marchese, G., Rashidi, M., Lorusso, M., Hryha, E., Manfredi, D., and Biamino, S. (2020). "Effect of heat treatment on microstructure and oxidation properties of Inconel 625 processed by LPBF." *J. Alloys Compd.*, 846, 156418.

Paul, S., Singh, R., and Yan, W. (2016). "Thermal model for additive restoration of mold steels using crucible steel." *J. Manuf. Process.*, 24, 346–354.

Peng, L., Shengqin, J., Xiaoyan, Z., Qianwu, H., and Weihao, X. (2007). "Direct laser fabrication of thin-walled metal parts under open-loop control." *Int. J. Mach. Tools Manuf.*, 47(6), 996–1002.

Piscopo, G., and Iuliano, L. (2022). "Current research and industrial application of laser powder directed energy deposition." *Int. J. Adv. Manuf. Technol.*, (0123456789).

Plessis, A. du. (2019). "Effects of process parameters on porosity in laser powder bed fusion revealed by X-ray tomography." *Addit. Manuf.*, 30.

Ramenatte, N., Vernouillet, A., Mathieu, S., Put, A. Vande, Vilasi, M., and Monceau, D. (2020a). "A comparison of the high-temperature oxidation behaviour of conventional wrought and laser beam melted Inconel 625." *Corros. Sci.*, 164(July 2019), 108347.

Ramenatte, N., Vernouillet, A., Mathieu, S., Put, A. Vande, Vilasi, M., and Monceau, D. (2020b). "A comparison of the high-temperature oxidation behaviour of conventional wrought and laser beam melted Inconel 625." *Corros. Sci.*, 164.

Reed, R. C. (2006). *The Superalloys fundamentals and applications. Cambridge Univ. Press*.

Robino, C. V. (1996). "Representation of mixed reactive gases on free energy (Ellingham - Richardson) diagrams." *Metall. Mater. Trans. B Process Metall. Mater. Process. Sci.*, 27(1), 65–69.

Rolland, R. (2012). "Study of water vapor influence in high temperature oxidation for a chromia forming nickel base alloy."

Rousseau, F., Guyon, C., Morvan, D., Bacos, M. P., Lavigne, O., Rio, C., Guinard, C., and Chevillard, B. (2021). "Low power plasma spray assisted thermal barrier coating repair without the plugging of cooling holes." *Surf. Coatings Technol.*, 412.

Sabau, A. S., Yuan, L., Raghavan, N., Bement, M., Simunovic, S., Turner, J. A., and Gupta, V. K. (2020). "Fluid Dynamics Effects on Microstructure Prediction in Single-Laser Tracks for Additive Manufacturing of IN625." *Metall. Mater. Trans. B Process Metall. Mater. Process. Sci.*, 51(3), 1263–1281.

Sachitanand, R., Svensson, J. E., and Froitzheim, J. (2015). "The Influence of Cr Evaporation on Long Term Cr Depletion Rates in Ferritic Stainless Steels." *Oxid. Met.*, 84(3–4), 241–257.

SAFARZADE, A., SHARIFITABAR, M., and SHAFIEE AFARANI, M. (2020). "Effects of heat treatment on microstructure and mechanical properties of Inconel 625 alloy fabricated by wire arc additive manufacturing process." *Trans. Nonferrous Met. Soc. China (English Ed.*, 30(11), 3016–3030.

Sahraoui, T., Fenineche, N. E., Montavon, G., and Coddet, C. (2004). "Alternative to chromium: Characteristics and wear behavior of HVOF coatings for gas turbine shafts repair (heavy-duty)." *J. Mater. Process. Technol.*, 152(1), 43–55.

Salarian, M., Asgari, H., and Vlasea, M. (2020). "Pore space characteristics and corresponding effect on tensile properties of Inconel 625 fabricated via laser powder bed fusion." *Mater. Sci. Eng. A*, 769(August 2019), 138525.

Schoinochoritis, B., Chantzis, D., and Salonitis, K. (2017). “Simulation of metallic powder bed additive manufacturing processes with the finite element method: A critical review.” *Proc. Inst. Mech. Eng. Part B J. Eng. Manuf.*, 231(1), 96–117.

Shankar, V., Bhanu Sankara Rao, K., and Mannan, S. L. (2001). “Microstructure and mechanical properties of Inconel 625 superalloy.” *J. Nucl. Mater.*, 288(2–3), 222–232.

Shao, J., Yu, G., He, X., Li, S., Chen, R., and Zhao, Y. (2019). “Grain size evolution under different cooling rate in laser additive manufacturing of superalloy.” *Opt. Laser Technol.*, 119(March), 105662.

Shinjo, J., and Panwisawas, C. (2022). “Chemical species mixing during direct energy deposition of bimetallic systems using titanium and dissimilar refractory metals for repair and biomedical applications.” *Addit. Manuf.*, 51.

Shoemaker, L. E. (2012). “Alloys 625 and 725: Trends in Properties and Applications.” 409–418.

Sousa Malafaia, A. M. de, Oliveira, R. B. de, Latu-Romain, L., Wouters, Y., and Baldan, R. (2020). “Isothermal oxidation of Inconel 625 superalloy at 800 and 1000 °C: Microstructure and oxide layer characterization.” *Mater. Charact.*, 161.

Special Metals Corp. (2013). “INCONEL alloy 625.” *Spec. Met. Datasheets*, 625(2), 1–28.

Steinhilper, R. (1998). *Remanufacturing: The ultimate form of recycling. Proc. Air Waste Manag. Assoc. Annu. Meet. Exhib.*

Su, C. Y., Chou, C. P., Wu, B. C., and Lih, W. C. (1997). “Plasma transferred arc repair welding of the nickel-base superalloy IN-738LC.” *J. Mater. Eng. Perform.*, 6(5), 619–627.

Sui, S., Chen, J., Fan, E., Yang, H., Lin, X., and Huang, W. (2017). “The influence of Laves phases on the high-cycle fatigue behavior of laser additive manufactured Inconel 718.” *Mater. Sci. Eng. A*, 695, 6–13.

Sui, S., Chen, J., Ma, L., Fan, W., Tan, H., Liu, F., and Lin, X. (2019). “Microstructures and stress rupture properties of pulse laser repaired Inconel 718 superalloy after different heat treatments.” *J. Alloys Compd.*, 770, 125–135.

Sun, G. F., Shen, X. T., Wang, Z. D., Zhan, M. J., Yao, S., Zhou, R., and Ni, Z. H. (2019). “Laser metal deposition as repair technology for 316L stainless steel: Influence of feeding powder compositions on microstructure and mechanical properties.” *Opt. Laser Technol.*, 109, 71–83.

Sun, Y., Chen, L., Li, L., and Ren, X. (2020a). “High-temperature oxidation behavior and mechanism of Inconel 625 super-alloy fabricated by selective laser melting.” *Opt. Laser Technol.*, 132.

Sun, Z., Guo, W., and Li, L. (2020b). “Numerical modelling of heat transfer, mass transport and microstructure formation in a high deposition rate laser directed energy deposition process.” *Addit. Manuf.*, 33.

Suryanarayana, C., and Norton, M. G. (1998). *X-Ray Diffraction*. *Choice Rev. Online*, Boston, MA: Springer US.

Svensson, H., Knutsson, P., and Stiller, K. (2009). “Formation and healing of voids at the metal-oxide interface in NiAl alloys.” *Oxid. Met.*, 71(3–4), 143–156.

Tan, J. C., Looney, L., and Hashmi, M. S. J. (1999). “Component repair using HVOF thermal spraying.” *J. Mater. Process. Technol.*, 92–93, 203–208.

Tong, X., Wu, G., Zhang, L., Wang, Y., Liu, W., and Ding, W. (2020). “Microstructure and mechanical properties of repair welds of low-pressure sand-cast Mg–Y–RE–Zr alloy by tungsten inert gas welding.” *J. Magnes. Alloy.*

Toyserkani, E., Khajepour, A., and Corbin, S. (2004). “3-D finite element modeling of laser cladding by powder injection: Effects of laser pulse shaping on the process.” *Opt. Lasers Eng.*, 41(6), 849–867.

Underhill, J. W. (2012). “Refurbishment of superalloy components for gas turbines–scope and reward.” *Mater. Sci. Technol.*, 1(8), 604–607.

Vafadar, A., Guzzomi, F., Rassau, A., and Hayward, K. (2021). “Advances in metal additive manufacturing: A review of common processes, industrial applications, and current challenges.” *Appl. Sci.*, 11(3), 1–33.

Vahdatkhah, P., Tabatabaee Kopaee, S. R., and Vahdat khah, H. (2022). “Weld repair of gas turbine disc: optimization of pulsed TIG welding process parameters and microstructural analysis of Cr–Mo-V Steel.” *Int. J. Adv. Manuf. Technol.*, 123(1–2), 213–232.

Vikram, R. J., Singh, A., and Suwas, S. (2020). “Effect of heat treatment on the modification of microstructure of selective laser melted (SLM) IN718 and its consequences on mechanical behavior.” *J. Mater. Res.*, 35(15), 1949–1962.

Wang, J., Prakash, S., Joshi, Y., and Liou, F. (2002). “Laser Aided Part Repair - A review.” *13th Annu. Solid Free. Fabr. Symp.*, (May), 57–64.

Wang, J., WANG, X. wei, LI, B., CHEN, C., and LU, X. feng. (2021a). “Interface repairing for AA5083/T2 copper explosive composite plate by friction stir processing.” *Trans. Nonferrous Met. Soc. China (English Ed.*, 31(9), 2585–2596.

Wang, J., Wang, Y., Su, Y., and Shi, J. (2021b). “Evaluation of in-situ alloyed Inconel 625 from elemental powders by laser directed energy deposition.” *Mater. Sci. Eng. A*, (November), 142296.

Wang, N., Shen, J., Hu, S., and Liang, Y. (2020). “Numerical analysis of the TIG arc preheating effect in CMT based cladding of Inconel 625." *Eng. Res. Express*.

Wang, X., Huang, J., Huang, Y., Fan, D., and Guo, Y. (2017a). "Investigation of heat transfer and fluid flow in activating TIG welding by numerical modeling." *Appl. Therm. Eng.*, 113(November), 27–35.

Wang, X., Jiang, J., and Tian, Y. (2022a). "A Review on Macroscopic and Microstructural Features of Metallic Coating Created by Pulsed Laser Material Deposition." *Micromachines*, 13(5), 1–23.

Wang, Z. D., Sun, G. F., Chen, M. Z., Lu, Y., Zhang, S. B., Lan, H. F., Bi, K. D., and Ni, Z. H. (2021c). "Investigation of the underwater laser directed energy deposition technique for the on-site repair of HSLA-100 steel with excellent performance." *Addit. Manuf.*, 39.

Wang, Z. D., Yang, K., Chen, M. Z., Lu, Y., Bi, K. D., Sun, G. F., and Ni, Z. H. (2022b). "Investigation of the microstructure and mechanical properties of Ti–6Al–4V repaired by the powder-blown underwater directed energy deposition technique." *Mater. Sci. Eng. A*, 831.

Wang, Z., Denlinger, E., Michaleris, P., Stoica, A. D., Ma, D., and Beese, A. M. (2017b). "Residual stress mapping in Inconel 625 fabricated through additive manufacturing: Method for neutron diffraction measurements to validate thermomechanical model predictions." *Mater. Des.*, 113, 169–177.

Wang, Z., Palmer, T. A., and Beese, A. M. (2016). "Effect of processing parameters on microstructure and tensile properties of austenitic stainless steel 304L made by directed energy deposition additive manufacturing." *Acta Mater.*, 110, 226–235.

Wong, H., Dawson, K., Ravi, G. A., Howlett, L., Jones, R. O., and Sutcliffe, C. J. (2019). "Multi-Laser Powder Bed Fusion Benchmarking—Initial Trials with Inconel 625." *Int. J. Adv. Manuf. Technol.*, 105(7–8), 2891–2906.

Wu, C. S. (2010). *Welding Thermal Processes and Weld Pool Behaviors*. China Machine Press.

Xia, P. C., Chen, F. W., Xie, K., Qiao, L., and Yu, J. J. (2015). "Influence of microstructures on thermal fatigue property of a nickel-base superalloy." *Front. Mater. Sci.*, 9(1), 85–92.

Xu, M., Li, J., Jiang, J., and Li, B. (2015). "Influence of powders and process parameters on bonding shear strength and micro hardness in laser cladding remanufacturing." *Procedia CIRP*, 29, 804–809.

Yadroitsev, I., Yadroitsava, I., Plessis, A. du, and MacDonald, E. (2021). "Fundamentals of Laser Powder Bed Fusion of Metals." *Fundam. Laser Powder Bed Fusion Met.*

Yang, F., Dong, L., Hu, X., Zhou, X., Xie, Z., and Fang, F. (2020). "Effect of solution treatment temperature upon the microstructure and mechanical properties of hot rolled Inconel 625 alloy." *J. Mater. Sci.*, 55(13), 5613–5626.

Yang, L. X., Peng, X. F., and Wang, B. X. (2001). "Numerical modeling and experimental investigation on the characteristics of molten pool during laser processing." *Int. J. Heat Mass Transf.*, 44(23), 4465–4473.

Yangfan, W., Xizhang, C., and Chuanchu, S. (2019). "Microstructure and mechanical properties of Inconel 625 fabricated by wire-arc additive manufacturing." *Surf. Coatings Technol.*, 374, 116–123.

Zacharia, T., David, S. A., Vitek, J. M., and Debroy, T. (1989). "Weld pool development during GTA and laser beam welding of type 304 stainless steel Part II. Experimental correlation." *Weld. J. (Miami, Fla)*, 68(12), 510–520.

Zawada-Michałowska, M., Kuczmaszewski, J., Legutko, S., and Pieśko, P. (2020). "Techniques for thin-walled element milling with respect to minimising post-machining deformations." *Materials (Basel).*, 13(21), 1–17.

Zeng, Y., Li, L., Huang, W., Zhao, Z., Yang, W., and Yue, Z. (2022). "Effect of thermal cycles on laser direct energy deposition repair performance of nickel-based superalloy: Microstructure and tensile properties." *Int. J. Mech. Sci.*, 221(February), 107173.

Zhu, J., Li, L., Li, D., Li, X., Zhong, H., Li, S., Lei, L., Li, J., and Zhang, Y. (2022). "Microstructural evolution and mechanical properties of laser repaired 12Cr12Mo stainless steel." *Mater. Sci. Eng. A*, 830.

Zhuo, Y., Yang, C., Fan, C., Lin, S., Chen, C., and Cai, X. (2020). "Microstructure and mechanical properties of wire arc additive repairing Ti–6.5Al–2Sn–2Zr–4Mo–4Cr titanium alloy." *Mater. Sci. Technol. (United Kingdom)*, 36(15), 1712–1719.

LIST OF PUBLICATIONS BASED ON PHD RESEARCH WORK

Sl No.	Title of the paper	Authors (in the same order as in the paper. Underline the Research Scholar's name)	Name of the Journal/ Conference, Vol., No., Pages	Month, Year of Publication	Category
1	Effect of deposition strategy and post processing on microstructure and mechanical properties of serviced Inconel 625 parts repaired using laser directed energy deposition	**Jitender K Chaurasia**, AN Jinoop, CP Paul, KS Bindra, Vamsi Krishna Balla, Srikanth Bontha	Optics & Laser Technology Volume:168 Article No.:109831	January 2024 (Accepted in August 2023)	1
2	Study of melt pool geometry and solidification microstructure during laser surface melting of Inconel 625 alloy	**Jitender K. Chaurasia**, A.N. Jinoop, Parthasarathy P, C.P. Paul, K.S. Bindra, Srikanth Bontha	Optik: International Journal for Light and Electron Optics, Volume 246, page 1-12	November, 2021	1
3	Understanding thermo-fluid behaviour during Laser Surface Melting of IN625	**Jitender K. Chaurasia**, A N Jinoop, Parthasarathy P, Srikanth Bontha, C. P. Paul, K.S. Bindra	National Metallurgists' Day and the Annual Technical Meeting (NMD -ATM) of Indian Institute of Metals 2019, Trivandrum	November, 2019	4
4	An enthalpy based finite element approach to predict single track geometry during Laser Directed Energy Deposition of Inconel 718	**Jitender K. Chaurasia**, Danish Ashraf, A N Jinoop, Srikanth Bontha, C. P. Paul, K.S. Bindra	International Conference on Precision, Meso, Micro & Nano Engineering, IIT-Indore	December, 2019	4
5	Understanding thermal behaviour during Laser Surface Melting of SS 316L	Sai Krishna VP, **Jitender Kumar Chaurasia**, S.M. Shariff, Srikanth Bontha	National Metallurgists' Day and the Annual Technical Meeting (NMD -ATM) of Indian Institute of Metals, 2018, Kolkata	November, 2018	4

OTHER PUBLICATIONS

6	Effect of build orientation on anisotropy in tensile behaviour of laser powder bed fusion fabricated SS316L	Raja S. Thanumoorthy, **Jitender K. Chaurasia,** V. Anil Kumar, P.I. Pradeep, ASS Balan, B. Rajasekaran, Ankit Sahu, Srikanth Bontha	Journal of Materials Engineering and Performance	June, 2023	1
7	Integrated Numerical Modelling and Machine Learning Approaches to Predict Melt Pool Dimensions during Deposition of SS316L Single Tracks using Laser Powder Bed Fusion Process	Raja S. Thanumoorthy, **Jitender K. Chaurasia**, Srikanth Bontha, A.S.S. Balan, V. Anil Kumar	International Conference on Product Life Cycle Modelling, Simulation and Synthesis (PLMSS) - Product Life Cycle – Space Systems Perspective	December, 2021	4
8	Analytical modelling to predict dimensions of single tracks during Laser Direct Energy Deposition of Inconel 625	M. Mithun Kumar, Amit K. Praharaj, Raja S. Thanumoorthy, **Jitender K. Chaurasia**, G. Ravi Chandan, ASS Balan, P. S. Suvin, V. Anil Kumar, Srikanth Bontha	National Aerospace Manufacturing Seminar (NAMS 2022) held at Vikram Sarabhai Space Centre, ISRO	May, 2022	4
9	Analytical and Numerical Modelling to Predict Track Geometry of Laser Directed Energy Deposited Titanium Aluminide Alloy	G. Ravi Chandan, M. Mithun Kumar, **Jitender K. Chaurasia**, Prasad Krishna, Srikanth Bontha	Metal Additive Manufacturing Symposium 2022 held at Taj Vivanta Yeshwantpur, Bengaluru	July, 2022	4

Category*. 1. Journal paper, full paper reviewed
2. Journal paper, Abstract reviews
3. Conference/Symposium paper, full paper reviewed
4. Conference/Symposium paper, abstract reviewed
5. others (including papers in Workshops, NITK Research Bulletins, Short notes etc.)

17/08/23
Jitender Kumar Chaurasia
Research Scholar
Name & Signature, with date

22/08/2023
Dr. Srikanth Bontha
Research Guide
Name & Signature, with date

BIO-DATA

1	**Name**	**:**	Jitender Kumar Chaurasia
2	**Fathers Name**	**:**	Mahadev Prasad Chaurasia
3	**Date of Birth**	**:**	20 December 1990
4	**Nationality**	**:**	Indian
5	**Marital status**	**:**	Married
6	**Address**	**:**	House No. 208, Chaudhary Charan Singh Colony, Mauli Jagran Complex, Chandigarh – 160102
7	**Mobile number**	**:**	9780331644
8	**Email id**	**:**	jitender.chaurasia@gmail.com

9 Educational qualifications

Qualification	University/Board	Year of passing
Ph.D. (Mechanical Engineering)	National Institute of Technology Karnataka, Surathkal, India	2023
M.Tech. (Manufacturing Engineering)	Vellore Institute of Technology (VIT University), Vellore, Tamil Nadu, India	2016
B.Tech. (Mechanical Engineering)	Punjab Technical University, Kapurthala, Punjab, India	2013
Diploma in Engineering (Mechanical Engineering)	Punjab State Board of Technical Education & Industrial Training, Chandigarh, India	2010